TECHNISCHE UNIVERSITÄT MÜNCHEN
Fakultät für Maschinenwesen
Lehrstuhl für Leichtbau

Shape and Sizing Optimization of Aircraft Structures with Aeroelastic and Induced Drag Requirements

Sebastian Moritz Deinert

Vollständiger Abdruck der von der Fakultät für Maschinenwesen der Technischen Universität München zur Erlangung des akademischen Grades eines

Doktor-Ingenieurs (Dr.-Ing.)

genehmigten Dissertation.

Vorsitzender:	Univ.-Prof. Dr.-Ing. Mirko Hornung
Prüfer der Dissertation:	
1.	Univ.-Prof. Dr.-Ing. Horst Baier
2.	apl. Prof. Dr.-Ing. Christian W. M. Breitsamter

Die Dissertation wurde am 02.05.2016 bei der Technischen Universität München eingereicht und durch die Fakultät für Maschinenwesen am 18.10.2016 angenommen.

To my parents.

Acknowledgements

I would like to express my thanks to my supervisor, Univ.-Prof. Dr.-Ing. Horst Baier, for his advice and guidance.

Furthermore, I would like to thank apl. Prof. Dr.-Ing. Christian Breitsamter for his interest in my work and for co-reviewing this thesis.

I am very grateful to Dr. Fernaß Daoud and Dr. Gerd Schuhmacher for giving me the opportunity to carry out my research at Airbus Defence and Space.

Furthermore, I would like to thank my colleagues Paul Bronny, Ögmundur Petersson, Reinhold Maierl, Markus Wagner, Dr. Rainer Zotemantel, Dr. Alexander Hörmann and Daniel Nussbächer for the fruitful every day discussions and insights.

Last but not least, I would like to express my deep gratitude to my parents for supporting and encouraging me throughout this work.

München, November 2016 Sebastian Moritz Deinert

Abstract

In this dissertation a framework for multidisciplinary shape and sizing optimization focusing on aeroelastic analysis and induced drag suitable for application in aircraft design is developed. In order to enable application already in early aircraft design phases, where a great shape design freedom is still present, low or medium fidelity analysis methods are employed in a coupled manner in the stationary aeroelastic analysis. For large scale problems with an extensive design criteria model that guarantee feasibility of the results, a single optimization loop architecture employing a gradient based optimization algorithm is devised. The required shape parametrization approach is based on the CPACS data format (developed by the DLR) and a central parametric geometry model is applied allowing robust and consistent shape manipulations of all involved analysis models. Aerodynamic influence coefficient matrices are used to efficiently evaluate pressure distributions, as well as, the overall induced drag coefficient based on the Trefftz Plane method during the aeroelastic analysis. Applying the developed framework, the different aspects of such a shape and sizing optimization problem are studied. Along this course, the questions of what characterizes a good wing design and how to reach it using different objective functions are treated. Furthermore, different shape design variable types and the issues their combinations can cause regarding the optimization's design space are examined. Finally, a robust approach for applying the aeroelastic shape and sizing optimization framework to aircraft wing design problems is developed and tested. Employing this approach, the model of a transport aircraft of industrial scale size and complexity is optimized showing the advantages of the chosen approach.

Kurzfassung

In dieser Dissertation wird ein Framework zur multidisziplinären Form- und Dickenoptimierung mit Fokus auf aeroelastischer Analyse und induziertem Widerstand entwickelt, welcher Anwendung im Prozess des Flugzeugentwurfs findet. Um eine Verwendung schon in der frühen Flugzeugentwicklungsphase, wo noch große Entwurfsfreiheit zur Verfügung steht, zu ermöglichen, werden Analysemethoden von geringer bis mittlerer Genauigkeit verwendet und zu einer stationären aeroelastischen Analyse gekoppelt. Zur Anwendung bei großen Optimierungsproblemen mit einem umfangreichen Kriterienmodell, das die technische Verwertbarkeit der Ergebnisse sicherstellt, wird eine Architektur mit einer einzigen übergeordneten Optimierungsschleife unter Einsatz von gradientenbasierten Optimierungsalgorithmen entworfen. Der dazu notwendige Ansatz zur Geometrieparametrisierung verwendet das CPACS Datenformat (entwickelt vom DLR) zusammen mit einer zentralen parametrischen Geometrie, wodurch robuste sowie konsistente Formmanipulationen aller beteiligten Analysemodelle ermöglicht wird. Aerodynamische Einflusskoeffizientenmatrizen werden während der aeroelastischen Analyse zur effizienten Auswertung der Druckverteilungen wie auch des induzierten Widerstandes basierend auf der Trefftzebenen Analyse verwendet. Bei der Anwendung des entworfenen Frameworks werden verschiedene Aspekte solcher Form- und Dickenoptimierungsprobleme erforscht. Darunter werden Fragen wie “Was charakterisiert einen guten Flügelentwurf?” und, wie man einen solchen durch verschiedene Zielfunktionen erreichen kann, behandelt. Darüber hinaus werden verschiedene Formvariablentypen und Probleme betreffend des Entwurfsraumes, die durch bestimmte Kombinationen von Variablen verursacht werden können, untersucht. Abschließend wird eine robuste Herangehensweise, um den entwickelten Framework zur Form- und Dickenoptimierung bei Flügelentwurfsproblemen anzuwenden, hergeleitet und getestet. Zur Demonstration dieses Ansatzes wird das Modell eines Transportflugzeuges von industrieller Größe und Komplexität optimiert und die Vorteile der Herangehensweise aufgezeigt.

Contents

List of Figures

List of Tables

Nomenclature

α_{ind}	Induced angle of attack
$\alpha_{L0}(y)$	Zero lift angle of attack of local spanwise wing section in case of wing camber
$\alpha_{Twist}(y)$	Twist angle of local spanwise wing section at position y
$\boldsymbol{\lambda}$	Adjoint vector
ΔC_P	Difference in pressure coefficient between upper and lower side of wing panel
Δy	Vortex lattice panel span in y-direction
ϵ	Structural strain
Γ	Horse-shoe vortex singularity strength
γ	Wing dihedral angle
Λ	Wing aspect ratio
$\mathbf{AIC}$	Downwash aerodynamic influence coefficient matrix
$\mathbf{AIC}_{C_D}$	Aerodynamic influence coefficient matrix for induced drag coefficient
$\mathbf{AIC}_w$	Aerodynamic influence coefficient matrix for downwash velocities in Trefftz Plane
$\mathbf{A}$	Diagonal matrix of panel areas
$\mathbf{B}$	Finite element strain-displacement matrix
$\mathbf{b}_c$	Aerodynamic boundary condition
$\mathbf{C}$	Aeroelastic load dependency matrix of displacements
$\mathbf{f}_{Ae_r}$	Rigid aerodynamic loads independent of structural displacements
$\mathbf{f}_{Ae}$	Forces from aerodynamic pressure distribution
$\mathbf{f}_{St}$	Static forces
$\mathbf{g}(\mathbf{x})$	Vector of all defined inequality constraint functions
$\mathbf{H}$	Hessian matrix (second order function derivatives)
$\mathbf{J}$	Finite element Jacobi matrix

$\mathbf{K}$	Structural stiffness matrix
$\mathbf{l}$	Vortex segment length vector
$\mathbf{n}$	Unit normal vector of panel
$\mathbf{T}_{AS}$	Transformation matrix from structural to aerodynamic system
$\mathbf{T}_{SA}$	Transformation matrix from aerodynamic to structural system
$\mathbf{u}$	Structural displacement vector
$\mathbf{v}_{ind}$	Velocity induced by a vortex singularity
$\mathbf{x}$	Vector of design variables
$\mathbf{x}_{lb}$	Vector of design variable lower bounds
$\mathbf{x}_{ub}$	Vector of design variable upper bounds
μ	Dynamic viscosity
ω	Relaxation factor for iterative aeroelastic solution
ψ_m	Fuel mass fraction
ρ	Air density
σ	Structural stress
b	Wing Span
b_w	Span of the wake in the Trefftz Plane
$b_{c_{elastic}}$	Aerodynamic boundary condition from elastic deformation
$b_{c_{shape}}$	Aerodynamic boundary condition from shape (e.g. camber, twist)
$b_{c_{state}}$	Aerodynamic boundary condition from flight state
c	Chord length
C_P	Aerodynamic pressure coefficient
C_{D_0}	Lift independent drag coefficient
$C_{D_{ind}}$	Lift induced drag coefficient
C_L	Overall aerodynamic lift coefficient
C_l	Local section lift coefficient
c_{ref}	Wing reference chord length
D	Aerodynamic drag force
D_{ind}	Aerodynamic induced drag force

E	Young's modulus
e	Oswald Span Efficiency factor
$f(\mathbf{x})$	Objective function
g	Acceleration of gravity
g_{geom}	Geometrical constraint
g_{mass}	Structural FE mass constraint
$g_{stability}$	Structural stability (buckling) constraint
$g_{strength}$	Structural strength constraint
g_{trim}	Flight mechanical trimming constraint
L	Aerodynamic lift force
M_{Cr}	Cruise Mach number
m_{FE}	Structural Finite Element Mass
m_{Fuel}	Fuel Mass
m_{MTOM}	Maximum Take-Off Mass
m_{ZFM}	Zero Fuel Mass
MAC	Mean Aerodynamic Chord
n	Load factor
n_{DV}	Number of design variables
n_g	Number of defined constraint functions
n_{LC}	Number of analysis load cases
n_P	Number of vortex lattice panels
q	Dynamic pressure
R	Reserve factor
r	System response value for a constraint evaluation
R_{Br}	Breguet range
r_{crit}	Boundary value for a system response constraint
s	Wing half span
S_i	Area of vortex lattice panel i
s_i	Span/width of vortex lattice panel i

S_{ref}	Wing reference area
$TSFC$	Thrust Specific Fuel Consumption
v	Flight velocity
x_{fibre}	Composite fibre angle design variable
x_{shape}	Geometric shape design variable
x_{size}	Structural sizing design variable
x_{trim}	Flight mechanical trimming design variable
AVL	Athena Vortex Lattice
Descartes	Parametric geometry program based on TIGL Viewer by DLR
Lagrange	Airbus Defence and Space in-house multidisciplinary analysis and optimization program
NLPQL	Non-Linear Programming by Quadratic Lagrangian
SQP	Sequential Quadratic Programming
AIC	Aerodynamic Influence Coefficient matrix
CAD	Computer Aided Design
CeRAS	Central Reference Aircraft data System [RSS+14]
CFD	Computational Fluid Dynamics
CPACS	Common Parametric Aircraft Configuration Scheme
DLM	Doublet Lattice Method
DLR	Deutsches Zentrum für Luft- und Raumfahrt (German Aerospace Centre)
DV	Design Variable
FCS	Flight Control System
FEM	Finite Element Method
FFD	Free Form Deformation
FSI	Fluid-Structure Interaction
HLP	High Level Primitives
HTP	Horizontal Tail Plane
KKT	Karush-Kuhn-Tucker condition
MDO	Multidisciplinary Design Optimization

MMA	Method of Moving Asymptotes
MTOM	Maximum Take-Off Mass
RANS	Reynolds Averaged Navier-Stokes
UAV	Unmanned Aerial Vehicle
VLM	Vortex Lattice Method
ZFM	Zero Fuel Mass

1 Introduction

The design of an aircraft is an inherently multidisciplinary process, as strong interrelations between the involved design disciplines exist. Therefore, a good aircraft design can only be found by seeking beneficial compromises between the competing design disciplines. The aircraft development process can be split into three different phases according to Raymer [Ray06, pp. 3-8]: conceptual, preliminary and detailed design.

The conceptual design phase starts with a set of abstract requirements usually regarding the future aircraft's performance characteristics and its usability (e.g. design mission). This entails a great design freedom coupled with high uncertainty regarding the aircraft parameters at this stage so that assumptions are often based on statistics of existing aircraft. First concepts are created based on these requirements and trade-off studies are conducted in order to find a configuration that fulfils them to the best extent while keeping development and life cycle costs low. Mainly the exterior layout of the aircraft and its impact on the different disciplines is studied here (e.g. wing/tail configuration, wing sweep or span etc.). Also the question of which technologies (e.g. carbon composites, active load alleviation etc.) are to be used for this aircraft is addressed here. First performance numbers for the designed concepts are estimated often based on statistics or low fidelity analysis methods. At the end of this phase, the most promising concept is selected for further development.

During the subsequent preliminary design phase the overall aircraft configuration is frozen and only smaller changes are made. Here, the design matures, while the level of detail and the complexity of the applied analysis methods increases. During this phase, the different competence departments (e.g. aerodynamics, structures, mass, stability and control) analyse the concept regarding their field of interest in order to confirm the decisions and results of the previous phase. One main task of preliminary design is lofting, which means describing the outer surface of the entire aircraft mathematically with, for example CAD (Computer Aided Design) tools. Additionally, first testing and experiments are conducted. By the end of this phase, a design proposal for the following detailed development is given. Thus, this phase increases the confidence in the chosen design regarding the questions of cost and development time targets.

In the final aircraft development phase of detailed design the previously global or component wise examinations are broken down into the smallest aspects (e.g. bolt holes, fasteners, etc.), since in this phase the actual components that are finally manufactured are designed. This means that at the end of each detailed study mechanical drawings of the concerned element are produced. For this, a great share of numerical simulation is performed. Based on the detailed knowledge about the aircraft at this point, also the manufacturing process is devised. Apart from numerical simulations, the actual components are now tested to verify assumptions and simulations up to here. The end of this phase

is marked by the first aircraft being manufactured.

Due to the competing requirements from different design disciplines, iterative design loops are run through inside each of these phases; sometimes going back to the previous phase, if severe design flaws are uncovered. Generally, the level of detail increases over the course of these phases; coarse at conceptual to ready-to-build after the detailed phase. Since the use of computer analysis and simulation to assess the physical properties of a concept has become a cornerstone of aircraft development, the level of detail or fidelity of the applied methods also follows this gradient. With the rising level of detail, the design freedom is being limited further and further with every design step, as the number of aspects already established increases. Therefore, major design changes become more and more expensive, as they involve redesigning all dependent aspects, on which a certain design effort has already been spent [see e.g. BM05]. Hence, the general target in current research is to rely further on numerical analyses during the early design phases in an attempt at safeguarding the design choices made there. Otherwise, design flaws introduced during early phases become the more expensive to mend the later they are discovered in the development process. Thus, it is often attempted to shift application of simulation methods with higher fidelity, usually employed later in the process, towards the beginning of the design process [see e.g. CRR+08a; Wun13; JKM14]. This promises that assumptions and statistical data can be verified sooner by an independent source uncovering possible issues. This is especially of importance when unconventional designs are pursued, where no or limited statistical data are available for the first assumptions.

Yet, applying such sophisticated analysis methods early in the development process causes several issues. Mostly, substantial effort is involved in order to prepare the required inputs for these methods. In combination with the high design uncertainty and concept studies with large scale modifications during the early development phases, the time factor for such simulations may impede their useful application. Furthermore, in order to provide relevant results these methods may require specific details not yet determined at early stages. Generally results of such methods can at maximum be expected to be of the same precision/fidelity as the input values were. Hence, the enterprise of shifting high fidelity analysis towards the beginning of the aircraft design process offers numerous challenges.

Generally, any design process can be seen as an optimization according to Vanderplaats [Van07]. Thus, one attempts to develop a product with as good characteristics as possible, while certain restrictions limiting the design have to be satisfied. In many cases such problems can be described in a mathematical form allowing the usage of numerical optimization. Hence, a computer algorithm (i.e. optimizer) is applied to the mathematical problem adjusting a set of design variables in order to iteratively improve a given objective function restricted by a number of constraint functions. Thus, the manual process of iteratively changing parameters and evaluating the effects through simulation or experiments is automated in a directed search conducted by the optimizer. Especially, since aircraft development is a process driven by many competing disciplines, which makes predicting the effects of a design change very complic-

ated, numerical optimization can offer great benefits in that area. This field of optimization is called multidisciplinary design optimization (MDO) , as it applies the so called responses (i.e. state variables) of several disciplines (obtained through different simulation methods) in the optimization process. During the MDO process, these disciplines, as well as, their respective influences on each other are considered while manipulating the design parameters to find an improved and feasible (i.e. all constraints satisfied) solution. Constraint functions are employed to guarantee the applicability or usefulness of the design. In other words, constraints assure requirements that are needed for certification and operation of the final aircraft (e.g. structural integrity of the aircraft). Thus, design criteria not considered during an optimization are often later found to be violated [see e.g. BM05] especially for designs where an optimization found a solution closely bordered by constraints. Therefore, an extensive design criteria model is very important during MDO to ensure the resulting design's suitability for further development.

Two of the most directly competing design disciplines in aircraft development are aerodynamics and structures [SSK+14], whose interaction forms the field of aeroelasticity. In aerodynamics, properties such as lift or drag forces are optimized, which directly influence the flight performance of the aircraft. Improving these characteristics, however, often causes negative effects on the structural behaviour, as the means of improving aerodynamic attributes (e.g. more slender wing with greater span) conflict with the requirements of the structural designers. This is additionally complicated by aeroelastic effects introducing a circular dependency between both disciplines, where structural elastic deformations influence aerodynamic loads and vice versa. For instance, it has been discussed that the lift induced drag, a major part of the overall drag force, often has a strong dependency on aeroelastic deformations (cf. e.g. [RMS95; WDD00]). Thus, when attempting to find a beneficial trade-off between the requirements of these two disciplines their interaction through aeroelastic effects needs to be taken into account as well. This is especially the case for aircraft with sail plane like configurations such as unmanned aerial vehicles (UAV), where aeroelastic effects and their influence on performance and drag are of great importance.

A major part of formulating a multidisciplinary design optimization problem is the choice of design variables, since they inherently define the design freedom and consequently determine which solutions are obtainable through an optimization. For example a sizing optimization, which changes the thickness of structural elements to support a given load, is powerful for structural design, but has rather limited influence on the aerodynamic properties of the aircraft. Yet, providing the shape parameters of a wing (e.g. wing span, sweep angle, area) as design variables in an optimization allows much greater influence on the overall characteristics of structure and aerodynamics at the cost of increased complexity. On the other hand, performing a shape optimization of the overall wing geometry may be beneficial during conceptual design, whereas during the detailed phase the results of such an optimization may very well go beyond the scope of applicability. Therefore, a harmonization between the design problem, the considered design parameters and the desired solution is crucial when

applying MDO.

With these aspects in mind the present work treats the issues of developing and applying a multidisciplinary shape and sizing optimization approach for early aircraft design with focus on static aeroelastic effects and induced drag, which is mostly affected by parameters determined early in the development process. Through this, the benefits of employing numerical analysis methods during early design phases can be combined with the advantages of using an optimization algorithm to automatically explore the vast design space available at that stage in the search of beneficial aircraft concepts. Since early design mainly determines the geometric layout of the aircraft, shape optimization is required to provide the necessary design freedom. In order to have sufficiently detailed influence on the structural aspects of the design, the geometric shape variables are completed with sizing variables. Hence, aerodynamic, as well as, structural aspects together with their aeroelastic interaction are taken into account representing two of the main design driving disciplines in aircraft development. As aerodynamic induced drag can be effectively manipulated through geometric variations [Kro01], special focus was put on this component of drag and its dependency on aeroelastic effects during the optimizations. Additionally, the structural mass resulting from an extensive structural design criteria model was considered as one major design property. Along this course, the choice of shape design variables, a way of characterising good designs, as well as, a suitable objective function to achieve beneficial designs are discussed. Finally the developed framework and approach are applied to the problem of optimizing the wing of a transport aircraft of industrial scale size and complexity.

1.1 Multidisciplinary Design Optimization in Aircraft Design

The present work focused on devising a multidisciplinary shape and sizing optimization approach for aircraft wings including aerodynamic, as well as, structural aspects through aeroelastic analysis. An overview of the existing research in the field of multidisciplinary wing design optimization is given in the following paragraphs. The numerous applications of optimization considering only a single discipline (e.g. aerodynamics) or ones that do not employ shape changes to affect the design are considered out of scope for this work.

In 1933, Ludwig Prandtl [Pra33] already studied the problem of finding the best spanwise lift distribution regarding induced drag for a wing with a given lift load and a so called *lifting moment of inertia* using analytical formulations. He discovered that deviating from the theoretically ideal elliptic lift distribution would allow increasing the wing span without penalties on the root bending moment. In sum, this resulted in a reduced overall induced drag. Although this was achieved without the use of numerical optimization algorithms, this can be seen as an early MDO application in the scope of this work, as Prandtl aimed to improve an aerodynamic characteristic while considering constraints from other disciplines. Similar studies were conducted, for example, by Jones

[Jon50], who also studied the relation of lift distribution, induced drag and bending moment, or Iglesias and Mason [IM01], who related deviation from elliptic lift load to weight savings and Breguet range performance increase using numerical analysis methods. However, none of these researches considered the effect of aeroelasticity on the spanwise lift load distribution, which can be significant in some cases (see e.g. [RMS95]). Furthermore, the structural aspects of the wing design were mainly represented through mass and bending moment, which prevents evaluation of an extensive set of structural criteria.

With the advances in numerical computations today, many approaches of MDO involving computerized analysis methods, as well as, numerical optimization algorithms to solve problems in aircraft design have been devised.

For example, Gur et al. [GBM+10; GBS+10] from the Virginia Polytechnic Institute developed an MDO framework to apply gradient based optimization to the conceptual design of truss-braced wing aircraft. They covered a wide range of design disciplines such as aerodynamics, structures, weights, mission and point performance, propulsion and aeroelasticity using low fidelity analysis methods. This allowed conceptual shape optimization with a nested structural sizing loop on the example of a truss-braced aircraft design. The abilities of this framework have been extended by Shirley et al. [SSK+14] adding, for example, vortex lattice aerodynamics (VLM) to refine the previously assumed elliptic lift distribution. Also the possibility of genetic algorithm optimization was added, which was used to study the competing requirements of aerodynamics and structures by means of pseudo-Pareto fronts.

A related MDO approach was done by Gundlach [Gun04] at the Virginia Polytechnic Institute, who also used genetic algorithm optimizers to improve UAV designs. He combined Trefftz Plane [Tre21] lift distribution aerodynamics with analytical formulations for an idealized wingbox structure based on a parametric geometry model disregarding aeroelastic effects. Together with other conceptual design stage evaluation methods for performance, weights, propulsion, avionics and subsystems multidisciplinary optimizations of UAV designs were conducted. Here, wing shape, thrust to weight ratio and fuel weight fraction design variables were optimized by the genetic algorithm considering constraints from the various analysis methods.

Another MDO framework for conceptual aircraft design was developed at Ryerson University by Neufeld et al. [NCB08]. This algorithm allowed configurational aircraft sizing by combining an aerodynamic vortex lattice method with semi-empirical methods for drag and weights to improve mission and point performance of an aircraft design subject to airworthiness requirements. In this framework a combination of a genetic algorithm and sequential quadratic programming (SQP) was applied to solve problems with continuous and discrete variables. Due to the missing structural response analysis, no aeroelastic interactions are included in this framework.

Focusing on the conceptual design of morphing wing aircraft, de Breuker [De 11] developed a gradient based MDO methodology including effects of aeroelasticity. For this he used the Weissinger aerodynamics method [Wei47] coupled with a FEM beam model. Employing an MMA algorithm optimizations of three morphing shape changes (folding, twisting and shearing) subjected to

constraints on root bending moment and local lift coefficient were performed considering the required energy to perform the morphing motion against the aeroelastic loads. This work concentrated on the interaction of the aerodynamic and structural disciplines taking into account drag and wing bending moments.

Wakayama and Kroo [WK95] conducted aeroelastic shape optimizations on aircraft wings using vortex lattice aerodynamics and an analytical beam formulation for the structural responses. This allowed to optimize the wing planform for improved drag characteristics while considering weights, bending and buckling, local maximum lift coefficient and static aeroelasticity. Further work by one of the authors [Wak00; GWR02] involved the multidisciplinary shape optimization of blended wing body configurations including aeroelastic loads. For this, a sequence of several optimizations was conducted each with different design variables, constraints and objective functions. The vortex lattice method together with semi-empirical drag estimations was calibrated with Navier-Stokes CFD results and coupled to a structural beam model for this. Finally, a medium sized optimization problem of 147 design variables and 1091 constraints was solved by a gradient based optimizer in this study.

Researchers at Georgia Institute of Technology [RMS95] devised a method for optimizing wing twist and camber in combination with structural sizing. This was realized in two interacting optimization loops, where an outer aerodynamic shape optimization loop determined the geometry, which was provided to the inner structural sizing process that also conducted aeroelastic analysis. With this approach the fuel and empty weight of the aircraft design was optimized based on mission performance requirements.

An extension of aeroelastic shape optimization to also include flight control system (FCS) servos was realized by Haghighat et al. [HML12] in a cooperation of the University of Toronto and the University of Michigan. A particle swarm optimization algorithm was used here to modify the aerodynamic planform, structural sizing and FCS control variables in search for improved mission range performance. As analysis methods, VLM was used for the aerodynamic response and coupled to a structural beam FEM model for elasticity evaluations. The FCS component was employed for active load alleviation in gust load cases. The result of this showed performance improvements compared to the approach where FCS was only applied for flight state control. Because of the gradient free optimization approach only a small number of design variables and constraints could be included in this approach.

Another cooperation between Politecnico di Milano and the Royal Institute of Technology (KTH) by Cavagna et al. [CRR+08b; CRR+08a; CRR09; CRT10b; CRT10a] during the SimSAC project resulted in a similar MDO framework for early aircraft design. This also consisted of two nested optimization loops, where the outer loop performed an aerodynamic shape optimization repeatedly evaluating the inner optimization loop to obtain a sizing optimized structure based on aeroelastic loads. During this process, criteria from aerodynamics, structures, weights and balance, static aeroelasticity and flutter were evaluated. Recent undertakings were the framework's extension from the initially low fidelity methods (VLM, structural beam model) to higher fidelity analyses such as Euler aerodynamics.

A more specific approach at improving wing designs using MDO was conducted by Kuzmina et al. [KIK+03; KIK04] at TsAGI. They applied a quadratic programming algorithm to minimize the induced drag based on an aeroelastic flight state. For this, an aerodynamic doublet lattice method (DLM) and a structural FEM analysis were coupled adjusting the wing twist distribution to improve the aeroelastic induced drag. This method was further extended over time [CIK06; CIK+10; CIK12; CIK14], so that structural sizing can be combined with aerodynamic lift to drag shape optimization. Again, this was realized with two optimization loops, where the sizing optimization loop is performed for every iteration of the outer aerodynamic optimization loop. Even though static, as well as, unsteady (i.e. flutter) aeroelastic constraints can be considered during these optimizations, only twist shape variables are available to change the aircraft design. The planform of the wing stayed constant during the optimizations due to limited parametrization.

A study by Jansen et al. [JPM10] about non-planar lifting surfaces and their effects on drag reduction applied aeroelastic shape optimization to find promising wing planforms. For this, an aerodynamic panel method was coupled with a structural beam model to allow aeroelastic analysis. The Trefftz Plane method [Tre21] was used for induced drag analysis and the viscous drag components were calculated through semi-empirical relations. Applying a particle swarm optimizer, wing span, area, taper, twist, sweep and dihedral were modified in order to reduce drag or improve the Breguet range. A selection of multidisciplinary constraints (e.g. section lift, stress, trim) was enforced to obtain feasible designs.

Another approach to aeroelastic shape and sizing optimization was done by De Baets et al. [DMS04]. They applied an aerodynamic panel method together with structural FEM (beam fuselage with detailed wing and tail) using a number of commercial analysis and optimization tools. Their so-called BLISS (bi-level integrated system synthesis) approach was used here to optimize an aircraft conceptual design problem at system as well as discipline level. The discipline optimizations were run independently creating response surface models of their result which were coupled and optimized at the system level to lower the objective function comprised of weight and deformation. For this, shell thickness and beam areas were used for sizing, while shape optimization was performed on the wing planform geometry but also thrust, wing loading and take off mass considering flutter and divergence speed constraints.

Researchers at Bombardier Aerospace (Piperni et al. [PAK04]) devised an MDO approach for designing transport aircraft wings, where a small disturbance transonic aerodynamic solver was coupled with a structural beam model. Based on this, a three fold optimization process using manually iterated aeroelastic loads and displacements was carried out. Along this course, the airfoil profiles were optimized at constant planform, after that the lift load distribution and finally the wing planform were modified by the optimizer. Due to the increased computational effort of the analysis, an approach of scaling the available loads for a number of iterations before recomputing the actual aeroelastic state was followed. The cash operating costs were employed as the objective given a prescribed mission calculating the wing structural mass by extrapola-

tion from the beam elements.

In his dissertation, Hürlimann [Hü10] proposed a method for estimating the wing box weight of an aircraft using design optimization with aeroelastic loads during the preliminary design phase. For this, he used a central parametric geometry model in a commercial CAD programme, from which the aerodynamic (full potential theory with boundary layer) and the structural (beam reinforced shell FEM model) analysis models were derived. This allowed analysis models of high detail considering e.g. landing gear placement, high lift devices and fuel distribution. Due to performance limitations of the analysis methods only the cruise load case was analysed for its static aeroelastic response, the structural dimensioning manoeuvre load cases were calculated without aeroelastic coupling. Due to the computational effort of the model generation, optimization was only applied to the structural sizing process keeping the wing geometry constant during the process.

Another approach at MDO in aircraft design was made by Ghoman et al. [GKC+12] using the commercial analysis tools of Zona Technology. With this, they realized a way of performing combinations of topology, shape and sizing optimization of an aircraft wing including static, as well as, flutter aeroelasticity. An Euler or panel method was coupled to a structural finite element solver for the aeroelastic evaluations. Morphing based on design/domain elements [Sam99] was used on both types of models to execute the shape changes dictated by the optimizer on the analysis models. A nested optimization loop approach was followed with an aerodynamic shape optimization as the outer loop and a structural sizing loop based on aeroelastic loads applying fully stressed design and mathematical programming inside. The gradient based optimization algorithm applied for improving weight or Breguet range was found to provide unsatisfying results so that a particle swarm optimizer was finally chosen for better handling of local minima. The optimization was carried out considering criteria regarding structural integrity, flutter, point and mission performance, as well as, stability and control.

James et al. [JKM14] also followed the notion of combining shape and topology optimization in combination with aeroelastic loads. In the course of their research, an aerodynamic panel method was coupled with a FEM volume mesh to enable aeroelastic analysis. Sequential Quadratic Programming (*SQP*) was applied to the objectives of induced drag and compliance modifying the twist and material distributions in the wing. The differences between concurrently optimizing shape and topology and consecutive optimization were discussed showing advantages of the concurrent variant. Caused by the adjoint gradient computation only a small number of constraints was considered during these optimizations.

Kennedy [Ken12] developed an aeroelastic shape optimization framework for large-scale optimizations of composite wings. A finite element method using the formulations for composite elements developed in this work was combined with an aerodynamic panel method, which is currently being replaced with an Euler approach. In order to parametrize the shape of the wing, the Free Form Deformation method [e.g. Sam99] was used. In combination with an SQP optimizer and adjoint gradient computation, large scale shape and sizing optim-

izations (roughly 1000 design variables and 900 constraints) were performed minimizing induced drag. Negative effects on structural mass or viscous drag were abated by constraints on mass and wetted area.

Another approach to aeroelastic shape optimization using higher fidelity finite volume based Euler aerodynamics and finite element structures was pursued by Maute et al. [MNF01]. In order to apply a Sequential Quadratic Programming optimizer, analytical gradients were derived for the aeroelastic problem with respect to the shape design variables. The design element method using Coons patches was applied for parametrizing the shape of the aerodynamic and the structural model. Based on this, a combined shape and sizing optimization was conducted on an aircraft wing to improve the lift to drag ratio in transonic flight. Due to the analytical gradients calculated with the direct approach the optimization could be performed with 8 design variables and over 2400 constraint functions.

Martins [Mar02] also used the combination of Euler aerodynamics and finite element shell models for aeroelastic shape optimization. He, however, used the adjoint calculation approach for the analytical gradients for the SQP algorithm. Shape parametrization, as well as, aeroelastic coupling were realized through a parametric geometry model. This allowed to efficiently optimize a supersonic business jet configuration with a larger number of design variables (92, shape and sizing) but only a small set of constraint functions (2, stress and overall lift). A linearised version of the Breguet range equation (weighted sum of induced drag and weight) was applied as an objective function for this. Limited by the small number of constraint functions, the wing planform stayed constant during the optimizations so that wing twist and camber were modified by the shape design variables.

A methodology devised by Kenway et al. [KKM10] enabled high fidelity aeroelastic shape optimization based on Euler and FEM without requiring a CAD geometry program for parametrization. Hence, they used Free Form Deformation [e.g. Sam99] to parametrize the shape of both analysis models combined with a linear elasticity ansatz to propagate the surface shape changes into the Euler volume mesh. Since finite differences were used to calculate the sensitivities required by the SQP optimizer, only a very small number of design variables (8 shape, sizing and trim) and constraints (3 lift trim and stress) were included in the optimizations. This framework was later extended by analytical adjoint gradient computation [KKM12] allowing to address significantly larger optimization problems. Also the drag estimation was extended to also represent viscous drag based on semi-empirical skin friction coefficients and form factors. Based on this, a combined shape and sizing optimization with a total of 476 design variables and 57 constraints was conducted minimizing fuel burn or maximum take-off weight for a given aircraft and mission.

Furthermore, Hwang and Martins [HM12] proposed a framework architecture for high fidelity MDO applications in aircraft design called GeoMACH. This framework featured a central parametric geometry model based on high level primitives [LT08] linking the CFD and the FEM model together so that both shape parametrization, as well as, aeroelastic coupling could be realized via the geometry model. For this, the analysis models were mapped onto the

geometry and the obtained relative coordinates on the geometric surfaces were kept constant during shape deformations. However, as the framework was still under development, no optimization was demonstrated.

In his dissertation, Wunderlich [Wun13] also developed a framework for MDO of transport aircraft wings with special consideration of static aeroelasticity. Here, he applied high fidelity Reynolds Averaged Navier-Stokes (RANS) aerodynamics together with FEM structural analysis. Wunderlich's methodology was based on CAD geometries with the analysis meshes being re-generated after every design change. For this reason, a gradient free Subplex optimization algorithm was used to perform the shape optimization, while structural sizing was carried out inside the aeroelastic loop using S_BOT [NRM+06; NKS08] based on the maximum stress constraints. In order to save computational effort the structurally design driving load cases were scaled from the levelled cruise result and the induced drag computation disregarded the aeroelastic deformation. With this the wing planform was optimized for different objective functions such as lift to drag ratio, Breguet range or fuel consumption over range and payload. The wing design could be successfully optimized, yet, due to the complexity of the problem some faulty evaluations were identified during the optimizations.

The effects of aeroelastic deformations on the laminar/turbulent flow characteristics around a wing were investigated by Barcelos and Maute [BM08]. To achieve this, a Navier-Stokes flow solver was coupled to a flat plate composite model in non-linear FEM. Sequential Quadratic Programming was used to modify sweep, twist and skin thickness of the wing (5 design variables in total) in order to maximize lift over drag and in a second case to minimize drag. In both optimizations, constraints on overall lift, wing tip displacement and structural stress were enforced accounting for 2412 constraint functions. A comparison between an inviscid optimization result and one obtained by the developed approach considering turbulence showed that the inviscid approach is sufficient for a first step towards the general wing configuration, however, laminar and turbulence effects need to be included for detailed and reliable performance improvements.

A summary of these existing approaches is given in Table 1.1. Many of the low fidelity approaches applicable to the early design phases use beam models for structural analysis, which do not allow full representation of structural requirements during the optimization. However, the higher order solutions employing Euler or Navier-Stokes aerodynamics are difficult to apply in early design phases due to the low level of data precision and reliability available at this stage making the results of such demanding methods questionable with the available input. Additionally, many of the presented solutions separate the respective optimization tasks (e.g. sizing and shape) into consecutive or nested loops. By decoupling the design variable types into separate optimization loops the algorithm cannot fully exploit possible interactions preventing e.g. effective aeroelastic tailoring. Some of the found approaches use gradient-free optimization algorithms such as genetic algorithms, particle swarms or Simplex. For the intended industrial application with large scale problems (great number of design variables and constraints), this represents an issue, as gradient-free meth-

ods are much less efficient with these types of problems than gradient based algorithms [Mar02; Van07].

Therefore, in present work an aeroelastic shape and sizing optimization framework was developed using medium/low fidelity analysis methods with one global gradient based optimization loop for application in early aircraft design. This should allow large scale aeroelastic shape and sizing optimizations with detailed representation of the structural requirements.

1.2 Thesis Overview

Subsequent to the introduction, Chapter 2 provides an overview and discussion of the existing methods required to realize the proposed shape optimization process including aeroelastic analysis. Thus, the fields of structural, as well as, aerodynamic analysis are examined regarding available methods and their differences. Based on the requirements for the specific application at hand, the methods for both analysis disciplines are selected. Furthermore, the question as to, how to couple the two disciplines to allow aeroelastic analysis, is discussed.

The second part of this chapter focuses on numerical optimization. Here, the different available optimization algorithms are discussed and an appropriate approach is selected. Furthermore, the issue of consistently parametrizing the shape of the respective analysis models is covered. A trade-off between shape design freedom, complexity and applicability to the problem at hand is made and a shape parametrization approach devised. Additionally, the known theory regarding convergence of optimizations and the specifics of multi-objective optimizations are covered.

In Chapter 3 the discussed theory is then applied to develop a framework that enables shape optimization of aircraft structures based on aeroelastic analysis including induced drag calculations. Therefore, the layout of the framework with its three main parts is presented. This chapter is sectioned following the components required to set up the aeroelastic shape optimization problem. Hence, regarding the design parametrization the definition of the applied sizing, shape and trimming design variables is described. The specifics of the aeroelastic analysis using aerodynamic influence coefficient (AIC) matrices are discussed. Furthermore, the induced drag evaluation based on aeroelastic analysis is also presented here. Relying on the results of the aeroelastic analysis, the next part describes the different applied constraint functions that form the multidisciplinary criteria model. Also the set of employed objective function formulations are highlighted in this section. Finally, the interaction of the presented components inside the framework and the processes during a shape optimization run are addressed.

With a functional shape optimization framework established, its abilities are applied and tested on aircraft wing structures in Chapter 4. The first part of this chapter focuses on validation of the results obtained by elements of the framework. After that the best way to apply the developed framework is studied covering the question of what characterises a good wing design and how to reach it with the developed abilities. Along this course, certain issues concern-

Table 1.1: Summary of aircraft shape MDO approaches

Reference	Aerodynamic Method	Structural Method	Optimizer	Design Variables
[GBM+10; GBS+10]	Trefftz ellipse, VLM	FEM beam model	gradient, genetic	shape, sizing, performance
[Gun04]	Trefftz ellipse	analytical	genetic	shape, mass, engine
[NCB08]	VLM	weight estimation	genetic, SQP	shape, mass, performance
[De 11]	Weissinger	FEM beam model	MMA	shape
[WK95; GWR02]	VLM	analytical/FEM beam	SQP	shape, fuel fraction
[RMS95]	VLM	analytical/FEM	?	shape, sizing
[HML12]	VLM	FEM beam model	particle swarm	shape, sizing, FCS
[CRR+08b; CRT10a]	VLM/DLM	FEM beam/plate model	gradient based	shape, sizing
[KIK+03; CIK14]	DLM	FEM	SQP	twist
[JPM10]	Panel	FEM beam model	particle swarm	shape
[DMS04]	Panel	FEM	?	shape, sizing
[PAK04]	Small disturbance	FEM beam model	Simplex/gradient/ genetic	shape
[Hü10]	Potential w. bound. layer	FEM	fully stressed/genetic	sizing
[GKC+12]	Panel/Euler	FEM	gradient/particle/ fully stressed des.	shape, sizing
[JKM14]	Panel	FEM volume mesh	SQP	twist, topology
[Ken12]	Panel	FEM	SQP	shape, sizing
[MNF01]	Euler	FEM	SQP	shape, sizing
[Mar02]	Euler	FEM	SQP	shape, sizing
[KKM10]	Euler	FEM	SQP	shape, sizing
[HM12]	t.b.d.	t.b.d.	t.b.d.	shape
[Wun13]	RANS	FEM	Subplex, stress based	shape, sizing
[BM08]	Navier-Stokes w. turbulence	non-linear FEM	SQP	shape, sizing

ing the interaction of the chosen analysis methods and the numerical optimization process are studied. Different objective function formulations, as well as, shape design variable combinations are examined and evaluated regarding their results and behaviour during the optimization process. With this, a number of differing possibilities to approaching this aeroelastic shape optimization problem are tested and compared regarding their result quality and efficiency. At the end of this first part, a technique of applying the developed framework effectively to the problem of aircraft wing design is established.

This approach is then applied to an aircraft model of industrial scale complexity and size in the second part of this chapter. Here, an aeroelastic shape optimization problem of large scale with respect to design variables and constraints is solved proving the applicability of the developed framework to real life development problems. Along this course, the benefits of the developed approach but also its limitations are highlighted and discussed.

Chapter 5 provides a summary and conclusions of the present work. Apart from the achievements of this work also future aspects are discussed. Further improvements and extensions to the developed shape optimization process are outlined.

2 Methods for Aeroelastic Analysis and Shape Optimization

2.1 Aeroelastic Analysis and its Components

Aeroelastic analysis addresses the problem of interaction between structural deformations due to elasticity and aerodynamic loads. In other words, the aerodynamic flow around an aircraft, creates a pressure distribution on its surface which exerts loads on the aircraft structure. Due to these loads, the elastic structure deforms, and thus, alters the aerodynamic flow conditions around the aircraft creating a new pressure distribution on the surface (see Fig. 2.1). This results in a circular dependency between disciplines, which means that such a problem can only be solved by evaluating both disciplines taking into account the results of the respective other.

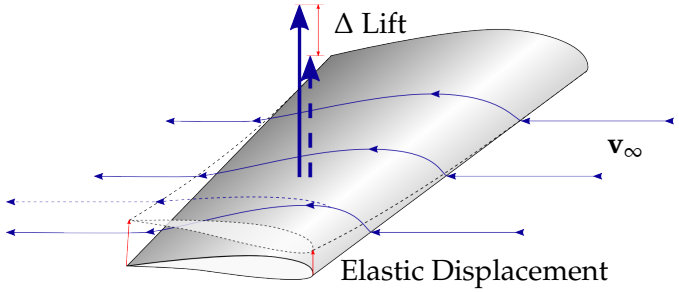

Fig. 2.1: Interaction between aerodynamic forces and structural elasticity

Two main fields of aeroelasticity can be found according to Bisplinghoff et al. [BAH96]:

Static aeroelasticity as the interaction between aerodynamic and elastic forces; Examples for this are: Load distribution, control surface effectiveness, divergence etc.

Dynamic aeroelasticity as the interaction between inertial, aerodynamic and elastic forces; examples are: Flutter, gust response, buffeting etc.

This work focuses on static aeroelasticity regarding its influence on the aerodynamic load distribution and induced drag generation using shape optimization to exploit this behaviour for improved aircraft designs.

Generally, when solving multidisciplinary problems such as aeroelasticity two common approaches exist (see e.g. [FP04]):

Monolithic approach All involved disciplines are solved simultaneously as part of one comprehensive problem formulation.

Partitioned approach The problem is separated into the respective fields. Each of the disciplines is solved individually considering the requirements enforced by the remaining fields at their common boundaries. Depending on the problem this approach may require an iterative approach to find a valid solution.

The advantage of the monolithic approach is that the problem is solved on only one model simultaneously considering the states of all included fields. However, the modelling, as well as, the stability of the solving process can become cumbersome when attempting to represent all disciplines equally well. The partitioned approach, on the other hand, has the benefits of solving each field with methods and models adapted specifically to the respective field's requirements. Hence, for each discipline results with higher quality can be expected. Furthermore, this allows modular architectures, where the methods for each discipline may be exchanged to adjust for e.g. different fidelity demands. Yet, special attention has to be paid to the way of translating the boundary conditions back and forth between disciplines. Here, it is very important to assure the physically sound interaction, while accounting for numerical needs such as convergence of the solution.

Hence, the partitioned approach was selected based on the higher modularity allowing different analysis methods to be used at different aircraft development stages. Thus, in the following chapters the different possibilities of analysis for the separate disciplines, as well as, the coupling method between the disciplines are discussed.

2.1.1 Structural Analysis Approaches

The structural analysis component in static aeroelastic analysis is used to determine the elastic behaviour of the structure. Furthermore, in the course of MDO the structural analysis is applied to evaluate structural design criteria. This yields a number of requirements to the analysis method:

- Realistic representation of structural flexibility
- Feasible computational effort
- Evaluation of local structural integrity (e.g. strength, stability)
- Good description of shape influence on structural stiffness

According to these requirements an approach of simulating the structural responses was selected. The reasoning for this together with a short description of the methods functionality are presented in the following paragraphs. This was done without claim of completeness as the described method is a standard in today's technical applications.

For numerical simulation of the elastic behaviour of structures an idealization of the component has to be performed. In technical applications this is usually done by discretisation, as continuous approaches either exhibit very high complexity solving differential equations or can only be handled efficiently

for very simple exceptions (e.g. cantilever beam [Kle07]). Different approaches to discretisation such as the Finite Element Method (FEM), the Finite Difference Method (FDM) or the Finite Volume Method (FVM) among others exist (see e.g. [Fel14]). The standard for this in science and industry, when simulating elastic structural behaviour, is the finite element method (FEM). It uses a library of different structural elements (such as rods, bars, membranes, shells etc.) of different shapes and characteristics to describe a structure and its physical properties. Each element has nodes that allow the connection to other elements. In most cases such, as in this thesis, a solution to the continuous field of elastic deformation or stresses due to an applied load is sought. In the finite element method these values can be obtained at the discrete nodes while the field is interpolated in between through the attached elements depending on their formulation (ansatz function). FEM also allows different approaches of relating the applied load to the elastic displacements e.g. linear or non-linear. The static linear finite element method is shown in Eq. (2.1), which is essentially based on Hooke's law of elasticity using constant stiffness. This approximation provides good results for small displacements (i.e. geometric linearity and small strains) without plastic deformation (cf. e.g. [ZT05]). Non-linear FEM, on the other hand, can be used to simulate non-linear geometric (instability) or material effects that are important for example in crash simulations. However, this is achieved at the cost of an iterative solution process (cf. e.g. [Kle07]).

For this thesis the linear static finite element method was selected, as only relatively small deformations due to static aeroelastic effects were to be expected making the additional computational effort of a non-linear approach unnecessary.

Thus, using Eq. (2.1) one can solve for the elastic displacement $\mathbf{u}$ under given boundary conditions and load sets $\mathbf{f}$ acting on the structural model represented by its stiffness matrix $\mathbf{K}$. This global stiffness matrix is assembled from the different stiffness matrices of the elements comprising the structural model. With the resulting displacement vector $\mathbf{u}$ it is possible to evaluate a number of further system responses such as element strains and stresses, local stability etc.

$$\mathbf{K} \cdot \mathbf{u} = \mathbf{f} \tag{2.1}$$

This method is also often employed in combination with numerical optimization, as it can be used to adjust the thickness or cross section area of the finite elements to achieve an improved design (also done in this thesis, Section 4). This is usually called sizing optimization and is in most cases conducted to reduce the structural mass of a component. In order to guarantee the structural integrity of the component during the sizing optimization, structural responses such as displacements, strains and stresses are applied in stiffness, strength and stability design criteria.

Aeroelastic applications with FEM may employ different modelling techniques. For example an aircraft wing is often idealized with simple bar elements that receive their properties from the structural topology and material of the actual wing (see for example [De 11; CRR09; HML12]). This provides a good approximation with low computational effort, if only the general wing bending and torsional displacements influencing the aerodynamic solution are of

interest. However, for detailed sizing optimization, as in the present thesis, this approach proves insufficient as many local effects, which are included as constraints, cannot be reproduced. Therefore, another common option is the full representation of a wing as a thin walled shell structure (e.g. [Che13; DAK+13; Giu99; MTC11; MAR08; Wun13]). This allows separate evaluation of the different structural components (e.g. ribs, spars or skin) obtaining responses for stresses and strains.

Hence, the linear finite element method modelling the aircraft components as thin-walled shell structures was applied for the aeroelastic shape optimization developed in this thesis. Through this, the requirements of realistic representation of the structural elastic behaviour for static aeroelasticity, as well as, the ability to evaluate local structural responses without excessive computational effort were given. Also, due to the idealization as a thin walled shell model, the aircraft geometry and the effects of shape changes could be represented with sufficient accuracy. The usage of this method and its implementation into the aeroelastic shape optimization framework are described in more detail in Chapter 3.

2.1.2 Aerodynamic Analysis Methods

Generally, aerodynamic analysis is used to solve for the flow field conditions (i.e. velocity field) around an arbitrary body in a free stream flow. From this flow field solution other information such as pressures or loads (e.g. pressure difference ΔP, lift L, drag D) can be derived. For better comparison, these loads are usually transformed into dimensionless coefficients using the dynamic pressure q and a reference area S_{ref} [ST01a]:

$$\begin{aligned} \Delta P &= q \Delta C_P \\ L &= q S_{ref} C_L \\ D &= q S_{ref} C_D \end{aligned} \tag{2.2}$$

With

$$q = \frac{\rho}{2} v_\infty^2 \tag{2.3}$$

In the case of aeroelastic analysis, as in this thesis, the focus lies on the load or pressure distribution, which causes the elastic deformation of the structure. Since aeroelastic analysis is used here to simulate wings or complete aircraft in steady flight, a static three dimensional aerodynamic solution is required.

One other aspect that is examined in this thesis is the aerodynamic drag of an aircraft. As it is a crucial design characteristic that directly translates into fuel consumption and flight performance, it must be considered for every geometric design change. Therefore, the main purpose of aerodynamic analysis in this thesis is the repeated evaluation of pressure distribution and drag in order to assess the effects of the design changes made by the optimizer.

From these points several requirements towards the aerodynamic analysis method can be deduced:

- Realistic representation of load distribution

- Drag prediction
- Possibility to apply elastic deformations on aerodynamic model
- Feasible run-time for aerodynamic solution (required for iterative aeroelastic analysis and optimization)
- Representation of shape changes and their effects
- Modelling effort and level of detail suitable for early design phases
- Robustness

Drag consists of several components originating from different aerodynamic effects. Thus, based on the effects that are responsible for each component the overall drag can be divided into (see e.g. [KP01; ST01a; Ray06]):

Induced drag is caused by the generation of aerodynamic lift

Viscous drag i.e. form, friction and interference drag caused by the viscosity of the fluid

Wave drag originates from compression shocks when travelling at transonic or supersonic speed

Generally, all aerodynamic analysis methods are based on the Navier-Stokes equations as shown for example in Schlichting et al. [ST01a, pp. 261-265]. These equations cannot be solved analytically for any of the complex problems that usually occur in aircraft design [Ray06]. Therefore, similar to the structural analysis in the previous section different approaches of idealizing these have been devised solving the equations at different levels of simplification. These levels of idealization already have an influence on which effects and with what precision can be represented.

Due to the high complexity of this analysis field, a substantial number of different approaches with different levels of fidelity and computational requirements exist. A selection of them is presented shortly in the following in order of decreasing fidelity. All discussed methods provide a pressure or load distribution precise enough for aeroelastic analysis of a global aircraft model at early design phases. Therefore, the focus will be put on the ability to describe effects causing the different components of drag.

Navier-Stokes (e.g. Large eddy or Reynolds averaged Navier-Stokes) Directly solves the full Navier-Stokes equations depending on different idealization models for turbulence [Ray06, pp. 354-364]. It uses a volume mesh modelling for the space around the surface of the aircraft up to the undisturbed far-field. It can reproduce viscous effects and compressibility yielding a solution for the velocity field in the entire volume. Thus, the Navier-Stokes method can estimate all three drag components listed above.

Euler Solves the Navier-Stokes equations with the viscous terms eliminated [ST01a, pp. 43-45]. Also uses a volume mesh very similar to the Navier-Stokes approach. Therefore, cannot simulate viscous drag, but induced and wave drag are possible. Since they consider effects of compressibility, Euler methods can be used to analyse transonic flows accurately with lower effort than for the Navier-Stokes methods.

Potential Theory Additional to the simplifications of Euler, potential theory assumes incompressible and irrotational flow [ST01a, pp. 49-53]. Some effects of compressibility are included through the Prandtl-Glauert Transformation (see e.g. [ST01a, p. 171]), which can be extended to supersonic applications of potential theory. However, the transonic flight regime is not covered by that (see e.g. [BAH96]). This means wave drag can only be calculated reliably in supersonic flight states with this method leaving only induced drag to be consistently available. Potential theory does not require to idealize the entire flow field, so in most cases it is sufficient to provide a mesh of the aircraft's geometry and the wake extending behind it (refer to [KP01]). Thus, so-called singularities (basic solutions such as a source, vortex or doublet) are used to model the geometry of the aircraft. Here, also different levels of idealization exist:

Panel Method uses 2D singularities to model the surface shell of the aircraft and its wake. It solves for the singularity strengths while enforcing the Kutta condition for physically sound flow conditions at the trailing edges (cf. e.g. [KP01]). From this, the velocity distribution on the surface can be deducted including effects of air displacement through the volume of the aircraft.

Lattice Method uses a lattice of 1D singularity filaments (i.e. vortex lines) shaped like horse-shoes to model the planform of the aircraft (based on the lifting line theory [KP01]). Hence, this method describes the behaviour of flat plates in free stream. Some adjustments can be made for twisted or cambered surfaces. From the solution to the singularity strengths the lift force for each horse-shoe is calculated using the Kutta-Joukowski Theorem [KP01].

The list given above is by no means complete and focuses on the scope of the intended application in this thesis.

2.1.2.1 Selection of the Aerodynamic Analysis Approach

Analysing the abilities of all presented methods regarding drag estimation, shows that only the Navier-Stokes method is able to calculate all drag components. However, since the quality of the Navier-Stokes results is strongly dependent on the applied turbulence model (mostly statistical), these analysis runs often need to be calibrated using wind tunnel data to obtain realistic data as described by Raymer [Ray06, pp. 360-361]. On the other hand, all presented methods are able to calculate the lift induced drag component, as it mainly depends on the lift distribution over the wings. As some of the effects that are disregarded by

some of the methods can have an influence on the lift distribution (e.g. compression shocks), the quality of induced drag prediction also varies with the different methods.

Regarding the modelling effort of the different approaches a gradual decrease in required preparation can be found from Navier-Stokes to the lattice method. Navier-Stokes and Euler require breaking the space between the aircraft surface and the boundary of the simulated region into small volume elements (usually tetra- or hexahedrons) paying special attention to the boundary layer close to the aircraft's surface in case of Navier-Stokes, as this has a major influence on the viscous effects [Ray06]. Potential theory methods require less effort modelling only the aircraft itself, where Panel methods use the aircraft loft and lattice methods are limited to the planform geometry. Additionally potential theory methods necessitate modelling of the wake, which is responsible for guaranteeing physically sound flow conditions behind and near the trailing edges of the aircraft model. Due to the focus on early design phases of this thesis, detail and modelling effort has to be considered under the premise that many geometric details are still unknown or large parameter changes may occur during design studies making methods with lower modelling effort preferable.

This modelling effort, as well as, the complexity of the analysis mesh relates directly to the required computational time to run an analysis. Thus, the lattice method solves within seconds, the panel method in minutes increasing from hours to days over Euler to the Navier-Stokes methods. This point is of special interest when combining the aerodynamic analysis method with optimization and aeroelastic analysis. Both necessitate repeated evaluation of the flow conditions iterating to a converged solution. Thus, the runtime of one analysis evaluation greatly affects the runtime of the entire shape optimization.

Furthermore, the requirement of applying the aeroelastic deformations on the aerodynamic mesh so that the current flight state may be evaluated reveals differences between the presented methods. Due to the volume mesh that Navier-Stokes and Euler methods use, the elastic displacements of e.g. the wing need to be applied not only to the surface mesh of the wing but also the displacement needs to be propagated from the surface into the flow field so that the quality of the mesh is not deteriorated excessively by this movement. There exist methods to do that, but the general issue with this affects the robustness of the methods when conducted automatically. Finite volume analysis methods such as Euler or Navier-Stokes were applied to aeroelastic problems for example by [FLL98; Giu99; MA04; HGR06; MAR08; KKM10; Wun13]. In case of the potential theory methods, this problem does not occur, as they only model the geometry of the aircraft itself. Therefore, together with the lower runtime this makes potential theory methods more appropriate for aeroelastic analysis under the condition that the phenomena in scope can be captured with it. Examples for potential theory analysis in the context of aeroelasticity can be seen for example in [IC03; KE06; CRR09; De 11; HML12; DAK+13] with lattice discretisation or [SCH+07; Ken12; JKM14] using panel methods.

Due to these issues, the Navier-Stokes and the Euler methods were ruled out for application in this thesis as their demands for modelling detail and runtime were deemed too high for the early development phases. Additionally, the dif-

ficulties with shape changes through shape optimization or aeroelastic deformation would seriously inhibit the robustness of the optimization. Thus, the potential theory methods were considered further. Here, the main advantage of the panel theory allowing to describe the volumetric geometry of the aircraft as opposed to the planform with the lattice method was found to be outweighed by the additional complexity of the model. As the induced drag could be estimated by both methods, the quality of the lift distributions was found to be comparable in the most common flight states such as levelled cruise flight. Hence, the lattice method (i.e. vortex lattice) was selected for application in the multidisciplinary optimizations of this thesis.

Since the selected analysis method was unable to predict the viscous and wave drag components, other approaches were used to estimate these. For the viscous drag semi-empirical methods based on flat plate skin friction with form factors [Ray06, p. 329] such as FRICTION by W. Mason et al. [Mas02] were used, which are often employed in the early design phases this thesis focused on. The received values were taken as constant throughout the optimization, but a further implementation of such methods into the optimization process was identified as future work. In case of wave drag, this component was disregarded entirely for the first applications, as it only occurs in specific flight regimes.

For implementation in the actual shape and sizing optimization framework the vortex lattice code *AVL* by M. Drela et al. at the Massachusetts Institute of Technology [DY10] was selected.

2.1.2.2 Principle of Vortex Lattice

The vortex lattice method (developed by Hedman [Hed66]) subdivides the planform of a lifting surface (e.g. wing) into a number of panels idealized by a horseshoe shaped vortex line (see Fig. 2.2). These horse-shoe elements are comprised of a bound leg positioned at 25 % relative panel chord length and two trailing legs at the root and tip end of the panel extending infinitely far downstream parallel to the flow direction (satisfying the Helmholtz requirement that no vortex line may end in the flow field [ST01a, p. 89]). The bound legs generate the aerodynamic lift following the Kutta-Joukowski Theorem (cf. [KP01, p. 67]) depending on the individual vortex strength Γ_i of each horse-shoe element i and the length and orientation vector $\mathbf{l}_i$ of the bound leg (Fig. 2.3).

$$\mathbf{f}_i = \rho \Gamma_i \mathbf{v}_\infty \times \boldsymbol{l}_i \tag{2.4}$$

The vortex strength itself is found by enforcing the Neumann boundary condition (Eq. (2.6), [KP01, p. 207]) at the collocation/Pistolesi point of each panel (at 75 % panel chord, see Fig. 2.2), which guarantees the impermeability of each panel so that free stream and induced velocities normal to each panel cancel out. The formed system of equations follows as:

$$\mathbf{AIC} \cdot \mathbf{\Gamma} = \mathbf{b}_c \tag{2.5}$$

with

$$b_{c_i} = -\mathbf{v}_\infty \cdot \mathbf{n}_i \tag{2.6}$$

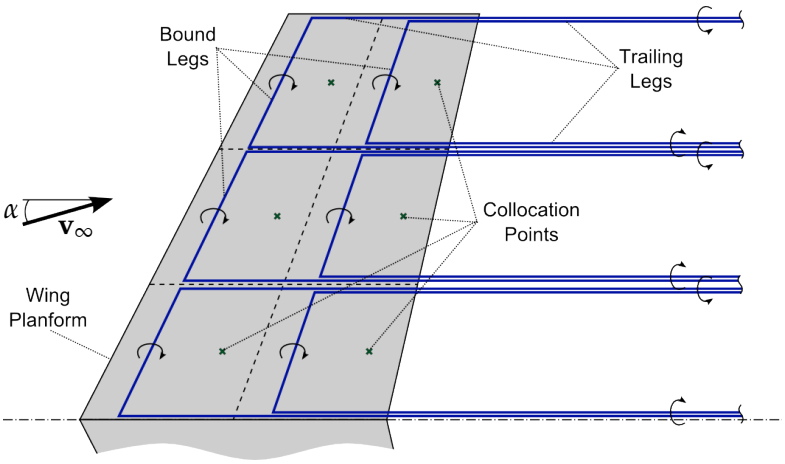

Fig. 2.2: Wing discretisation with vortex lattice

The aerodynamic influence coefficient matrix (**AIC**) is built up using the Biot-Savart law for the induced velocity of a straight vortex segment (see [KP01, pp. 38-41]). The AIC matrix is mainly based on the geometry of the model (relative position between the vortex elements and their orientation) and the Mach number (through Prandtl-Glauert Transformation [KP01, p. 92]). Hence, this AIC matrix provides the induced downwash velocity (perpendicular to the panel orientation) at each collocation point depending on the vector of vortex strengths $\mathbf{\Gamma}$ and is, therefore, called downwash AIC matrix.

Since the AIC matrix is a quadratic but not symmetric matrix, the system of equations can be solved by e.g. matrix inversion, LU decomposition or other numerical solution methods. For simplicity of notation, matrix inversion is used from here on to present the mathematical relations. Eq. (2.4) is then employed to calculate the lift force of each panel, from which also the pressure difference can be derived.

2.1.2.3 Calculation of the Pressure Coefficient AIC Matrix for Aeroelastic Analysis

AIC matrices are often used in aeroelastic analysis, since the solved matrix can be repeatedly applied to different boundary conditions altered by elastic effects without having to resolve the aerodynamic system each time. This is a standard approach to aeroelastic analysis with vortex lattice and was discussed by [Hed66; AR68; KL09] among others. The following derivations shown here were done analogue to Kier and Looye [KL09].

In order to have the aerodynamic solution independent of the flow velocity, all velocities in the following equations are normalized by $|\mathbf{v}_\infty|$. Through this, it is possible to apply the solution for any given flight state in the valid region of the analysis method by scaling it with the corresponding dynamic pressure q. Therefore, Eq. (2.5) only depends on the geometry of the aircraft and on the Mach number through the Prandtl-Glauert transformation. Only if one of these properties is altered, the aerodynamic system of equations has to be set up again based on the new data.

In order to directly obtain the pressure distribution form the vortex lattice

solution of Eq. (2.5), the pressure difference coefficients ΔC_{p_i} can be computed (see e.g. [KL09]) with the geometric definitions of an arbitrary vortex lattice panel in Fig. 2.3:

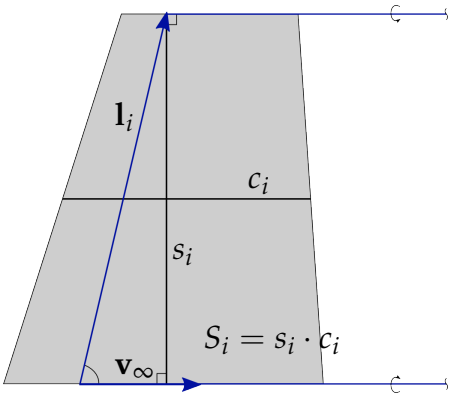

Fig. 2.3: Geometry of arbitrary vortex lattice panel i

$$\Delta C_{P_i} = \frac{2}{c_i} \cdot AIC_{ij}^{-1} \cdot b_{c_j} = AIC_{C_{P_{ij}}} \cdot b_{c_j} \tag{2.7}$$

Which defines the pressure coefficient AIC matrix using the mean chord length c_i of the ith vortex lattice panel. With this matrix the pressure difference coefficients can directly be evaluated for any given aerodynamic boundary condition vector $\mathbf{b}_c$ during aeroelastic analysis to repeatedly update the aerodynamic response to the elastic deformations.

2.1.2.4 Methods for Calculating Drag Based on Vortex Lattice

So far, only the calculation of lift or pressure distributions with vortex lattice and its applicability to aeroelastic analysis have been discussed. Here, the estimation of the different drag components listed at the beginning of Section 2.1.2 based on the results of a vortex lattice analysis are examined briefly. Note that the wave drag component was not considered any further, as it only occurs during transonic flight and could only be influenced effectively with shape changes of smaller dimensions than the ones intended for the targeted aircraft development phase.

Induced Drag is caused by the generation of aerodynamic lift [KP01, Section 8.1.3]. The trailing vortices forming at the tips of a lifting surface such as a wing induce a downwash velocity on the flow. Through this downwash velocity the effective angle of attack α is reduced by the induced angle of attack α_{ind}, which causes that a part of the produced lift force acts as drag (see e.g. [KP01, pp. 168-173]).

For small angles of attack a quadratic relation between overall lift and induced drag can be found [ST01a, p. 385], as described in the equations of [Ray06, p. 309].

For planar wings:

$$C_D = C_{D_0} + \frac{C_L^2}{\pi \Lambda e} \tag{2.8}$$

For non-planar wings (i.e. with camber/twist):

$$C_D = C_{D_{min}} + \frac{\left(C_L - C_{L_{min\ drag}}\right)^2}{\pi \Lambda e} \tag{2.9}$$

With the wing aspect ratio defined as:

$$\Lambda = \frac{b^2}{S_{Ref}} \tag{2.10}$$

In both equations the induced drag is represented by the rightmost term of the sum, which shows a relation between the overall lift coefficient C_L, the wing aspect ratio Λ and the Oswald span efficiency factor e. It has been found that for a wing with a given aspect ratio the lowest possible induced drag can be achieved with an elliptic spanwise lift distribution (cf. [KP01, pp. 177-181]). Eqs. (2.11) to (2.13) show the definition of such a distribution based on the equation of a quarter ellipse and the dependency between the vortex strength Γ and the lift distribution $\frac{C_l(y)c(y)}{c_{ref}}$. In this case, the Oswald span efficiency factor takes the value $e = 1.0$, otherwise it ranges from 0.0 to 1.0 for planar wings. Changing twist or chord length along the wing span can be effectively applied to adjust the lift distribution for improved Oswald factors. Non-planar wing configurations can also reach values above one (see e.g. [Kro01]).

$$\Gamma_{ideal}(y) = \sum_i \Gamma_i \Delta s_i \frac{4}{\pi s} \sqrt{1 - \frac{y^2}{s^2}} \tag{2.11}$$

$$C_l(y) = \frac{2}{c(y)} \Gamma(y) \tag{2.12}$$

$$\frac{C_l(y) \cdot c(y)}{c_{ref}} = \frac{2\Gamma(y)}{c_{ref}} \tag{2.13}$$

Two major methods exist for calculating the induced drag based on a potential theory method result. These methods are studied and compared by Smith and Kroo [SK93]. The first approach is to correct the actual free stream flow direction for every horse-shoe vortex by the local induced angle of attack and use trigonometric functions to calculate the portions of lift acting as drag before summing up these drag forces (see e.g. [KP01, pp. 172-173]). The second one is the Trefftz Plane analysis [Tre21; KP01], which integrates the velocities perpendicular to the movement direction in a plane infinitely far downstream of the aircraft to obtain the induced drag force. In their study Smith and Kroo concluded that the Trefftz Plane analysis provided good results with low sensitivity to panel density or angle of attack. Its accuracy was validated for a small example in Section 2.1.2.6. Due to this, and because it is well suited for combination with vortex lattice, the Trefftz Plane analysis was selected for induced drag estimation in this thesis. A more detailed description of the method and how it was realized in combination with aeroelastic analysis can be found in Section 2.1.2.5.

Viscous Drag In an incompressible viscous fluid there are only viscous and inertial forces acting on the flow. The ratio between these two forces is expressed by the Reynolds number Re [ST01a, Section 1.32]:

$$Re = \frac{\rho v l}{\mu} \tag{2.14}$$

With ρ being the fluid density, v the velocity, l a reference length and μ the dynamic viscosity of the fluid. For typical technical applications with air as a fluid, such as aircraft design, the Reynolds numbers are usually very high (i.e. 10^{+6} to 10^{+8}, [KP01, p. 17]), which means that the flow is dominated by the inertial forces. Therefore, a good approximation can be reached by assuming the flow to be inviscid and neglecting these viscous forces, as it is done in potential theory. However, in the so called boundary layer close to the aircraft's surface the relative velocity is reduced to zero caused by friction (see Fig. 2.4, [ST01a, Section 4.2]). The reduced velocities here lead to lower Reynolds numbers underlining that viscous effects, which cause the drag forces, cannot be neglected in this region without errors.

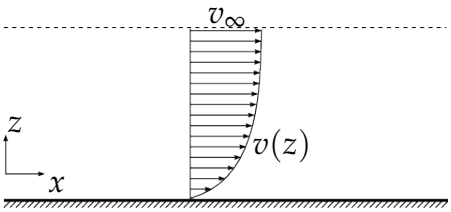

Fig. 2.4: Boundary layer over a solid surface

To represent the viscous effects in the boundary layer either the full Navier-Stokes equations need to be solved using one of the Navier-Stokes solution methods listed at the beginning of this Section 2.1.2 or the flow domain is split into the inviscid outer flow region and viscous boundary layer using different methods to solve each domain (see [KP01, pp. 17-19]). The second approach would then iterate between the outer flow solution (e.g. by potential theory) and the boundary layer conditions (derived by Prandtl, see [ST01a, Chapter 4.4]) adjusting the boundary conditions between the two domains. This would also entail high computational effort, as well as, require detailed geometric surface information, due to which this approach was also ruled out for application in this thesis.

Based on the level of information detail available in early aircraft design phases, the possibility of semi-empirical viscous drag estimation (see [Ray06, Chapter 12.5]) was consequently considered here. Such methods calculate the viscous drag coefficients aircraft component wise (i.e. wing, fuselage, etc.) and combine them to an overall coefficient respecting interference between closely grouped components. For this it takes into account different flow conditions (laminar/turbulent) calculating a component's flat plate skin friction coefficient C_f (Eq. (2.15)) and adjusts for the general shape of a component through form factors FF (e.g. thickness to chord ratio). Thus, the method only requires information that is well available even at early stages of aircraft design. Furthermore, it requires low computational effort to calculate the viscous drag representing the major effects for the most common flight states. Therefore, such

methods are often used for early phase design optimizations [see e.g. CIK12; Gun04; GBM+10; KKM12; SSK+14; WK95].

$$C_{D_0} = \sum_{i=1}^{n} \frac{Q_i FF_i C_{f_i} S_{wet_i}}{S_{Ref}} \tag{2.15}$$

Here Q is the interference factor, S_{wet} the wetted surface area and S_{Ref} the reference surface of the aircraft. Values for Q and FF are taken from semi-empirical relations presented for example in Raymer [Ray06].

In this thesis the combination of vortex lattice for lift distribution and induced drag (through Trefftz Plane Analysis) and the semi-empirical component build up method was applied. In a first approach the viscous drag coefficient was assumed constant during the shape optimizations evaluating initial and final design for reference. This approach was verified in Sections 4.2.1.3 and 4.3.4 for two different models showing that the viscous drag change during shape optimization has a small influence on the aircraft performance. Thus, for first shape optimizations it can be assumed constant but must be monitored. In the developed framework, the program *FRICTION* developed by Mason et al. [Mas02] was selected.

2.1.2.5 Trefftz Plane Analysis for Induced Drag Calculation during Aeroelastic Analysis

In order to show the effects of aeroelasticity and shape modifications on induced drag the Trefftz Plane analysis was applied, which is described here in more detail, followed by the modifications that allow evaluating induced drag using an AIC matrix similar to the one derived in Section 2.1.2.3.

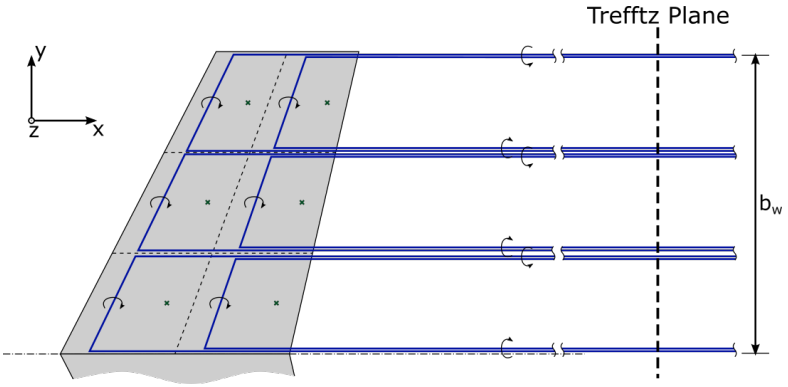

Fig. 2.5: Top view of wing and its Trefftz Plane

Fig. 2.5 shows a wing with its wake of trailing vortex filaments (vortex lattice idealization) and its Trefftz Plane that is located infinitely far downstream of the wing (x-direction) and oriented orthogonal to the free stream flow (i.e. yz-plane). The theory of Trefftz Plane analysis is described for example in Katz and Plotkin [KP01, Chapter 8.4]. Generally, it states that inside the Trefftz Plane only the wake of a wing (parallel to free stream there) generating lift has an influence on the flow conditions. Thus, the vortices of the wake induce perturbation velocities perpendicular to the free stream flow and do not contribute to the lift

generation (Eq. (2.4)). Due to this, the energy required to induce these velocities in the Trefftz Plane is lost and can be used as a measure for the induced drag force. Finally, an integral over the wake of the wing can be formulated taking into account the local vortex strength $\Gamma(y)$ and the induced downwash velocity w_{ind} perpendicular to the wake that yields the induced drag force [KP01, p. 203]:

$$D_{ind} = -\frac{\rho}{2} \int_{\frac{-b_w}{2}}^{\frac{b_w}{2}} \Gamma(y) w_{ind} \, dy \tag{2.16}$$

The integration is performed over the span of the wake b_w in y-direction (Fig. 2.5) assuming a flat wing without dihedral, otherwise the integration would be carried out over the span direction of the wing.

The discretised form of this equation suitable for vortex lattice, where the wake is represented by the trailing legs of the horse-shoe vortex elements (see Fig. 2.5, follows as:

$$D_{ind} = -\frac{\rho}{2} \sum_{i=1}^{n_P} \Gamma_i w_{ind_i} s_i \tag{2.17}$$

Which uses the span s_i of panel i going over all n_P vortex lattice panels. The downwash velocity w_{ind_i} at the collocation point of panel i (perpendicular to the wake of that panel) induced by all panels is defined like this [KP01, Chapter 12.1]:

$$w_{ind_i} = \sum_{j=1}^{n_P} \mathbf{n}_i \cdot \mathbf{v}_{ind_{ij}} \tag{2.18}$$

As the evaluation of Eqs. (2.17) and (2.18) is done in the Trefftz Plane, the collocation points and the trailing vortices of the vortex lattice model are projected into this plane. The bound vortex legs of the horse-shoe elements have no influence here, as they are located on the wing infinitely far upstream and their influence is inversely proportional to distance (Biot-Savart law, [ST01a, Chapter 2.46]). Fig. 2.6 shows this procedure as well as the projected geometry of one vortex lattice panel. Here, the velocities $\mathbf{v}_{ind_{ij}}$ induced by the trailing legs of panel j at the projected collocation point of panel i can then be evaluated and multiplied with its projected panel normal $\mathbf{n}_i$.

If viewed from the location of the Trefftz Plane, the trailing vortices of the vortex lattice model extend to infinity in upstream, as well as, downstream direction. Thus, the flow conditions inside the Trefftz Plane can be formulated as a two dimensional problem with point vortices, where the trailing legs penetrate the Trefftz Plane (cf. [KP01, p. 337]). This is illustrated in Fig. 2.7.

Figure 2.7 depicts how the induced velocity $\mathbf{v}$ at an arbitrary point P located at (y, z) in the Trefftz Plane depends on the two trailing vortices (subscripts 0 and 1) of a vortex lattice panel. The corresponding velocity components $\mathbf{v}_0$ and $\mathbf{v}_1$ induced by either one of the point vortices can be calculated through Eq. (2.19) (see [KP01, pp. 58-60]).

$$\begin{aligned} v_{iy} &= -\frac{\Gamma_i}{2\pi} \frac{z - z_i}{(z - z_i)^2 + (y - y_i)^2} \\ v_{iz} &= \frac{\Gamma_i}{2\pi} \frac{y - y_i}{(z - z_i)^2 + (y - y_i)^2} \end{aligned} \quad \text{for} \quad i = 0, 1 \tag{2.19}$$

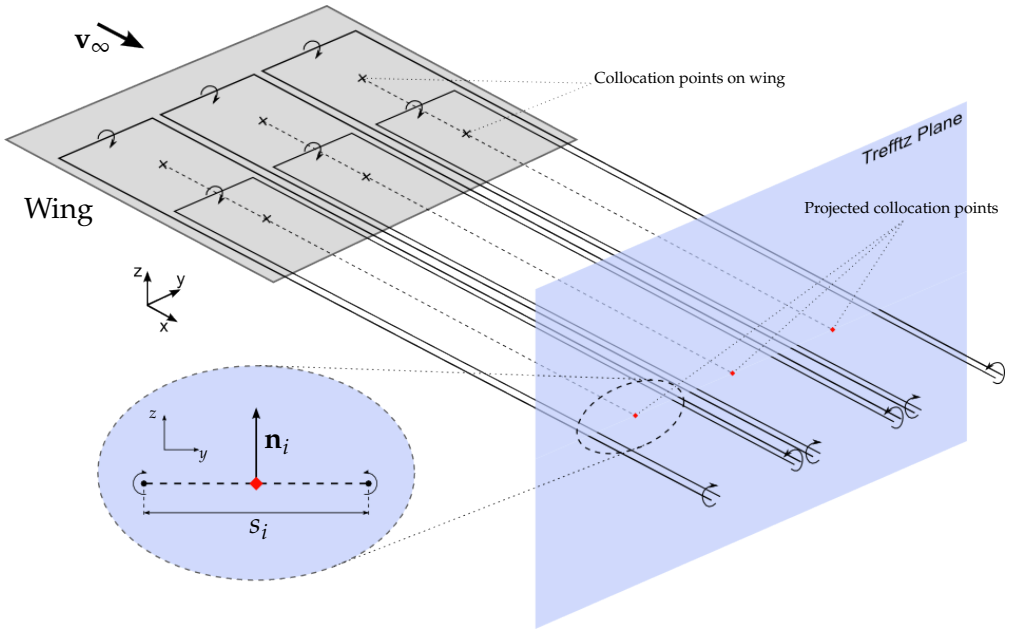

Fig. 2.6: Projection of collocation points to Trefftz Plane

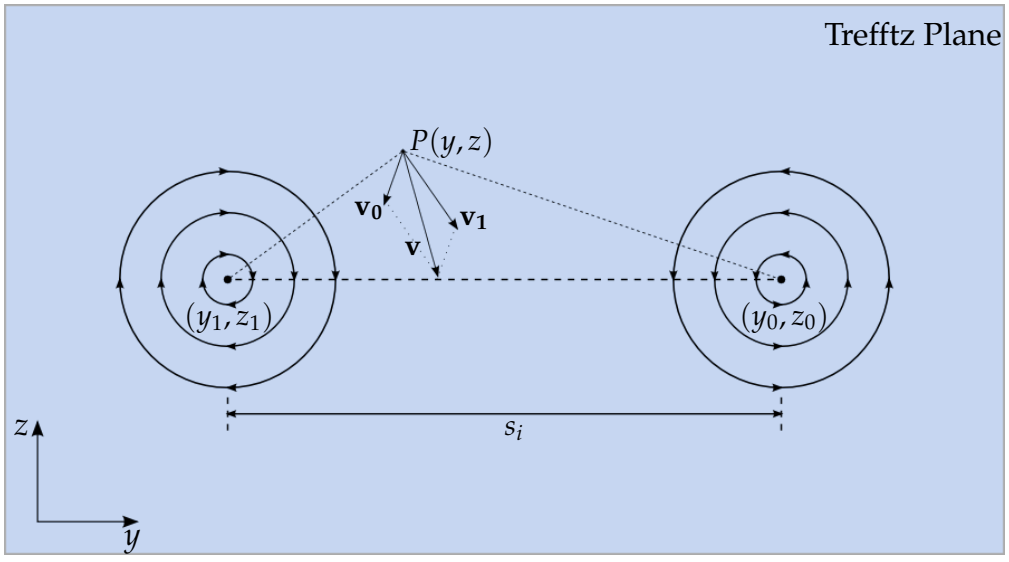

Fig. 2.7: Induced velocities of a horse-shoe vortex in the Trefftz plane

With Eq. (2.19) the y- and z-components of the velocity induced by one of the trailing vortices (0,1) can be calculated. From this, the overall induced velocity **v** can be derived by vector summation.

Evaluating these relations at the projected collocation point of each vortex lattice panel for all defined panels allows setting up an aerodynamic influence coefficient matrix similar to Eq. (2.5) in the Trefftz Plane. Including the relation to the projected panel normal of Eq. (2.18) leads to a Trefftz Plane downwash AIC matrix $\mathbf{AIC}_w$ such as:

$$\mathbf{w}_{ind} = \mathbf{AIC}_w \cdot \mathbf{\Gamma} \tag{2.20}$$

Inserting this into Eq. (2.17) and using the drag coefficient definition Eq. (2.2) allows defining the induced drag AIC matrix $\mathbf{AIC}_{C_D}$:

$$C_{D_{ind}} = \mathbf{\Gamma} \cdot \mathbf{AIC}_{C_D} \cdot \mathbf{\Gamma} \tag{2.21}$$

with

$$\mathbf{AIC}_{C_D} = -\frac{1}{S_{ref}} \begin{pmatrix} a_{11}s_1 & a_{12}s_1 & \dots & a_{1n_P}s_1 \\ a_{21}s_2 & a_{22}s_2 & \dots & a_{2n_P}s_2 \\ \vdots & \vdots & \ddots & \vdots \\ a_{n_P1}s_{n_P} & a_{n_P2}s_{n_P} & \dots & a_{n_Pn_P}s_{n_P} \end{pmatrix} \tag{2.22}$$

To use the coefficient definition and remove the dependency on the flight state the velocities are normalized by the free flow velocity v_∞ analogue to the procedure in Section 2.1.2.3. With this definition it is possible to calculate the induced drag coefficient $C_{D_{ind}}$ based on the projected geometry of the vortex lattice method and the current vector of vortex strength $\mathbf{\Gamma}$ that is obtained from solving the vortex lattice system of equations Eq. (2.5) repeatedly for changing boundary conditions during aeroelastic analysis.

Similar approaches of deriving such an induced drag AIC matrix were presented in [KP01; KL09; KIK04].

The lift coefficient in the Trefftz Plane corresponding to the induced drag is given by (cf. [KP01, p. 203]):

$$C_L = \frac{2}{S_{ref}} \sum_{i}^{n_P} \Gamma_i \cdot \Delta y_i \tag{2.23}$$

Here, $\Delta\mathbf{y}$ represents the span in y-direction of every panel in the aerodynamic model, so that only the lift components acting in global z-direction are represented in C_L.

2.1.2.6 Validation of Aerodynamic Method

The general quality of vortex lattice results has been verified and discussed for example by Hedman [Hed66] or Melin [Mel00]. The method assumes small disturbance, therefore, its results are only reliable for small angles of attack. Furthermore, thin lifting wings with large aspect ratios ($\Lambda \geq 4$) are presumed for vortex lattice [KP01]. Due to the Prandtl-Glauert transformation compressibility effects can be covered for all sub-critical Mach numbers [Hed66]. That means transonic flight conditions with areas of supersonic speeds cannot be represented by this method.

Aside of these general characteristics of the method, a comparison with available benchmark data was conducted here. This was also carried out to verify the extension made regarding the induced drag AIC matrix calculations. For this, the *AVL* vortex lattice program selected in Section 2.1.2.1 was extended with the ΔC_P and the Trefftz Plane AIC capabilities described in Sections 2.1.2.3 and 2.1.2.5. This modified version was then used to calculate the vortex lattice results shown in the following.

The wind tunnel results for induced drag of a rectangular wing found by Brune and Bogotaj [BB90] were compared with the solution obtained by the vortex lattice method. In their study Brune and Bogotaj conducted wind tunnel measurements in the wake flow field behind a wing to estimate lift and induced drag forces of this wing. Fig. 2.8 shows this comparison in the form of a lift curve and induced drag polar.

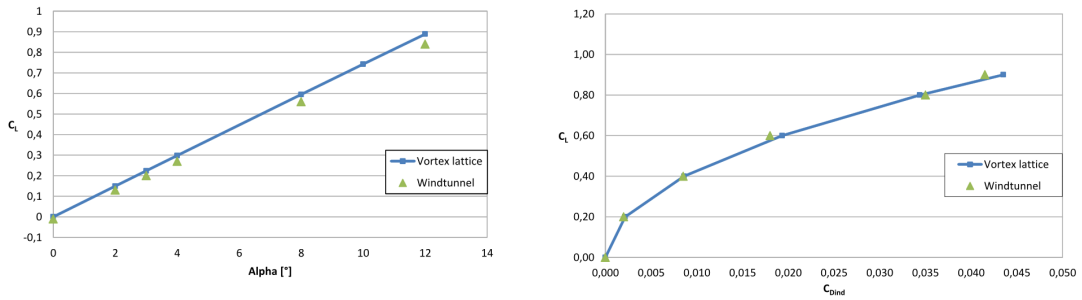

(a) Lift slope

(b) Induced drag polar

Fig. 2.8: Comparison of *AVL* and wind tunnel results

The measurements were taken from a rectangular wing with an aspect ratio of $\Lambda = 6$ and a symmetric profile. The vortex lattice model of this wing was discretised with 10 panels chordwise and 60 in spanwise direction. Cosine distributions were used in both directions allocating more panels near leading and trailing edge, as well as, towards the wing tips. In Fig. 2.8, the vortex lattice method generally shows good agreement with the wind tunnel data for smaller values, while the error increases with higher lift coefficient values. Thus, the selected approach using the vortex lattice method and Trefftz plane analysis provides a good approximation of the aerodynamic problem at early aircraft design phases.

2.1.3 Fluid-Structure Coupling

When using a partitioned approach to solve the aeroelastic or fluid-structure interaction (FSI) problem, the solutions of one discipline influencing the result of the other need to be translated between the different domains. Since, in case of aeroelasticity, both disciplines affect the respective other, this is done iteratively going back and forth between aerodynamic and structural solution (see Fig. 2.9). In other words, the two disciplines of aerodynamic and structural analysis need to be coupled by exchanging data that affects the respective other discipline.

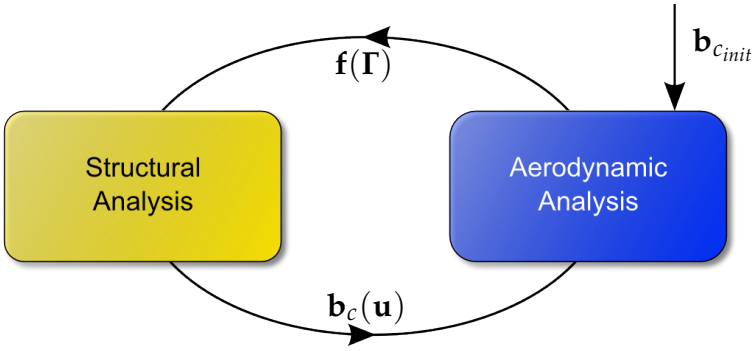

Fig. 2.9: Schematic of aeroelastic iteration

In case of aeroelastic analysis with the methods selected in Sections 2.1.1 and 2.1.2, this information consists of the aerodynamic loads $\mathbf{f}$ acting on the structure in Eq. (2.1) and the aerodynamic boundary conditions $\mathbf{b}_c$ affected by elastic deformation in Eq. (2.5). This is illustrated in Fig. 2.9 and Eq. (2.24).

$$\mathbf{K} \cdot \mathbf{u} = \mathbf{f} \tag{2.1 revisited}$$

$$\mathbf{AIC} \cdot \mathbf{\Gamma} = \mathbf{b}_c \tag{2.5 revisited}$$

with

$$\mathbf{f} = f(\mathbf{\Gamma}) \quad \text{and} \quad \mathbf{b}_c = f(\mathbf{u}) \tag{2.24}$$

When solving the aeroelastic problem with the partitioned approach an iteration between the separate disciplines is performed. First, the aerodynamic problem is solved based on the initial boundary conditions $\mathbf{b}_{c_{init}}$ (cf. Fig. 2.9). These reflect the rigid flight state without any effects of elasticity. The aerodynamic solution $\mathbf{\Gamma}$ corresponding to this is then transformed to the structural system and applied in form of the loads $\mathbf{f}$. With this, the structural problem is solved calculating the elastic displacement vector $\mathbf{u}$. Based on the elastic displacements the new aerodynamic boundary condition $\mathbf{b}_c$ can be evaluated. After applying this to the aerodynamic system the new flow solution can be determined based on the updated boundary conditions, which yields a new load state for the structural system starting over the loop. This loop is iterated until convergence is reached and the differences in displacements and aerodynamic loads become small.

Two steps are required for coupling the two analysis disciplines. Not only do the values have to be converted into quantities the respective other discipline can process, but also need these quantities be transferred between two analysis systems with differing models, discretisations and coordinate systems.

Since the primary solution of the vortex lattice method is the vortex strength vector $\mathbf{\Gamma}$, this has to be transformed into forces or moments before it can be applied to the structural system. Using the derivations of Section 2.1.2.3 the pressure coefficient AIC matrix can be used to directly calculate the aerodynamic loads with:

$$\Delta \mathbf{C}_P = \mathbf{AIC}_{C_P} \cdot \mathbf{b}_c \tag{2.25}$$

$$\mathbf{f}_{A_i} = qS_i \mathbf{n}_i \Delta C_{P_i} \tag{2.26}$$

In this section, the subscripts A and S are used for quantities in the aerodynamic or structural system respectively. The preceding equations yield the force in the aerodynamic system for panel i, with its unit normal vector $\mathbf{n}_i$ and panel area S_i. To apply it to the finite element structural problem it needs to be transformed to $\mathbf{f}_S$ in the structural system. In case of the resulting structural displacements $\mathbf{u}_S$ a similar procedure needs to be carried out. First transferring the displacement vector into the aerodynamic system $\mathbf{u}_A$ and then using geometric relations to determine the change in angle of attack of each panel due to the deformation leading to $\mathbf{b}_c$.

$$\mathbf{b}_c = \mathbf{b}_{c_{init}} + \mathbf{b}_c(\mathbf{u}_A) \tag{2.27}$$

These transformations between analysis systems are represented by transformation matrices as follows:

$$\mathbf{u}_A = \mathbf{T}_{AS} \cdot \mathbf{u}_S \tag{2.28}$$

$$\mathbf{f}_S = \mathbf{T}_{SA} \cdot \mathbf{f}_A \tag{2.29}$$

To generate these matrices the infinite plate spline method developed by Harder and Desmarais [HD72] was applied. For this method the points of each model are projected into a common interpolation plane (here the plane of the vortex lattice wing segment) and a two dimensional interpolation function is fitted through the points where data is given. The general form of this infinite plate spline interpolation function w for N independent points with data is given as [HD72]:

$$w(x,y) = a_0 + a_1 x + a_2 y + \sum_{i=1}^{N} F_i r_i^2 \ln r_i^2 \tag{2.30}$$

with

$$r_i^2 = (x - x_i)^2 + (y - y_i)^2$$

The derivative with respect to x (flow direction) gives the slope of a panel based on the elastic displacements, which can directly be applied to the aerodynamic boundary condition:

$$\frac{\partial w(x,y)}{\partial x} = a_1 + 2\sum_{i=1}^{N} F_i(1 + \ln r_i^2)(x - x_i) \tag{2.31}$$

Evaluating this interpolation function at the set of discrete points, where the data shall be interpolated to, allows deriving such interpolation matrices, as introduced in the previous paragraph.

Using the infinite plate spline transformation together with the derived AIC matrix and the structural solver allows the iterative solution of the aeroelastic problem. Here the aerodynamic system only needs to be solved once in advance to gain the AIC matrix for the matrix-vector product in Eq. (2.25), while the structural system is evaluated in each iteration.

2.2 Aspects of Numerical Design Optimization

Traditionally the design process in technical applications is characterised by adjusting design parameters to improve a certain feature as far as possible while satisfying a set of prescribed constraints [Van07, p. 3]. Nowadays, this traditional process can be automated to a certain degree by applying numerical analysis methods to reduce the number of costly experiments and using optimization algorithms in a directed search to find beneficial combinations of parameter values that yield improved performance features. Yet, the result's quality depends on how well the physical reality of the problem can be described by mathematical relations (e.g. numerical analysis models), on which the optimizer program operates. Using this kind of automated process often has advantages, whenever the number of design variables or the interrelations between them become too convoluted, yielding results that outperform those found through the manual approach by an engineer.

The general formulation of a design optimization problem can be written as (see e.g. [Van07; BSS06]):

$$\min f(\mathbf{x}) \quad \text{subject to} \quad \mathbf{g}(\mathbf{x}) \leq 0 \quad \text{with} \quad \mathbf{x}_{lb} \leq \mathbf{x} \leq \mathbf{x}_{ub} \tag{2.32}$$

With $f(\mathbf{x})$ being the objective function that describes the design property to be improved (i.e. minimized). This objective function is usually compiled of so called system responses originating from numerical analysis results. The vector $\mathbf{x}$ represents the design variables influencing the objective. Each of the variables in this vector has an upper x_{ub} and a lower bound (or gage) x_{lb}, in between which the values for the variable may be chosen. In a constrained optimization, a vector of constraint functions $\mathbf{g}(\mathbf{x})$ is provided that need to be satisfied in order to achieve a sound (i.e. feasible) design. Generally, one distinguishes between equality $\mathbf{h}(\mathbf{x})$ and inequality constraints $\mathbf{g}(\mathbf{x})$; in this thesis, only inequality constraints are considered. Thus, together with the design variables and their gages the objective function spans the so called design space. Design spaces can be convex (i.e. contain only one global optimum) and non-convex (i.e. several local optima) [BSS06, pp. 47-48]. Within the design space, the feasible domain is comprised by all feasible solutions (constraint functions satisfied) that can be obtained using any allowed combination of design variable values.

Hence, the design problem that has to be solved by an optimization is to find a feasible location inside the design space that features a minimal objective function value. A subcategory of such optimization problems is called multidisciplinary design optimization (MDO) [BSS06; Van07]. This specifies that the objective or any of the constraint functions are established using system responses from more than one analysis discipline. An example for this that is treated in this thesis is aeroelasticity, which combines responses from structural elasticity and aerodynamic loads. One approach would be to optimize the disciplines sequentially and combine the results. However, experience has shown that in most cases 'the sum of optimum components is not an optimum system' as stated by Vanderplaats [Van07, p. 436]. This is especially the case when the disciplines have competing preferences requiring a compromise. Therefore, considering all involved disciplines simultaneously during the optimization usu-

ally provides better results. Under these aspects MDO can help finding good designs that balance the requirements of the different disciplines.

Hence, in the following chapters the issues and benefits of applying numerical design optimization to developing aircraft airframes comprised of aerodynamic shape and internal structure subjected to aeroelastic and inertial loads is studied.

2.2.1 Methods and Approaches to Structural Design Optimization

Optimization is frequently used in structural design, where load bearing members need to be constructed to withstand specific load cases. Depending on the choice of design variables certain classes of structural optimization can be defined (see e.g. [Har08]).

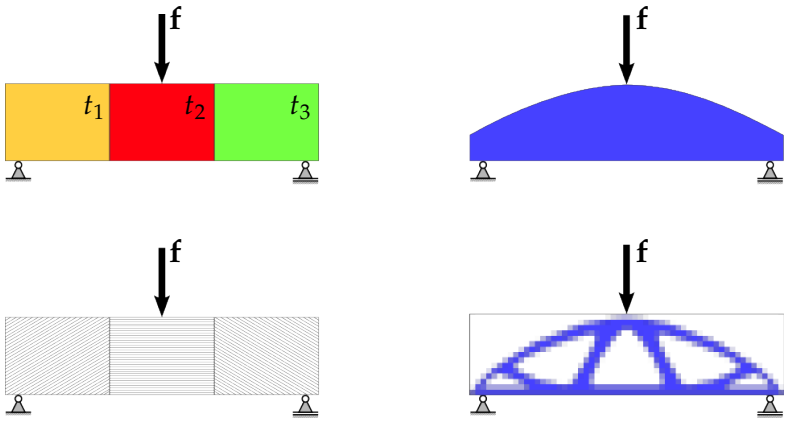

Fig. 2.10: Examples for structural sizing, shape, topology and material optimization (clockwise from top left)

Fig. 2.10 classifies these different types of structural optimization. A sizing optimization, for example, modifies the element thickness ($t_{1,2,3}$ in Fig. 2.10, upper left) or cross section area of a given analysis model. The shape optimization (upper right), on the other hand, changes the geometric definition of the analysis model to achieve improvements, thus, allowing more design freedom compared to sizing. The approach of topology optimization (lower right) is to redistribute material to locations where it is needed. Hence, an even higher design freedom can be realized with this, however, at the cost of a much greater number of design variables. The last variant of structural optimization shown in Fig. 2.10 is the material optimization (lower left), which is similar to sizing in the way that for an existing model the properties of its members are modified. Here, however, instead of elements' thickness the material characteristics are changed (e.g. fibre orientation angle of carbon composites).

In this thesis, the combination of sizing with shape optimization was studied. That means, the sizing optimization can improve the elastic attributes of the structure, while the shape optimization influences the aerodynamic flow around the aircraft, as well as, its structural characteristics. Thus, both disciplines that are combined in aeroelasticity can be manipulated directly with this optimization approach.

2.2.2 Optimization Algorithms

Generally, optimization algorithms fulfil the task of searching for extrema of a function subjected to possible constraints. There exists a great variety of optimization algorithms that can be applied to technical design problems. Usually an iterative approach is used to adjust the design variable values repeatedly until convergence on an optimum is reached. Many different methods for solving such tasks can be found with individual characteristics and requirements to the optimization problem. However, neither of these algorithms is able to solve every given optimization problem equally well [BSS06]. This means that depending on the specific optimization problem at hand (see e.g. Fig. 2.10) a suitable optimization algorithm needs to be selected.

Some of the aspects that need to be factored into this choice are:

- Number of design variables
- Types of design variables (discrete/continuous)
- Convexity of design space (one global or many local optima)
- Quality of objective and constraint functions (e.g. smoothness, continuity)
- Number of constraint functions
- Availability of gradients
- Non-linearity of involved functions

2.2.2.1 Classes of Optimization Algorithms

The many different existing optimization algorithms can be classified based on their approach to solving an optimization problem. Multiple ways of carrying out this classification can be found in literature [see Mar02; Dao05; BSS06; Van07; Har08; Wun13], yet, all generally distinguish the algorithms by their method of progressing through the design space, as well as, the required information about the considered functions. Based on this, two main classes of optimization algorithms can be identified as deterministic and stochastic.

Deterministic Algorithms use objective function information for a directed search from a start point to the (usually) nearest minimum in the design space. These algorithms can be subdivided further depending on the order of function information they apply in this search. In other words, algorithms of 0^{th} order only use the function value itself, 1^{st} order ones additionally compute the first order function derivatives, while 2^{nd} order methods also apply the second order derivative matrix (i.e. Hessian matrix). Examples for these different order methods are *Simplex*, *steepest descent* and *sequential quadratic programming* (*SQP*) respectively (see for example [BSS06; Van07] for further information). With increasing order the ability to handle non-linear problems improves as well. One characteristic of deterministic methods is that they always converge on the same

optimum, if the optimization is repeated from the same starting point with unchanged settings. The gradient based methods (i.e. 1^{st} and 2^{nd} order) are very efficient and usually reach the minimum with only few required function evaluations. This makes them suitable for large scale problems with many design variables and constraints [Mar02]. Yet, the optimization problem must allow calculating sensitivities (usually analytical or at least semi-analytical) of sufficient quality for this, which requires smooth continuous functions. The main disadvantage of these methods is that for non-convex problems (i.e. more than one optimum exists [Van07]) they converge on one local minimum depending on their problem approximation. This means, one cannot be sure to have found the globally best possible solution once the optimization converged.

Stochastic Algorithms determine the design variable values of the next iteration not based on a directed search but use stochastic methods (randomly or semi-randomly adjusting design variables). This means no gradients are computed making them methods of 0^{th} order. Examples for such algorithms are *random search*, *simulated annealing* [Har08] or *genetic algorithms* [Van07]. Due to their approaches, these methods are naturally able to handle discrete variables, as opposed to the deterministic ones [Van07]. They also generally have a better chance of finding the global optimum of a design problem [Van07], since they do not adhere to the slope of the objective function looking for the optimum. Caused by the principle of randomness, two consecutive optimizations with the same starting point and settings will not necessarily lead to the same result. As no gradient information needs to be calculated, smoothness and continuity of the design space is not critical here [Dao05]. However, the amount of required function evaluations increases rapidly with the number of design variables, which makes these methods very inefficient for large scale problems, where function evaluations are costly [Mar02]. Additionally, for problems with a great number of constraints, finding feasible solutions can become cumbersome with this approach.

2.2.2.2 Selection of an Optimization Algorithm

In order to choose an appropriate optimization algorithm, the character of the problem at hand needs to be clarified. The optimization problem to be solved here is a combination of sizing and shape optimization coupled to an aeroelastic analysis method. Thus, sizing design variables are defined for single elements or small groups of elements in the structural analysis model in order to have a sufficiently precise influence on the stiffness properties of the structure. Additional to the shape variables, this results in a great number of design variables ($> 10^{+3}$). Furthermore, the structural integrity of the proposed designs must be guaranteed, which leads to a great number of constraints ($> 10^{+4}$), as they are defined element wise over several load cases. Since the mathematics for the considered analysis methods are known and the functions are expected to be reasonably smooth and continuous, gradient calculation is possible. No discrete variables are present, as only thicknesses and geometrical quantities (i.e. angles and lengths) are applied. Also, due to the coupled aeroelastic analysis, system

evaluation effort might become significant with larger models. Therefore, an optimization algorithm with few required system evaluations and iterations is to be preferred.

Based on these aspects, a 2nd order deterministic optimization algorithm was selected. Specifically, the *NLPQL* algorithm by Schittkowski (Non-Linear Programming by Quadratic Lagrangian, [Sch86]) was chosen. This algorithm is a modified version of the *SQP* [BSS06; Van07] including the iterative approximation of the Hessian matrix (i.e. no original second order information is required). Its performance for different structural optimization problems was compared to other algorithms in [Sch86].

2.2.3 Specifics of Shape Optimization

Compared to sizing optimization, realizing shape optimization capabilities involves a number of specific issues (some of them were addressed in [HG85; Dao05]). While during a sizing optimization the analysis model is kept unchanged and only the physical properties of the model's elements are re-assigned, shape optimization requires to modify the geometric definition of the analysis model. This can have a severe influence on the quality of the discretisation, which in turn is directly related to the precision of the analysis results [Dao05]. An example is shown in Fig. 2.11, where the topmost approach to shape modification leads to a degeneration of quadrilateral elements to triangles (still having four nodes). One obvious solution would be to regenerate the analysis mesh discretisation each time the shape was changed by the optimizer (Fig. 2.11, middle). Yet, in order to make use of the efficient gradient based optimization techniques discussed in Section 2.2.2, re-meshing of the analysis model would inhibit calculation of consistent gradients, as this can cause discontinuities originating from e.g. changing numbers of elements or nodes. Therefore, a method for applying the shape changes on the existing models without deteriorating their quality or re-meshing would be beneficial (Fig. 2.11, bottom). The task of realizing such shape changes, as well as, providing shape design variables to the optimizer is generally carried out by the shape parametrization. An overview of existing methods for this is given in Section 2.2.3.1.

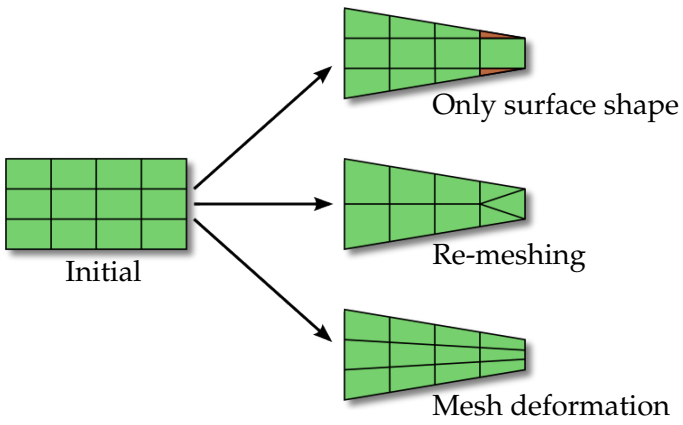

Fig. 2.11: Possibilities for shape modifications of an analysis mesh

Another issue with shape optimization in the context of this work is the multidisciplinary character of the optimization problem. Part of solving the aeroelastic problem with the partitioned approach (described in Section 2.1) is to separate the problem into its involved disciplines (i.e. aerodynamics and structures). However, since in the physical reality all effects occur in one combined system, it is crucial that the different analysis models of the separate disciplines represent the same design at every stage of the shape optimization. This places great importance on the consistency between the different analysis models during the repeated shape modifications. Yet, since the various analysis models place their focus on entirely different aspects of the model, the parametrization method needs to enforce consistency, where needed, while accounting for the required differences specific to each analysis discipline.

From the point of view of the optimization algorithm, shape parametrization is responsible for providing the shape design variable definition, with which the geometry of the aircraft can be modified. There exist many different ways to define shape design variables with respect to the area of influence of one shape variable and the complexity of shape change it can cause. Here, it is critical to find a good balance between requiring as few shape design variables as possible but allowing as wide a range of shape modifications as possible not to limit the design freedom unnecessarily. Furthermore, the shape design variable definition must enable calculating the required gradient information for the gradient based optimizer.

Since the developed method shall be applicable in early aircraft design stages but also allow future extensions for advanced and more detailed applications, the shape parametrization technique has to account for such scalability. Therefore, early system level configuration studies but also very detailed shape adjustments of a limited region should be supported. In the context of aircraft development, a shape parametrization method would be preferable that allows usage of shape variables that correlate to common aircraft engineering parameters (e.g. chord length). This would alleviate determining sensible gages for the shape variables, as well as, allow direct interpretation of shape optimization results.

Based on these requirements and the existing shape parametrization approaches described in the next section a method suitable for the proposed multidisciplinary shape optimization was selected.

2.2.3.1 Overview of Existing Shape Parametrization Approaches

A great number of shape parametrization approaches applicable to two dimensional (e.g. wing airfoil) and three dimensional (e.g. complete wing) aircraft development can be found in the literature. An extensive overview and comparison of the different approaches was conducted by Samareh [Sam99] but also [Str12; Wun13] compare existing approaches. Generally, most parametrization techniques can be classified by their primary way of influencing the shape. This yields two main groups: Mesh based parametrization directly modifies the nodal positions of the analysis meshes, while CAD (i.e. computer aided design) parametrization first affects the geometric representation from which the ana-

lysis models are derived. This means that mesh parametrization works very close to the analysis models, which allows modifying existing meshes without regeneration but mostly requires a greater number of design variables. CAD parametrization, on the other hand, exploits the higher logic of geometric object definitions so that greater shape changes can be realized with less design variables while simplifying consistency issues between involved analysis models. However, a link between the geometry description and the analysis meshes needs to be established often involving regeneration of the analysis models with every shape change (see e.g. [DDK+06; BRM+10; Wun13]). Within these two categories further differentiation can be found:

Mesh Based Parametrization The most basic concept here is the discrete approach [Sam99], where the coordinates of every concerned node in the mesh are declared design variables. This offers great design freedom but also involves a substantial number of design variables to achieve shape changes (applications in [CE04; Dao05; Fir10]).

An attempt at limiting the number of design variables by creating a geometric relation between the mesh nodes is the basis vector approach (see e.g. [Sam99]). With this, a weighted sum of basis vectors for predefined deformations of the mesh nodes is used to alter the mesh shape based on the weighting factor design variables. Yet, the approach entails a limited design freedom, as only shapes that were considered in the generation of the basis vectors can be described.

One frequently applied mesh based technique is the Free Form Deformation (FFD) [Bar87; SP86]. FFD uses a control volume that is defined around the original mesh geometry. To perform a shape change the control points defining this volume can be moved and the analysis mesh deforms accordingly to the distortion of its control volume, as the coordinates of the analysis mesh nodes relative to the volume are kept constant. This allows directly deforming meshes with a great number of nodes only requiring a relatively small set of shape variables. However, this approach also limits the design freedom, as the control volume can only twist, bend, taper, compress and expand the original model [Str12]. Especially structural models with internal structure (e.g. ribs/spars) would suffer from this way of parametrization, because the internal structure would distort with the external loft (e.g. warped spar due to wing twist). One speciality of FFD is that it can also be applied on the definition of geometric surfaces instead of analysis meshes. This places this approach between the two categories. Examples for this way of application are presented in [MAL+14; NBK+12].

CAD Based Parametrization A basic form of this approach is the shape representation through geometric functions such as splines or polynomials [Sam99]. The small set of parameters or control points of these objects can then be used as shape variables to deform the spline/polynomial shape. This has the advantage of having a smooth and continuous mathematical description of the shape allowing calculation of derivatives, as well as, having control over the permissible geometric shapes. On the other hand, this method of shape parametrization is limited to rather simple geometries, as the definition of the spline/polynomial

functions quickly is impeded with increasing shape complexity. Furthermore, the geometric representation needs to be linked somehow to the definition of the analysis meshes in order to conduct an optimization. Examples for shape parametrization with splines can be found in [CN07; BG03; PCK07]

An extended version of this approach is the CAD parametrization using available CAD graphical programs such as Open Cascade [Ope13] to describe and parametrize the desired geometries. This allows a great freedom in defining user specific shape variables while employing the extensive geometric functionalities of these tools (e.g. NURBS surfaces). Also, the number and impact of shape variables can be adjusted according to the current goals of the shape optimization (i.e. few parameters with great influence for concept finding or many variables with local impact for detail problems). Although CAD programs allow constructing geometries of great complexity, setting up a parametric CAD model suited for automatic shape optimization and enabling automated access to it can represent a major effort, which has to be repeated for every new problem. Furthermore, the issue of linking the geometric CAD description to the actual analysis models, which provide the system responses to the optimizer, must be solved. In many cases, this is done by regenerating the analysis meshes for every design change [HNS+08; BRM+10; Wun13]. However, in combination with gradient based optimization techniques, this regenerating of meshes can introduce discontinuities to the system functions that inhibit good quality sensitivities. Also, for the combined sizing and shape optimization in this work that would require substantial effort redefining sizing variables and structural constraints after each re-meshing step.

A variant of CAD parametrization is provided by generating the geometric models using so called high level primitives [LT08]. These high level primitives (HLP) are geometric elements already dedicated to a specific engineering component outfitted with a predefined set of available parameters (e.g. a wing with a span parameter). The geometry for these components is still generated using the abilities of a CAD tool as before, but the recurring task of constructing parametric geometries of aircraft components with basic geometric entities is reduced to setting the appropriate parameters of a high level primitive and combining it with others. The great advantage of this approach is providing a standardization to parametrizing specific aircraft geometries which increases the efficiency and robustness of the process while using common engineering parameters to do so. However, due to the dedication of the different high level primitives, their applicability is also limited to a certain field of engineering problems (here aircraft development). Examples for such programmes are the Multi Model Generator developed at TU Delft [LT08] or Vehicle Sketch Pad at NASA [Hah10].

2.2.3.2 Selection of Shape Parametrization Method

In his comparison of shape parametrization techniques, Samareh [Sam99] has provided a number of criteria with which to assess the available methods. The most crucial of those identified for the current application are consistency, number of design variables, mesh deformation/re-usage and smoothness. In order

to select a shape parametrization method appropriate for the proposed sizing and shape optimization coupled with aeroelastic analysis, these aspects combined with the specific requirements identified at the beginning of this section were assessed.

Due to the main requirement of consistency between the different analysis models, all mesh based parametrization methods except the Free Form Deformation could be ruled out, since high effort would be required to realize consistency with shape parameters based on the individual meshes. Even though FFD could satisfy consistency, if all involved analysis models were manipulated by the same control volume, the limited possibilities to modify the shape and the drawbacks regarding internal structure also led to disregard this approach.

Thus, a CAD parametrization approach using the high level primitive concept was developed [MPD13; DPD+13b]. This features great design freedom with smooth, controllable geometries requiring only a small number of shape variables. The high level primitives approach prevents issues of producing parametrized aircraft geometries while providing a great variety of different shape parameters to choose from. Also, shape parameters with different levels of influence (see Section 3.3) were defined so that scalability between the different aircraft development phases is given. The main issue of linking the analysis meshes to the parametric geometry model was solved by applying the basic idea of free form deformation on the CAD geometry. This means that the analysis meshes are initially derived from the parametric geometry and then mapped back onto the geometric surfaces using relative coordinates (similar to [HM12]). Thus, a link from the CAD model to the analysis meshes is established, which guarantees consistency between all involved models. The idea of a central geometry model between the different analysis disciplines was also expressed by [SB00; HM12]. An application for shape parametrization with a similar approach for aerodynamic shape optimization can be found in [MAW+10]. Through such a mapping procedure, the existing analysis meshes can be deformed to a great extend without requiring re-meshing or causing mesh deterioration, as illustrated in Fig. 2.11. Therefore, none of the mentioned issues regarding gradient computation or element based constraint formulation in case of sizing have to be expected.

This developed shape parametrization approach is described in more detail in Section 3.3.

2.2.4 Approaches to Sensitivity Analysis

When using gradient based optimization algorithms, it is necessary to calculate the sensitivities (i.e. gradients) of the objective function, as well as, of all included constraint functions with respect to the design variables. The first order derivatives are shown in Eq. (2.33) [e.g. Van07, p. 462] for an optimization problem with n_{DV} design variables and n_g inequality constraints.

$$\begin{aligned} \nabla f(\mathbf{x}) &= \frac{\partial f(\mathbf{x})}{\partial x_i} \quad \text{for} \quad i = 1 \dots n_{DV} \\ \nabla g_j(\mathbf{x}) &= \frac{\partial g_j(\mathbf{x})}{\partial x_i} \quad \text{for} \quad i = 1 \dots n_{DV} \quad \text{and} \quad j = 1 \dots n_g \end{aligned} \tag{2.33}$$

Thus, a vector of objective function gradients and a matrix of constraint function gradients (i.e. Jacobi matrix) have to be determined. When using second order optimization algorithms, the Hessian matrix $\mathbf{H}$ of second order objective function derivatives is required as well:

$$\mathbf{H}(\mathbf{x}) = \nabla^2 f(\mathbf{x}) = \frac{\partial^2 f(\mathbf{x})}{\partial x_i \partial x_j} \quad \text{for} \quad i,j = 1 \dots n_{DV} \tag{2.34}$$

However, the selected NLPQL optimization algorithm [Sch86] uses the BFGS method developed by Broyden, Fletcher, Goldfarb and Shanno ([see e.g. Fle70; Gol70; Sha70]) to approximate the inverse Hessian matrix instead of its costly explicit evaluation. Therefore, the second order derivatives do not need to be calculated directly in order to apply this optimization algorithm. Consequently, this section will only focus on the first order derivatives.

Generally, one can categorize the existing approaches of finding function gradients numerically into three classes. These are finite differences, analytical and semi-analytical approaches. These categories differ in numerical precision and stability, evaluation time but also in implementation effort.

2.2.4.1 Finite Differences

Finite differences [see e.g. Har08] or often called numerical gradients represent the most basic approach to calculating the gradient of an arbitrary function $f(x)$ with respect to a design variable x, since no information about the mathematical relations in this function is necessary (only function evaluations need to be available). For this, $f(x)$ is approximated using a Taylor series (see e.g. [MV01]) at a small distance Δx from its current point x. Truncating the series after the first order derivative yields the so called forward differences (Eq. (2.35)), while the central differences also respect the second order derivative term (cf. Eq. (2.36)).

$$\frac{df(x)}{dx} \approx \frac{f(x+\Delta x) - f(x)}{\Delta x} \tag{2.35}$$

$$\frac{df(x)}{dx} \approx \frac{f(x+\Delta x) - f(x-\Delta x)}{2\Delta x} \tag{2.36}$$

Due to consideration of the second order derivative, the central differences approach usually features gradient information of higher precision. However, the function needs to be evaluated at $f(x+\Delta x)$ and $f(x-\Delta x)$ for n_{DV} design variables requiring $2n_{DV}$ system solutions instead of $n_{DV}+1$ with forward differences. Also higher order differences taking into account more terms of the Taylor series exist that further increase the number of required system evaluations with the benefit of better gradient precision.

A general issue with the finite difference approach is the so called step-size dilemma finding the most suitable value for Δx, as discussed for example in [HG92; Kim90; Dao05]. Smaller step sizes would minimize the truncation error of the Taylor series, but might cause issues with coarse or oscillating functions or might trigger machine round-off errors, if too small. A short study on this is conducted later in Section 3.6.2.4.

Apart from this issue, the great advantage of finite differences is the fact that only discrete function evaluations are required for differentiation. Thus, it can be applied even if the mathematical relations are unknown or unavailable (e.g. by commercial programs without source code access). On the other hand, the number of required system evaluation rises quickly with increasing number of design variables. Hence, the computational effort of a system evaluation together with the number of design variables need to be taken into account.

2.2.4.2 Analytical Derivation

As opposed to the finite differences approach, the analytical gradient calculation approach requires detailed insight into the mathematical relations of the governing functions. These functions are analytically differentiated with respect to the existing design variables to calculate the gradients. This requires much higher implementation effort, but promises sensitivity calculation in the time frame of one system evaluation with high gradient accuracy. In the following, the analytical derivation approach is illustrated based on the equations of the structural FE method (see Section 2.1.1, Eq. (2.1)).

Eq. (2.37) clarifies the general differentiation of an arbitrary objective function $f(\mathbf{x})$ and a set of inequality constraints $\mathbf{g}(\mathbf{x})$ with respect to the design variable $x_i \in \mathbf{x}$.

$$\begin{aligned} \frac{df(\mathbf{x})}{dx_i} &= \frac{\partial f(\mathbf{x})}{\partial x_i} + \frac{\partial f(\mathbf{x})}{\partial \mathbf{u}} \frac{\partial \mathbf{u}}{\partial x_i} \\ \frac{d\mathbf{g}(\mathbf{x})}{dx_i} &= \frac{\partial \mathbf{g}(\mathbf{x})}{\partial x_i} + \frac{\partial \mathbf{g}(\mathbf{x})}{\partial \mathbf{u}} \frac{\partial \mathbf{u}}{\partial x_i} \end{aligned} \qquad \text{for} \quad i = 1 \dots n_{DV} \tag{2.37}$$

As apparent here, the function derivatives can be split into the explicit and the implicit partial derivative. The explicit term (first on right hand side in Eq. (2.37)) originates from a direct dependency of the function on the design variable. The implicit derivative (second right hand side terms in Eq. (2.37)), however, contains the indirect dependency through the solution of the analysis system (here the displacement vector $\mathbf{u}$) that itself has a gradient with respect to the design variable. The following paragraphs will focus mainly on the implicit partial gradient calculation, as it usually involves the more complex dependencies.

The gradient of the structural displacement vector $\frac{\partial \mathbf{u}}{\partial x_i}$ can be calculated by differentiating the finite element basic system of equations (Eq. (2.1)):

$$\mathbf{K} \cdot \frac{\partial \mathbf{u}}{\partial x_i} = -\frac{\partial \mathbf{K}}{\partial x_i} \cdot \mathbf{u} + \frac{\partial \mathbf{f}}{\partial x_i} \qquad \text{for} \quad i = 1 \dots n_{DV} \tag{2.38}$$

Since this equation is very similar to Eq. (2.1) with the displacement derivative instead of $\mathbf{u}$ as the unknown variable, the same solution approach can be followed here reusing the already solved stiffness matrix available from the previous analysis and applying it to the so called *pseudo load vector* on the right hand side.

Inserting the solution of this equation back into Eq. (2.37) yields the following relation for the example of the overall constraint function gradients:

$$\frac{d\mathbf{g}}{dx_i} = \frac{\partial \mathbf{g}}{\partial x_i} + \underbrace{\frac{\partial \mathbf{g}}{\partial \mathbf{u}} \cdot \overbrace{\mathbf{K}^{-1}\left(-\frac{\partial \mathbf{K}}{\partial x_i} \cdot \mathbf{u} + \frac{\partial \mathbf{f}}{\partial x_i}\right)}^{\frac{\partial \mathbf{u}}{\partial x_i}}}_{\boldsymbol{\lambda}} \qquad \text{for} \quad i = 1 \ldots n_{DV} \tag{2.39}$$

There exist two basic approaches for carrying out these calculations; the direct (i.e. design space) and the adjoint (i.e. state space) gradient computation [see e.g. Van07]. The overall calculations for both methods are exactly the same, they only differ in the sequence of matrix multiplications [Van80].

The direct approach would first solve for the displacement derivative $\frac{\partial \mathbf{u}}{\partial x_i}$ for all load cases and design variables ($n_{LC} \cdot n_{DV}$ system solutions). The adjoint method on the other hand first solves for one adjoint vector $\boldsymbol{\lambda}$ for each of the n_g constraint functions (n_g system solutions). Thus, depending on the optimization problem definition either the direct ($n_g \geq n_{LC} \cdot n_{DV}$) or the adjoint derivation ($n_g < n_{LC} \cdot n_{DV}$) is computationally more efficient, as it requires less system solutions involving the usually large stiffness matrix [Van80]. In this consideration the objective function can be counted as one additional constraint function.

Thus, the direct approach should be more efficient for the calculations in this work in most cases, because a high number of structural constraints is required for the combination of sizing and shape optimization, which usually surmounts the number of design variables multiplied with load cases by far.

Compared to the finite differences approach of the last section, the analytical differentiation is much more efficient [Van07, p. 312]. This is explained by the fact that the stiffness matrix does not need to be built up and factorized/inverted for each design variable. In case of the adjoint approach the number of system solutions is even independent of the number of design variables making it appropriate for optimization problems with large numbers of design variables. However, all the partial derivatives shown in Eq. (2.37) to Eq. (2.39) have to be calculated analytically, which represents a major implementation effort. Particularly in case of shape optimization, the partial derivative of the stiffness matrix with respect to nodal movements proves to be highly complex [Dao05; Van07; Fir10]. Yet, the gradients through analytical differentiation are of much higher quality than those obtained by finite differences, as they do not contain the truncation error mentioned before.

2.2.4.3 Semi-Analytical Derivation

The semi-analytical sensitivity calculation [see e.g. BH88; Van07] represents a combination of the analytical and the finite difference approaches described before, where some of the required partial derivatives are obtained by finite differences. Through this, expensive or even unavailable partial derivatives can be calculated without knowing the involved mathematical functions. Hence, semi-analytical gradients can offer higher accuracy than finite differences, as the analytical relations are applied for most parts.

Hence, for example the stiffness matrix derivative in the pseudo load vector in Eq. (2.38) can be calculated by e.g. forward differences (indicated by Δ):

$$\mathbf{K} \cdot \frac{\partial \mathbf{u}}{\partial x_i} = -\frac{\Delta \mathbf{K}}{\Delta x_i} \cdot \mathbf{u} + \frac{\partial \mathbf{f}}{\partial x_i} \qquad \text{for} \quad i = 1 \dots n_{DV} \tag{2.40}$$

$$\frac{\Delta \mathbf{K}}{\Delta x_i} = \frac{\mathbf{K}(x_i + \Delta x) - \mathbf{K}(x_i)}{\Delta x} \qquad \text{for} \quad i = 1 \dots n_{DV} \tag{2.41}$$

Using the partial derivatives obtained by finite differences the remaining steps of the gradient calculation are carried out in analogy to the analytical derivation. Because of that, the semi-analytical gradients can be combined with both the direct, as well as, the adjoint method described in the previous section.

The semi-analytical gradient computation is often applied in combination with shape optimization [Van07], as it allows to circumvent the costly analytical differentiation of the stiffness matrix with respect to nodal deformations mentioned earlier.

Through the combination of finite differences and analytical differentiation, the semi-analytical approach also combines their advantages and disadvantages. Due to the usage of analytical terms it gains in accuracy compared to the finite differences approach but also shows the perturbation step size dilemma and the dependency on the number of design variables that was discussed in Section 2.2.4.1. Depending on the numerical characteristics of the partial derivatives that are obtained by finite differences, the step size problems can even cause a worse overall gradient accuracy than full finite differences [BH88]. A short study of the quality of semi-analytical gradients is presented in Section 3.6.2.4 and compared to the finite differences approach.

2.2.5 Convergence Criteria

As numerical algorithms rarely converge on exactly the expected analytical value due to their numerical approximations, convergence criteria are required that decide with a certain precision when to stop an optimization procedure and whether an optimum has been found. Some of the different existing approaches [Van07, pp. 119-121], [BSS06, p. 131] are presented in this section.

The most basic termination criterion is specifying a maximum number of iterations. As this criterion has no influence on the state in which the optimization is stopped, setting the correct number involves mostly experience, but it may be the only means of terminating certain optimization algorithms (e.g. genetic algorithms) [Har08]. Also, it can be used in combination with other criteria to prevent unwanted infinite loops.

Other approaches involve the absolute or relative change in the objective function value or the design variables between iterations so that the optimization is stopped if the value falls below a certain boundary [Van07, p. 119].

From the mathematical point of view, a minimum is characterized by the first derivative being equal to zero and the second order derivative greater than zero. For a problem with multiple design variables this leads to:

$$\nabla f = 0 \quad \text{and} \quad \mathbf{H} = \nabla^2 f \quad \text{is positive definite} \tag{2.42}$$

Here, the first condition is regarded as necessary while the second is sufficient for the presence of a minimum.

For constrained optimization problems the first part of this condition was extended yielding the so-called Karush-Kuhn-Tucker (KKT) criterion [Van07, p. 25]:

$$\nabla f(\mathbf{x}^*) + \sum_j \lambda_j \nabla g_j(\mathbf{x}^*) = 0 \quad \text{with} \quad \lambda_j \geq 0 \tag{2.43}$$

Here, the KKT criterion was expressed for an optimization problem with only inequality constraints. A prerequisite for Eq. (2.43) is that the design point $\mathbf{x}^*$ must be feasible (i.e. $g_j(\mathbf{x}^*) \leq 0$) and only the active constraints (i.e. $g_j(\mathbf{x}^*) = 0$) are considered. This means that for convergence at $\mathbf{x}^*$ the gradient of the objective function must cancel out with the weighted sum of active constraint function gradients. Due to numerical inaccuracies, a small threshold value ε_{KKT} for the absolute value is applied below which the KKT criterion is assumed as fulfilled. The default value for this in the developed framework is $\varepsilon_{KKT} = 10^{-6}$.

Generally, for convex problems the KKT conditions are necessary and sufficient for a minimum; in case of a non-convex design space these conditions are only necessary and the minimum has to be confirmed otherwise.

One issue with applying the KKT in large scale optimizations is the numerical precision of its weighted sum. This means the more constraint functions are active the more constraint gradients are included in the weighted sum. Assuming each constraint has a small numerical error, adding all those errors up can yield a larger error in the sum. This makes it more difficult to satisfy the KKT for small ε_{KKT} values preventing convergence. Hence, it may be necessary to increase this threshold for large scale optimizations with many constraint functions. A short study on this is performed in Section 4.1.4.2.

2.2.6 Multi-Objective Optimization

A special branch of problems are the multi-objective or vector optimization problems. Here, more than one objective function needs to be optimized forming a vector of objective functions (Eq. (2.44)), as done later in Section 4. This section shall provide a short introduction to the particularities of such optimization problems also described in for example: [BSS06; Van07; Har08].

$$\min \ \mathbf{f}(\mathbf{x}) = \begin{pmatrix} f_1(\mathbf{x}) \\ f_2(\mathbf{x}) \\ \vdots \\ f_{n_f}(\mathbf{x}) \end{pmatrix} \quad \text{so that} \quad \mathbf{g}(\mathbf{x}) \leq 0 \quad \text{and} \quad \mathbf{x}_{lb} \leq \mathbf{x} \leq \mathbf{x}_{ub} \tag{2.44}$$

Since the included objective functions hardly ever reach their individual minima all for the same vector $\mathbf{x}^*$ of design variable values, the previously optimal point is transformed into an optimal region (see Fig. 2.12a). Often the objective functions have opposing preferences so that a compromise between them is required.

In this context the Pareto front [e.g. BSS06; Har08] (see Fig. 2.12b) is defined as the set of all solutions, where one objective function can only be improved by

deteriorating the value of one or more of the remaining objective functions (see Fig. 2.12a).

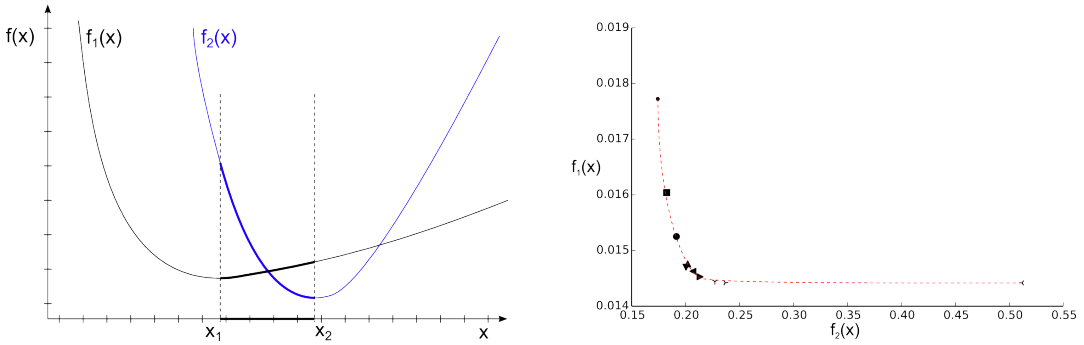

(a) Optimal region of two arbitrary objective functions [e.g. BSS06]

(b) Pareto front of two objectives

Fig. 2.12: Multi-Objective problem examples

In order to find a suitable solution for the multi-objective problem an additional criterion is required [BSS06, p. 184]. One could evaluate the entire Pareto front of the problem and pick the one solution that has the best combination of characteristics for the application at hand. However, generating the Pareto front can be very expensive requiring a great number of optimizations.

In order to allow application of the established optimization algorithms to multi-objective problems, the objectives are often combined into one scalar objective function. However, one has to consider that the way of combination can already limit which points on the Pareto front can be reached with the combined function.

One approach for combining a number of n_f objectives into one scalar objective function is a weighted sum:

$$\tilde{f}(\mathbf{x}) = \sum_{j}^{n_f} w_j f_j(\mathbf{x}) \tag{2.45}$$

The weighting factors w_j can be used to scale the influence of each objective function. Thus, by varying the weighting factors the Pareto front could be evaluated. However, it cannot be guaranteed that an equal distribution of weighting factors will yield an equal distribution of points on the Pareto front. This means predicting which weighting factor combination will yield a useful or beneficial result is a very difficult task. Hence, with this approach usually more than one set of weightings need to be evaluated to find a promising combination (see Section 4.2.1.2).

Other methods of creating a scalar objective function from several objectives as for example presented by Harzheim [Har08] exist, which are not discussed here in further detail.

3 Developing a Multidisciplinary Shape Optimization Framework

After the selection of methods to be applied in this work, the main question was: With what architecture can the desired multidisciplinary shape and sizing optimization functionality be reached? One option would be to include all involved analysis methods and their interactions into one all-encompassing program forming a monolithic architecture. Another possible way is to create a framework of different tools interacting with each other. On the one hand, the monolithic approach would have the big advantage of usually high performance, since data could be exchanged within one program. The framework approach, on the other hand, has the benefit of higher flexibility allowing to adjust or exchange one or several of its components without having to address the remaining components. Therefore, due to the multidisciplinarity and the intention of allowing application of the developed method at different stages of the aircraft design process, it was decided to follow the framework approach. Even though the performance of a framework would be lower than the monolithic approach caused by the slower data transfer between components, the flexibility of the distributed architecture outweighed these disadvantages.

The developed framework and its components are presented in this chapter.

3.1 Layout of the Framework

An overview over the developed shape optimization framework with its different components and involved models is shown in Fig. 3.1. The process is based on the initial CPACS model [LH11] that provides the parametric aircraft definition and meta-data for the analysis models. The three main components of this framework are the parametric geometry program *Descartes*, the multidisciplinary design optimization tool *Lagrange* and an aerodynamic solver (i.e. *Athena Vortex Lattice*). Combining these programs in a framework with a common design variable model and analysis data exchange allows shape and sizing optimization based on aeroelastic analysis with consistently updated manoeuvre loads.

The first framework component, *Descartes*, is based on the *TIGLViewer* program and the *TIGL* programming libraries developed by DLR [LH11]. *Descartes* is currently being further developed and enhanced at Airbus Defence & Space [MPD13]. It uses the open source CAD environment Open Cascade [Ope13] to generate a geometric representation of the parametric CPACS dataset defining the aircraft. Founded on this geometry, the analysis meshes for the different disciplines (e.g. structural FEM model or aerodynamic vortex lattice model, see Fig. 3.1) are derived and mapped back onto the geometry. This way, in case shape parameters changes, the analysis models can be updated without having

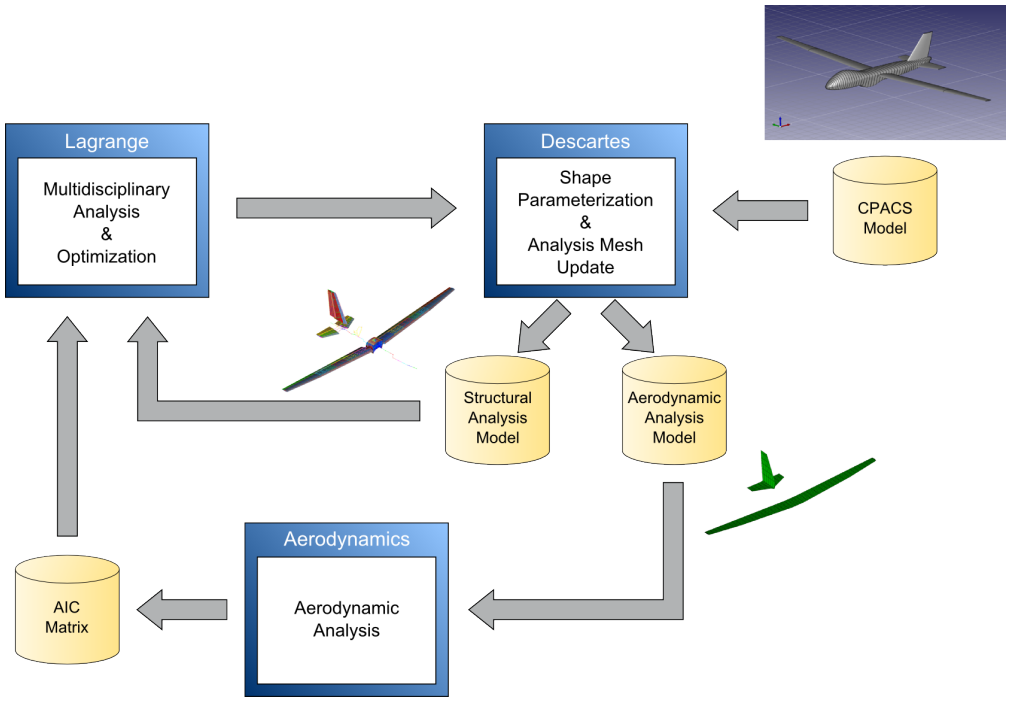

Fig. 3.1: Layout of the multidisciplinary shape optimization framework

to regenerate them. For application in the shape optimization process, *Descartes* allows declaration of shape design variables based on its parametrization, as well as, geometric constraint functions.

Lagrange is an in-house multidisciplinary design optimization program. It is being developed at Airbus Defence & Space over the last 30 years and incorporates its own linear finite element solver [see e.g. DPD+12; SDP+12]. Thus, it unifies two framework components in one: an analysis method and an optimization algorithm. The program allows fully coupled aeroelastic optimization using sizing or fibre angle design variables. *Lagrange* features an extensive design criteria model consisting of strength, stability, manufacturing, aeroelastic effectiveness, flutter, gust, trim and modal constraints [SDP+12]. A selection of gradient based optimization algorithms is applied to solve multidisciplinary problems in aircraft development. Since fully analytical gradients are available in *Lagrange*, it is possible to address large scale problems very efficiently. All loads are calculated based on realistic aeroelastic flight states and are updated continuously during the optimization. Through the combination of *Lagrange* and the geometric parametrization capabilities of *Descartes* fully coupled aeroelastic shape and sizing optimization can be realized.

As an aerodynamic solver for load evaluation during an aeroelastic analysis, the open source vortex lattice program *Athena Vortex Lattice* (i.e. *AVL*) was chosen. This aerodynamic analysis program is being developed at the Massachusetts Institute of Technology by Drela and Youngren [DY10]. Based on its results, a Trefftz Plane analysis [Tre21] can be conducted in order to estimate the corresponding induced drag. As described in Section 2.1.2.3, the vortex lattice solver was modified to provide aerodynamic influence coefficient (AIC) matrices [AR68; KL09; VIW+11]. Together with a conventional C_P-AIC matrix an induced drag

AIC matrix based on the Trefftz method is provided to the framework by the aerodynamic analysis (Section 2.1.2.5) for application during the aeroelastic analysis.

In the following sections the functionality and characteristics of the different components in the framework are discussed more in detail.

3.2 Realization of Aeroelastic Analysis

In the course of this section, the currently implemented solution of the aeroelastic problem in *Lagrange* is described. Also, details about the integration of the aerodynamic solver in the aeroelastic analysis with induced drag evaluation are given.

Generally, the data generated by the analysis part illustrated in the following are provided as system responses to the optimization algorithm. That means, based on the results of these analyses, the constraint and objective functions, as well as, their sensitivities are evaluated during the optimization.

3.2.1 Aeroelastic problem formulation

During aeroelastic analysis, aerodynamic loads $\mathbf{f}_{Ae}$ are added to the structural load vector $\mathbf{f}_{St}$ acting on the aircraft, hence, the basic equation Eq. 2.1 introduced in Section 2.1.1 transforms into:

$$\mathbf{K} \cdot \mathbf{u} = \mathbf{f}_{St} + \mathbf{f}_{Ae}(\mathbf{u}) \tag{3.1}$$

The aerodynamic forces are evaluated as discussed in Section 2.1.3 taking into account their dependency on structural displacements $\mathbf{u}$. The static forces, on the other hand, have no dependency on the deformation.

With the pressure coefficient AIC matrix derived in Section 2.1.2.3 and the aero-structural coupling from Section 2.1.3 the aerodynamic loads in the structural system are given as:

$$\mathbf{f}_{Ae} = \mathbf{T}_{SA} \cdot q \cdot \mathbf{A} \cdot \mathbf{AIC}_{C_P} \cdot \mathbf{b}_c \tag{3.2}$$

With

$$b_{c_i} = -\mathbf{v}_\infty \cdot \mathbf{n}_i \tag{2.6 revisited}$$

Here, $\mathbf{A}$ represents the diagonal matrix containing the areas of all vortex lattice panels, q is the dynamic pressure as defined in Eq. (2.3) and $\mathbf{T}_{SA}$ is the aero-structural transformation matrix introduced in Section 2.1.3.

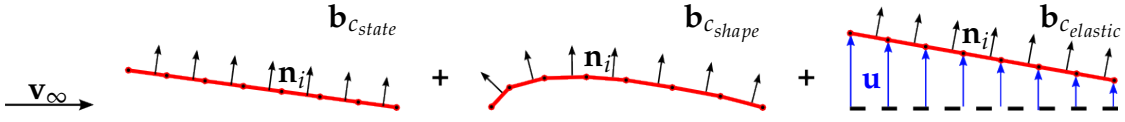

Fig. 3.2: Components of the aerodynamic boundary condition

The aerodynamic boundary condition $\mathbf{b}_c$ (Eq. (2.6)) required in Eq. (3.2) is comprised by several different components originating from differing factors.

Therefore, in analogy to Fig. 3.2 the aerodynamic boundary condition for a vortex lattice problem can be split into a flight state condition for the flat plate lifting surfaces $\mathbf{b}_{c_{state}}$, a geometric component accounting for wing twist or camber $\mathbf{b}_{c_{shape}}$ and the influence of the elastic deformation of the aircraft on the aerodynamic solution $\mathbf{b}_{c_{elastic}}$:

$$\mathbf{b}_c = \mathbf{b}_{c_{state}} + \mathbf{b}_{c_{shape}} + \mathbf{b}_{c_{elastic}}(\mathbf{u}) \tag{3.3}$$

The shape boundary condition can be calculated by assigning the mean slope of the camber line (e.g. Fig. 3.2) to each chordwise panel, while the aeroelastic component applies the transformation matrix from Section 2.1.3 on the displacement vector.

$$\mathbf{b}_{c_{elastic}} = \mathbf{T}_{AS} \cdot \mathbf{u} \tag{3.4}$$

In the applied aeroelastic analysis approach, this boundary condition definition is simplified using the assumptions shown in Eq. (3.5). Here, the normalization of equations by the free stream velocity $\mathbf{v}_\infty$ described in Section 2.1.2.3 applies.

$$\mathbf{n}_i \cdot \mathbf{v}_\infty = |\mathbf{n}_i| \cdot |\mathbf{v}_\infty| \cdot \cos\left(\frac{\pi}{2} - \alpha_i\right) = |1| \cdot |1| \cdot \sin\alpha_i \approx \alpha_i \tag{3.5}$$

This approximation is only valid for small angles of attack α and does not consider wing dihedral angles γ. Thus, in case of dihedral $\gamma \neq 0$, the angles of attack α have to be adjusted manually by $cos(\gamma)$. However, these simplifications have the advantage of linearising the aerodynamic problem, which facilitates the definition of flight mechanical trimming variables (see Section 3.3.3).

The combination of Eqs. (3.1) to (3.4) yields:

$$(\mathbf{K} - \mathbf{C}) \cdot \mathbf{u} = \mathbf{f}_{St} + \mathbf{f}_{Ae_r} \tag{3.6}$$

Where the matrix $\mathbf{C}$ represents the dependency of the aeroelastic loads on the displacement vector $\mathbf{u}$, while $\mathbf{f}_{Ae_r}$ combines the rigid aerodynamic loads of the first two boundary condition components of Eq. (3.3). Solving Eq. (3.6) directly can be numerically inefficient due to the size and shape of the resulting matrix on the left hand side. Hence, a different approach of solving the aeroelastic problem through a relaxed fix point iteration [see e.g. BSM+01] is pursued:

$$\mathbf{K} \cdot \mathbf{u}_{i+1} = \mathbf{f}_{St} + \omega \mathbf{f}_{Ae}(\mathbf{u}_i) + (1 - \omega)\,\mathbf{f}_{Ae}(\mathbf{u}_{i-1}) \tag{3.7}$$

After the convergence of equation Eq. (3.7) the aeroelastic forces $\mathbf{f}_{Ae}$ and the final structural displacements $\mathbf{u}$ are obtained. The final structural displacement vector can be used to provide the aeroelastic boundary conditions for further aerodynamic evaluations such as the induced drag analysis. Furthermore, based on this displacement the structural design criteria can be evaluated.

Thus, the induced drag AIC matrix derived in Section 2.1.2.5 can be applied to obtain the induced drag of the aeroelastically deformed model based on Eq. (2.21) and Eq. (3.8):

$$C_{D_{ind}} = \mathbf{\Gamma} \cdot \mathbf{AIC}_{C_D} \cdot \mathbf{\Gamma} \tag{2.21 revisited}$$

$$\mathbf{\Gamma} = \mathbf{AIC}^{-1} \cdot \mathbf{b}_c \tag{3.8}$$

Therefore, evaluation of induced drag in the aeroelastic state requires the boundary condition vector $\mathbf{b}_c$ derived in Eq. (3.3) based on the converged aeroelastic displacement vector $\mathbf{u}$.

3.2.2 How Shape Modifications Affect the Aeroelastic Analysis

Many aspects of the aeroelastic analysis that were described in the previous sections are dependent on the geometry of the aircraft. Due to the coupling of two analysis disciplines, both the aerodynamic and the structural model consistently have to take into account modifications to the geometry during a shape optimization in order to provide the physically correct analysis result. The geometric features of these models are updated through the shape parametrization approach described in Section 3.3.1. Once the models are adapted to the current state, the analysis data affected by this change has to be re-calculated so that the new configuration may be analysed. This introduces two issues when performing shape optimization in iterative loops. First of all, a sophisticated shape update procedure is required to keep the computational effort of numerous re-evaluations at a manageable level. And secondly, gradient information needs to be made available when using gradient based optimization algorithms. Therefore, especially the dependencies between shape design variables x_{shape} and system responses need to be examined so that gradient computation is possible. Hence, this section focuses on the dependencies between aeroelastic analysis results and the geometric shape of the aircraft.

Based on the following three equations reprinted from Section 3.2.1 the dependencies of the aeroelastic problem on shape changes through the shape variables x_{shape} can be illustrated.

$$\mathbf{K} \cdot \mathbf{u} = \mathbf{f}_{St} + \mathbf{f}_{Ae}(\mathbf{u}) \tag{3.1 revisited}$$

$$\mathbf{f}_{Ae} = \mathbf{T}_{SA} \cdot q \cdot \mathbf{A} \cdot \mathbf{AIC}_{C_P} \cdot \mathbf{b}_c \tag{3.2 revisited}$$

$$\mathbf{b}_c = \mathbf{b}_{c_{state}} + \mathbf{b}_{c_{shape}} + \mathbf{b}_{c_{elastic}}(\mathbf{u}) \tag{3.3 revisited}$$

The structural displacement vector $\mathbf{u}$ as the primary result of the aeroelastic analysis has significant sensitivities to the geometric shape of the aircraft. These can be written in the following manner:

$$\mathbf{u}\left(x_{shape}\right) = \mathbf{u}\left(\mathbf{K}^{-1}\left(x_{shape}\right), \mathbf{f}_{St}\left(x_{shape}\right), \mathbf{f}_{Ae}\left(x_{shape}, \mathbf{u}\left(x_{shape}\right)\right)\right) \tag{3.9}$$

Due to the implicit equation (3.1) with respect to $\mathbf{u}$ the solution for the displacement vector is found iteratively as explained in Section 3.2.1. This implicit relation for $\mathbf{u}$ is also shown in its dependencies.

Eq. (3.9) shows that on the structural side the stiffness matrix through its dependency on the finite element geometry and in some cases the static load vector (e.g. inertia loads) exhibit sensitivities towards shape design variables.

Focusing on the aerodynamic part of the aeroelastic analysis in Eq. (3.1), the aerodynamic forces $\mathbf{f}_{Ae}$ show a strong sensitivity with respect to the aircraft geometry but also to elastic deformations (see Eq. (3.9)), which causes the implicit

character of the aeroelastic equation. These dependencies are broken down in the following equation composed from Eq. (3.2) and (3.3):

$$\begin{aligned}\mathbf{f}_{Ae} = \mathbf{f}_{Ae}\big(&\mathbf{A}\left(x_{shape}\right), \mathbf{AIC}_{C_P}\left(x_{shape}\right), \\ &\mathbf{b}_c\left(x_{shape}, \mathbf{u}\left(x_{shape}, \mathbf{T}_{AS}\left(x_{shape}\right)\right)\right), \mathbf{T}_{SA}\left(x_{shape}\right)\big)\end{aligned} \tag{3.10}$$

The aerodynamic loads depend on the panel area matrix $\mathbf{A}$ and the aerodynamic influence coefficient matrix $\mathbf{AIC}_{C_P}$ (cf. Eq. (3.2)), which both are based on the geometry of the aircraft (see Section 2.1.2). Additionally, the loads are affected by the boundary condition vector $\mathbf{b}_c$ (Eq. (3.3)), where the shape boundary condition component $\mathbf{b}_{c_{shape}}$ depends on wing twist and camber shape variables, while the elastic component $\mathbf{b}_{c_{elastic}}$ has a sensitivity to shape changes via the aeroelastic displacement vector $\mathbf{u}$ and the coupling matrix $\mathbf{T}_{AS}$. Transforming the aerodynamic loads back onto the structure introduces the last dependency to $\mathbf{T}_{SA}$ shown here.

As described in section 2.1.3, the infinite plate spline method is applied for calculation of the coupling matrices $\mathbf{T}_{AS}$ and $\mathbf{T}_{SA}$ used in Eq. (3.2) and Eq. (3.3). Due to its approach based on the distances of the interpolation points, the coupling matrices also depend on the shape design variables and should be regenerated after each shape change. However, in the scope of this thesis, these matrices were kept constant during the optimization to avoid deterioration of the load distribution quality. This was founded on a test of regenerating the coupling matrices based on the new nodal positions after a shape optimization showing that the quality of the regenerated coupling matrices was reduced. Thus, the unmodified coupling matrices represented the aerodynamic loads more realisticly than the updated spline matrices, which exhibited oscillations due to the altered nodal positions. Keeping the coupling matrices constant would, however, cause an issue if the dihedral angle was part of the optimization. In that case, the orientation of the aerodynamic loads would not be perpendicular to their respective aerodynamic surface any longer inducing an error proportional to the dihedral change. Since dihedral changes were not considered during the shape optimization in the present work, the sensitivities of all system quantities in this framework with respect to altered fluid structure coupling are disregarded.

In case of induced drag evaluation during the aeroelastic analysis, additional sensitivities in the aerodynamic model with respect to the shape design variables have to be considered. Thus, since all three of the AIC matrices described in the previous sections mainly depend on the planform geometry of the aircraft, the induced drag analysis (see Section 3.2.1) is also influenced by altered aircraft geometries and the AIC sensitivities need to be considered.

$$\begin{aligned}\mathbf{AIC}_{C_P} &= \mathbf{AIC}_{C_P}\left(x_{shape}\right) \\ \mathbf{AIC}^{-1} &= \mathbf{AIC}^{-1}\left(x_{shape}\right) \\ \mathbf{AIC}_{C_D} &= \mathbf{AIC}_{C_D}\left(x_{shape}\right)\end{aligned} \tag{3.11}$$

3.3 Employed Design Parametrization

Design variables, which form the so-called parametric model, are the means of the optimization algorithm to influence the system behaviour (i.e. here: the aircraft's physical properties) in order to find a solution to a given optimization problem. Shape, trimming and structural sizing variables comprise the parametric model of the developed framework. Due to the prerequisites of the applied components, the parametrization is split between *Descartes* and *Lagrange*. In the following sections, these types of design variables, their characteristics and the corresponding framework component will be presented.

3.3.1 Geometric Parametrization

In Section 2.2.3.1 it was briefly described that a CAD based shape parametrization approach using a high level primitive philosophy was applied in this thesis. Furthermore, a mapping procedure was devised to allow consistent deformation of analysis models. In the following sections, a detailed description of this is provided.

3.3.1.1 Levelled Shape Parametrization Approach

As mentioned before, the developed shape optimization procedure shall be applicable to different stages of aircraft development with varying levels of detail. In order to reflect this purpose in the shape parametrization approach, a levelled classification of shape parameters was devised (similar to [MAR08]) with classes roughly corresponding to different aircraft development phases or addressing a specific analysis discipline.

First level shape variables allow global modifications of the aircraft (Fig. 3.3a). Parameters of this class influence entire components (e.g. wing/fuselage) of an aircraft configuration. Representatives of this level are wingspan, wing area or wing dihedral angle etc. The large influence of these shape variables enables early concept studies of the aircraft covering an extensive design space.

Second level shape parameters (see Fig. 3.3b) affect a part of an aircraft component. Examples for this level are section chord length, wing twist or local airfoil thickness. These parameters allow shape modifications to a specific aircraft component, while its global properties are already determined; for example, changing chord length distribution of a wing that has wing area and span fixed in order to improve aerodynamic or structural properties. Shape optimizations with this level of parameters may be conducted between conceptual and preliminary design, as soon as the overall concept of the aircraft has been determined.

Third level shape design variables have point wise influence and allow detailed shape changes (see Fig. 3.3c). Here, the control points of the geometric objects representing the design (e.g. control points of a B-spline

surface) are varied. An example for this would be an optimization focusing on aerodynamic aspects using higher fidelity analysis tools to improve laminar flow around an airfoil. With this type of shape variables only higher fidelity aerodynamic solver should be applied, since the vortex lattice method selected for this thesis lacks in many cases the ability to resolve such minute shape changes appropriately. Due to the very localized effects of these parameters and the necessity of higher fidelity analysis methods, shape design variables of this level should be applied in the detailed design phases.

Internal structure shape variables do not influence the outer shape of an aircraft design but affect the structural properties of the vehicle (see Fig. 3.3d). Spar, rib and stringer positions, as well as, their orientation angles, among others, belong to this category. This class of shape parameter has the particularity that it only affects one specific analysis discipline model as opposed to the outer shape that influences virtually the models of every considered aircraft discipline. With this type of shape variables, for example, the best chordwise position for a wing spar could be determined through shape optimization, which borders on the field of topology optimization (see Section 2.2.1).

Despite grouping shape parameters into different classes, the framework allows combining shape design variables out of different levels in the same shape optimization.

3.3.1.2 Shape Parametrization using CPACS and Descartes

The task of shape parametrization in the developed optimization framework is divided into three components. The first component is a parametric aircraft description that contains all the required information to define the aircraft design entirely and offers the parameters for usage as shape design variables. The second part is the parametric geometry model that is based on the information in the parametric model and provides the actual geometric shape of the aircraft from which analysis models can be derived. The third shape parametrization component is the permanent linking of the derived analysis models to the parametric geometry model creating the connection between the geometric parameters in the aircraft description and the analysis models.

The Common Parametric Aircraft Configuration Scheme (CPACS) forms the first parametrization component in this framework. CPACS uses the XML data format to parametrically describe complete aircraft configurations including missions and other information related to the designed aircraft. CPACS is being developed by the DLR (German Aerospace Centre) under an open-source license [LH11] and is intended to be the central exchange data format, through which different disciplines can pass results and data among each other during the aircraft development process.

The features of an aircraft are defined using an approach similar to the high level primitives (HLP) method mentioned in Section 2.2.3.1. This means an aircraft model is built up hierarchically using HLP components for wings and

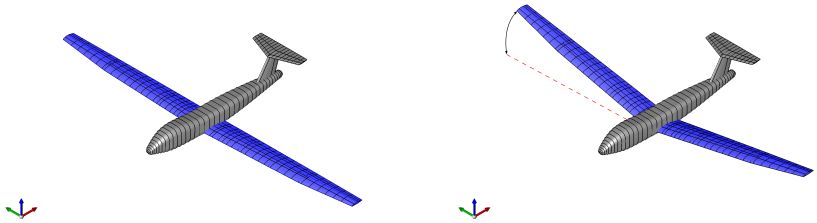

(a) First level example: Wing dihedral

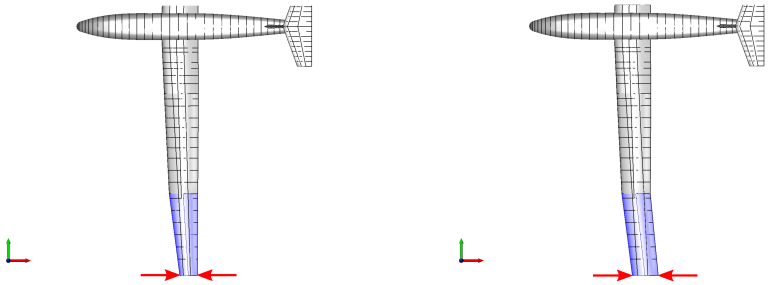

(b) Second level example: Section chord length

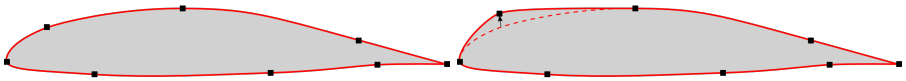

(c) Third level example: Airfoil profile shape

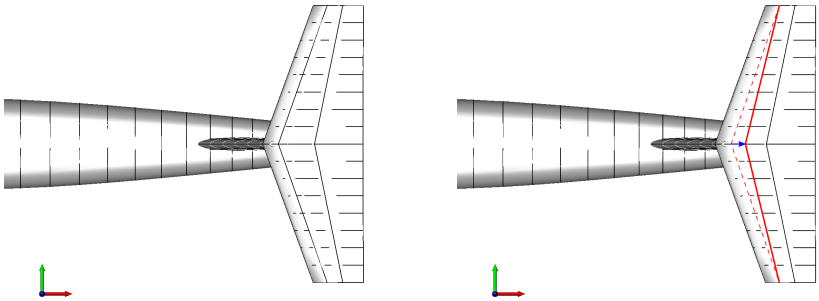

(d) Internal shape example: Front spar position

Fig. 3.3: Different levels of shape parameters

fuselages. A wing (see Fig. 3.4) consists of an arbitrary number of joined wing segments. Each segment is defined by its two limiting sections that are located at a prescribed distance and relative position. In every section an airfoil profile specified through standardized 2D point coordinates is referenced to establish the shape of the local wing cross section. Aircraft fuselages are described in a similar fashion using fuselage segments and cross section profiles. This approach allows creating aircraft designs of high complexity by applying these components and combining them in the desired way. Since every element in the hierarchy is constructed by its own specific set of parameters, CPACS allows modifications of the design in variable levels of detail. This parametrization philosophy can directly be related to the levelled shape design variable approach described in Section 3.3.1.1. With this method only few shape design variables are required to modify the aircraft design through a wide range of detail.

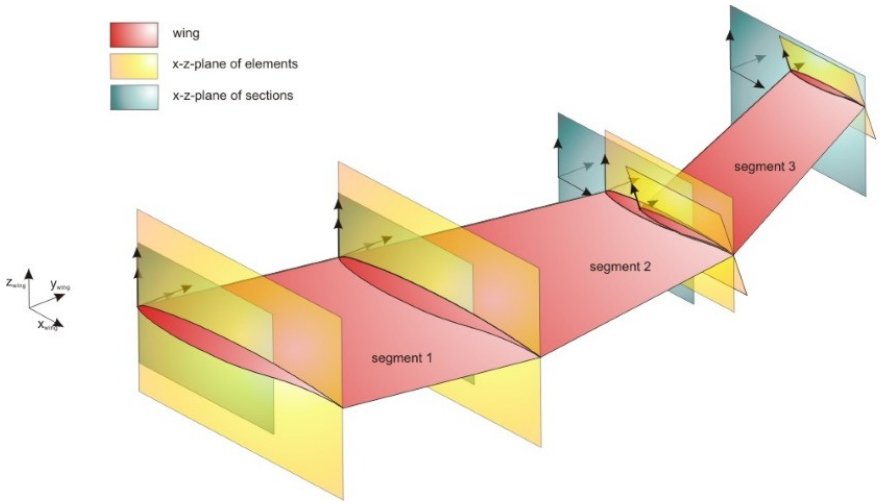

Fig. 3.4: CPACS definition of a wing [BD13]

There is also the possibility to define further shape parameters that are derived from CPACS parameters. One example for such parameters would be the overall wingspan equal to the sum of the spanwise length of all segments forming a wing. Generally, most parameters applied in CPACS have a physical meaning, defining lengths, positions or angles. Compared to other parametrization methods as for example Free Form Deformation [Bar87; SP86; Sam99], where only the control point positions of the control volume are used as shape variables, this alleviates creation and interpretation of CPACS shape design variables. This way, it is possible to work with every day engineering parameters (e.g. wing aspect ratio, dihedral etc.) when optimizing aircraft designs without having to deduct those parameters from a number of obscure design variables such as control volume points.

Not only the loft shape of an aircraft is parametrized in CPACS also the parametric description of the internal structure complete with spars, ribs, stringers, spar caps etc. is possible both for wing and fuselage components. This gives additional control over the shape of the internal structure compared to the other

approaches described in Section 2.2.3.1. Therefore, either the shape of the internal structure could be optimized with this definition or its design rules can be frozen while the outer shape is optimized.

CPACS does not only contain data for the geometric description of an aircraft. Meta-data such as materials, skin thickness, system masses or fuel tanks could be used to derive other analysis models than the aerodynamic and structural models applied in this work. However, due to its HLP approach oriented towards aircraft design, it is limited to this specific field of engineering.

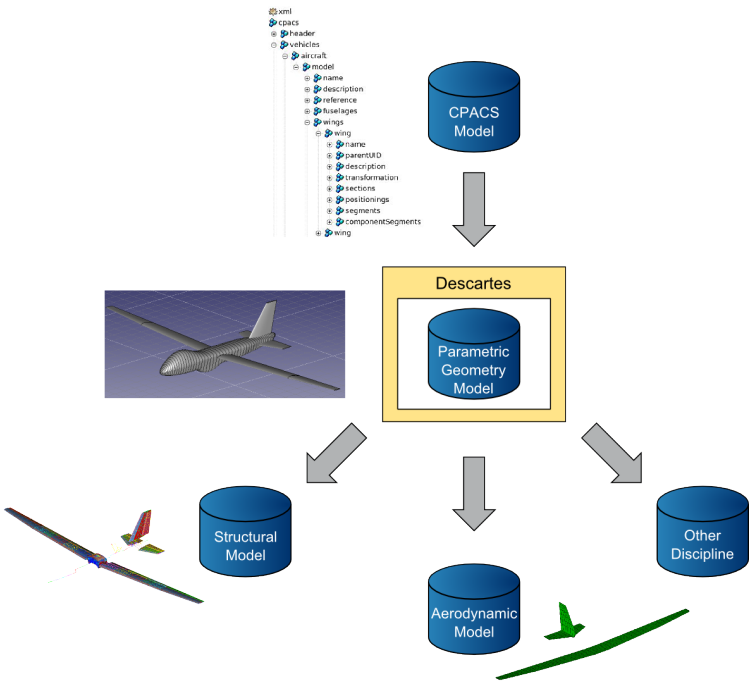

Fig. 3.5: Shape parametrization with parametric geometry model in *Descartes*

Based on the parametric CPACS description of an aircraft, a central parametric geometry model forming the second part of the shape parametrization approach is derived. The idea of a central geometry model and its advantages for multidisciplinary applications was also discussed for example in [SB00]. By placing a geometry model in the centre to act as basis for all considered analysis disciplines, one can secure consistency between disciplines but also reduce the number of required parameters for a common parametrization. In this framework, the program *Descartes* (see Fig. 3.5) is used to create such a central parametric geometry model. The program is being developed and extended at Airbus Defence & Space (cf. [MPD13; DPD+13b]). It relies on the open-source CAD kernel Open Cascade [Ope13] and on the TIGL tool chain developed by the DLR [LH11]. Inside *Descartes* the parametric description of CPACS is transformed into a geometric representation of the aircraft design. For this study, the full loft of an aircraft, as well as, the internal wing structure with stringers, ribs, spars, spar- and rib-caps is represented in the geometry.

The level of detail of this geometric *Descartes* model combined with the stored meta-data allows generation of several types of analysis meshes. Thus, all analysis models (e.g. aerodynamic CFD model, structural FE model) that are con-

sidered during the shape optimization are created from this geometry. After their generation, the models are linked to the parametric geometry using relative coordinates (similar to [HM12]). In other words, the analysis mesh nodes are etched onto the surfaces of the parametric geometry (see Fig. 3.6). This represents the third part of the shape parametrization approach. Through such a linking, shape modifications to the parametric geometry during an optimization are mirrored by all analysis models. This allows simultaneous and consistent shape changes to a number of analysis meshes without having to recreate or re-mesh the analysis models while using only one global set of shape parameters. Since the higher logic of the parametrized geometry supports all analysis meshes, even great shape changes may be realized without significantly deteriorating their mesh quality. In case any analysis mesh should degrade to a level where no reliable results can be expected, the shape optimization can be stopped and individual re-meshing for this specific discipline carried out, while the connection to the remaining disciplines stays intact. Hence, the issues caused by discontinuities in the system functions through re-meshing during gradient based optimization can be circumvented. Through the linking to one central geometry model the consistency between analysis models can also be guaranteed throughout the shape optimization.

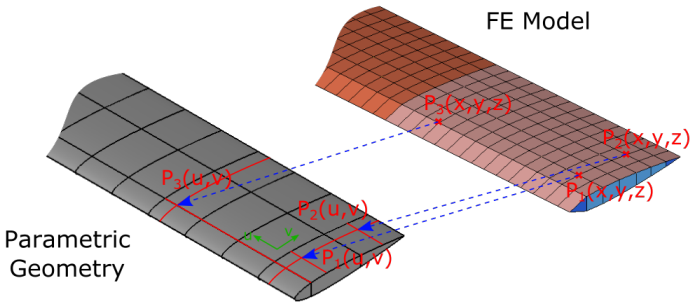

Fig. 3.6: Example for mapping an FE model to the parametric geometry

In the current state, the framework allows shape parametrization for the wing class of CPACS. Table 3.1 lists these available shape design variables in *Descartes* consisting of CPACS and derived parameters together with their respective parameter levels (defined in Section 3.3.1.1). At this point, the previously mentioned level 3 parameters, which would, for example, cause point-wise changes to an airfoil defined at a specific wing section, are not yet included in the framework. Figs. 3.7 and 3.8 shall illustrate the function of each of these parameters.

3.3.1.3 Limitations of the Developed Parametrization Approach

Beside the considerable functionality and advantages this shape parametrization approach holds, the decisions taken in the course of its development also led to some limitations which will be discussed in this section.

Table 3.1: Wing shape parameters available in *Descartes*

Wing Parameters		
CPACS Element	Parameter	Level
Wing	Length	1
	Span	1
	Area	1
	Aspect Ratio	1
	Installation Angle X	1
	Installation Angle Y	1
	X-Position	1
	Y-Position	1
	Z-Position	1
Segment	Length	2
	Area	2
	Aspect Ratio	2
	Taper Ratio	2
	Twist	2
	Dihedral	2
	Sweep	2
Section	Chord Length	2
	X-Rotation	2
	Y-Rotation	2
	Z-Rotation	2
Inner Structure	Spar Position Start	internal
	Spar Position End	internal
	Rib Position	internal
	Rib X-Rotation	internal
	Rib Z-Rotation	internal

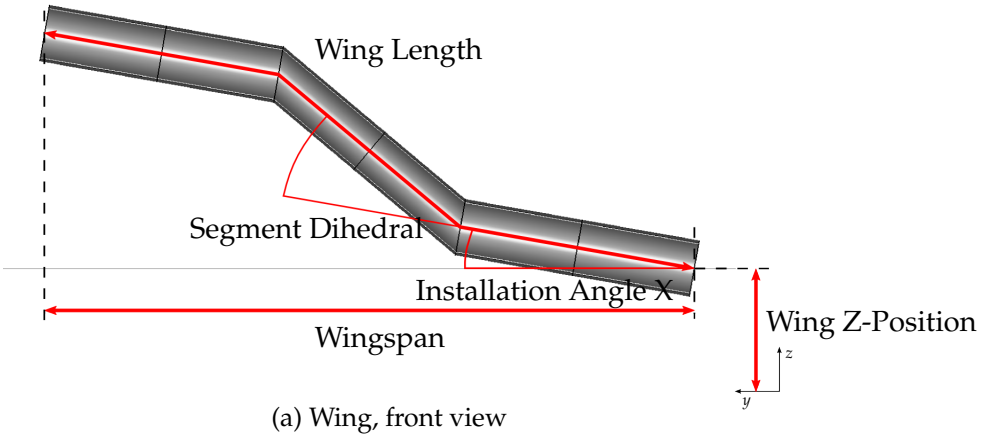

(a) Wing, front view

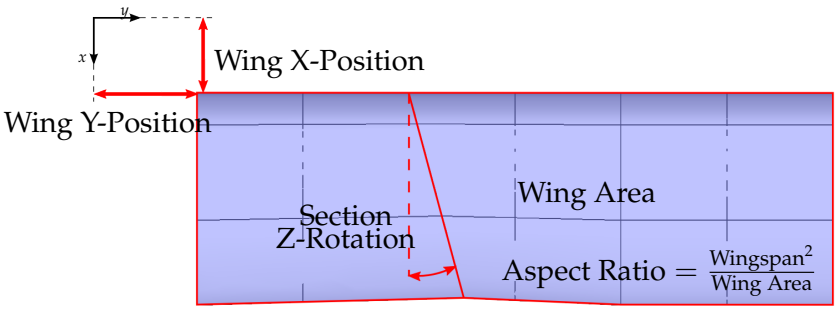

(b) Wing, top view

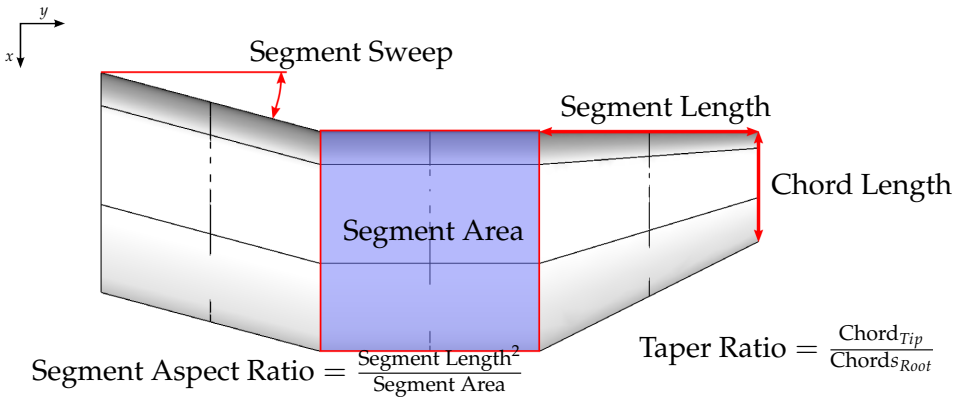

(c) Wing segments, top view

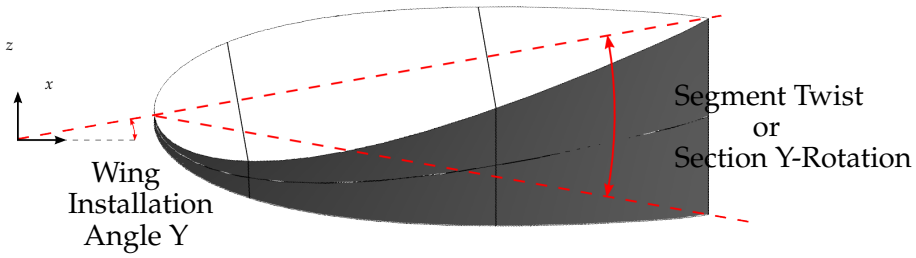

(d) Wing segments, side view

Fig. 3.7: *Descartes* shape parameters

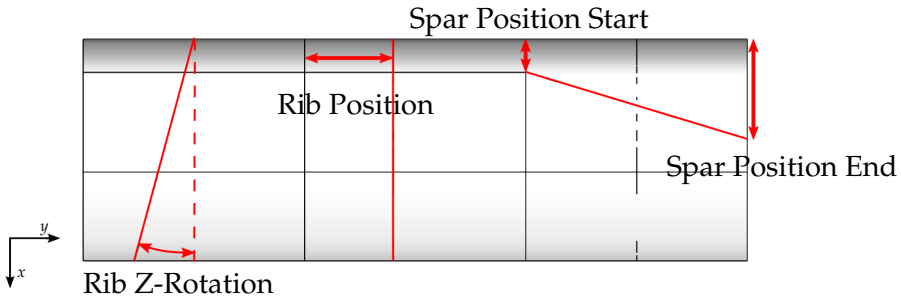

(a) Inner structure, top view

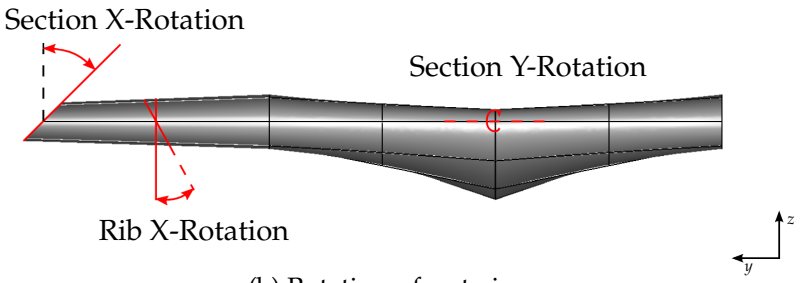

(b) Rotations, front view

Fig. 3.8: *Descartes* shape parameters, continued

Due to the fact that all considered analysis models in this framework have to be based on the parametric geometry model in order to be parametrized for shape optimizations, a compromise must be found that balances the requirements of each analysis model towards the parametric geometry. There might be differences in idealization of the aircraft (e.g. stick model versus volume model), but also in the level of detail with which the aircraft is represented. Examples for such details could be fairings or ram air inlets that must be modelled for aerodynamic analysis while the structural discipline would disregard these components, as they do not contribute to the structural stiffness properties. However, in order to link all analysis models back to the parametric geometry, the geometry must contain all features that are present in any of the analysis models. In some cases this could lead to conflicts between the disciplines' requirements. Hence, the applied analysis models have to be balanced regarding fidelity and level of detail they examine so that a consistent parametric geometry can represent all of them.

By using the high level primitive approach the complexity of the shapes that can be constructed is limited to the applications in aircraft design. This means, this developed method can only be applied on models one can construct from wings and fuselages. Due to the decision of using CAD parametrization the great design freedom of discrete mesh parametrization can also not be reached. However, these aspects were accepted in the context of developing a shape optimization framework for aircraft design.

The modular approach of connecting different arbitrary analysis models to a central parametric geometry also entails complexity through required interfaces and data conversion. Yet, with the prospect of expandability to other analysis disciplines with different levels of fidelity, this approach could be justified.

3.3.2 Structural Sizing Parametrization

Additionally to the shape design variables of the previous section, structural sizing design variables are applied in this work. Compared to shape parameters, sizing variables have a much more focused influence, sometimes limited to only one finite element, affecting specifically the structural properties of the aircraft. This way, it is possible to satisfy structural constraints, such as e.g. wing skin stresses, much more selectively than by modifying the shape variables in the respective part of the aircraft.

The definition of these structural design variables is made available by the multidisciplinary analysis and optimization program *Lagrange*. It is possible to specify sizing (x_{size}) and composite fibre angle (x_{fibre}) design variables. In this thesis, only the sizing functionality of *Lagrange* is considered in combination with shape optimization. Sizing design variables relate to the thickness of 2D shell elements or to the cross section area of 1D elements such as rods or bars. In case composite materials are used, the thickness of different fibre layers in shell elements can also be parametrized independently so that layers with different fibre orientation can be altered individually. Hence, with a set of sizing variables defined, the optimization process can redistribute structural material in a directed manner improving the objective while satisfying the given constraints. The structural design variable types used in this work have already been available in *Lagrange* (see e.g. [SDP+12]), and therefore, will not be discussed in great detail.

3.3.3 Flight Mechanical Trimming Parametrization

Lagrange also enables flight mechanical trimming of aeroelastic flight states (see [SDP+12]). Here, elastic trimming refers to the process of adjusting the angles of attack of aerodynamic surfaces to reach equilibrium of aerodynamic and inertia loads while considering the aeroelastic responses of the structure. As aeroelastic deformation caused by flexible structures may have a significant influence on the actual aerodynamic loads, it is crucial to include effects of static aeroelasticity during the trimming procedure.

This procedure is implemented in *Lagrange* in the form of an optimization problem. Thus, the desired state (e.g. Lift = Weight) is prescribed using inequality constraints limiting the feasible region of the design space to a small range around that state (see Section 3.4.3). Trimming design variables (x_{trim}) can be assigned to angles of attack for wings and stabilizers or deflection angles of control surfaces. These trimming design variables and constraints are added to the general optimization problem comprised of other design variables, constraints and an objective function assuring trimmed aeroelastic loads for each iteration.

In *Lagrange* the available trimming design variables are realized as scaling factors that are applied on the aerodynamic boundary condition of the respective flight state. Since they shall only influence the angle of attack of a lifting or control surface, these scaling factors only affect the flight state component $\mathbf{b}_{c_{state}}$ of the aerodynamic boundary condition described in Eq. (3.3) in Section 3.2. Furthermore, the flight state component of the boundary condition is linearised

through Eq.(3.5) so that the scaling factors can be applied directly to the angles of attack.

3.4 Multidisciplinary Criteria Model

In most cases, a shape and sizing optimization based on the design parametrization and the aeroelastic analysis described in the two previous chapters requires a criteria model in order to specify further limitations to the design. Such constraints are necessary to enforce requirements from any number of disciplines during the optimization. This means in MDO the design criteria are based on the responses of any of the included analysis disciplines limiting the feasible design space for the optimizer. In industrial development, this shall guarantee that the result of an optimization represents a feasible starting point for further development in the aircraft design process already satisfying a crucial amount of certification requirements. Experience shows that in MDO only extensive design criteria models considering all crucial constraints yield results useful for further development [SDP+12], as the optimization often drives the solution towards the boundaries of the feasible design space. Therefore, constraints that were not included during an optimization are most likely found violated when evaluated afterwards.

Most of the constraint types (e.g. strength, stability, aeroelastic or trimming) applied in this thesis were already available through *Lagrange* (see [SDP+12]), geometrical constraints to control shape characteristics were added in the course of this work. In order to provide a complete understanding of the criteria model of this framework, the existing constraint types not developed during this work will also be documented briefly in the following sections.

Since this work focuses on the shape optimization capabilities of the developed framework, the dependencies on arbitrary shape parameters x_{shape} will be highlighted for all presented constraint types.

Generally, the developed framework supports inequality constraints g with a basic formulation as:

$$g \leq 0 \quad \text{with} \quad g = \left(1 - \left(\frac{r}{r_{crit}}\right)\right) \cdot (\pm 1) = \left(1 - \left(\frac{1}{R}\right)\right) \cdot (\pm 1) \tag{3.12}$$

With r being an arbitrary system response limited by the value r_{crit}. Depending on whether r_{crit} represents the maximum or the minimum allowed value, the expression in brackets is multiplied by -1 (maximum constraint) or $+1$ (minimum constraint). Alternatively this expression can also be formulated using the reserve factor R, which has advantages for certain types of constraints (e.g. buckling, Section 3.4.2.2). The calculation of r is highly dependent on the nature of the constraint (e.g. strength, trimming etc.). In the following sections these different types of design constraints will be discussed.

3.4.1 Geometric Constraints

Geometry constraints enforce limitations to the allowable aircraft shape during an optimization. Such shape constraints are mostly based on manufacturing

requirements or may even be dictated by non-physical regulations or specifications. One example for this would be the maximum allowed wingspan at an airport guaranteeing that the aircraft fit into their parking positions at the gate.

A number of different shape constraints was implemented on the basis of the parametric geometry model. The first available shape constraint is the wing length or span. This can be realized either by providing a minimum/maximum value for each parametric CPACS wing segment to exert local influence or by setting one boundary for the overall wing length.

The respective response values for both options are shown in Eqs. (3.13) and (3.14) for the case of the wing length (i.e. following any dihedral angle changes), which are applied in Eq. (3.12).

$$r = l_{segment} \tag{3.13}$$

$$r = \sum_{i=1}^{n} l_{segment_i} \tag{3.14}$$

Both definitions are applicable to a CPACS wing consisting of n segments with $l_{segment}$ being the length of a single wing segment.

Similar to the wing length constraints, the planform areas of wing segments or the whole wing are available as constraint functions. Again, the value of a single CPACS segment (see Eq. (3.15)), as well as, the sum of all segment areas in one wing (see Eq. (3.16)) can be limited with a maximum or minimum boundary. The response values required for Eq. (3.12) are defined as:

$$r = S_{segment} = \frac{1}{2} \left\| \mathbf{d}_1 \times \mathbf{d}_2 \right\| \tag{3.15}$$

$$r = \sum_{i=1}^{n} S_{segment_i} \tag{3.16}$$

Where the planform area of one segment is calculated by the cross product of its two diagonal vectors $\mathbf{d}_1$ and $\mathbf{d}_2$ presuming the planform shape of a general convex quadrilateral. During aircraft development the wing planform area is a key value specified rather early in the process. Modifying this value after it was set, usually causes much effort redesigning the aircraft features, since many other factors are based on it. Thus, the area constraints are typically defined in pairs of minimum and maximum constraints to limit the change in planform area to a certain degree.

As the geometric constraint functions can only be influenced by shape design variables, they do not exhibit any dependencies on the other design variable types described in Section 3.3. This yields a very limited dependency for gradient calculations (Eq. (3.17)), which can be evaluated directly in the geometry model.

$$g_{geom} = g(x_{shape}) \tag{3.17}$$

3.4.2 Structural Constraints

All structural constraints applied in this developed framework during the shape optimizations were already available in the MDO program *Lagrange*. Hence, these constraints were only applied to the newly developed shape optimization capabilities. Therefore, this section will only provide a brief overview and illustrate the influence of shape modifications on these constraints.

3.4.2.1 Strength Constraints

When designing structural components to withstand given loads, the principle means to evaluate the structural integrity under these conditions are strength criteria. They provide a relation between the actual stresses or strains on the structure and their allowable limits from literature or experiments, where material failure occurs. The main distinction for these criteria is made between isotropic materials such as metals and anisotropic or orthotropic materials such as composites. Depending on this, many different models to predict material failure based on stresses or strains are available. In general, only usage of the maximum constraint formulation of Eq. (3.12) is reasonable for strength constraints, as most criteria depend on the absolute loading or a distinction between tension and compression is made.

For isotropic materials, the widely used von Mises stress criterion (Eq. (3.18) developed by Huber, von Mises and Hencky, see for example [SM01; San72]) can be applied to calculate an equivalent stress value for a load state. Material values from literature or experiments are then set as allowables for the von Mises stress constraint.

$$r = \sigma_v = \sqrt{\frac{1}{2}\left[\left(\sigma_{xx}-\sigma_{yy}\right)^2+\left(\sigma_{yy}-\sigma_{zz}\right)^2+\left(\sigma_{zz}-\sigma_{xx}\right)^2\right]+3\left(\tau_{xy}^2+\tau_{yz}^2+\tau_{zx}^2\right)} \tag{3.18}$$

Where σ and τ represent the normal and the shear stresses for the three dimensional case.

Anisotropic and orthotropic materials such as composites require a different evaluation so that several other failure criteria exist in this case. For instance, the uni-axial maximum strain criterion but also the multi-axial Tsai-Hill, Hoffman or Tsai-Wu (cf. e.g. [VS86], [San72]) failure criteria are available in *Lagrange* [SDP+12]. As the present work only considers isotropic materials, these methods are not discussed here in more detail.

Regardless of which specific failure criterion is applied to the problem, all are based either on the element stresses or strains originating from the displacements. Therefore, the influence of shape modifications on the structural displacements and subsequently on the finite element strains and stresses have to be taken into account during shape optimizations.

The constitutive equation in the finite element theory [e.g. Fel14; ZT05] gives the relation between element stresses $\boldsymbol{\sigma}_j$ and strains $\boldsymbol{\epsilon}_j$ for a finite element j.

$$\boldsymbol{\sigma}_j = \mathbf{E}_j \cdot \boldsymbol{\epsilon}_j \tag{3.19}$$

The elasticity matrix $\mathbf{E}_j$ depends on the material properties of the element j. The strain $\boldsymbol{\epsilon}_j$ for an n-noded 2D element can be evaluated for example by (see [Fel14;

ZT05]):

$$\boldsymbol{\epsilon}_j = \mathbf{B}_j \cdot \mathbf{u}_{elem_j} = \begin{bmatrix} \frac{dN_1}{dx} & 0 & \frac{dN_2}{dx} & 0 & \dots & \frac{dN_n}{dx} & 0 \\ 0 & \frac{dN_1}{dy} & 0 & \frac{dN_2}{dy} & \dots & 0 & \frac{dN_n}{dy} \\ \frac{dN_1}{dx} & \frac{dN_1}{dy} & \frac{dN_2}{dx} & \frac{dN_2}{dy} & \dots & \frac{dN_n}{dx} & \frac{dN_n}{dy} \end{bmatrix}_j \cdot \begin{bmatrix} u_{1x} \\ u_{1y} \\ u_{2x} \\ u_{2y} \\ \vdots \\ u_{nx} \\ u_{ny} \end{bmatrix}_{elem_j} \tag{3.20}$$

with $\mathbf{u}_{elem_j}$ being the element node displacements derived from the global displacements $\mathbf{u}$ and N the element shape functions. The strain-displacement matrix $\mathbf{B}$ for the element j is formed by the derivatives of the form functions with respect to the coordinate directions x and y.

Hence, the presented strength constraints are affected by shape modifications through the change in displacements caused by the altered stiffness matrix but also by new loads depending on the analysis type (e.g. aeroelasticity). Furthermore, the strain-displacement matrix $\mathbf{B}$ is influenced, since the element shape function derivatives may be changed through shape parameters x_{shape}:

$$g_{strength} = g\left(\boldsymbol{\epsilon}\left(\mathbf{B}\left(x_{shape}\right), \mathbf{u}\left(\mathbf{K}\left(x_{shape}\right), \mathbf{f}\left(x_{shape}\right)\right)\right)\right) \tag{3.21}$$

3.4.2.2 Stability Constraints

Stability criteria are used to assess a structure in terms of crippling for 1D components and buckling for 2D components. These phenomena are caused by compression, bending or shear loads on slender structures. Local buckling of components causes sudden displacements of rather large magnitude that may have negative effects on the overall structure [Hö93]. Since aircraft are mainly built from thin-walled structures consisting of skin patches sectioned by spars, ribs and stringers, stability often represents the dimensioning effect for such components.

In this work, only 2D skin buckling was considered as constraints during the shape optimizations. Therefore, this section will focus only on the 2D stability constraints. For load cases with a combination of compression and shear loads, which is a common case for realistic flight loads, the buckling constraints are evaluated by calculating an overall reserve factor R. This factor is determined through the following interaction relationship (cf. [Bru73]) for application in Eq. (3.12):

$$\frac{1}{R} = \left(\frac{\sigma}{\sigma_{cr}}\right)_{compression} + \left(\frac{\tau}{\tau_{cr}}\right)^2_{shear} \tag{3.22}$$

Similar to the strength constraints only the maximum formulation of Eq. (3.12) is reasonable for assessing structures regarding their buckling behaviour, since buckling is a reaction to excessive strain on the structure. For this, e.g. the wing skin is sectioned into a number of so called buckling fields using spars, ribs and stringers as boundaries. The average normal and shear stress σ and τ on the buckling field in Eq. (3.22) can be derived from the solution of the global

FE problem (see Eqs. (3.19), (3.20)), yet, the critical buckling stresses σ_{cr} and τ_{cr} have to be calculated depending on the type of material, the load state and the geometric dimensions and support of the buckling field. The applied buckling theory implemented in *Lagrange* can be applied for isotropic, as well as, orthotropic materials (see Hörnlein [Hö93]). It supports the combination of bi-axial compression and shear for simply supported flat rectangular buckling fields of uniform thickness. Assuming simple support of the buckling field boundaries introduces some conservativeness, since in reality the bordering elements around the buckling field offer some additional bending stiffness effectively increasing the critical buckling load [Hö93].

Based on this method described in detail by Hörnlein [Hö93], one can summarize that the critical buckling stresses σ_{cr} and τ_{cr} exhibit a sensitivity to shape design variables x_{shape} through the dimensions and the aspect ratio of the buckling field. Additionally, the applied stresses σ and τ show the same dependencies as discussed in the previous section. This leads to the following relations between a stability constraint and the shape design variables:

$$g_{stability} = g\left(\sigma_{cr}\left(x_{shape}\right), \tau_{cr}\left(x_{shape}\right), \boldsymbol{\sigma}\left(\boldsymbol{\epsilon}\left(x_{shape}\right)\right)\right) \tag{3.23}$$

Due to limitations of the current implementation of this type of constraint in *Lagrange*, the influence of the changing buckling field geometry caused by manipulating shape design variables cannot be reflected in the constraint functions. Therefore, the initial buckling field geometry is assumed constant throughout the optimization removing the dependency on σ_{cr} and τ_{cr} from Eq. (3.23), while considering the changes in applied stresses caused by the shape changes. The extent of the error introduced by this was established through test optimizations based on the aircraft model applied later in Section 4.3. There, the result of a shape optimization was re-analysed with updated buckling field definitions and a sizing optimization was conducted to satisfy the new buckling constraints. Through this, the objective function value was deteriorated by less than 1.0 %. Thus, for this work it was concluded to employ the buckling constraints with this assumption while monitoring the error, as this still results in more realistic designs than without buckling constraints altogether.

3.4.2.3 Mass Constraints

In some cases it becomes necessary to limit the mass of an aircraft model during an optimization. This means external weight restrictions need to be enforced during an optimization. An example for this can be found in [DPD+13a], where the optimization added extensive structural weight to reduce the induced drag objective function resulting in a suboptimal design.

The response value for the structural mass constraint is calculated from the sum of all finite element masses as follows:

$$r = m_{FE} = \sum_{i=1}^{n_{elem}} m_{elem_i} = \sum_{i=1}^{n_{elem}} \rho_i V_{elem_i} \tag{3.24}$$

Due to shape changes the volume of the finite elements V_{elem} may change and given the material density ρ this affects the weight m_{elem} of the elements (Eq. (3.25)).

$$g_{mass} = g\left(V_{elem}\left(x_{shape}\right)\right) \tag{3.25}$$

3.4.3 Flight Mechanical Constraints

Flight mechanical trimming, which means achieving equilibrium between aerodynamic and weight or inertial loads, is of great importance during aeroelastic shape optimizations. For example, the induced drag coefficient of a flight state has a direct dependency on the acting aerodynamic lift force. This lift force including aeroelastic effects, on the other hand, needs to balance the weight and inertia forces acting on the model in order to achieve a stationary flight state.

In *Lagrange*, this trim task is realized in the form of an optimization problem based on the aeroelastic analysis results using trimming design variables (Section 3.3.3) and constraints [SDP+12]. As these design variables provide the means to influence the flight conditions, the trimming constraints described in this section allow defining the desired flight state. Thus, for a given combination of Mach number, dynamic pressure and possibly static loads, flight mechanical constraints may be specified that limit the overall loads in any of the six flight mechanical degrees of freedom. For symmetric flight states this usually means prescribing equilibrium of aeroelastic lift and weight/inertia loads, as well as, a zero pitching moment (see Fig. 3.9).

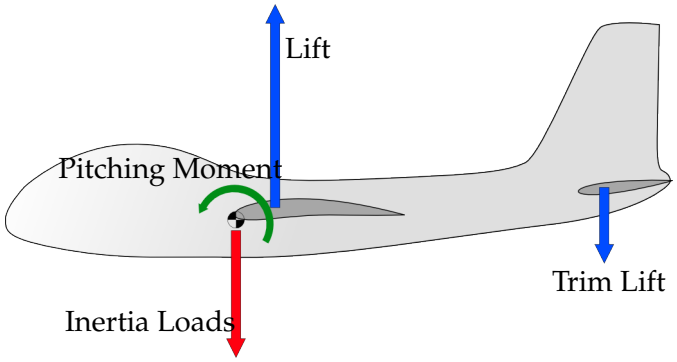

Fig. 3.9: Trimming loads on an aircraft for the lift and pitching moment degree of freedom

Since only inequality constraints are supported by *Lagrange*, an allowable range for the resulting loads in the desired degree of freedom is set by a minimum and a maximum constraint. This region is typically defined as small as possible for high trimming precision but without deteriorating the quality of the optimization problem too severely. In case the allowed interval is set too small, the feasible region of the optimization problem is significantly limited, hence, complicating convergence for the optimizer.

By default, the aerodynamic forces used for the constraint definition are based on the elastic result of the aeroelastic analysis. This creates a dependency of the trimming constraints on the elastic deformation of the structure, and thus, the structural stiffness. If this is not desired, the rigid aerodynamic forces may be used for the loads evaluation instead. In this case, the trimming constraint uses

loads based on the rigid undeformed flow conditions to calculate its response value.

The loads considered by these trimming constraints are summed up in the respective degree of freedom using the global coordinate system of the finite element model (see Fig. 3.9). A choice can be made whether to include structural static loads (such as inertia loads) that are superposed in the aeroelastic analysis in this summation or not. In other words, the trimming constraint either restricts the sum of aerodynamic and structural loads to nullify each other (Eq. (3.27a)), or the constraint is defined to prescribe a fixed aerodynamic load of a certain value (Eq. (3.27b)).

$$r \geq r_0 - \frac{1}{2}\delta \quad \text{and} \quad r \leq r_0 + \frac{1}{2}\delta \tag{3.26}$$

with

$$r = \sum f_{aero} + \sum f_{static} \tag{3.27a}$$

or

$$r = \sum f_{aero} \tag{3.27b}$$

Where δ is the interval size between the minimum and the maximum constraint and r_0 the trimming target value. If structural loads are included, r_0 is usually set to zero enforcing the aerodynamic and structural loads to cancel out. In the other case, r_0 represents the desired value for the aerodynamic load.

If the structural static loads are calculated taking into account the current mass of the model, the relative formulation in Eq. (3.27a) already includes possible weight savings during an optimization in the trimming constraint. This means, when mass is reduced during the optimization, lower lift forces are required to guarantee equilibrium of loads, which alleviates the loads on the structure possibly allowing further weight savings. The absolute formulation has its advantages, if for some reason constant lift states are required during the optimization.

The formulations of Eq. (3.27a) and Eq. (3.27b) are focused on forces but are also applicable to moment constraints. For this, a reference point is given, around which the sum of moments is evaluated (see Fig. 3.9), and the same formulations are applied only summing up moments with forces multiplied with their respective lever arms.

One disadvantage of defining the trimming conditions in the form of inequality constraints, due to unavailability of equality constraints in the framework, is that a range of solutions exist that satisfy the trimming constraints, where only one solution represents the physically correct state (e.g. Lift = Weight). This small range of permitted states (δ in Eq. (3.26)) can induce some fuzziness in the loads along the optimization possibly leading to convergence issues.

However in some cases, a direct relation between the trimming loads and the objective function or another constraint function exists that favours one trimming boundary value over the other, as it might feature a lower objective function value or satisfy the other constraint. This constellation can be exploited by choosing the trimming constraint boundaries according to that. One example for such a case would be an optimization with minimal induced drag

as objective, where lower drag values could be reached simply by reducing the overall lift. This would cause the optimizer to adjust the trimming variables accordingly leading to stable lift load values at the lower trimming constraint boundary over the course of optimization with low fuzziness.

This type of constraint is affected by shape changes in x_{shape} during an optimization through numerous effects (Eq. (3.28)). Firstly, changes to the aerodynamic shape (e.g. camber, twist, wing planform) strongly influence the rigid aerodynamic loads which are used either directly for the trimming or as an initial point for the aeroelastic analysis. Due to the dependency of the structural stiffness on the shape, the resulting elastic aerodynamic loads based on the structural deformations $\mathbf{u}$ are affected by geometric modifications as well. Furthermore, shape variations cause changes in the mass of the finite elements influencing the inertia and aeroelastic loads.

$$g_{trim} = g\left(\mathbf{f}_{aero}\left(x_{shape}, \mathbf{u}\left(\mathbf{K}\left(x_{shape}\right)\right)\right), \mathbf{f}_{static}\left(m\left(x_{shape}\right)\right)\right) \tag{3.28}$$

3.5 Formulation of Objective Functions

As already introduced in Section 2.2, the aim of an optimization is to improve (i.e. minimize) an objective function with a given set of design variables while satisfying all constraint functions. Together with the design variables the objective function defines the design space which is limited by the constraints. In case of MDO, the objective function usually depends on a combination of system responses obtained from differing analysis methods. The different objective function definitions applied in this work are presented in this section.

A major focus of this work lies on the induced drag of aircraft configurations including aeroelastic and structural effects. Thus, the primary choice as objective function is the induced drag itself. However, due to the multidisciplinary character of aircraft design, it might be unfavourable to singularly use induced drag as an objective function (see e.g. [DPD+13a]). Therefore, several other possibilities of considering a combination of induced drag and structural mass in the objective function were included as well.

As before, the dependencies of the functions on the design variables are highlighted for each case.

3.5.1 Induced Drag Objective

Lift induced drag represents a major component of the overall drag (cf. Section 2.1.2) and, therefore, has a great impact on the flight performance of an aircraft. Furthermore, induced drag can be significantly affected by changes to the flow conditions caused by structural deformations and aeroelastic effects [RMS95; WDD00]. The combination of these two aspects makes induced drag a promising object for MDO. Since the induced drag can already be influenced by design parameters that are determined in the earlier development stages, it shows high potential of improvement through the developed multidisciplinary shape optimization framework.

Thus, an objective function was implemented in this framework that uses the induced drag system response:

$$f_{C_{D_{ind}}}(\mathbf{x}) = C_{D_{ind}}(\mathbf{x}) \tag{3.29}$$

Instead of the drag force, the induced drag coefficient (definition in Eq. (2.2)) is applied in the objective function. This allows independence of the chosen model units and flight state (e.g. speed, altitude). The reference area S_{ref} used for the normalization of the induced drag coefficient is kept constant during the optimization procedure to allow comparability of the results.

Based on the relations presented in Section 3.2 repeated in the following, the induced drag coefficient can be evaluated for the rigid ($\mathbf{u} = 0$) and the aeroelastic state.

$$C_{D_{ind}} = \mathbf{\Gamma} \cdot \mathbf{AIC}_{C_D} \cdot \mathbf{\Gamma} \tag{2.21 revisited}$$

with

$$\mathbf{\Gamma} = \mathbf{AIC}^{-1} \cdot \mathbf{b}_c \tag{3.8 revisited}$$

$$\mathbf{b}_c = \mathbf{b}_{c_{state}} + \mathbf{b}_{c_{shape}} + \mathbf{T}_{AS} \cdot \mathbf{u} \tag{3.3 revisited}$$

In order to calculate the gradients of the objective function, the dependencies of induced drag with respect to an arbitrary shape design variable have to be studied. These are shown in Eq. (3.30) based on the relations discussed in Section 3.2.2.

$$f_{C_{D_{ind}}} = C_{D_{ind}}\left(\mathbf{AIC}_{C_D}\left(x_{shape}\right), \mathbf{\Gamma}\left(\mathbf{AIC}^{-1}\left(x_{shape}\right), \mathbf{b}_c\left(x_{shape}, \mathbf{u}\left(x_{shape}\right)\right)\right)\right) \tag{3.30}$$

Thus, an explicit dependency between the induced drag and a shape variable exists through the two involved AIC matrices ($\mathbf{AIC}_{C_D}$ and $\mathbf{AIC}^{-1}$) that reflect the aircraft planform geometry. Furthermore, the induced drag coefficient is influenced implicitly by the aeroelastic displacement $\mathbf{u}$ acting through $\mathbf{\Gamma}$ and $\mathbf{b}_c$. Additionally, one component $\mathbf{b}_{c_{shape}}$ of the boundary condition vector $\mathbf{b}_c$ itself, has a direct dependency on shape variables (i.e. twist/camber). The relation between the displacement vector $\mathbf{u}$ and an arbitrary shape design variable has already been covered in Section 3.2.2 (cf. Eq. (3.9)).

As this analysis type and objective function was newly implemented, also the dependencies regarding the remaining design variable types such as structural sizing or trim variables have to be examined.

$$f_{C_{D_{ind}}} = C_{D_{ind}}\left(\mathbf{\Gamma}\left(\mathbf{b}_c\left(\mathbf{u}\left(x_{size}\right)\right)\right)\right) \tag{3.31}$$

For structural design variables only the implicit dependencies seen in Eq. (3.30) remain, since the geometry of the aerodynamic model cannot be altered by them. Therefore, only the dependency through $\mathbf{\Gamma}$,$\mathbf{b}_c$ and $\mathbf{u}$ appears in Eq. (3.31).

$$f_{C_{D_{ind}}} = C_{D_{ind}}\left(\mathbf{\Gamma}\left(\mathbf{b}_c\left(x_{trim}, \mathbf{u}\left(x_{trim}\right)\right)\right)\right) \tag{3.32}$$

Flight mechanical trim variables have an additional influence on the induced drag, since they can directly affect the aerodynamic boundary condition $\mathbf{b}_c$

through its flight state component $\mathbf{b}_{c_{state}}$ of Eq. (3.3). Apart from that, trim variables show the same influence through $\mathbf{u}$ on induced drag as structural variables. The only difference there is that trim variables affect the load vector instead of the stiffness matrix compared to structural variables (Eq. (3.1)).

The fact that induced drag mainly shows an implicit dependency (through $\mathbf{u}$) on structural and trim variables, causes their influence to vanish for a rigid evaluation. Merely the direct effect of trim variables on the boundary condition remains.

One particularity of induced drag as an objective function is that it has a single defined minimal value for certain problem definitions. As shown in Section 2.1.2 Eq. (2.8), the minimal induced drag for a given lift coefficient and wing aspect ratio of a planar wing is obtained by an elliptic lift distribution over the wingspan (corresponding to the Oswald factor value $e = 1$). This effect is examined later in a study in Section 4.2.2.2, where it is shown that many different shape parameter combinations achieving this minimum are available.

3.5.2 Structural Mass Objective

Virtually every design discipline over the entire course of aircraft development is influenced by mass, which makes it a key figure of aircraft design. Usually the overall mass of an aircraft is determined at the beginning of development. This overall mass has to be divided into structural, fuel, payload and other masses. Due to this, the percentage of structural mass directly influences the allowable payload and fuel masses, which dictate the operational characteristics of an aircraft such as range and payload capacity. Therefore, the general task is to minimize structural mass under the constraint of guaranteeing structural integrity. This makes structural mass a common objective for MDO applications in aircraft design.

For application in this shape optimization framework, the overall FE mass is employed as an objective function.

$$f_m(\mathbf{x}) = m_{FE}(\mathbf{x}) = \sum_{i=1}^{n_{elem}} m_{elem_i}(\mathbf{x}) \tag{3.33}$$

Whereas each element mass is calculated from its volume and material density:

$$m_{elem} = V_{elem} \cdot \rho_{elem} \tag{3.34}$$

As the density of the elements is taken from the material definition in the finite element model and is kept constant throughout the optimizations, the mass can only be modified through the finite element volume. This leads to the following dependency with respect to the applied design variable types:

$$f_m = m_{FE}\left(V_{elem}\left(x_{shape/size}\right)\right) \tag{3.35}$$

Depending on the type of design variable, the element volume is either altered by repositioning of the element nodes (x_{shape}) or by scaling through thickness or cross section area (x_{size}). Trim design variables have no influence on the structural mass at all, because no volume changes are caused by them. This objective

function was already provided by *Lagrange* [SDP+12] so that only the influence of the newly devised shape design variables had to be considered.

Generally, structural FE mass does not represent the structural mass of the finally built aircraft, as this quantity is derived from an idealized model. Many aspects such as manufacturing masses (e.g. rivets, screws, bolts, glue), as well as, other weight contributions (e.g. pipework, wiring, paint) are not considered by it. However, the structural mass computed from a finite element model can provide a good indicator to the aircraft's real structural mass if combined with statistical methods.

3.5.3 Combined Induced Drag and Structural Mass Objective

As previously mentioned, considering the system response of only one discipline as an objective function for multidisciplinary shape optimization might lead to results where the attributes of the disciplines not regarded in the objective are severely worsened in order to improve the objective, causing penalties on the overall performance (see [DPD+13a]).

Thus, a weighted sum objective function of induced drag and finite element mass was implemented in the framework (see Section 2.2.6). In order to represent both system responses equally in the objective function and remove any dependency on model units, the components were scaled with their initial values (see Eq. (3.36) subscript 0) before the summation.

$$f_{sum}(\mathbf{x}) = a\frac{C_{D_{ind}}(\mathbf{x})}{C_{D_{ind_0}}} + b\frac{m_{FE}(\mathbf{x})}{m_{FE_0}} \tag{3.36}$$

The weighting factors $a > 0$ and $b > 0$ were included as well so that the influence of the two objective function components can be shifted. Hence, the optimizers search direction can be biased towards one or the other system response by adjusting these weights in advance of an optimization.

Since the dependencies of the two contributing system responses remain unchanged through their summation, this objective function is affected by a combination of both singular objectives discussed in the previous sections.

$$f_{sum} = f\left(C_{D_{ind}}\left(x_{shape}\right), m_{FE}\left(x_{shape}\right)\right) \tag{3.37}$$

Also the dependencies with respect to the remaining design variable types such as sizing and trimming follow this paradigm.

With this objective function definition, the requirements of both design disciplines can be considered simultaneously during the shape optimizations. However, the possibility of different weightings between the contributions of aerodynamic and structural responses introduces the issue of finding the appropriate weighting factors in advance of an optimization that yield the desired improvements. Optimizations with different weightings may be required to identify a promising design on the resulting Pareto front using an additional criterion (cf. Section 2.2.6).

This objective function formulation may help solving the issues regarding the induced drag behaviour indicated in Section 3.5.1 that many designs with the same induced drag value can exist. Through the combination in the weighted sum a preference for some of these designs can be introduced as the FE mass is used additionally to assess them.

3.5.4 Breguet Range Objective

Another way of combining drag and mass into one objective is the Breguet range equation Eq. (3.38) (see for example [Ray06]), which is commonly applied in early aircraft design optimization [e.g. IM01; GKC+12; GBM+10; HML12; JPM10; KKM12; Wun13]. This has the advantage of relating the two system responses without the need of artificial weighting factors in a physically meaningful manner by calculating the achievable range for a given mission and aircraft configuration.

$$R_{Br} = \frac{v}{g\ TSFC} \cdot \frac{C_L}{C_{D_{ind}} + C_{D_0}} \cdot \ln\left(\frac{m_{init}}{m_{final}}\right) \tag{3.38}$$

The Breguet range considers one leg of a mission with a constant flight state taking into account the overall mass at the beginning m_{init} and at the end m_{final} of that segment. The difference between these two masses represents the fuel burned during the mission leg. Applying a given mission profile, these two boundary masses are usually calculated using the fuel fraction method (see e.g. [Ray06]). Apart from this, the flight velocity v, the acceleration of gravity g, the thrust specific fuel consumption $TSFC$ and the lift to drag ratio (aerodynamic efficiency) are considered as well.

In order to transform this into an objective function applicable for optimization in the developed framework, some modifications were made to the Breguet range formulation. Terms that stay constant during the proposed shape and sizing optimizations were removed (i.e. first fraction in Eq. (3.38)). Also it was assumed that the lift coefficient remains unchanged during an optimization, as it is always constrained by the trimming constraints. The viscous drag component C_{D_0} of the overall drag coefficient C_D was assumed constant as well. Its value was initially estimated and kept constant during the optimizations. A study regarding this assumption was conducted later in Sections 4.2.1.3 and 4.3.4 showing that the influence is small but needs to be monitored. As the standard optimization problem involves minimization of the objective, the negative Breguet range was used to incorporate that.

With these modifications, the following objective function was implemented:

$$f_{Br}(\mathbf{x}) = \frac{1}{C_{D_{ind}} + C_{D_0}} \ln\left(\frac{m_{fixed} + m_{FE}}{m_{init}}\right) \sim -R_{Br} \tag{3.39}$$

$$m_{fuel} = m_{init} - m_{FE} - m_{fixed} \tag{3.40}$$

A similar objective function was derived by Kenway et al. [KKM10].

In order to allow for different missions and models to be specified, the mass ratio was split up into several components. The segment's initial mass m_{init}, is

specified as the overall aircraft mass at the beginning of the mission segment containing the masses of fuel, FE structure, systems and everything that was not modelled in the FE model. The final mass m_{final} was separated into m_{fixed}, which sums up all aspects excluding fuel that are not represented in the FE model and are assumed to stay constant, and m_{FE} as the overall mass of the FE model. With this definition, the overall mass of the aircraft is accounted for independently of how detailed the FE model masses were defined. This also means, that during an optimization all weight savings that are achieved on m_{FE} are directly assigned to higher fuel mass capacity regardless of any tank volume restrictions (see Eq. (3.40)), while m_{init} is kept constant.

Since the implemented Breguet range equation only provides a different way of combining the system responses of induced drag and FE mass into one objective, the dependencies of this function are the same as for the weighted sum.

$$f_{Br} = f(C_{D_{ind}}(x_{shape}), m_{FE}(x_{shape})) \tag{3.41}$$

This also holds for the remaining types of design variables (i.e. structural, trim).

3.6 Optimization Procedure

After discussing all components of the developed shape optimization framework individually in the preceding sections, a short overview over the collaboration of these components and the work flow of the framework shall be given here. Also the possibilities of calculating the sensitivities required for gradient based optimization considering all involved models and disciplines is discussed in this section.

3.6.1 Work Flow of the Shape Optimization Framework

Two basic procedures are distinguished in this shape optimization framework. Initially, a preparation work flow that creates input data and analysis models has to be completed. Later, the information of this process is used during the multidisciplinary shape and sizing optimization, which represents the second work flow of the framework. The following description of these processes presumes fully numerical gradient calculation with respect to shape design variables and analytical sensitivities for the remaining variable types.

To prepare the shape optimization, a CPACS model needs to be provided to *Descartes* (see Fig. 3.10). This CPACS model can be created manually or based on existing geometry models of commercial CAD programs. Using the CPACS definition, *Descartes* constructs the parametric geometry model, which is used to generate the analysis models for all disciplines (i.e. here aerodynamic *AVL* and structural FEM model). After the analysis meshes have been created, they need to be linked back to the parametric geometry in order to allow consistent shape modifications during the optimization. This is done in *Descartes* by mapping all analysis mesh nodes onto the surfaces of the parametric geometry using relative coordinates (Section 3.3.1.2). In case of the aerodynamic *AVL* model, this step is not required for the aerodynamic mesh, since *AVL* uses an input logic

very similar to CPACS (cf. Fig. 3.4) and can be regenerated consistently with only low effort directly from the CPACS definitions after every shape modification. After that, shape variables can be defined in *Descartes* by selecting the desired shape parameters and providing minimal and maximal gages. If necessary, also geometric constraints (see Section 3.4.1) may be specified. The definitions of both, the constraints and the shape variables, are transferred, together with their initial values, to the *Lagrange* input using a file. All the information, which has been defined in *Descartes* up to this point, is stored in a separate database so that all definitions and relations are available when *Descartes* is called repeatedly during the shape optimization. In *Lagrange*, the generated aerodynamic and structural models are referenced and fluid-structure-coupling (see Section 2.1.3), analysis load cases, as well as, non-structural mass distributions are defined. If desired, further design variables such as structural sizing or trimming variables (see Section 3.3), as well as, additional constraints (e.g. strength, stability, trimming etc., see Section 3.4) may be added to the optimization problem. One of the available objective function formulations (Section 3.5) needs to be selected. With the combination of the two *Descartes* files, the analysis models and the *Lagrange* input definitions (Fig. 3.10) a multidisciplinary shape optimization can be initiated.

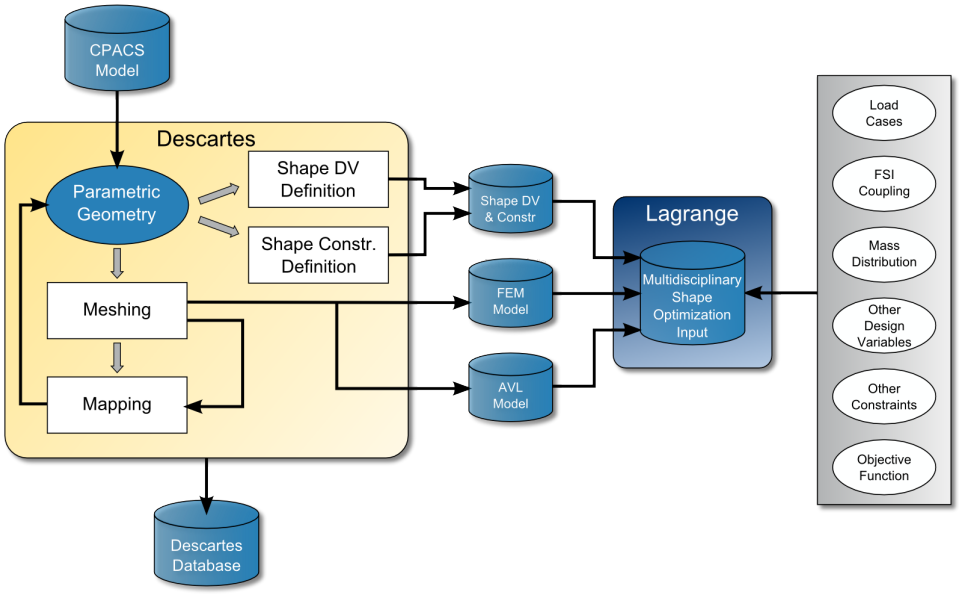

Fig. 3.10: Preprocessing work flow

Figure 3.11 illustrates the work flow and interactions in the framework during the subsequent shape optimization run. Such an optimization is initiated through *Lagrange*, using its problem definition from the preceding preparation procedure. After processing all the input, the optimization loop is entered and an initial system evaluation is conducted. In order to obtain the analysis model geometries corresponding to the current shape design variable settings, a shape update of all involved analysis meshes is requested from *Descartes*. For this, all definitions and model relations are read from a database and the current design variable values are applied on the parametric geometry model using the mapping information to deform the analysis meshes accordingly. In case the

aerodynamic model (here *AVL*) is affected by the defined shape design variables, the AIC matrices and the geometric boundary conditions are adjusted to this configuration by an aerodynamic solution. After the shape update and the aerodynamic evaluation, the new finite element mesh geometry and the aerodynamic AIC matrices are handed back to *Lagrange*. If geometric constraints have previously been defined, the resulting values of these constraint functions are transferred as well. With the updated shape, the settings of the remaining design variable types (e.g. sizing) are applied and the aeroelastic analysis evaluating the system responses required for constraints and the objective function is conducted.

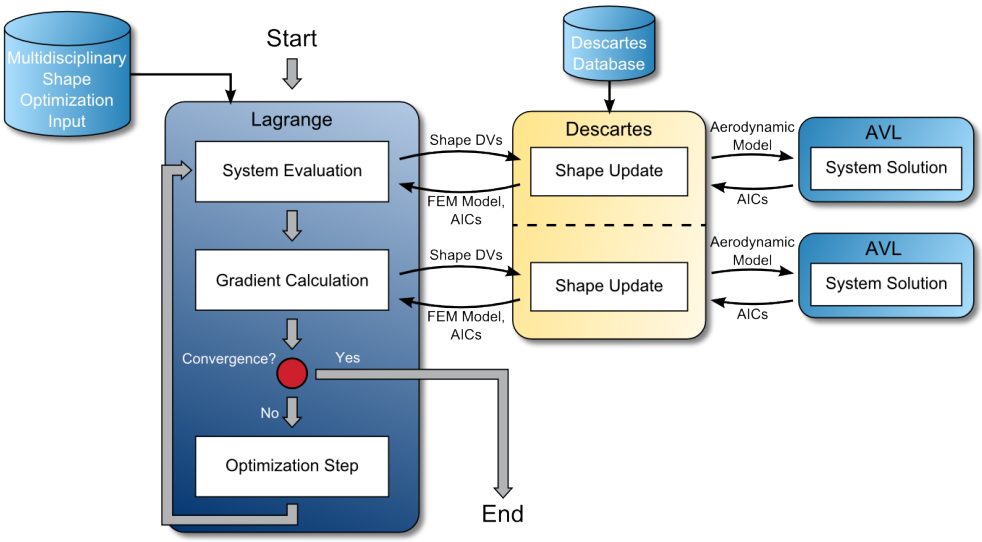

Fig. 3.11: Shape optimization work flow

In order to determine a step towards the next feasible minimum of the objective function using gradient based optimization, the gradients of constraints and the objective function are required. The analytical sensitivity calculation with respect to the established design variable types in *Lagrange* (i.e. sizing and trimming design variables [SDP+12]) is not part of this research and is not described here. Regarding the gradients with respect to the geometric design variables finite differences are applied (see Section 2.2.4.1). Thus a loop over all shape design variables is executed sequentially perturbing each and initiating a shape update to calculate the difference quotient (cf. Section 3.6.2).

Once the gradients of constraints and objective function with respect to every design variable are calculated, a convergence check is executed. In case the convergence criteria (e.g. Karush-Kuhn-Tucker, Section 2.2.5) are satisfied the optimization loop ends at this point. Otherwise, the optimizer uses the gradients and function values to determine the next set of design variable values conducting an *optimization step* as shown in Fig. 3.11.

After that, the optimization loop is rerun with the newly assigned design variable values evaluating system responses and gradients as previously described. The optimization loop is repeated until the convergence criteria are met.

Even though numerical gradient computation was assumed for this descrip-

tion of the optimization work flow, analytical or semi-analytical gradients with respect to the shape design variables are also possible. For semi-analytical gradient computation, the shape update during the gradient calculation step in Fig. 3.11 would remain unchanged, only the sensitivity logic is adapted. In case of analytical sensitivities, computation of gradients instead of mere shape updates would be required in *Descartes*. The returned partial derivatives would then have to be utilized in *Lagrange* to determine the overall derivative.

3.6.2 Sensitivity Analysis - Realized Approaches and Assessment

Since a gradient based optimization algorithm is applied in this framework, the sensitivity analysis (or gradient calculation) forms a central part of the framework. In the subsequent sections, the three different gradient evaluation approaches described in Section 2.2.4 are clarified based on the developed shape design variables in this framework.

As only the derivatives with respect to shape design variables are discussed, they will be denoted by the vector $\mathbf{x}$ to prevent index cluttering. The gradients will always be formulated for an arbitrary objective function $f(x)$ and a vector of constraint functions $\mathbf{g}(x)$.

3.6.2.1 Numerical Gradient Calculation

In the developed framework the forward differences approach from the variants described in Section 2.2.4.1 was selected and validated.

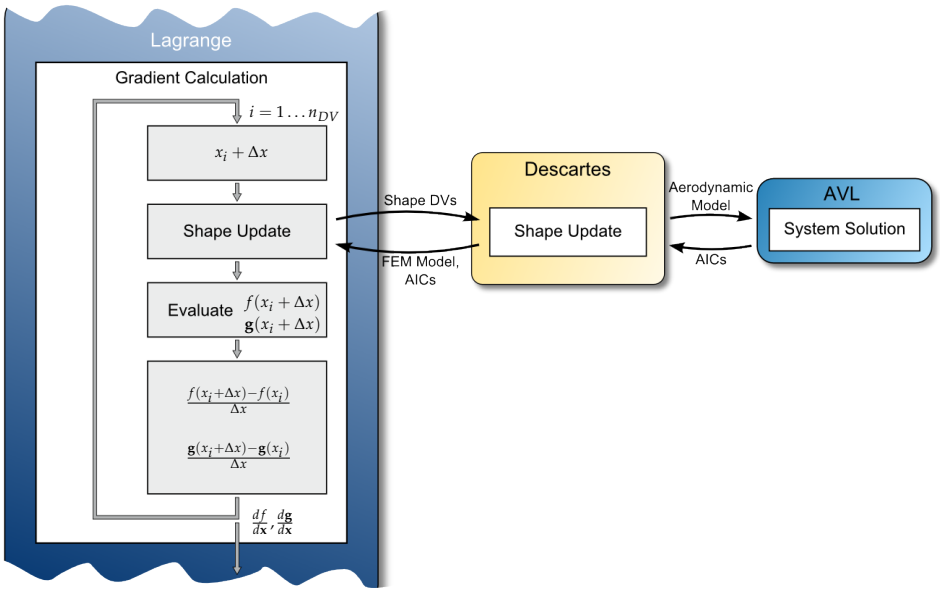

Fig. 3.12: Shape design variable gradients through forward differences

Fig. 3.12 represents a cut-out of Fig. 3.11 focusing on the gradient calculation step. It shows the sequential perturbation of shape design variables in a loop with following analysis model shape update, before the perturbed state

(i.e. $f(x_i + \Delta x)$ and $\mathbf{g}(x_i + \Delta x)$) is aeroelastically analysed. The gradients are then evaluated using a difference quotient

Since the levelled shape parametrization approach allows extensive shape changes with only few design variables, the known issues regarding computational effort of the finite difference approach do not represent a problem for the developed framework. However, using this approach for gradient calculation enables reducing the interface complexity between the components of the framework, since only function evaluations need to be exchanged.

The finite difference approach was implemented as the primary sensitivity analysis method with respect to shape design variables in this framework. For the remaining design variable types such as sizing or trimming variables the existing analytical gradients were applied in *Lagrange* [SDP+12]. Hence, the additional computational effort for the finite differences gradients is only limited to the small number of shape design variables.

In order to validate the implemented gradient calculation method, the sensitivity of the gradients with respect to the normalized perturbation step size was studied. It was found that the forward difference gradients in this framework exhibit only low variation with respect to the perturbation step size over a rather wide window (see Table 3.2 and Fig. 3.13). Overall, one can summarize that stable gradient values (variation less than 1 %) can be expected for forward differences with perturbation step sizes of $\Delta x \leq 10^{-2}$. Above that, the truncation error of the Taylor series approximation discussed in Section 2.2.4.1 becomes significant.

Table 3.2: Forward difference sensitivities with varying perturbation for chord length design variable 3 in Fig. 3.13

Perturbation	**Gradient Value**		
Step Size	Induced Drag Objective	Stress Constraint	Lift Trim Constraint
10^{-0}	0.107557	-0.0118484	-0.000507426
10^{-1}	0.113516	-0.0393864	-0.000780710
10^{-2}	0.116653	-0.0444960	-0.000843292
10^{-3}	0.117066	-0.0450822	-0.000849900
10^{-4}	0.117097	-0.0451349	-0.000850469
10^{-5}	0.117101	-0.0451386	-0.000850534
10^{-6}	0.117107	-0.0451586	-0.000850571
10^{-7}	0.117098	-0.0448006	-0.000850528

Therefore, shape design variable gradient calculation using forward differences represents a good first approach. However, once the applied aerodynamic analysis method becomes computationally more demanding, the finite differences approach reaches its limits due to the repeated evaluation of the aerodynamic system in the gradient loop (Fig. 3.12).

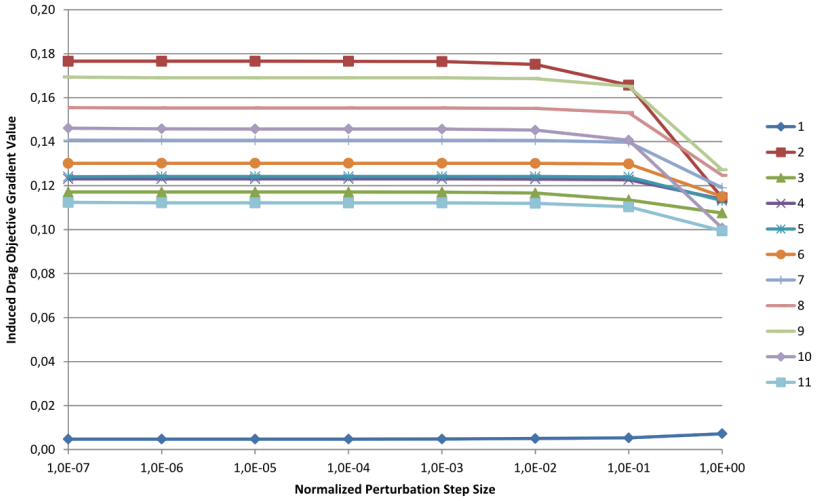

(a) Induced drag objective gradient

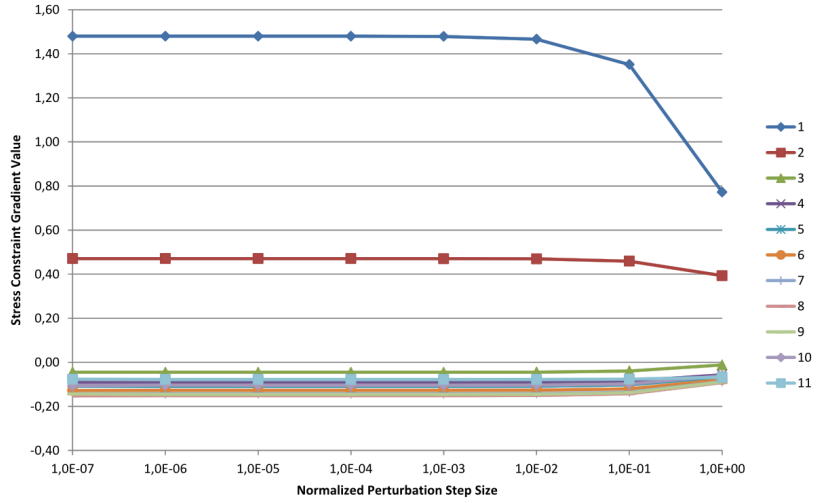

(b) Von Mises stress constraint gradient

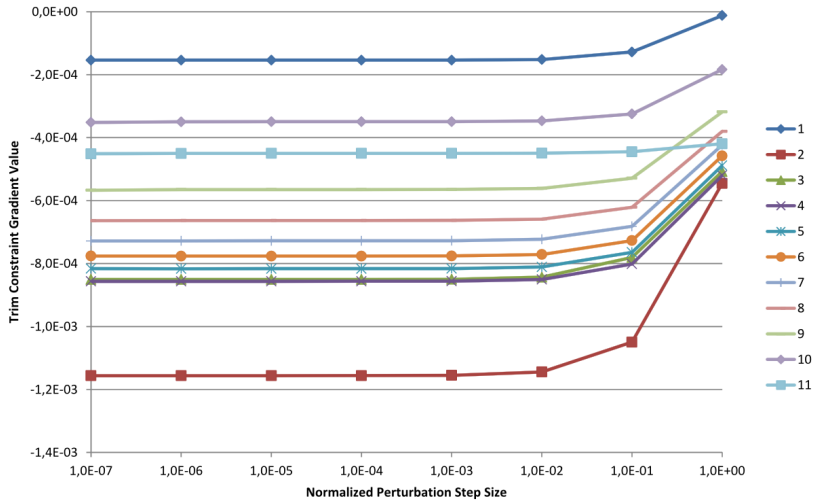

(c) Lift trim constraint gradient

Fig. 3.13: Example of forward difference gradients for rectangular wing (Section 4.1.1.1) over different perturbation step sizes (variable 1: root chord length to 11: tip chord length)

3.6.2.2 Analytical Gradient Calculation

The analytical differentiation developed in Section 2.2.4.2 is now applied to the present problem of aeroelastic shape optimization. Only shape design variables are regarded, as the other design variable types already had analytical gradient formulations available [SDP+12]. As stated before, the direct gradient calculation approach is followed here due to the specifics of the optimization problem at hand.

This approach was not yet realized in the framework. Therefore, only the basis for differentiating the governing equations is given here subsequently used for the semi-analytical method.

Displacement derivative Through the aeroelastic problem formulation Eq. (3.1) the gradient calculation with respect to the shape design variable x_i given in Eq. (2.38) is extended to:

$$\mathbf{K} \cdot \frac{\partial \mathbf{u}}{\partial x_i} = -\frac{\partial \mathbf{K}}{\partial x_i} \cdot \mathbf{u} + \frac{\partial \mathbf{f}_{St}}{\partial x_i} + \frac{\partial \mathbf{f}_{Ae}}{\partial x_i} \tag{3.42}$$

The right hand side of Eq. (3.42) (i.e. pseudo load vector) now consists of the partial gradients of the stiffness matrix $\mathbf{K}$, the static $\mathbf{f}_{St}$ and the aeroelastic load vector $\mathbf{f}_{Ae}$. These terms need to be calculated, before the equation can be solved for the displacement derivative vector $\frac{\partial \mathbf{u}}{\partial x_i}$.

The derivative of the global stiffness matrix $\mathbf{K}$ is a function of the assembled derivatives of the finite element stiffness matrices. Each of these matrices depends on the element's strain-displacement matrix $\mathbf{B}$ [ZT05; Fel14], which must be differentiated, if the nodal positions are affected by the design variable. This also requires the gradient of the element Jacobi matrix $\mathbf{J}$ with respect to the shape design variable. As these mathematical relations strongly depend on the type of applied finite elements and their element technology, only the general dependencies for chain derivation are shown:

$$\frac{\partial \mathbf{K}}{\partial x_i} = \frac{\partial}{\partial x_i} \mathbf{K} \left(\mathbf{K}_{elem_j} \left(\mathbf{B}_j \left(\mathbf{J}_j \right) \right) \right) \tag{3.43}$$

An example for the analytical sensitivities of a shell element can be found in [CE04].

The second partial derivative in the pseudo load of Eq. (3.42) is the static load derivative, which vanishes in most cases unless e.g. inertia loads are applied in the aeroelastic analysis.

$$\frac{\partial \mathbf{f}_{St}}{\partial x_i} = \frac{\partial}{\partial x_i} \mathbf{f}_{St} \left(V_{elem_j} \right) \qquad \text{for} \quad j = 1 \dots n_{elem} \tag{3.44}$$

In case of inertia loads, the static inertia load derivative only depends on the change in element volumes V_{elem_j}, which has a sensitivity to shape variables.

The gradient of the aeroelastic loads $\mathbf{f}_{Ae}$ (third term on the right in Eq. (3.42)) is derived from Eq. (3.2) assuming that the transformation matrices $\mathbf{T}_{AS}$ and $\mathbf{T}_{SA}$ are not affected by the shape design variable.

$$\frac{\partial \mathbf{f}_{Ae}}{\partial x_i} = q \mathbf{T}_{SA} \left(\frac{\partial \mathbf{A}}{\partial x_i} \cdot \mathbf{AIC}_{C_P} \cdot \mathbf{b}_c + \mathbf{A} \cdot \frac{\partial \mathbf{AIC}_{C_P}}{\partial x_i} \cdot \mathbf{b}_c + \mathbf{A} \cdot \mathbf{AIC}_{C_P} \cdot \frac{\partial \mathbf{b}_c}{\partial x_i} \right) \tag{3.45}$$

With the Neumann boundary condition gradient derived from Eq. (3.3):

$$\frac{\partial \mathbf{b}_c}{\partial x_i} = \frac{\partial \mathbf{b}_{c_{shape}}}{\partial x_i} + \mathbf{T}_{AS} \cdot \frac{\partial \mathbf{u}}{\partial x_i} \tag{3.46}$$

The preceding two equations show the multidisciplinary character of the analysis because they contain the derivatives of aerodynamic model quantities, as well as, structural ones. The gradients of the panel area matrix $\mathbf{A}$, the pressure coefficient matrix $\mathbf{AIC}_{C_P}$ and the geometric component of the Neumann boundary condition $\mathbf{b}_{c_{Shape}}$ have to be calculated in the aerodynamic model. On the other hand, the Neumann boundary condition also holds a sensitivity with respect to the structural displacement vector $\mathbf{u}$. This introduces the same implicit behaviour to the gradient calculation as described in the analysis (Section 3.2.1), since the derivative of the structural displacements influences both sides of Eq. (3.42). Hence, the same iterative solution approach as in the analysis is applied to this equation.

Objective and constraint function derivatives Once the displacement sensitivities are available, the objective and constraint functions can be fully differentiated. The gradients for the two basic objective functions described in Section 3.5 are given in the following.

Structural mass objective function (from Eq. (3.33)):

$$\frac{df_m(\mathbf{x})}{dx_i} = \sum_{j=1}^{n_{elem}} \rho_{elem_j} \frac{\partial V_{elem_j}}{\partial x_i} \tag{3.47}$$

As already shown for the static inertia loads, which also depend on the element mass distribution, the structural model mass is affected only through the finite element volumes. Therefore, only the explicit gradient is present for this objective function.

Induced drag objective function (from Eq. (2.21)):

$$\frac{df_{C_{D_{ind}}}(\mathbf{x})}{dx_i} = \frac{\partial \mathbf{\Gamma}}{\partial x_i} \cdot \mathbf{AIC}_{C_D} \cdot \mathbf{\Gamma} + \mathbf{\Gamma} \cdot \frac{\partial \mathbf{AIC}_{C_D}}{\partial x_i} \cdot \mathbf{\Gamma} + \mathbf{\Gamma} \cdot \mathbf{AIC}_{C_D} \cdot \frac{\partial \mathbf{\Gamma}}{\partial x_i} \tag{3.48}$$

with (from Eq. (3.8))

$$\frac{\partial \mathbf{\Gamma}}{\partial x_i} = \frac{\partial \mathbf{AIC}^{-1}}{\partial x_i} \cdot \mathbf{b}_c + \mathbf{AIC}^{-1} \cdot \frac{\partial \mathbf{b}_c}{\partial x_i} \tag{3.49}$$

This objective function shows both explicit and implicit partial derivatives with respect to shape design variables.

As a representative for a constraint function, an arbitrary strength constraint of those discussed in Section 3.4.2.1 is differentiated. Since all strength constraint functions depend on the structural strain (see Eq. (3.21)), only the universally valid derivative of the strain vector is shown here. Depending on the specific strength constraint formulation the missing $\frac{\partial g_{Strength}}{\partial \boldsymbol{\epsilon}}$ needs to be determined after that.

$$\frac{dg_{Strength_j}(\mathbf{x})}{dx_i} = \frac{d}{dx_i} g_{Strength_j}\left(\boldsymbol{\epsilon}\left(\mathbf{x}\right)\right) = \frac{\partial g_{Strength_j}}{\partial \boldsymbol{\epsilon}_j} \frac{\partial \boldsymbol{\epsilon}_j}{\partial x_i} \tag{3.50}$$

$$\frac{\partial \boldsymbol{\epsilon}_j}{\partial x_i} = \frac{\partial \mathbf{B}_j}{\partial x_i} \cdot \mathbf{u}_{elem_j} + \mathbf{B}_j \cdot \frac{\partial \mathbf{u}_{elem_j}}{\partial x_i} \tag{3.51}$$

Here, one can see that the derivative of the strain in finite element j is calculated out of the strain-displacement matrix $\mathbf{B}_j$ gradient, as well as, the element displacement sensitivities.

Since the analytical method is not yet realized in the framework, differentiation of the remaining constraint function types introduced in Section 3.4 is not examined here.

Derivative with respect to non-shape variables In order to employ fully analytical gradients for the other types of design variables available in the framework (i.e. sizing and trimming) the derivatives shown above were adjusted for these variables to be applied on the newly implemented objective functions (i.e. induced drag, Breguet range).Thus, analogue to Eqs. (3.48) and (3.49) the gradient of the induced drag value with respect to structural or trimming variables follows as:

$$\frac{df_{C_{D_{ind}}}(\mathbf{x})}{dx_i} = \frac{\partial \boldsymbol{\Gamma}}{\partial x_i} \cdot \mathbf{AIC}_{C_D} \cdot \boldsymbol{\Gamma} + \boldsymbol{\Gamma} \cdot \mathbf{AIC}_{C_D} \cdot \frac{\partial \boldsymbol{\Gamma}}{\partial x_i} \tag{3.52}$$

$$\frac{\partial \boldsymbol{\Gamma}}{\partial x_i} = \mathbf{AIC}^{-1} \cdot \frac{\partial \mathbf{b}_c}{\partial x_i} \tag{3.53}$$

As mentioned before, these functions only exhibit an implicit gradient with respect to these design variable types. Therefore, the dependency of the aerodynamic boundary condition and the displacements need to be considered.

$$\frac{\partial \mathbf{b}_c}{\partial x_i} = \frac{\partial \mathbf{b}_{c_{state}}}{\partial x_i} + \mathbf{T}_{AS} \cdot \frac{\partial \mathbf{u}}{\partial x_i} \tag{3.54}$$

The first term on the right hand side of Eq. (3.54) only holds a sensitivity with respect to the trimming design variables, for structural sizing variables it vanishes leaving only the second term.

Combining these last three equations with the existing computation of the displacement vector derivative allows fully analytical sensitivity analysis for the induced drag objective function with respect to all available non-shape design variable types.

In order to calculate the gradient of the weighted sum objective (Section 3.5.3), this must be simply combined with the existing FE mass derivatives, which is not shown here. The Breguet range objective (see Section 3.5.4) also combines these responses, as shown in the following relations:

$$\frac{df_{Br}(\mathbf{x})}{dx_i} = \frac{-\frac{\partial C_{D_{ind}}}{\partial x_i}}{\left(C_{D_{ind}} + C_{D_0}\right)^2} \ln\left(\frac{m_{fixed} + m_{FE}}{m_{init}}\right) + \frac{1}{C_{D_{ind}} + C_{D_0}} \frac{\frac{\partial m_{FE}}{\partial x_i}}{m_{fixed} + m_{FE}} \tag{3.55}$$

The analytical gradients of the FE mass objective, as well as, the considered constraint functions with respect to the non-shape design variable types were already available in *Lagrange* [SDP+12]. This allowed the mentioned combination of finite difference gradients with respect to shape variables and fully analytical gradients with respect to all other design variable types.

3.6.2.3 Semi-Analytical Gradient Calculation

The semi-analytical gradient computation method with respect to shape design variables was also realized in the shape optimization framework. As this approach applies the analytical derivative relations presented in Section 3.6.2.2 using a number of partial derivatives obtained through finite differences, these relations are reprinted in the following with Δ instead of ∂ to highlight the finite difference terms.

In this case, the gradient of the aeroelastic problem Eq. (3.42) is rewritten as:

$$\mathbf{K} \cdot \frac{\partial \mathbf{u}}{\partial x_i} = -\frac{\Delta \mathbf{K}}{\Delta x_i} \cdot \mathbf{u} + \frac{\Delta \mathbf{f}_{St}}{\Delta x_i} + \frac{\partial \mathbf{f}_{Ae}}{\partial x_i} \tag{3.56}$$

The partial derivatives of the stiffness matrix $\mathbf{K}$ and the static load vector $\mathbf{f}_{St}$ can be determined through e.g. forward differences as shown in Eq. (2.41).

The semi-analytical formulation for the partial derivative of the aeroelastic load vector is derived from Eqs. (3.45) and (3.46).

$$\frac{\partial \mathbf{f}_{Ae}}{\partial x_i} = q\mathbf{T}_{SA} \left(\frac{\Delta \mathbf{A}}{\Delta x_i} \cdot \mathbf{AIC}_{C_P} \cdot \mathbf{b}_c + \mathbf{A} \cdot \frac{\Delta \mathbf{AIC}_{C_P}}{\Delta x_i} \cdot \mathbf{b}_c + \mathbf{A} \cdot \mathbf{AIC}_{C_P} \cdot \frac{\partial \mathbf{b}_c}{\partial x_i} \right) \tag{3.57}$$

$$\frac{\partial \mathbf{b}_c}{\partial x_i} = \frac{\Delta \mathbf{b}_{c_{shape}}}{\Delta x_i} + \mathbf{T}_{AS} \cdot \frac{\partial \mathbf{u}}{\partial x_i} \tag{3.58}$$

Here, the partial derivatives of the aerodynamic panel area matrix $\mathbf{A}$, the pressure coefficient AIC matrix $\mathbf{AIC}_{CP}$ and the geometric Neumann boundary condition component $\mathbf{b}_{c_{shape}}$ are obtained numerically.

With these partial derivatives, Eq. (3.56) can be solved as described in Section 3.6.2.2 to obtain the displacement derivative vector $\frac{\partial \mathbf{u}}{\partial x_i}$. After that, the objective and constraint function sensitivities of Eq. (2.37) can be computed using the respective implicit and explicit partial derivatives. For the structural mass objective the semi-analytical gradient was realized as:

$$\frac{df_m(\mathbf{x})}{dx_i} = \sum_{j=1}^{n_{elem}} \frac{\Delta m_{elem_j}}{\Delta x_i} \tag{3.59}$$

In case of the induced drag objective function, the AIC matrices are differentiated numerically similar to the pressure coefficient AIC matrix required for the displacement vector gradient. Hence, the semi-analytical formulation of Eqs. (3.48) and (3.49) can be written as:

$$\frac{df_{C_D}(\mathbf{x})}{dx_i} = \frac{\partial \mathbf{\Gamma}}{\partial x_i} \cdot \mathbf{AIC}_{C_D} \cdot \mathbf{\Gamma} + \mathbf{\Gamma} \cdot \frac{\Delta \mathbf{AIC}_{C_D}}{\Delta x_i} \cdot \mathbf{\Gamma} + \mathbf{\Gamma} \cdot \mathbf{AIC}_{C_D} \cdot \frac{\partial \mathbf{\Gamma}}{\partial x_i} \tag{3.60}$$

$$\frac{\partial \mathbf{\Gamma}}{\partial x_i} = \frac{\Delta \mathbf{AIC}^{-1}}{\Delta x_i} \cdot \mathbf{b}_c + \mathbf{AIC}^{-1} \cdot \frac{\partial \mathbf{b}_c}{\partial x_i} \tag{3.61}$$

The example of an arbitrary strength constraint provided in Section 3.6.2.2 (Eqs. (3.50) and (3.51)) in semi-analytic formulation is:

$$\frac{dg_{Strength_j}(\mathbf{x})}{dx_i} = \frac{d}{dx_i} g_{Strength_j}(\boldsymbol{\epsilon}(\mathbf{x})) = \frac{\partial g_{Strength_j}}{\partial \boldsymbol{\epsilon}_j} \frac{\partial \boldsymbol{\epsilon}_j}{\partial x_i} \tag{3.62}$$

$$\frac{\partial \epsilon_j}{\partial x_i} = \frac{\Delta \mathbf{B}_j}{\Delta x_i} \cdot \mathbf{u}_{elem_j} + \mathbf{B}_j \cdot \frac{\partial \mathbf{u}_{elem_j}}{\partial x_i} \tag{3.63}$$

Here, only the strain-displacement matrix was differentiated numerically. The remaining relations again depend on the specific formulation of the strength constraint.

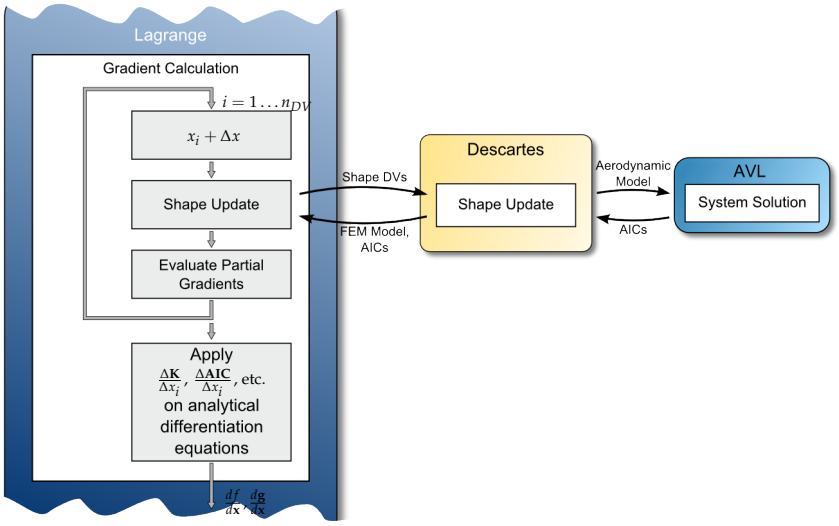

Fig. 3.14: Semi-analytical shape design variable gradient calculation using forward differences

Fig. 3.14 shows the work flow for the semi-analytical sensitivities. The general procedure of looping over the design variables and sequentially applying a perturbation to them is very similar to the global finite differences approach. Only after the shape update, the required partial derivatives (i.e. $\frac{\Delta \mathbf{K}}{\Delta x_i}$, $\frac{\Delta \mathbf{AIC}}{\Delta x_i}$, $\frac{\Delta \mathbf{B}}{\Delta x_i}$, etc.) are calculated, which are then applied to the full gradient calculation. Hence the semi-analytical method requires the same amount of shape perturbations and updates as the numerical approach. However, since Eq. (3.56) is solved analytically, the inversion or factorization of the stiffness matrix that was already done for the analysis can be reapplied taking less time than solving the equation anew for every perturbation as in the numerical approach. This semi-analytical procedure is only performed for the shape design variables in the framework. For all other types of design variables, the available fully analytical sensitivities [SDP+12] are exploited.

This sensitivity calculation method was implemented in the framework for a subset of finite element types and constraints.

3.6.2.4 Comparison of Semi-Analytical and Numerical Gradient Computation

As described in Section 2.2.4.1, the perturbation step size Δx can have a significant influence on the accuracy of finite difference gradients, which also affects the semi-analytical approach. In order to assess the behaviour of the semi-analytical sensitivity calculation, a range of different step sizes was tested. These results were compared to the global finite differences approach (cf. Section 3.6.2.1),

which exhibited a good-natured and stable behaviour for forward differences over a wide range of perturbation step sizes. The semi-analytical sensitivities were evaluated using forward but also central differences. As a basis for this comparison, the gradients of the induced drag objective function, the von Mises stress constraint of an arbitrary wing skin element near the wing root, as well as, a trim constraint limiting the maximum lift force were calculated. These functions, were differentiated with respect to one local chord length and the overall wingspan as examples of first and second level shape design variables (see Section 3.3.1.1).

Table 3.3 and Fig. 3.15 show the results of this comparison. One can see that for smaller normalized perturbation step sizes ($\Delta x < 10^{-3}$) all presented methods show a stable behaviour regarding the gradient value with good agreement between each other. However, at very small perturbation steps ($\sim 10^{-7}$) slight value changes can be observed independent of the gradient computation method. Here, round-off errors might start setting in (see Section 2.2.4.1). Yet, the small magnitude of these deviations allows neglecting them within the chosen step size range. At larger step sizes of $\Delta x \geq 10^{-3}$ one can observe that the semi-analytical gradient using forward differences deviates significantly from its original values in all presented function gradients. Compared to that, the semi-analytical derivative based on central differences shows a wider window of stable gradient values before it diverges. In most cases, the fully numerical gradient using forward differences exhibited the most stable behaviour of the presented methods.

The effect of lower stability in the semi-analytical gradient values at large perturbations was investigated more closely by evaluating the partial numerical derivatives applied in the differentiation chain (see Section 3.6.2.3). The behaviour of some of these partial differentials is presented in Fig. 3.16 over the same range of normalized perturbation step sizes as the overall gradients before. Since these partial derivatives all have matrix form, the trace of the matrices was plotted as an indicator for the gradient behaviour. The absolute value of the matrix trace has no real physical meaning, but it can reveal deviations in the matrix's values. The two most crucial partial derivatives are shown in Fig. 3.16. For the aerodynamic response the gradient of the inverted downwash AIC matrix and for the structural behaviour the derivative of the stiffness matrix were plotted here.

Comparing these results with Fig. 3.15 shows that the point, where the divergence of the overall gradient values sets in, coincides with the change in the partial derivative values. Furthermore, Fig. 3.16 supports the general observation of higher stability in the central difference gradients compared to forward differences, which show good agreement for small step sizes but diverge earlier with increasing perturbation steps. This can be explained with increased nonlinearity in the partial derivatives, which can be represented more accurately with central differences, as they are based on the Taylor series up to the quadratic term (see Section 2.2.4.1). Forward differences only employ the linear term of the Taylor series and, therefore, have a greater truncation error differentiating a non-linear function at large perturbation step sizes.

In comparison, one can say that the fully numerical sensitivities with re-

Table 3.3: Comparison between semi-analytical (forward and central differences) and numerical (forward differences) gradients for the wingspan variable shown in Fig.3.15

Induced Drag Objective					
Normalized Perturbation	Numerical Forward D.	Semi-Ana Forward D.	Difference to Numerical	Semi-Ana Central D.	Difference to Numerical
10^{-1}	0.139078	0.068377	50.84%	0.140743	-1.20%
10^{-2}	0.138971	0.131748	5.20%	0.138981	-0.01%
10^{-3}	0.138964	0.138240	0.52%	0.138963	0.00%
10^{-4}	0.138964	0.138891	0.05%	0.138963	0.00%
10^{-5}	0.138965	0.138953	0.01%	0.138960	0.00%
10^{-6}	0.139041	0.139043	0.00%	0.138985	0.04%
10^{-7}	0.139677	0.139116	0.40%	0.138705	0.70%
Von Mises Stress Constraint					
Normalized Perturbation	Numerical Forward D.	Semi-Ana Forward D.	Difference to Numerical	Semi-Ana Central D.	Difference to Numerical
10^{-1}	-0.803754	2.906710	461.64%	-0.892085	-10.99%
10^{-2}	-0.793873	-0.414154	47.83%	-0.793772	0.01%
10^{-3}	-0.792888	-0.754828	4.80%	-0.792789	0.01%
10^{-4}	-0.792785	-0.788979	0.48%	-0.792779	0.00%
10^{-5}	-0.792706	-0.792395	0.04%	-0.792792	-0.01%
10^{-6}	-0.792116	-0.792494	-0.05%	-0.792659	-0.07%
10^{-7}	-0.788915	-0.788797	0.01%	-0.794832	-0.75%
Lift Trim Constraint					
Normalized Perturbation	Numerical Forward D.	Semi-Ana Forward D.	Difference to Numerical	Semi-Ana Central D.	Difference to Numerical
10^{-1}	-0.003129	-0.002782	11.09%	-0.003122	0.22%
10^{-2}	-0.003115	-0.003080	1.14%	-0.003114	0.05%
10^{-3}	-0.003114	-0.003110	0.11%	-0.003114	0.00%
10^{-4}	-0.003114	-0.003113	0.01%	-0.003114	0.00%
10^{-5}	-0.003114	-0.003114	0.00%	-0.003114	0.00%
10^{-6}	-0.003114	-0.003114	0.00%	-0.003114	0.01%
10^{-7}	-0.003118	-0.003115	0.11%	-0.003112	0.20%

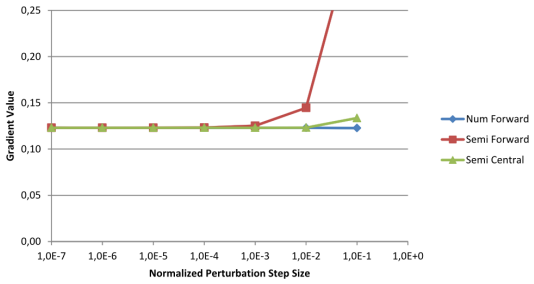

(a) Induced drag gradient w.r.t. chord length

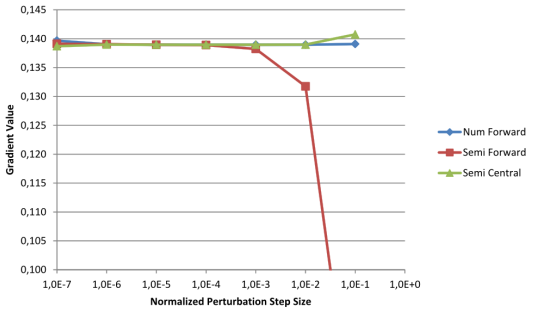

(b) Induced drag gradient w.r.t. wingspan

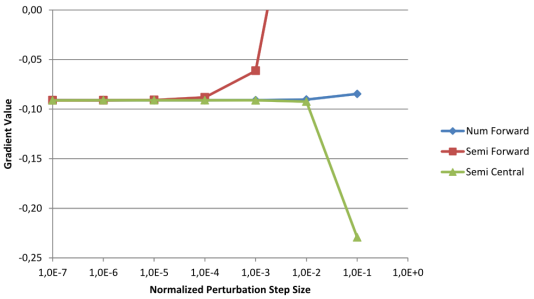

(c) Stress constraint gradient w.r.t. chord length

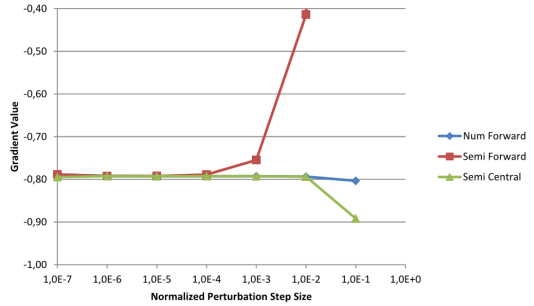

(d) Stress constraint gradient w.r.t. wingspan

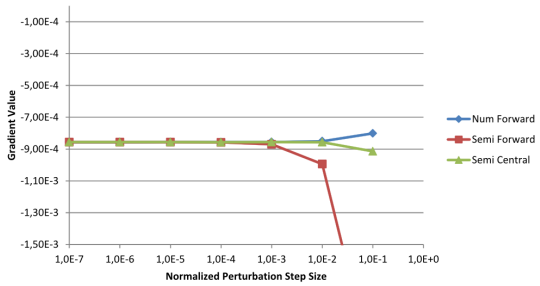

(e) Lift trim constraint gradient w.r.t. chord length

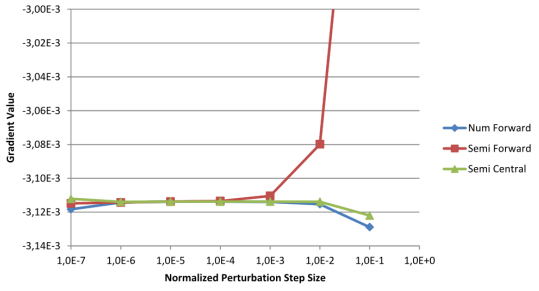

(f) Lift trim constraint gradient w.r.t. wingspan

Fig. 3.15: Comparison between semi-analytical (forward and central differences) and numerical gradients for chord length and wingspan design variables with different normalized perturbation step sizes

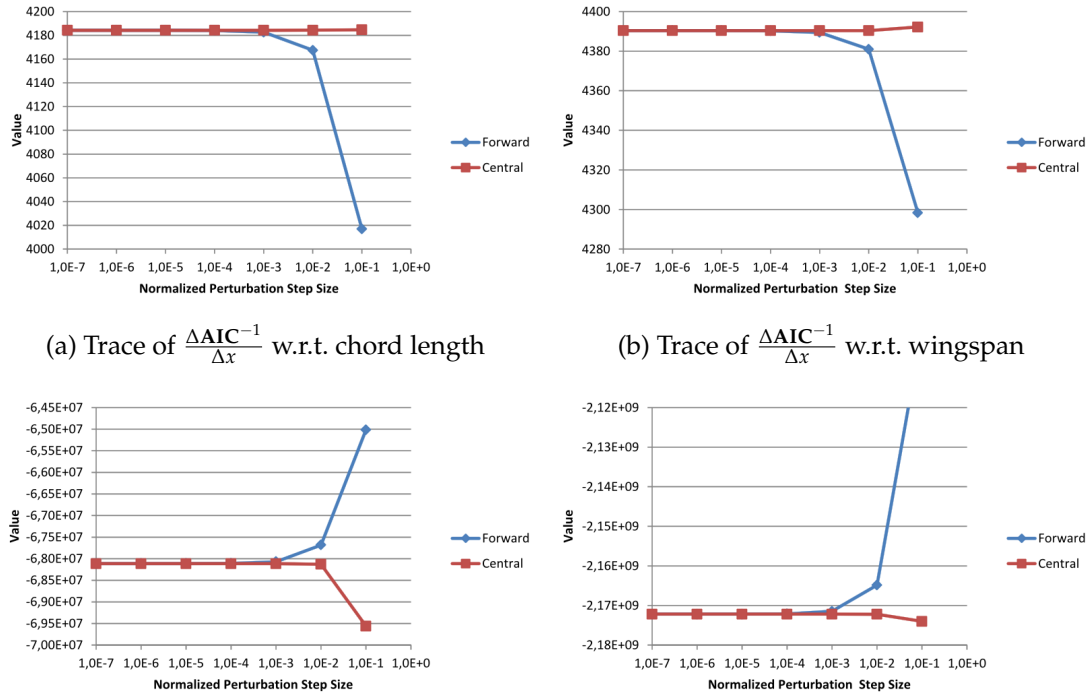

(a) Trace of $\frac{\Delta \mathbf{AIC}^{-1}}{\Delta x}$ w.r.t. chord length

(b) Trace of $\frac{\Delta \mathbf{AIC}^{-1}}{\Delta x}$ w.r.t. wingspan

(c) Trace of $\frac{\Delta \mathbf{K}}{\Delta x}$ w.r.t. chord length

(d) Trace of $\frac{\Delta \mathbf{K}}{\Delta x}$ w.r.t. wingspan

Fig. 3.16: Behaviour of partial matrix derivatives required for semi-analytical sensitivity calculation with respect to chord length and wingspan design variables over different normalized perturbation step sizes

spect to the overall functions f and $\mathbf{g}$ have more stable characteristics, since they allow differentiation using forward differences even with higher perturbation step sizes without loosing significant gradient precision. Similar sensitivity results can be obtained with all three methods. However, in case of the semi-analytical approach applying forward differences a higher focus needs to be put on the selection of a suitable perturbation step size to achieve this precision. While increasing gradient stability, the main disadvantage of central differences is the increased number of required system evaluations of $2 \cdot n_{DV}$ instead of $n_{DV} + 1$ necessary for forward differences resulting in much higher computational times.

Since the computational performance did not show any significant difference between the semi-analytical and the fully numerical approach, it appears that the shape update procedure of the analysis models required most of the effort. The number of these shape updates is equal between these two methods in case of forward differences. Therefore, together with the more good natured behaviour of the fully numerical sensitivity analysis, it was decided to apply overall finite differences for shape design variable sensitivities combined with analytical gradients with respect to the remaining design variable types in this framework.

4 Multidisciplinary Shape Optimization of Aircraft Components

In this chapter the developed shape optimization framework is applied to aircraft design problems. First, an academic model of a rectangular wing is optimized in order to verify the physically sound behaviour of the framework.

After that, a step by step approach of how to apply the shape optimization framework to the problem of early wing planform design is devised using the same wing model. This approach has the goal of finding the best wing planform design through aeroelastic shape optimization, which can used as a suitable starting point for the following aircraft development phases. Several possibilities are evaluated and compared to each other.

Finally, the found approach is applied to a full aircraft model of industrial level of detail discussing its benefits and studying the effects of higher complexity such as the influence of multiple lifting surfaces on the approach and its results.

4.1 Validation and Assessment of the Frameworks Functionality

For this section and the subsequent one, an academic model of the right half of a rectangular wing with high aspect ratio was created and optimized. The involved models, its parametrization and the corresponding structural criteria are presented in the following. Then, before the optimization approach itself was examined, the physically sound behaviour of the framework was validated by solving a number of benchmark optimization problems.

4.1.1 Description of the Optimization Problem

As a first application problem for the developed shape optimization framework, the right half main wing of a generic unmanned aerial vehicle (UAV) was chosen. This type of aircraft features long and slender wings such as those of a sail plane, however, supporting a significantly higher take-off mass compared to a sail plane. Due to this, aeroelastic effects play an important role in UAV wing design. Hence, optimizing such a wing with the developed framework offers great potential for improvements.

This section provides a description of the involved models, the applied load cases and the corresponding constraints that were used during the shape optimizations. Generally, only the right half of the wing was modelled exploiting its symmetry in order to keep the computational effort low.

Table 4.1: Aircraft data for the full model of a generic UAV

Maximum Take-Off Mass m_{MTOM}	5000 kg
Zero Fuel Mass m_{ZFM} (excluding structural wing mass)	2612 kg
Initial Fuel Mass m_{Fuel_0}	1321 kg
Initial Structural Wing Mass m_{FE_0}	1067 kg
Wingspan	20 m
Initial Chord Length	1.5 m
Reference Area S_{ref} (constant)	30 m^2
Reference Chord Length c_{ref} (constant)	1.5 m
Airfoil Profile	NACA 0012

4.1.1.1 Involved Models of Rectangular Wing

The initial UAV wing was defined on a rectangular planform with a symmetric airfoil profile. This was chosen to provide a neutral starting point for the shape optimizations allowing selective studies of different effects. Some specifications of the underlying aircraft are shown in Table 4.1. Here, all data is given for the full aircraft, yet, only the right half of the wing was modelled for optimization. The zero fuel mass given in the table does not contain the mass of the wing structure and was considered to stay constant throughout the optimizations. The wing structural mass, however, was subject to change during the shape optimizations and its initial value is listed separately. In this case, the zero fuel mass represented all components including payload that were not considered in the optimization models. The maximum take off mass (MTOM) was also kept unchanged during the optimizations. This means that any savings or increase in weight due to design variable changes directly influenced the fuel mass m_{Fuel} (its initial value is also given in the table). Apart from the mass data, some initial geometric specifications of the designed wing are also part of Table 4.1.

It has to be mentioned that the chosen rectangular planform of the wing combined with its internal structural layout makes the wing uncritical to aeroelastic effects. However, the rectangular planform was selected deliberately to act as a neutral starting point for all involved disciplines. Adding sweep would effectively increase aeroelastic effects on the wing but would also introduce secondary effects on the aerodynamics that were undesired for these first studies. The purpose of the studies on this model was the validation of the frameworks abilities and the establishment of a process for aeroelastic shape optimization in aircraft development. In order to validate the physically sound behaviour of the optimization framework with respect to aeroelasticity, a modified version of the rectangular wing with added sweep was studied later. However the studies of this chapter were mainly conducted on the unswept rectangular wing. During the application of the shape optimization framework on an industrial scale model in Section 4.3 more focus was put on aeroelastic behaviour.

Generally, the model described in this section is a modified version of the one investigated in [DPD+13b]. It has to be mentioned that the reference values listed here were kept constant through all shape optimizations.

As introduced in chapter 3, the basis of all considered analysis discipline models in this shape optimization framework is the CPACS definition. Hence, the right half of the rectangular wing shape was constructed in CPACS out of 10 segments with 1.5 m chord by 1 m segment length each. This sums up to the desired 10 m of half span with a constant chord length of 1.5 m (a screenshot of its respective parametric geometry is shown in Fig. 4.1). A definition such as this allowed great parametric influence on the shape, since 11 CPACS sections (marked blue in Fig. 4.1) could be used independently for declaration of shape design variables along the span (see Table 3.1 in section 3.3.1.2). At each of these sections a symmetric NACA 0012 airfoil was used to describe the wing profile. In terms of internal structure, two main spars were included at 15 % and 60 % of the chord length. Ribs were defined at the spanwise centre of each segment. Together with the end ribs at the wing tip and root, the total number of ribs amounted to 12. Spar caps and stringers were not defined in the CPACS format but added later directly in the finite element model. In Fig. 4.1, the internal structure is highlighted in red while the sections dividing the wing into segments are marked in blue.

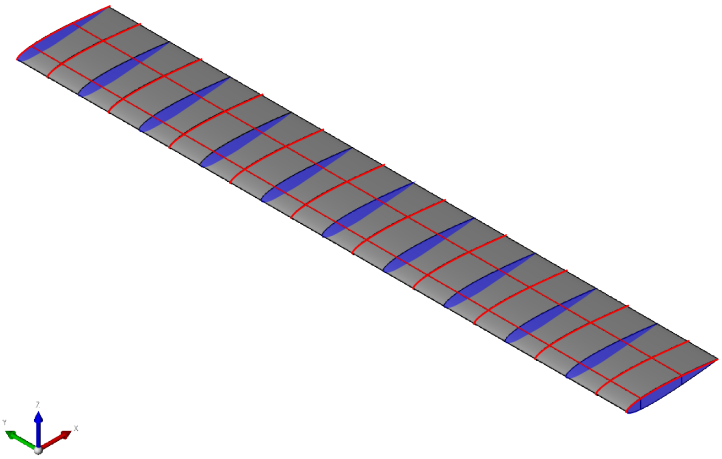

Fig. 4.1: CPACS parametric geometry model of the rectangular wing in *Descartes*

Based on this parametric geometry definition an *AVL* model for aerodynamic loads calculation and a finite element model for the structural response were created following the procedure described in section 3.6.1. Similar to the CPACS model only the right hand half of the wing was modelled for these analysis disciplines enforcing symmetry conditions at the wing root.

The aerodynamic model for *AVL* was created out of 504 horse-shoe vortex elements. In chord length direction, a discretisation of 9 panels was defined using a cosine distribution, while the span direction was divided into 56 vortex elements. Span wise the sections of the *AVL* input definition were aligned with the sections in the CPACS file (indicated in Fig. 4.2 with dashed lines). Inside each of these spanwise segments a linear distribution of panels was chosen except for

the root and tip most segments which featured a sine and a negative sine distribution respectively (see Fig. 4.2). This discretisation was determined through a number of test analyses increasing the number of panels repeatedly until the change in the aerodynamic results was negligibly small. The reason for the sine discretisation in the root and tip segment of the wing was the high gradient of the aerodynamic solution in these areas compared to the segments in between. Since the CPACS definition applied a symmetric airfoil profile, no camber or twist was defined for the initial *AVL* model of the rectangular wing. Due to the very low effort required to recreate the *AVL* input after a shape change, the aerodynamic model did not have to be explicitly mapped back onto the parametric model. However its definition could be permanently linked to the CPACS definition, which was sufficient to consistently regenerate the *AVL* input after any modification to the CPACS parameters.

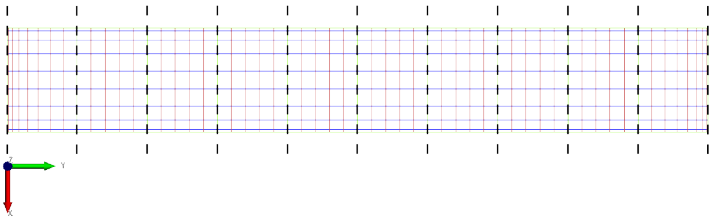

Fig. 4.2: Aerodynamic *AVL* model of the right half rectangular wing (With segment borders highlighted)

The structural finite element model was meshed with a commercial tool directly using the surfaces of the parametric geometry model. The resulting FEM mesh (see Fig. 4.3, cut open) consisted of 2D shell elements (CQUAD4 and CTRIA3), as well as, 1D elements (CROD and CBAR) in the *MSC Nastran* formulation (cf. [Nas]).

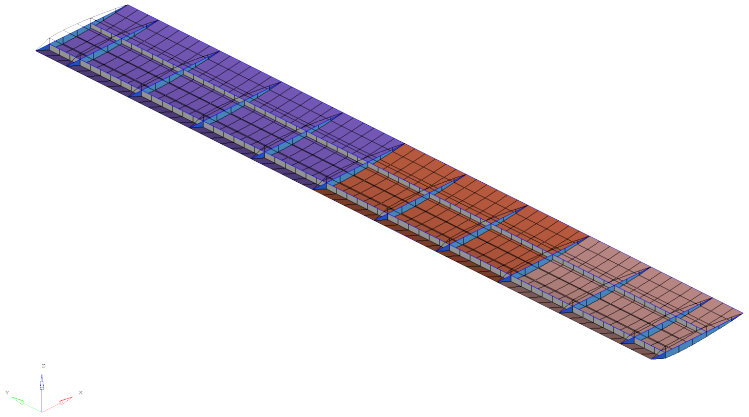

Fig. 4.3: Structural finite element model of the right half rectangular wing (Cut open to show internal structure)

Additional to the shell elements shown in Fig. 4.3, the skin of the wing box between the two spars was reinforced by stringers. Spar caps were also mod-

elled using rod elements of rectangular cross section. A skin thickness distribution of 7.5 mm in the root region reducing to 6 mm and 4 mm towards the wing tip was chosen for the initial design (see colours in Fig. 4.3). The entire structure was assigned the material properties of aluminium (AlZn1). Ribs and spars of the internal structure were defined with a uniform thickness of 3 mm and 4 mm respectively. The spar cap cross section area was set to 100 mm^2, while the stringers were initially sized to 50 mm^2. With these specifications, the total mass of the initial half wing model amounted to 533.5 kg (or 1067.0 kg for the full model as presented in Table 4.1). The complete structural finite element model was mapped onto the parametric geometry so that the positions of the mesh nodes were linked to the CPACS geometry definition.

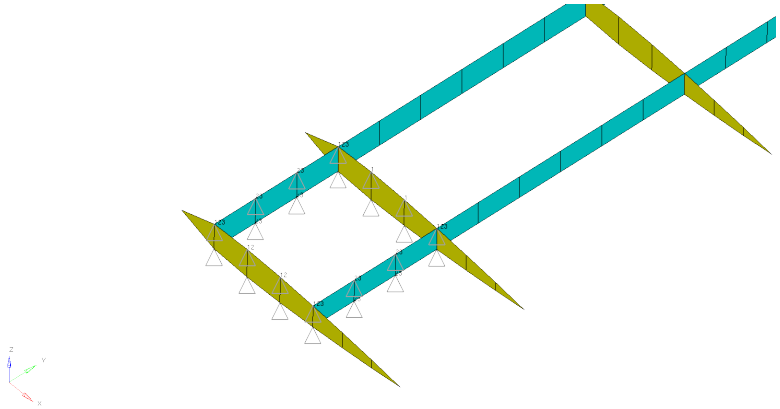

Fig. 4.4: Mounting of the wing model

In order to enable stationary aeroelastic analyses the structural model was mounted in the region between the two inner most ribs (cf. Fig. 4.4). The concept of wing fuselage connection was chosen to be a carry-through wing box leading through the fuselage. Hence, the root rib was fixed to the keel beam of the fuselage (not modelled) supporting it in x-direction and to satisfy the symmetry condition in y-direction. The second rib from the root was assumed to be connected to the skin of the fuselage fixing it in x-direction. The two spars were attached to fuselage frames supporting them in y- and z-direction.

A set of nodes was picked from the structural model which were employed the infinite plate spline interpolation (see section 2.1.3). These nodes were chosen at intersections of the upper skin of the wing with spars or ribs so that the structure could properly support the applied loads.

4.1.1.2 Analysis Load Cases

In order to have representative loads and responses for all included analysis disciplines, three aeroelastic load cases were considered during the shape optimizations. This represented a minimal set of load cases to demonstrate the abilities of the framework without increasing computational times excessively. All three load cases were defined at the same point in the flight envelope of the UAV aircraft only differing in their respective load factors. This point was chosen at cruise conditions with 0.28 Mach at 7500 m altitude. The mass configuration for this flight state was specified at maximum take-off mass m_{MTOM}

in order to provide worst case loads for the structural constraints. During the aeroelastic analysis of all cases, structural inertia, as well as, aerodynamic lift loads were considered. Based on this, all load cases were trimmed for the aeroelastic state using the definitions described in Section 4.1.1.4. The trim target lift was the maximum take-off weight, which was kept constant throughout the optimizations, multiplied by the respective load factor. Through this, constant lift coefficients could be obtained facilitating comparison between different optimization runs.

The first load case was created as a horizontal cruise flight for induced drag evaluation (see Table 4.2). Therefore, the load factor of this load case was given at $n = 1.0\,\mathrm{g}$. In case an induced drag objective function was defined during any of the shape optimizations, the objective function would refer to the aeroelastic results of this load case.

The second and third load case in Table 4.2 were defined to be structurally design driving so that critical aeroelastic loads are provided to the structural constraints. The push-over load case was established as a down bending state with a load factor of $n = -1.0\,\mathrm{g}$, whereas the third case simulated a pull-up manoeuvre with an inertial acceleration $n = 2.5\,\mathrm{g}$ causing the wing to bend upwards. In order to guarantee structural integrity of the wing, both of these load cases were provided with a safety factor of 1.5. This safety factor was applied on the aerodynamic and inertia loads. Concerning the induced drag objective these two structurally design driving load cases did not have any influence on the objective function.

Table 4.2: Load case definition for rectangular wing shape optimizations

Load Case	Mass	Mach Number	Altitude	Load Factor	Safety Factor
Cruise	m_{MTOM}	0.28	7500 m	1.0 g	1.0
Push-over	m_{MTOM}	0.28	7500 m	−1.0 g	1.5
Pull-up	m_{MTOM}	0.28	7500 m	2.5 g	1.5
Parking	m_{MTOM}	-	-	1.0 g	1.0

Additional to the aeroelastic load cases, a static load case with only inertia loads of $n = 1.0\,\mathrm{g}$ was included as well. This simulated the aircraft being parked on ground with no aerodynamic forces to counter the gravitational forces of 1 g.

4.1.1.3 Design Parametrization

The rectangular wing model was parametrized using sizing, trimming and shape design variables.

The specific set of shape design variables was prepared individually for each optimization case, yet, always relying on the CPACS definition described in section 4.1.1.1. This means, the eleven sections that were used to describe the wing (see Fig. 4.1) could be employed to define for example local shape variables. The first optimizations were conducted with chord length or y-rotation (i.e. twist) shape variables for validation of the framework, before the most effective combination of shape design variable types was studied later in this chapter.

Sizing design variables, on the other hand, were defined for the entire skin elements of the rectangular wing structural model. The sizing design variables were linked so that all shell elements located in the same skin patch (sectioned by ribs, spars and stringers) were assigned the same thickness values. This amounted to a total number of 110 2D sizing variables. The gages for these skin thickness design variables were set to the interval between 0.8 mm and 8.0 mm. Additional to the wing skin shell elements, the cross section areas of the skin stringer and spar cap elements were declared as 1D design variables. In analogy to the skin design variables, these were linked between neighbouring ribs. This way, an additional 88 1D sizing variables was specified. The stringer cross section values were allowed to vary between 50 mm^2 and 200 mm^2, whereas the spar caps were limited to the interval between 100 mm^2 and 500 mm^2. Hence, the total number of available sizing variables summed to 198.

In order to trim the three defined aeroelastic load cases to their respective load conditions, one trim variable per aeroelastic load case was defined. These trim variables affected the overall angle of attack through scaling so that the aerodynamic load could be adjusted taking into account the structural deformation and the inertia loads. Since only the main wing of the aircraft was modelled for these optimizations, no other trim variables (e.g. for pitch moment trimming) were required. Therefore, 3 trim design variables were used for all optimization runs.

4.1.1.4 Optimization Constraint Definition

Four different types of constraints were considered over the course of the conducted shape optimizations. These were stress and stability for the structural requirements, trim constraints for constant aeroelastic loads and mass constraints for the structural mass of the wing.

By default every structural finite element that was declared a sizing design variable was assigned a stress constraint to guarantee reasonable thickness values. Thus, every wing skin element was assigned a stress constraint limiting the von Mises stress to a maximum of 480 $\frac{N}{mm^2}$. The finite elements of stringers and spar caps forming the 1D design variables were assigned similar stress constraints. This yielded a total number of 1320 stress constraints per load case.

Structural stability constraints (buckling) were only defined for the skin of the wing box. The skin of the leading edge in front of the first spar was disregarded due to its strong curvature which makes it less critical to buckling. Similarly, the trailing edge skin rear of the last spar was also not assigned any buckling constraints, since it usually has a negligible contribution to the structural stability because of trailing edge devices (e.g. flaps, ailerons; not modelled here). Thus, the finite elements of the wing skin between the first and the second spar were divided into buckling fields. For this division the layout of spars, ribs and stringers was utilized. The buckling fields for the upper skin of the wing model are highlighted in Fig. 4.5. A similar distribution was applied on the lower side of the wing box. Therefore, a total number of 66 buckling constraints per load case was defined.

Each aeroelastic load case required two trim constraints to limit the overall

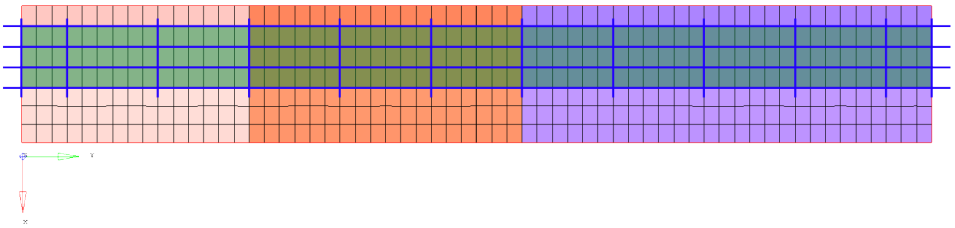

Fig. 4.5: Buckling field sectioning on rectangular wing model

lift force generated by the wing. The definition of these trim constraints was realized in such a way that a minimum and a maximum lift force constraint was defined adjacent to the desired value. These boundaries were placed in such a way around the target lift value that in combination with the possible induced drag objective the effect described in section 3.4.3 could be exploited. Therefore, very constant lift coefficients could be guaranteed throughout the shape optimizations. This was crucial to the induced drag comparisons but also the structural optimization benefited from this through small fluctuations in the aeroelastic loads.

In some optimization runs a structural mass constraint was included. In this case, the constraint limited the maximum FE mass of the wing model. This was used mainly to prevent the optimizer from excessively adding material to the wing not required for structural integrity in case the used objective function did not consider the mass response.

Hence, taking into account all 4 possible load cases and all types of constraints the maximum number of defined constraints with this wing model amounted to 5550 constraints with possibly an additional one for the FE mass.

4.1.2 Initial Analysis of the Wing

An aeroelastic analysis of the initial wing design defined in the sections above was conducted. This was done in order to establish the starting point conditions of constraints, objective function and other quantities.

The initial structural dimensions (see section 4.1.1.1) were chosen after a manual sizing process so that all structural constraints were satisfied. Also the trimming constraints were satisfied beforehand in order to conduct the simulations at the desired aeroelastic flight states. Figs. 4.6, 4.7 and 4.8 show the results of the initial analysis in terms of displacements, stresses and buckling reserve factors. The stress and displacement results of the pull-up and the push-over load cases are presented, as these involved the highest loads on the structure. The cruise and the parking load case both caused strains lower than the two presented cases and are not shown here.

The maximum wing tip displacements in Fig. 4.6 were about $+1.0\,\mathrm{m}$ and $-0.4\,\mathrm{m}$ for the pull-up and the push-over manoeuvre respectively. The wing exhibited only low torsional displacements due to the structural configuration and the unswept planform.

In Fig. 4.7 one can see that no elements violate the maximum allowed stress

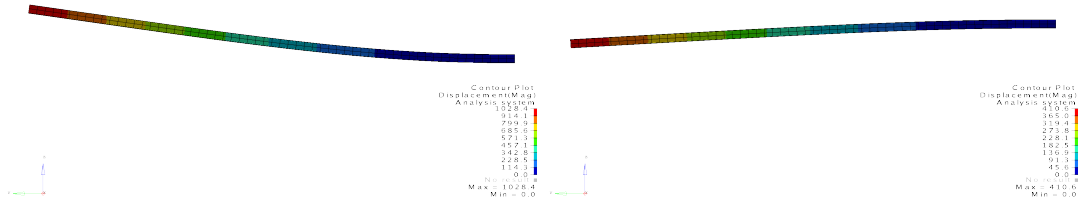

Fig. 4.6: Front view of aeroelastic displacements for pull-up (left) and push-over (right) load cases of initial design

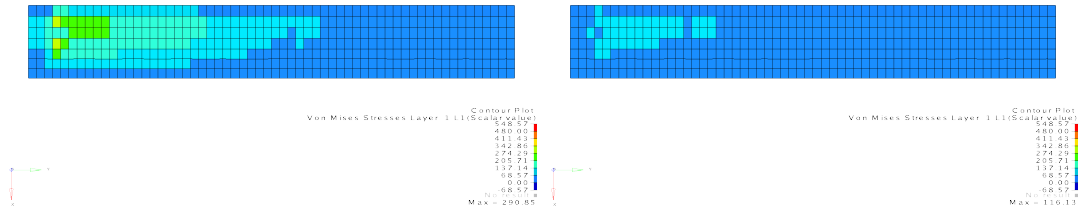

Fig. 4.7: Top view of von Mises stress for pull-up (left) and push-over (right) load cases of initial design

value (480 MPa). As expected the pull-up load case caused the most critical loads to the structure (i.e. 291 MPa) due to its higher load factor as opposed to the push-over manoeuvre with 116 MPa.

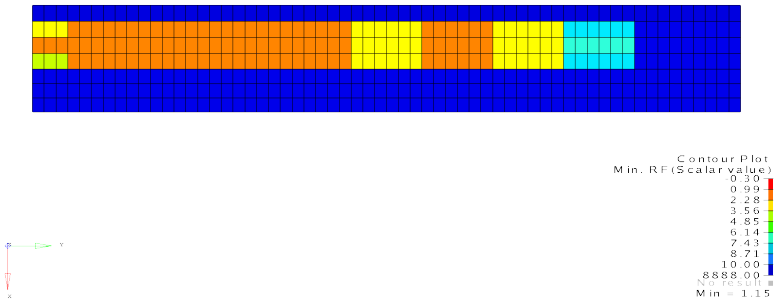

Fig. 4.8: Top view Buckling reserve factor of initial design (all load cases)

The buckling reserve factors displayed in Fig. 4.8 show for each buckling field the respective worst values reached in any of the considered load cases. One can see that all buckling constraints are satisfied with the region between root and mid-wing being critical, as the active constraints (i.e. $R \approx 1.0$) prevail there. Towards the wing tip the buckling behaviour turns less critical, since the compression loads in the skin decline with the distance to the root. These result agree with the general experience that for wing structures buckling constraints are usually more design driving than strength constraints.

In Fig. 4.9 the spanwise lift distribution during the cruise load case is shown for the rigid and aeroelastic configuration together with the ideal elliptic distribution as a reference. For this plot the product of local lift coefficient C_l and its corresponding local chord length c at a span wise position normalized by the reference chord length c_{ref} is plotted along the span direction (cf. e.g. [ST01a]).

This yields the contribution of a wing section to the overall lift, which provides information about the aerodynamic lift load on the structure but also on the induced drag characteristics of the wing, since it is proportional to the local vortex strength (see section 2.1.2). Integrating the lift distribution along the span yields the overall lift coefficient multiplied by the wing area. Therefore, in a graphical sense, all lift distribution curves of a wing representing the same lift state need to cover the same area underneath the curve.

The rigid configuration in Fig. 4.9 disregarded any effects of elasticity providing the purely aerodynamic result, while the elastic state was based on the solution of the aeroelastic analysis accounting for the interaction between aerodynamic loads and structural displacements. Additionally, the ideal elliptic lift distribution was calculated for the corresponding elastic overall lift coefficient as a reference (see Section 2.1.2.4, Eqs. (2.11) and (2.13)). The wing shows the typical lift distribution for a rectangular planform wing having a rather constant lift from wing root towards tip with an abrupt drop off near the wing tip to zero lift there. As one can see, the ideal elliptic distribution allocates higher local lift near the wing root and less in the wing tip region while covering the same area below the curve. A small difference between the rigid (thin green) and the elastic lift distribution (thick red) can be seen near the wing root. The fact that the elastic lift distribution lies above the rigid one indicates an increased overall lift coefficient caused by the elastic behaviour of the wing structure.

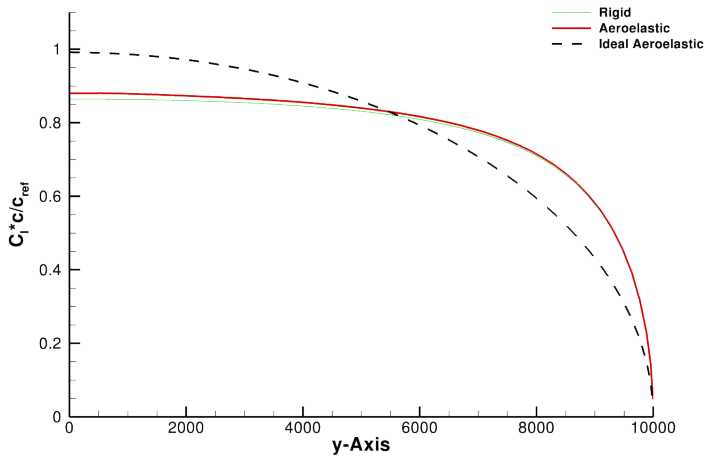

Fig. 4.9: Lift distribution of initial design during cruise load case

The following Table 4.3 provides a summary of the overall values obtained from the initial analysis. All values listed here are given for the aeroelastic result of the cruise load case. The Breguet range R_{Br}, whose definitions and mission profile are presented later in Section 4.2.1.1, is stated in this table for completeness.

4.1.3 Validation of Approach and Methods

Based on this initial configuration, a number of shape optimizations were conducted in order to validate the physically sound behaviour of the developed

Table 4.3: Results of initial aeroelastic analysis

Quantity	Value	
m_{FE}	0.5335	t
C_L	0.7787	
$C_{D_{ind}}$	0.0153	
R_{Br}	4860	km

shape optimization framework. The analysis the method for sensitivity analysis have been tested component wise in Section 2.1 and Section 3.6.2 respectively, so that now the entire framework is validated with respect to its optimization functionality.

4.1.3.1 Unconstrained Solutions for Induced Drag and Structural Mass

First of all, the two structurally unconstrained solutions for aerodynamics and structures were sought separately. This means one optimization for minimal induced drag and one for minimal structural weight was conducted without considering any structural requirements. The goal behind was to prove that the framework is capable of finding the known minima for these two limit cases. This would confirm the general, physically sound behaviour of the optimization framework. As no structural constraints were included in these first optimizations, only the cruise load case described in section 4.1.1.2 was simulated. Thus, the objective functions were formulated as:

$$\begin{aligned} f_1(\mathbf{x}) &= C_{D_{ind}}(\mathbf{x}) \\ f_2(\mathbf{x}) &= m_{FE}(\mathbf{x}) \end{aligned} \tag{4.1}$$

so that for both:

$$\mathbf{g}(\mathbf{x}) = \mathbf{g}_{trim}(\mathbf{x}) \leq 0 \tag{4.2}$$

All system responses for Eqs. (4.1) and (4.2) were calculated through aeroelastic analysis of the cruise load case. As explained in Section 3.5.1, the reference surface for the calculation of the induced drag coefficient was kept constant throughout the shape optimization in order to allow direct comparison of results but also to prevent the optimizer from exploiting that the induced drag coefficient is inverse proportional to the reference area.

In this case, the definition of trimming constraints for the aeroelastic overall lift was required to keep the flight state constant throughout the optimizations. Hence, two trimming constraints were formulated for each optimization providing a minimal and a maximal allowed overall lift force value for the aeroelastic cruise load case. The boundary values were set corresponding to the required loads for a 1.0 g level flight.

The chord lengths of the 11 CPACS sections x_{c_i} and one trimming variable x_α affecting the angle of attack were defined as design variables with their corresponding upper x_{ub} and lower bounds x_{lb} in Table 4.4. This shape parametrization was chosen, since the chord length distribution of the wing has a great

Table 4.4: Design variable definition for unconstrained shape optimizations

Design Variable x	Lower Bound x_{lb}	Upper Bound x_{ub}
Shape		
Chord Lengths x_{c_i}	300 mm	1700 mm
Trimming		
α Scale Factor x_α	-50	50

effect on both its aerodynamic and structural properties. Regarding the aerodynamics the spanwise lift distribution can be modified effectively by changing the chord length, while the structural stiffness is influenced by the chord length through the change of wing cross section area (thickness to chord ratio of the airfoil was kept constant). With this, the aerodynamic and structural properties of the wing could be changed very effectively while keeping the flight state trimmed using the angle of attack trimming variable.

The expected results of these were reliably predictable, since no interference with the minimal objective function value could be caused by constraint functions. Therefore, for the minimal induced drag optimization a planform shape with an elliptic chord length distribution was expected, which would generate an elliptic lift distribution [KP01] and thus minimal induced drag for this design (see section 2.1.2). The structural mass optimization, on the other hand, would simply have to minimize the finite elements' volumes in order to reach minimal mass (see section 3.5.2). Hence, the mass optimization should produce a design with all shape variables reduced to the minimal gage.

Both optimizations converged according to the KKT condition (see Section 2.2.5) after around 30 iterations. The resulting wing planform geometries of the two shape optimizations are shown in Fig. 4.10. In both pictures the initial planform shape is indicated by the red line as a reference.

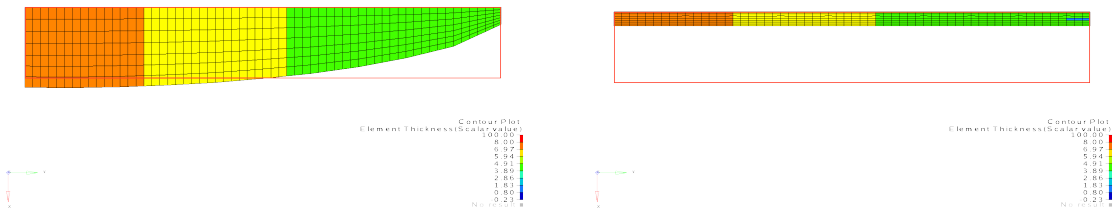

(a) Induced Drag (b) FE Mass

Fig. 4.10: Resulting planform and skin thickness distributions of unconstrained shape optimizations

The corresponding lift distributions to these planforms can be seen in Fig. 4.11.

Looking at both Figures 4.10 and 4.11 it becomes obvious that the purely aerodynamic optimization opted for the expected elliptic planform shape in order to reach an elliptic lift distribution, which corresponds to minimal induced drag. Changes in overall lift due to the new planform were trimmed using the angle of attack design variable to keep the overall lift forces constant. The

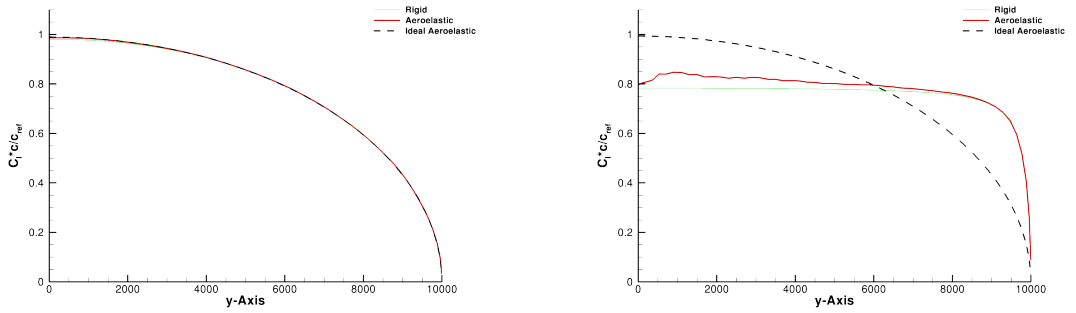

(a) Induced Drag (b) FE Mass

Fig. 4.11: Resulting lift distribution of unconstrained shape optimizations

lift distribution of this result (Fig. 4.11a) showed that the aeroelastic lift (red line) matched the ideal elliptic lift (black dashed line) very closely. Another effect to be observed is that the rigid lift distribution (thin green line) assumed an almost identical trend as the aeroelastic one. This means, that through the shape changes the effects of structural elasticity on the aerodynamics were almost eliminated. Hence, the optimizer reached the expected minimum reliably, while taking into account the elastic behaviour of the wing structure.

The mass optimization, on the other hand, showed that the optimizer reduced all available shape design variables to their minimal allowed gage of 300 mm, as expected. Here, the overall lift force was also kept constant by adjusting the trimming design variable. The lift distribution of this solution in Fig. 4.11b remained rather similar to the initial state in Fig. 4.9 only becoming more rectangular, which is an effect of the effective increase in aspect ratio [ST01b, p. 46].

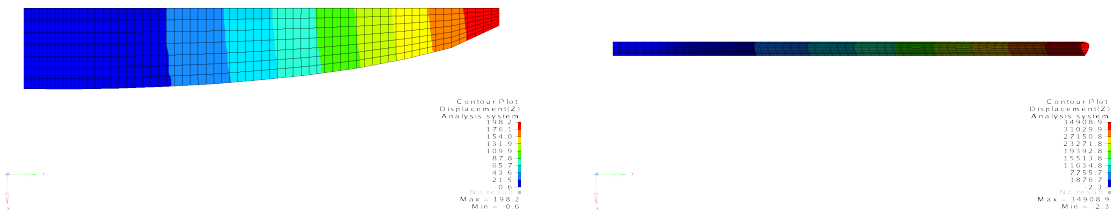

(a) Induced Drag (b) FE Mass

Fig. 4.12: Resulting displacements of cruise load case for unconstrained shape optimizations

Fig. 4.12 depicts the structural displacements of the aeroelastic cruise load case for both optimization results. From the tip displacements of both designs it is possible to generally assess the characteristics of the design. The induced drag result on the left side has a maximum wing tip displacement of 198 mm, while the minimum mass design on the right hand side experiences a maximum displacement of roughly 34 900 mm. For a wing span of 20 000 mm both results represent extreme cases. On one hand, 198 mm displacement is very low for a wing of these dimensions hinting at an overdimensioned structure with great mass reserves. On the other hand, 34 900 mm tip displacement repres-

ents such a massive deformation that the applied linear finite element analysis would not produce reasonable results any more, since the assumptions of small displacements are violated. Also, the large angles of attack required to produce the needed lift with a wing of such short chord lengths would cause severe flow separations (i.e. stall), which cannot be reproduced with the applied aerodynamic analysis method. However, regardless of the physical applicability of the analysis methods in this case, structural failure would represent the far greater issue, which is proven by the von Mises stress evaluation in Fig. 4.13. In the right figure depicting the minimal mass solution, most skin elements show stress values far greater than the material could bear. Yet, the stress plot of the minimal induced drag design confirms the impression of substantial structural material reserves, as the occurring stresses are negligible. However, since no structural constraints were provided to the optimizer, both results lie in the feasible design space of the given optimization problem.

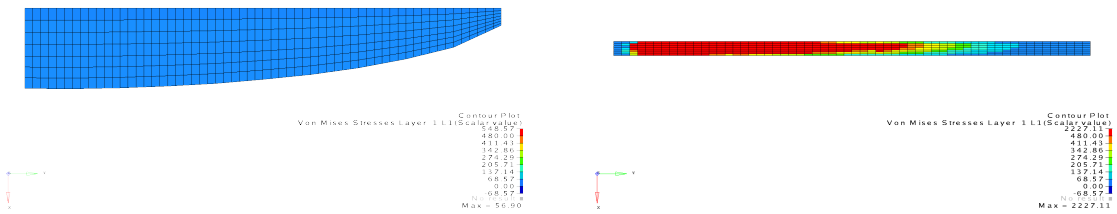

(a) Induced Drag (b) FE Mass

Fig. 4.13: Von Mises stress evaluation for cruise load case of unconstrained shape optimizations

Tables 4.5 and 4.6 provide summaries of both conducted shape optimizations. One can see that from the same initial point the induced drag optimization managed to reduce the aeroelastic induced drag by around 6 % while the mass optimization increased it by about 18 % with an approximately constant overall lift coefficient. In terms of structural mass both optimizations decreased the FE mass. However, a reduction of 78 % in case of the mass optimization renders the 4 % weight savings of the induced drag optimization negligible.

Table 4.5: Optimization summary of unconstrained induced drag shape optimization

	Initial	Final	Delta %
FE Mass [t]	0.5333	0.5111	-4.17
Elastic C_L	0.7787	0.7772	-0.20
Elastic $C_{D_{ind}}$	0.0153	0.0144	-5.84

Comparing the values shown in Table 4.5 with the theoretical results for the uncambered wing of Eq. (2.8) shows that in this case the theoretical optimum

Table 4.6: Optimization summary of unconstrained mass shape optimization

	Initial	Final	Delta %
FE Mass [t]	0.5333	0.1171	-78.04
Elastic C_L	0.7787	0.7803	+0.21
Elastic $C_{D_{ind}}$	0.0153	0.0181	+18.18

for the induced drag objective has been found. Thus, evaluating Eq. (2.8) with the values given in Table 4.1 for the induced drag coefficient (i.e. $C_{D_0} = 0$) yields the theoretically achievable induced drag value for this wing. As the ideal lift distribution corresponds to an Oswald factor of $e = 1.0$ (see Section 2.1.2), this value will also result in the minimal achievable induced drag for a planar wing configuration. It has been mentioned before that the reference area S_{ref} is kept constant during the shape optimization, therefore, the aspect ratio Λ needs to be calculated based on this area to guarantee consistency. With all this considered, the ideal induced drag value for a lift coefficient of $C_L = 0.7772$ results in $C_{D_{ind}} = 0.0144$ disregarding the viscous component C_{D_0}.

$$C_D = C_{D_0} + \frac{C_L^2}{\pi \Lambda e} \tag{2.8 revisited}$$

This shows that the aeroelastic shape optimization was able to find the induced drag minimum for this configuration known from literature.

In summary one can say that the optimizer reached the known minima of the two unconstrained optimization problems as expected, so the general behaviour of the shape optimization was found to be plausible. The physical application of the design results is hardly given, especially in the case of the structural mass optimization that will unveil severe drawbacks, once structural integrity has to be ensured. But, since this was not part of the optimization problem definition, it represents a feasible design point from the optimization algorithm's point of view.

This shows that the general physical analysis methods, their interaction in the framework and the calculated gradients for the optimization all reflect the physical principles known from literature. Thus, the aeroelastic shape optimization framework behaves as expected with the separate objective functions.

4.1.3.2 Solutions with Structural Criteria

In order to determine the difference in resulting designs caused by consideration of structural criteria, both of the presented shape optimizations were repeated, with structural strength and stability constraints included as described in section 4.1.1.4. For this, the two previously omitted aeroelastic load cases (push-over and pull-up, cf. Section 4.1.1.2) were considered as well so that the applied loads would be reasonably design driving on the structure.

$$\mathbf{g}(\mathbf{x}) = \begin{bmatrix} \mathbf{g}_{stress}(\mathbf{x}) \\ \mathbf{g}_{buckling}(\mathbf{x}) \\ \mathbf{g}_{trim}(\mathbf{x}) \end{bmatrix} \leq 0 \tag{4.3}$$

In order to have sufficient influence on local structural constraints, sizing design variables (defined in Section 4.1.1.3) were also included in these optimizations.

Table 4.7: Design variable definition for shape optimization with structural constraints

Design Variable x	Lower Bound x_{lb}	Upper Bound x_{ub}
Shape		
Chord Lengths x_{c_i}	300 mm	1700 mm
Sizing x_{Size}		
Skin	0.8 mm	8.0 mm
Stringer	50 mm^2	200 mm^2
Spar Caps	100 mm^2	500 mm^2
Trimming		
α Scale Factor x_α	−50	50

The induced drag objective shape optimization converged after 48 iterations satisfying the Karush-Kuhn-Tucker condition. Whereas, the FE mass objective did not reach convergence within 80 iterations, after which it was stopped automatically. Evaluation of the optimization history did not suggest convergence, so the optimization was restarted for another 80 iterations. After that, the KKT condition could still not be satisfied, yet, due to the small changes in the objective function value and the satisfied constraints over the last couple of iterations the optimization was assumed as converged.

Therefore, the induced drag result after 48 iterations and FE mass result after 160 iterations are compared in the following studies. The resulting planform shapes including the obtained skin thickness distributions are depicted in Fig. 4.14 and 4.15 and compared to their respective unconstrained counterparts.

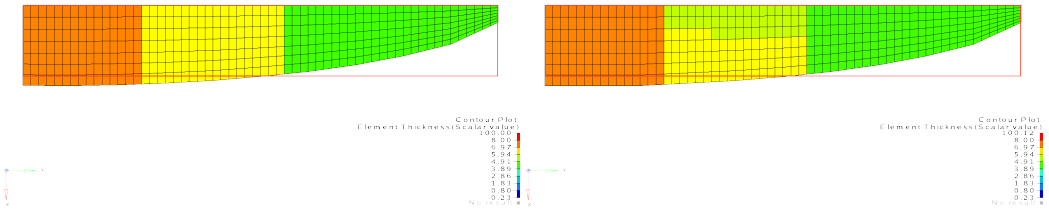

(a) No structural constraints (b) With structural constraints

Fig. 4.14: Influence of structural constraints on resulting planforms and thickness distribution for induced drag optimization

Fig. 4.14 shows that the addition of structural constraints caused no significant change in the wing design for the induced drag objective optimization. The planform geometry matches an elliptic chord length distribution in both cases and the changes made to the skin thickness distribution are negligible. The reason for this is that the initial design had all structural constraints satisfied and the optimization for an improved induced drag did not move in a direction

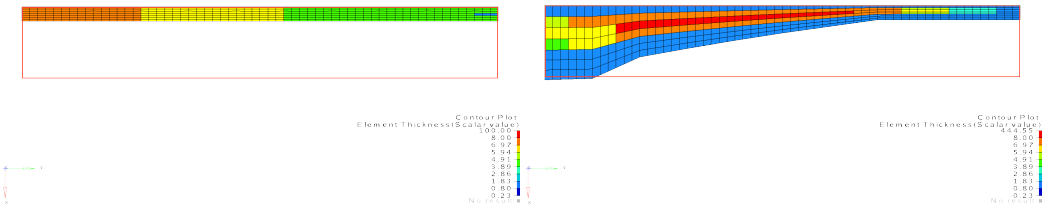

(a) No structural constraints (b) With structural constraints

Fig. 4.15: Influence of structural constraints on resulting planforms and thickness distribution for structural mass optimization

where the structure might have become critical. Thus, due to the initial point and the chosen objective function, the addition of structural constraints did not significantly alter the solution of this optimization. The found design produces an elliptic lift distribution as before, which corresponds to an Oswald factor $e = 1.0$ (see Fig. 4.16).

The FE mass optimization, on the other hand, shows a significant difference in the resulting planform with structural constraints added (Fig. 4.15). Through this extension of the optimization problem, a triangular shaped wing planform was created, which allows better support for the root bending moment, as it provides a higher cross section area of the wing box near the wing root, where the maximal bending moment occurs. Also, substantial changes to the skin thickness distribution can be seen in the comparison figure. Where possible, (e.g. forward and aft of the wing box) the skin thickness was reduced almost to the minimal allowed gage, while the skin thickness of the wingbox was increased to satisfy the stress and buckling constraints. The reason for the low values in the leading and trailing edge regions was that only stress constraints without any buckling criteria were defined there. Increased skin thickness can be seen in the middle of the wing box where the buckling fields are only bordered by stringers instead of spars.

Additional to the triangular planform for improved area moment of inertia, the chord length from about 75 % half span towards the tip was reduced to the minimal gage of 300 mm. Through this, effectively the wing span was reduced in terms of wing bending moment generation, since this shifted the lift load inwards towards the wing root (see Fig. 4.17). This means the strain on the structure was reduced in two ways; on the one hand, structurally by increasing the load bearing capabilities, on the other hand, aerodynamically by shifting the point of lift resultant inward towards the root reducing its lever while keeping overall lift constant.

Fig. 4.18 shows aeroelastic displacements during the cruise load case. The induced drag result again exhibits almost no change in displacement compared to the respective unconstrained solution from the previous chapter (Fig. 4.12). The maximum displacement was in both results around 200 mm. The remaining two aeroelastic load cases that were added for the constrained optimizations caused displacements of about -300 mm during push-over and for pull-up 740 mm, which are not shown here.

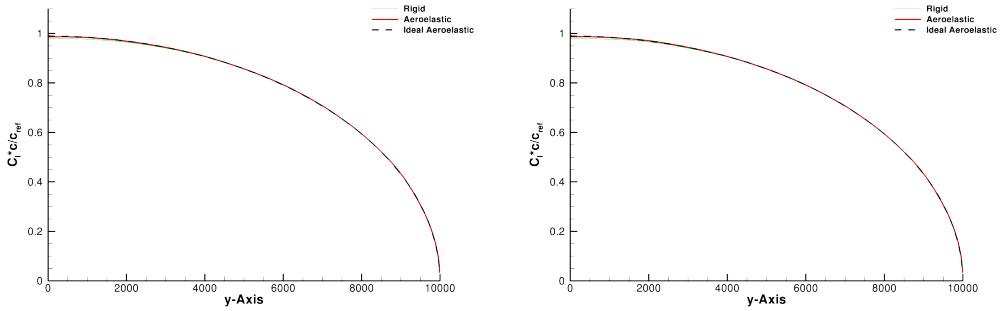

(a) No structural constraints (b) With structural constraints

Fig. 4.16: Influence of structural constraints on lift distribution for induced drag optimization

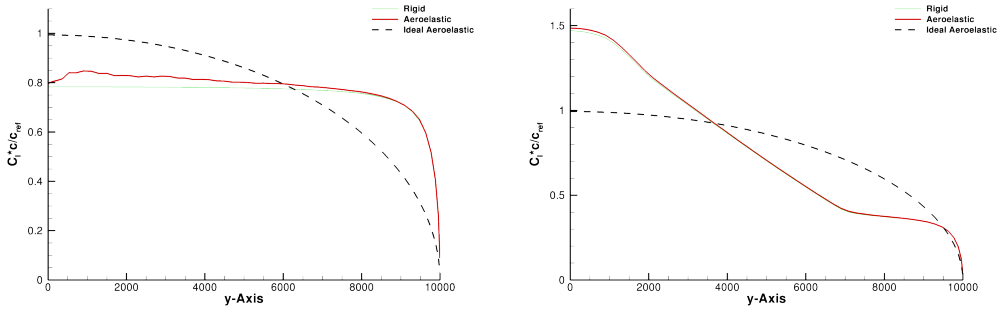

(a) No structural constraints (b) With structural constraints

Fig. 4.17: Influence of structural constraints on lift distribution for structural mass optimization

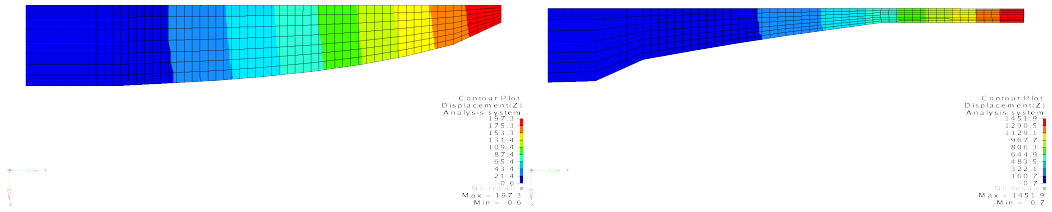

(a) Induced drag result (b) FE mass result

Fig. 4.18: Comparison of aeroelastic displacements during cruise

The structural mass result, however, experienced a significant change in wing tip displacement with now 1450 mm compared to previously around 34 900 mm. This was expected, as the structural constraints limited the stress in the finite elements that is inherently related to the strains and the node displacements (cf. Section 2.1.1. The additional aeroelastic load cases caused displacements of: push-over -2200 mm, pull-up 5400 mm on this design. Here, one has to keep in mind that the safety factor of 1.5 for the structurally design driving load cases was included in the loads. Therefore, the realistic displacements for the push-over and the pull-up load case without safety factor would be smaller than the values shown here.

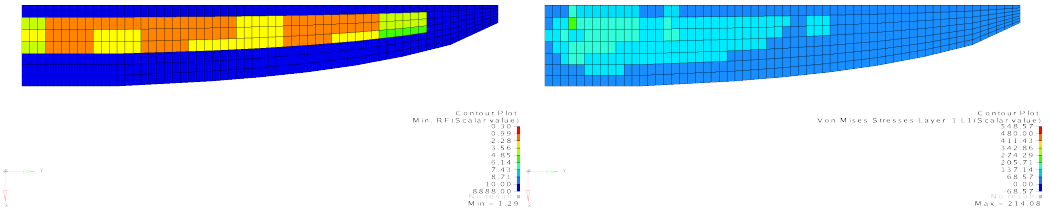

(a) Buckling reserve factor, all load cases (b) Von Mises stress, pull-up load case

Fig. 4.19: Structural constraint evaluation of induced drag optimization with structural constraints

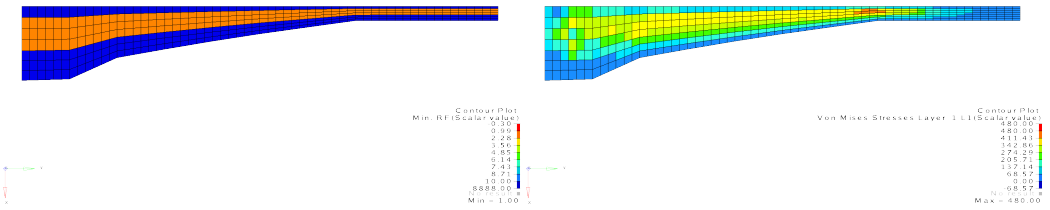

(a) Buckling reserve factor, all load cases (b) Von Mises stress, pull-up load case

Fig. 4.20: Structural constraint evaluation of structural mass optimization with structural constraints

In Fig. 4.19 one can see that stress and buckling constraints are uncritical in the induced drag optimization result ($R_{min} = 1.29$ and $\sigma_{max} = 214\,\text{MPa}$) as suggested before. All in all, most constraints are far from being active or violated, which shows that this design has significant material reserves. However, since the objective function did not contain any mass dependency, induced drag and structural constraints were considered by the optimizer without their influence on the weight of the model.

Fig. 4.20 shows the constraint evaluation of the FE mass optimization result where all structural constraints were satisfied with many of them being active ($\approx$500). Here, the buckling constraints have reserve factors of $R = 1.0$ and slightly above, while the maximum von Mises stress for the worst load case (pull-up) is limited to the stress allowable of $\sigma_{max} \leq 480\,\text{MPa}$. This shows that the structural reserves were exhausted by the optimizer, as FE mass and stress

or buckling constraints usually have inherently opposite gradients. A stress peak can be seen in the skin of the wing near the trailing edge kink where the chord length is reduced to the minimal gage. Comparing this to the structural displacement plot in Fig. 4.18 shows that this is the location with the most strain in the structure because the region between wing root and almost 50 % half span has been stiffened to an extent that it has almost no displacements. Therefore, the main deformations appear outboard of 50 % semi-span.

Table 4.8: Summary of induced drag shape optimization with structural constraints

	Initial	Final	Delta %
FE Mass [t]	0.5333	0.5119	-4.02
elastic C_L	0.7787	0.7772	-0.20
elastic $C_{D_{ind}}$	0.0153	0.0144	-5.84

Table 4.9: Summary of FE mass shape optimization with structural constraints

	Initial	Final	Delta %
FE Mass [t]	0.5333	0.1640	-69.25
elastic C_L	0.7787	0.7803	+0.21
elastic $C_{D_{ind}}$	0.0153	0.0198	+29.41

Table 4.8 shows a summary of the induced drag shape optimization with structural constraints. Comparing these values to the previous unconstrained optimization (Table 4.5) reveals that both optimizations virtually found the same result. Only a very slight difference in structural mass can be seen. This shows again that the addition of structural constraints had almost no effect on the induced drag optimization, since the structure was not critical in this design. As the final values for the induced drag coefficient are the same as for the unconstrained shape optimization, the optimizer still managed to find the theoretical optimum for this objective function (see Section 4.1.3.1) while considering the structural constraints.

The main difference between the FE mass optimization results in Tables 4.9 and 4.6 is the weight savings, which were limited by the structural constraints as expected. The induced drag increase through these changes was worse with structural constraints than without. This mainly had the reason that the lift distribution of the triangular planform deviates further from the elliptic ideal than the lift distribution of the rectangular planform which resulted from the unconstrained optimization.

All in all, one can say that the addition of structural constraints caused the expected effects. The induced drag optimization was not significantly influenced, simply because the design was structurally well feasible and because no objective or constraint gradient caused the optimization to move towards a structurally critical point in the design space. The FE mass optimization, on the other

hand, exhibited substantial differences, which could be physically explained. Thus, the addition of structural constraints enabled finding structurally feasible designs while minimizing the objective function value. The measures taken by the optimizer to satisfy the structural constraints, if necessary, showed the physically sound behaviour of the developed shape optimization framework.

4.1.3.3 Aeroelastic Versus Rigid Shape Optimization

In this section, the validity and benefits of considering aeroelastic effects during shape optimization is discussed. This was done by assessing the differences in shape optimization results that were conducted with and without aeroelastic analysis. Therefore, two shape optimizations, one with aeroelastic analysis, the other applying only rigid aerodynamic loads (no consideration of structural displacements for load calculation), were compared. As a basis for this comparison, the rectangular wing model that was already used in the previous sections was studied. However, due to its planform and internal structure, the aeroelastic effects on this model were very small. Thus, in order to increase the aeroelastic effects to a more significant level, the wing was swept forward by $-10°$ (cf. Fig. 4.21). This caused a stronger coupling between bending and torsion of the wing so that bending of the wing due to lift caused notable changes in elastic angle of attack, which in turn affected the aerodynamic loads on the structure [BAH96, pp. 474-475]. Apart from the added sweep angle, no other changes were made, and since the shape parametrization available through the CPACS definition was used to apply the sweep angle change, none of the involved analysis models required regeneration or re-meshing.

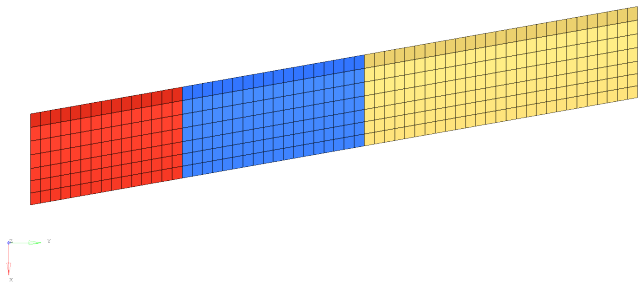

Fig. 4.21: Top view of forward swept wing FE model

For the following comparison, induced drag was chosen as objective function, since it can have a strong sensitivity to aeroelastic effects [WDD00]:

$$f(\mathbf{x}) = C_{D_{ind}}(\mathbf{x}) \tag{4.4}$$

The design variable definition in Table 4.10 shows that only twist and trimming variables were applied in this case. The reason for this was to have only little influence on the structural stiffness of the model while changing the aerodynamic behaviour through shape design variables. This would alleviate comparing the obtained results.

Only trimming constraints were used for the following optimizations so that the optimizer would purely focus on the solution to the objective function without

Table 4.10: Design variable definition for rigid/aeroelastic comparison

Design Variable x	Lower Bound x_{lb}	Upper Bound x_{ub}
Shape		
Twist x_{t_i}	$-10°$	$10°$
Trimming		
α Scale Factor x_α	-50	50

interference of structural constraints. Therefore, no structurally design driving load cases were required and only the cruise load case was simulated (see Section 4.1.1.2). The trimming constraints used in both cases were required to achieve the adequate aerodynamic forces for the 1 g cruise flight. In case of the aeroelastic optimization, trimming was applied to the aeroelastic forces (including effects of structural elasticity), while the rigid aerodynamic forces were trimmed for the rigid optimization in order to simulate the same flight state in both optimizations.

$$\mathbf{g}(\mathbf{x}) = \mathbf{g}_{trim}(\mathbf{x}) \leq 0 \tag{4.5}$$

Usually during the aeroelastic analysis, loads are calculated according to Eqs. (3.2) and (3.3). By eliminating the displacement dependent term from the aerodynamic boundary condition in Eq. (3.3), the rigid analysis with realistic aerodynamic loads using the provided AIC matrices was enabled:

$$\mathbf{b}_c = \mathbf{b}_{c_{state}} + \mathbf{b}_{c_{shape}} \tag{4.6}$$

Thus, the rigid aerodynamic loads were trimmed applying the trimming design variable on the flight state boundary condition component $\mathbf{b}_{c_{state}}$ accounting for changes to $\mathbf{b}_{c_{shape}}$ caused by the twist shape variables. Apart from this adjustment in the load calculation, the rest of the aeroelastic analysis theory remained unchanged. The modification above was only required for the rigid optimization case, the aeroelastic optimization used the original equations introduced in Section 3.2.

Both optimizations converged according to the KKT condition after 18 (rigid) respectively 20 (aeroelastic) iterations.

The general twist distributions of both results (see Fig. 4.22) show how the optimizer accounted for the effects of the forward swept wing by reducing the angle of attack near the wing root, as such a sweep angle usually causes lift accumulation near the wing root (see e.g. [KP01, p. 348]). Fig. 4.22 also shows that both results have a very similar twist distributions only that the aeroelastic solution is shifted slightly outboard having lower values near the wing root and higher twist near the tip.

The result of the rigid shape optimization was frozen and re-analysed with aeroelastic evaluation (see Fig. 4.23a) in order to determine the effects of elasticity on the found design. One can see that the rigid lift distribution (thin green line) matches the rigid ideal ellipse very closely (thin dashed blue line). The aeroelastic lift distribution, however, (thick red line) shows two significant deviations. First, it lies above the rigid one, which means that the elastic deformation caused the overall lift to increase, as the forward swept wing has a inherent

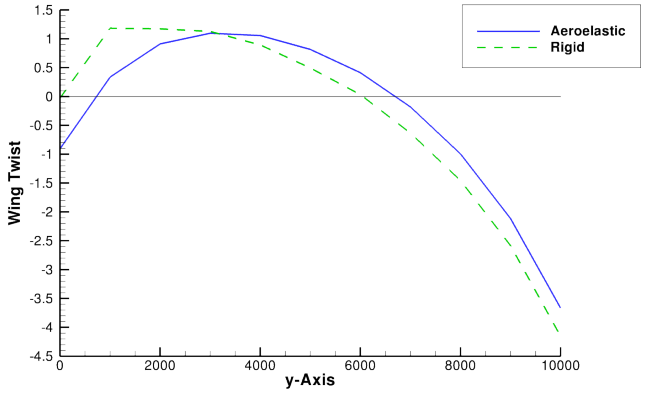

Fig. 4.22: Comparison of resulting twist distributions of rigid/aeroelastic shape optimizations

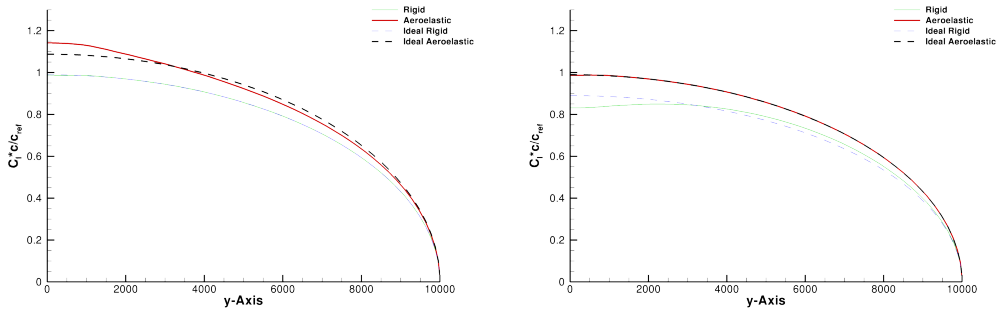

(a) Rigid result

(b) Aeroelastic result

Fig. 4.23: Comparison of resulting spanwise lift distributions

tendency for lift increase [BAH96, pp. 474-475]. Second, through elastic effects the red line deviates perceptibly from its ideal elliptic distribution (thick dashed black line). This would still be the case, if the model were trimmed back so that the aeroelastic overall lift matched the target lift for cruise. Furthermore, since a twist distribution only has its full effect for one specific angle of attack [Ray06, pp. 62-63], re-trimming would also worsen the rigid lift distribution depending on how big the changes to α are. Therefore, in a realistic flight state with aeroelastic effects this result would not reach the minimal induced drag value that it shows for the rigid analysis.

In comparison, Fig. 4.23b shows the spanwise lift distribution of the aeroelastic shape optimization result. Here, one can see that the aeroelastic result matches the ellipse, while its rigid lift distribution is lower and deviates from the rigid ellipse. This shows that the aeroelastic shape optimization accounted for the overall lift increase through the wing sweep characteristics, as well as, for the changes in spanwise lift distribution due to elastic deformations. Thus, the optimizer found a solution that only yields the minimal induced drag with aeroelastic effects included and has a worse drag value for the rigid case. Comparing both aeroelastic distributions of the rigid and the aeroelastic shape optimization reveals the effects of the different twist distributions of Fig. 4.22. The lower twist angle near the root of the elastic result causes its rigid distribution to lie below the ellipse in that region. The higher twist value of the rigid optimization result, on the other hand, can be seen in the elastic lift distribution (Fig. 4.23a) being situated above its respective ideal ellipse.

These findings are also visible in the overall coefficients compared in Table 4.11. The values that were considered in the respective shape optimization were printed bold. From this, it becomes obvious that both optimizations found the theoretical minimum with an Oswald factor $e = 1.0$, however, for different flight states. Thus, even though the rigid optimization found the same minimum, the acting aeroelastic effects created a different state deviating from that minimum.

Table 4.11: Comparison of rigid/aeroelastic shape optimization results

	Rigid Result	Aeroelastic Result
Rigid C_L	**0.7772**	0.6989
Aeroelastic C_L	0.8542	**0.7772**
Rigid $C_{D_{ind}}$	**0.014 42**	0.011 71
Aeroelastic $C_{D_{ind}}$	0.017 47	**0.014 42**
Rigid e	**1.000**	0.9955
Aeroelastic e	0.9971	**1.000**

Since under realistic flight conditions aeroelastic effects do occur, they have to be accounted for, which means that the aeroelastic shape optimization provides the more realistic, and thus, better result. For this wing shape, the aeroelastic tendency lift increase was to be expected due to the characteristics of the forward swept wing. However, when shape optimizations modifying the plan-

form of the wing are conducted, the aeroelastic properties of the design may change significantly compared to the initial design. This makes such a prognosis of aeroelastic tendencies impossible. Therefore, aeroelastic analysis should always be included during these kind of shape optimizations.

4.1.4 Optimization Behaviour of the Framework

In order to productively apply the developed shape optimization framework to aircraft engineering problems, its general characteristics needed to be clarified and an appropriate optimization process accounting for them had to be developed. In the following sections studies are conducted in order to improve understanding of the available design space and its effects on the optimization's progress.

4.1.4.1 Influence of Initial Point

A general problem of gradient based optimization algorithms is that they usually converge on a feasible local minimum in the design space close to the initial point. Hence, if the design space is not convex (see e.g. [BSS06, pp. 47-48]) and exhibits a number of local minima, the initial point from where the optimization was started has a significant influence on the solution on which it converges. In order to examine this for the available system responses of induced drag and FE mass, some shape optimizations presented in previous chapters were repeated from different starting points. This should yield a better understanding of the optimization problem at hand and allow devising an optimization strategy.

Induced Drag Regarding the design space connected to the aeroelastic induced drag objective function the shape optimization described in Section 4.1.3.2 was repeated from three different initial points. Hence, the design variables consisted of chord length, trimming and sizing (see Table 4.4). Also the constraints (stress, buckling and trimming) and the objective function were taken exactly as described in Section 4.1.3.2. Therefore, the only difference between the three optimizations was their initial configuration. Table 4.12 shows how the optimizations were distributed over the range of allowable initial chord length values. The first run represents the original run from Section 4.1.3.2, while the second and third run were started with lower and higher initial chord length (constant over span). The initial sizing variable values were the same for all runs. Apart from that, the initial flight state was trimmed for all three optimizations to account for the different wing areas so that the overall lift remained constant throughout the optimizations. In order to allow comparison between the results, the reference area (Table 4.1) for the aerodynamic coefficients was kept the same as in the previous examples.

All optimizations except run #2 converged according to KKT within the allowed 80 iterations. Therefore, the second run was restarted to see whether convergence could be reached. It continued for an additional 10 iterations without notable changes to the design variable values and then converged complying to KKT as well. The Tables 4.13 and 4.14 provide a comparison of the three found

Table 4.12: Initial points for induced drag shape optimizations

	Initial Chord Length
Run #1	1500 mm
Run #2	1000 mm
Run #3	1700 mm

results. Looking at the drag values it becomes obvious that all three optimizations found the same result, however, the different FE masses show that this result was reached by different designs. For this configuration it was shown in Section 4.1.3.1 that this induced drag value represents the theoretical optimum. Thus, it was possible to find this minimum from all considered starting points, yet with different configurations.

Table 4.13: Structural mass comparison for induced drag starting point study

	Initial Mass [t]	Final Mass [t]	Delta %
Run #1	0.5333	0.5119	-4.02
Run #2	0.3572	0.4638	+29.84
Run #3	0.6048	0.5047	-16.56

Table 4.14: Aeroelastic coefficient comparison for induced drag starting point study

	Initial C_L	Final C_L	Initial $C_{D_{ind}}$	Final $C_{D_{ind}}$	$C_{D_{ind}}$ Delta %
Run #1	0.7787	0.7772	0.0153	0.0144	-5.84
Run #2	0.7772	0.7772	0.0158	0.0144	-8.78
Run #3	0.7773	0.7772	0.0151	0.0144	-4.62

The resulting chord length distributions of all three optimization runs are plotted in Fig. 4.24 together with an ellipse manually fitted through the points of the results (dashed green line). Thus, as expected the results matched an elliptic planform shape very closely generating the elliptic lift distribution. Yet, they all converged with different average chord length values. The reason for this was the included trimming variable that was used during the optimizations to guarantee a trimmed flight state with constant overall lift loads. As the current wing area has a significant influence on the generated lift, the trimming variables were adjusted by the optimizer to satisfy the trimming constraints and keep the overall lift constant. This caused the optimization problem to become non-convex [BSS06, p. 47], since theoretically an infinite number of combinations between trimming variable and wing area (all with elliptic chord length distribution) exists that yields the same lift and induced drag coefficients. In this case, the local optima were also global optima because all of them reached the theoretically minimal induced drag (see Section 4.1.3.1) through an elliptic lift distribution.

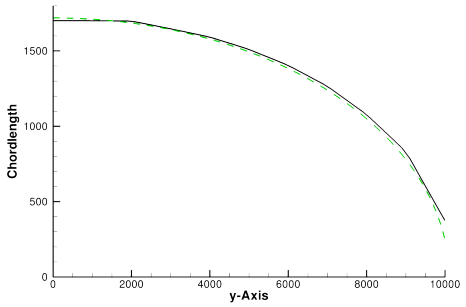

(a) 1st run

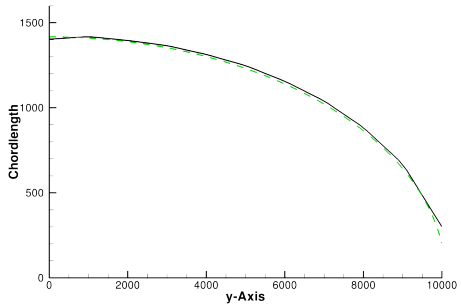

(b) 2nd run

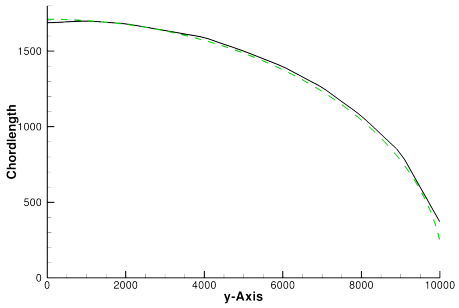

(c) 3rd run

Fig. 4.24: Final chord length distributions of induced drag optimizations with different initial points

To further explore this effect, the relation between wing area and trimming variable value was studied. Therefore, assuming linear dependency between trimming variable and lift force with negligible aeroelastic non-linearities for this model, the product of trimming variable and current wing area should be constant. This was compared in Table 4.15.

Table 4.15: Wing area/trimming variable relation of starting point study results

	Run #1	Run #2	Run #3
Current wing area S	$1.376 \cdot 10^{+7}\,\mathrm{mm}^2$	$1.135 \cdot 10^{+7}\,\mathrm{mm}^2$	$1.370 \cdot 10^{+7}\,\mathrm{mm}^2$
Trimming variable x_α	8.6590	10.2128	8.6913
$x_\alpha \cdot S$	$1.192 \cdot 10^{+8}\,\mathrm{mm}^2$	$1.159 \cdot 10^{+8}\,\mathrm{mm}^2$	$1.190 \cdot 10^{+8}\,\mathrm{mm}^2$
Delta w.r.t. Run #1	-	$-2.77\,\%$	$-0.17\,\%$

It becomes obvious that the difference in value of this product between the three runs is less than 3 %. These differences may come from aeroelastic effects that cause the dependency between trimming variable and lift to be non-linear. However, this shows that the optimizer established a similar relation between the trimming variable value and the current wing area in three independent optimization runs obtaining the same induced drag value.

From an engineer's point of view this simply describes the process of trimming different wing designs to a target lift, yet, for the optimization algorithm this creates a design space with an infinite number of minimal solutions that

feature the same objective function value creating this initial point problem. For practical applications a number of limiting factors come into play so that the theoretically infinite range of possible combinations between wing area and trimming variable is narrowed down. First, the applied structural constraints prevent designs with a too slender planform shape, because, at a certain point, the constant root bending moment cannot be supported any more. But also other aspects such as stall characteristics, wetted wing area or control surface requirements would limit the number of applicable solutions to this problem further. Additionally, in aircraft design the planform area is usually deducted from certain top level requirements and may not be changed by a great margin so that only few designs would comply with that.

In summary, a multi-modal behaviour of the induced drag design space was found for the combination of chord length and trimming design variables. The theoretically infinite number of optima is, however, reduced by practical considerations and design requirements. In order to guarantee constant overall lift during the shape optimizations this parameter combination cannot be prevented in most cases. Therefore, this effect on the induced drag design space has to be kept in mind and addressed where necessary.

FE mass Exactly the same study using the initial points defined above in Table 4.12 was repeated with FE mass as objective function instead of induced drag. Again, the result for the first run was taken from Section 4.1.3.2.

One major difference to the previous initial point study was the number of iterations each optimization took, since none of them converged according to KKT within the maximum number of 80 iterations. Therefore, all three shape optimizations were restarted for another 80 iterations (160 in total). After the restart they still did not converge according to KKT, however, due to the small changes in the objective function, the optimizations were not restarted any further. Hence, the results after 160 iterations are compared in the following. In this case, the two additional results looked very similar to the one found in the first run in Section 4.1.3.2. Yet, this time they also have a very similar chord length distribution (including average chord length) in contrast to the induced drag findings. These final chord length distributions of all three optimization runs are shown in Fig. 4.25.

Comparing the three chord length distribution results reveals that almost the same design was found by all runs. Only the root chord length exhibits small differences between the results. This may be caused by the way of mounting the wing (see Section 4.1.1.1), which causes only small loads on the wing root and thus low gradients, so that adjustments to that shape variable are less strongly driven than the other stations. The values compared in Tables 4.16 and 4.17 also support that approximately the same design was found.

The tables show that all three results have final FE masses and aeroelastic induced drag coefficients with less than 0.2 % and 1.0 % variation respectively. Especially since induced drag was not regarded in any way during these optimizations, planform shape and aeroelastic behaviour must be really similar for all three to achieve this kind of agreement.

In summary, no such multi-modal behaviour as with the induced drag ob-

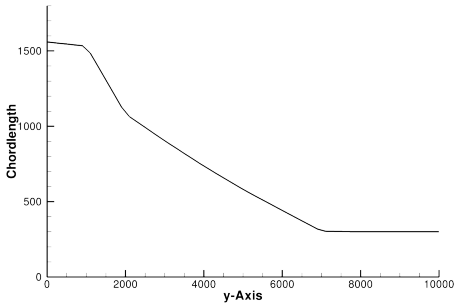

(a) Run #1

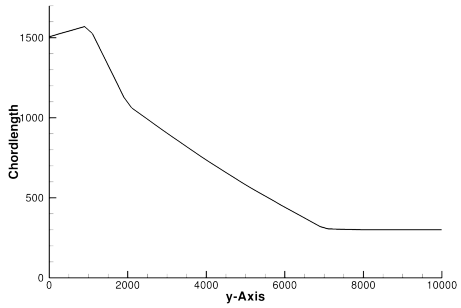

(b) Run #2

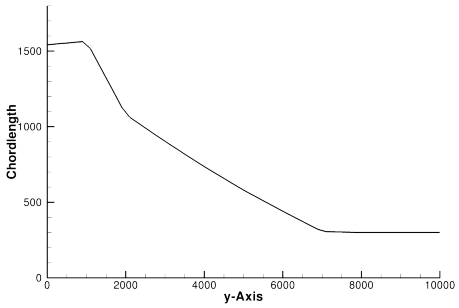

(c) Run #3

Fig. 4.25: Final chord length distributions of initial point study with mass objective

Table 4.16: Structural mass comparison for FE mass initial point study

	Initial Mass [t]	Final Mass [t]	Delta %
Run #1	0.5333	0.1640	-69.25
Run #2	0.3572	0.1643	-54.00
Run #3	0.6048	0.1642	-72.85

jective could be found with the FE mass objective function for the considered design variables. All optimizations independently managed to find the same solution to the given problem starting at different points in the design space. This shows a significantly different behaviour of the FE mass design space compared to the findings for the induced drag objective before.

4.1.4.2 Convergence Characteristics

As significantly different convergence behaviour could be witnessed in the shape optimizations that were conducted up to this point, a study of these differences and their causes was conducted.

Generally, the conducted induced drag optimizations were able to find a solution that fulfils the Karush-Kuhn-Tucker condition (KKT, see Section 2.2.5), whereas the attempts with an FE mass objective exhibited difficulties satisfying the KKT with the default precision of 10^{-6}. In Table 4.18 the different shape optimizations conducted up to this point are listed together with their required

Table 4.17: Aeroelastic induced drag comparison for FE mass initial point study

	Initial C_L	Final C_L	Initial $C_{D_{ind}}$	Final $C_{D_{ind}}$	$C_{D_{ind}}$ Delta %
Run #1	0.7787	0.7803	0.0153	0.0198	+23.53
Run #2	0.7772	0.7772	0.0158	0.0196	+24.05
Run #3	0.7773	0.7772	0.0151	0.0197	+30.46

number of iterations to convergence according to KKT, as well as, the number of active constraints at the initial and final state of each optimization.

All optimizations in Table 4.18 reached convergence according to KKT in the shown number of iterations except the ones marked with ">", which were terminated manually after that amount of iterations. As expected, the addition of structural constraints increased the necessary number of iterations to KKT convergence, due to the gain in complexity of the optimization problem (see Section 2.2.5). In case of the induced drag objective, only a slight increment in iteration numbers could be witnessed, however, for the FE mass objective the required number of iterations was raised significantly so that none of the mass optimizations could satisfy the KKT within 160 iterations. Apart from this, the difference in iterations between aeroelastic and rigid analysis of the forward swept wing during shape optimizations was insignificant. Since the KKT condition uses a weighted sum of active constraint gradients and the objective function gradient to determine convergence, fulfilling this criterion becomes more complex with increasing number of active constraints (see Section 2.2.5).

The rightmost two columns of Table 4.18 show the number of active constraints at the beginning and the end of each shape optimization. Comparing these values with the number of iterations until convergence supports the statement of longer optimization durations with higher number of active constraints. For example, the induced drag run #2 had a significantly increased number of active constraints at its initial and final point compared to its two corresponding optimizations at different starting points. This roughly doubled the amount of required iterations relative to the other two optimizations. Also, the three shape optimizations minimizing FE mass from the initial point study show the highest number of active constraints in their final states so that none of them managed to fulfil the KKT within 160 iterations. The remaining optimizations in this table only included trimming constraints so that no change in active constraints over the course of the optimizations could be seen.

These numbers also reveal some general tendencies of the different applied objective functions. As one can see in the induced drag optimizations, no clear connection between the active constraints at the beginning and end of an optimization could be established. The optimizations with FE mass objective, on the other hand, always raised the number of active constraints along their progress independently of the initial state. The reason for this is that, in simplified terms, removing mass from a model makes the structure more prone to failure while adding mass in the correct places strengthens the structure and allows satisfying structural integrity requirements. In the context of optimization, this means that the FE mass objective normally has a gradient pointing in the op-

Table 4.18: Numbers of iterations to convergence

Optimization	Objective	Design Variables	No. of Iterations	Initial active constraints	Final active constraints
No structural constraints	$C_{D_{ind}}$	Chord, trim	35	2	2
No structural constraints	m_{FE}	Chord, trim	27	2	2
Constrained Run #1	$C_{D_{ind}}$	Chord, sizing, trim	48	37	18
Constrained Run #2	$C_{D_{ind}}$	Chord, sizing, trim	89	465	42
Constrained Run #3	$C_{D_{ind}}$	Chord, sizing, trim	39	17	24
Constrained Run #1	m_{FE}	Chord, sizing, trim	> 160	37	716
Constrained Run #2	m_{FE}	Chord, sizing, trim	> 160	465	711
Constrained Run #3	m_{FE}	Chord, sizing, trim	> 160	17	712
Forward swept	$C_{D_{ind}}$	Twist, trim	20	2	2
Forward swept, rigid	$C_{D_{ind}}$	Twist, trim	18	2	2

posite direction as the structural constraint gradients (discussed more in detail in Section 4.2.2.2). Therefore, when minimizing FE mass, more and more structural constraints become active as the material reserves are diminished by the optimizer up to the point where the structure becomes critical. Yet, the induced drag objective does not have this inherent behaviour in correlation with structural constraints (see Section 4.2.2.2), as it does not necessarily reduce FE mass during the optimization. Therefore, with induced drag it mainly depends on the initial point of the optimization whether more or less structural constraints become active along the iterations.

One approach to the different convergence behaviour between the different objective functions, could be to adjust the KKT precision value depending on the objective function type. With this, however, the ability to compare the results of different optimizations would depend on the current epsilon settings. Therefore, for the following shape optimizations a maximum number of iterations (e.g. 80) after which the optimization is terminated automatically was set. This way, optimizations that did not manage to satisfy the KKT conditions within this number of iterations could be examined manually by studying the iteration history in terms of changes to objective function or design variable values, as well as, active constraints. Depending on this, optimizations could be restarted, if the history suggested further possible improvements, otherwise convergence would be assumed regardless of the unsatisfied KKT condition.

4.2 Developing a Process for Aeroelastic Shape Optimization

There exist numerous ways of applying the developed aeroelastic shape and sizing optimization framework to the problem of aircraft development. However, not every design that represents a minimum for the optimization algorithm necessarily has to prove as a good design candidate for further development. Therefore, a procedure of applying the developed optimization approach to aircraft development problems was identified in the following sections that yields the most promising wing designs for further development. Along this course, the questions of which objective function and which combination of design parameters to use, as well as, the general way of approaching such optimization problems were covered.

4.2.1 Achieving Useful Wing Designs

Before deriving an optimization procedure for aircraft development, an understanding of what characteristics distinguish a *useful* wing design had to be established. Once the key properties of a design had been identified, the aeroelastic shape optimization problem could be formulated in a way that would produce results with good performance in these fields. Table 4.19 provides an overview of general wing characteristics without the claim of completeness. The different properties were classified from an engineer's point of view into

fixed requirements that need to be satisfied and features that need to be as good as possible.

Table 4.19: Performance characteristics of a wing

Property	Requirements
Structural mass	As good as possible
Aerodynamic lift	
Aerodynamic drag	
Structural integrity	Must satisfy
Aeroelastic effectiveness	
Flutter behaviour	
Gust response	
Flight mechanical stability	
Modal requirements	
etc.	

Among others, the elements gathered in Table 4.19 need to be considered during the development of an aircraft wing. The ones marked with *Must satisfy* are necessary for the wing to reliably and safely perform its task. The features provided with the attribute *as good as possible* assess the performance of a wing design. Translating this into the logic of numerical optimization means that the first group of characteristics (*as good as possible*) would be considered as objectives, which are to be minimized or maximized, while the second group can be realized by constraints which guarantee the functionality of the wing (*must satisfy*).

Therefore, structural mass, aerodynamic lift and drag were selected as system responses for the objective function. The aerodynamic lift has a special role in this context, as wings usually are designed to have good properties at a specific lift coefficient that is derived from a flight state. Hence, aerodynamic lift was not considered as an objective function, since it is prescribed by flight mechanics. Regarding aerodynamic drag, only the lift dependent component of the overall drag (see Section 2.1.2) were considered in this thesis. The lift independent viscous drag component was estimated before and after the optimizations using semi-empirical methods (see Section 2.1.2.4).

The structural mass, on the other hand, is driven by requirements on structural integrity and represents a very central property that influences most of the other design disciplines. Usually a trade off between aerodynamic demands and structural mass has to be found during aircraft development. Thus, structural mass and induced drag were selected as a promising combination for possible shape optimization objective functions. However, in order to measure and compare the results assessing the found trade-offs, a performance or quality criterion needed to be specified.

4.2.1.1 Measuring the Quality of a Wing Design

After a shape optimization has concluded the resulting design needs to be reviewed and possibly compared to other results regarding its quality or performance. For this, a way of measuring its quality was required so that promising designs could be identified. As seen in Section 4.1.3, separate consideration of induced drag or structural mass would not yield useful engineering results. Especially due to the fact mentioned before that a trade off between aerodynamic (i.e. lift, drag) and structural (i.e. mass, stress etc.) requirements usually has to be performed during aircraft development, the quality of a wing design cannot be determined by looking only at one discipline or the other. Therefore, a way of combining these properties into one quality measure needed to be devised.

Because of the very different effects changes in structural mass or induced drag have on a wing's performance, the exact combination of these quantities in a single measure had great influence on its conclusions. Depending on the weighting of the two system responses the criterion's preference might change from one design to another. Hence, a method of equally representing the effects of drag and mass was sought. Finally, the Breguet range equation (Eq. (3.38)) was selected as a measure of performance for the different shape optimization results. This function is often used for multidisciplinary design optimizations of aircraft configurations [e.g. IM01; GKC+12; GBM+10; HML12; JPM10; KKM12; Wun13]. The great advantage of this formulation was that it puts drag and mass into a physically meaningful relation by providing a flight range for a given mission. Furthermore, this equation is frequently used at early aircraft design phases such as the conceptual design and, thus, represents a relevant performance attribute of an aircraft.

$$R_{Br} = \frac{v}{g\ TSFC} \cdot \frac{C_L}{C_{D_{ind}} + C_{D_0}} \cdot ln\left(\frac{m_{init}}{m_{final}}\right) \qquad \text{(3.38 revisited)}$$

Design Mission Profile In order to calculate the Breguet range of an aircraft for a realistic mission, a mission profile including all segments of the mission needed to be specified. The mission profile chosen for this was the ferry range of the aircraft (see Fig. 4.26). This means the aircraft takes off, climbs to cruise altitude, travels as far as it can go, then descends and lands with the last of its fuel. As the mission profile was only used to provide the Breguet range as a quality measure for wing designs, this basic profile was chosen in lack of any detailed information on the purpose of the developed aircraft. Usually a design mission is generated at the beginning of development, which can replace the chosen mission profile here. The mass of fuel burnt in each segment of the mission was estimated using the fuel fraction method (see e.g. [Ray06, p. 18]). The corresponding fuel mass fractions for this mission are given in Table 4.20 using the numbering provided in the mission profile. During the cruise leg, a constant lift coefficient was assumed so that the aircraft gradually climbs to higher flight levels while loosing weight due to fuel burn.

The Breguet equation was used to estimate the range of the cruise leg (segment 5 in Table 4.20). Among other values, such as the flight velocity v, the

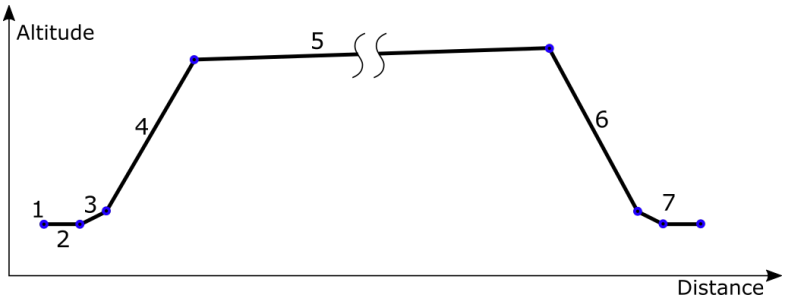

Fig. 4.26: Mission profile for the Breguet range design mission

Table 4.20: Breguet Mission Segments (taken from [ET14])

No.	Segment	Mass Fraction ψ_{m_i}
1	Start & Warm-up	0.990
2	Taxi	0.995
3	Take-off	0.995
4	Climb	0.985
5	Cruise	$\frac{m_{final}}{m_{init}}$
6	Descent	0.985
7	Landing & Taxi	0.995

thrust specific fuel consumption $TSFC$ and the viscous drag coefficient C_{D_0}, the mass fraction of the aircraft mass at the beginning and end of the cruise segment is required in Eq. (3.38). Using the data in Table 4.20 the masses in this fraction were derived:

$$\begin{aligned} m_{init} &= m_{MTOM} \cdot \prod_{i=1}^{4} \psi_{m_i} \\ m_{final} &= \frac{m_{ZFM} + m_{FE}}{\psi_{m_6} \psi_{m_7}} \end{aligned} \tag{4.7}$$

For this, the mission was assumed to start with the maximum take-off mass m_{MTOM} and the fuel mass fractions ψ_{m_i} of Table 4.20 were applied up to the beginning of the cruise mission leg. The mass at the end of the whole mission was defined to be the sum of the structural wing FE mass m_{FE} and the zero fuel mass m_{ZFM}, which includes all structures that were not represented in the FE model, as well as, the systems and payload masses. These values were taken from Table 4.1 accounting for the fact that only the right half of the aircraft was represented in the models.

Assumptions Some assumptions were required to calculate the Breguet range for this aircraft configuration. These values are summarized in Table 4.21. The flight velocity v was calculated from the cruise load case described in Section 4.1.1.2. With some additional assumptions about the outer aircraft geometry, the semi-empirical Friction program (see [Mas02], Section 2.1.2.4) was used to estimate the viscous drag coefficient C_{D_0} for this flight state. Regarding the

thrust specific fuel consumption, however, no actual data was available so that a value was assumed using data on similar UAV types. As the Breguet range was used only for rating the different optimization results, the precision of the absolute range values that were affected by these assumptions were not of significant interest in this application. Since these quantities were kept constant for all conducted optimizations, they had no influence on the comparison data.

Table 4.21: Data for Breguet range mission of the half model

Parameter	Value	Unit
v	86.8	$\frac{\mathrm{m}}{\mathrm{s}}$
$TSFC$	$1.41 \cdot 10^{-5}$	$\frac{\mathrm{kg}}{\mathrm{Ns}}$
C_{D_0}	0.013	1
g	9.81	$\frac{\mathrm{m}}{\mathrm{s}^2}$

Hence, the remaining values of $C_{D_{ind}}$, C_L and m_{FE} required for evaluation of Eqs. (3.38) and (4.7) were taken from the aeroelastic analysis in the shape optimization framework. This means, the Breguet range was influenced during the shape/sizing optimizations through the resulting aeroelastic induced drag and the structural mass. The aerodynamic lift coefficient did not have a significant influence, because it was trimmed to stay constant. Hence, the Breguet range could be directly calculated for the resulting system responses of the aeroelastic shape optimizations providing a quality measure to the current design.

4.2.1.2 What Objective Function Leads to Useful Wing Designs?

It was already stated in the previous section that at least induced drag, as well as, structural mass should be considered simultaneously when attempting to find useful wing designs. The main reason for this is that these two properties usually represent conflicting interests that have to be brought into agreement. Therefore, an objective function for shape optimization devised to drive the optimizer towards wing designs with a good performance measure would also have to include these two system responses. Thus, the question of how to formulate an objective function that leads to wing designs with good performance features had to be solved.

Since the Breguet range was decided to function as a quality measure, the obvious choice would be to use this equation as an objective function as well. However, as a numerical optimization algorithm is applied to the objective function, additional considerations about the mathematical complexity and the numerical good nature of the objective function had to be taken into account. Otherwise, issues with many local minima or simply slow optimization progress could become a problem. Hence, different ways to formulate an objective function using a combination of induced drag and FE mass were studied. The goal was to find a numerically good natured objective function leading to physically useful results.

The first most straight forward possibility was a weighted sum between induced drag and FE mass (see Section 3.5.3). From a numerical point of view this

had the advantage of having a simple combination of the two system responses, which would not add additional numerical complexity beyond the separate system response's levels. Yet, one issue with this method was finding the appropriate weighting factors that would produce useful wing designs with a good performance measure. However using this objective function formulation allows studying the gradual differences on the resulting designs when shifting the weightings between the components enabling a better understanding of the optimization problem at hand.

Additional to the first formulation, a version of the Breguet range equation as described in Section 3.5.4 was studied as well. Here, no appropriate weightings would have to be determined, since they were inherently included in the formulation of the Breguet equation. On the other hand, the mathematically complex formulation using logarithms and quotients could cause numerical problems as the design space generated by it was difficult to predict. With this formulation, agreement between design space and assessment criterion could be ensured.

Objective function comparison In order to evaluate the differences in objective functions and their respective results, several shape optimizations with changing objective function definitions were conducted. The goal was to find the objective function formulation that produces the wing design with the best performance suitable for further development. For this, the optimization problem was defined analogue to the previous *single objective* runs discussed in Section 4.1.3.2, only adding the wing span shape variable for additional design freedom. Thus, the CPACS sections were used to define 11 chord length shape variables together with the wing span of the entire wing, which were combined with sizing and trimming variables as specified in Table 4.22.

Table 4.22: Design variable definition for objective function study

Design Variable x	Lower Bound x_{lb}	Upper Bound x_{ub}
Shape		
Chord Lengths x_{c_i}	300 mm	1700 mm
Wing half span x_s	8000 mm	15 000 mm
Sizing x_{Size}		
Skin	0.8 mm	8.0 mm
Stringer	50 mm^2	200 mm^2
Spar Caps	100 mm^2	500 mm^2
Trimming		
α Scale Factor x_α	-50	50

$$\mathbf{g}(\mathbf{x}) = \begin{bmatrix} \mathbf{g}_{stress}(\mathbf{x}) \\ \mathbf{g}_{buckling}(\mathbf{x}) \\ \mathbf{g}_{trim}(\mathbf{x}) \end{bmatrix} \leq 0 \tag{4.8}$$

Also, the optimization constraints were included as declared in Section 4.1.1.4. In order to provide design driving loads for the structural criteria all four load

cases defined in Section 4.1.1.2 were simulated. Regarding the objective function, several combinations were studied. The weighted sum objective function (see Eq. (3.36)) was defined with a number of different weightings so that the effects of the weighting on the results could be investigated. These results were then tested against the design of a shape optimization with Breguet range objective function (Eq. (3.39)). Also the single objectives of induced drag and FE mass were included for reference purposes. A summary of all considered objective functions is listed in Table 4.23 including their weightings between the responses.

Table 4.23: Objective function formulations

Objective Function	**Response Combination**	
	m_{FE} Weighting	$C_{D_{ind}}$ Weighting
Induced Drag	-	1.00
	0.10	0.90
	0.25	0.75
	0.40	0.60
Weighted Sum	0.50	0.50
	0.60	0.40
	0.75	0.25
	0.90	0.10
FE mass	1.00	-
Breguet Range	see Eq. (3.39)	

The sets of weighting factors given in Table 4.23 were distributed in this manner, because a more or less balanced solution between FE mass and induced drag was expected to achieve the best performance with respect to the selected quality measure. Thus, the region around equal weighting between the two properties was resolved with finer weighting steps increasing towards the extreme solutions on each side. This approach of distributing the shape optimizations across the weighting range was later verified against the result of the Breguet range objective function. For this objective function the definitions in Section 4.2.1.1 were applied.

In order to simplify notation, the following format of "$xm + yd$" was used to refer to the different weighted objective optimizations with x and y being the respective FE mass and induced drag weightings of Table 4.23 in percent.

Because all eight combined shape optimizations included the FE mass as a system response, the effect of not reaching KKT convergence observed in Section 4.1.4.2 could also be witnessed here. Therefore, all optimizations ran over 80 iterations after which they were stopped automatically without satisfying the KKT convergence criterion. Yet, based on their individual iteration history, the optimizations were considered as converged, since no significant further changes to the design were to be expected at that point.

The resulting planform shapes and skin thickness distributions can be seen in Fig. 4.27. As a reference, the initial planform outline was included as a red box, the maximum allowed wing span was also indicated by a red line.

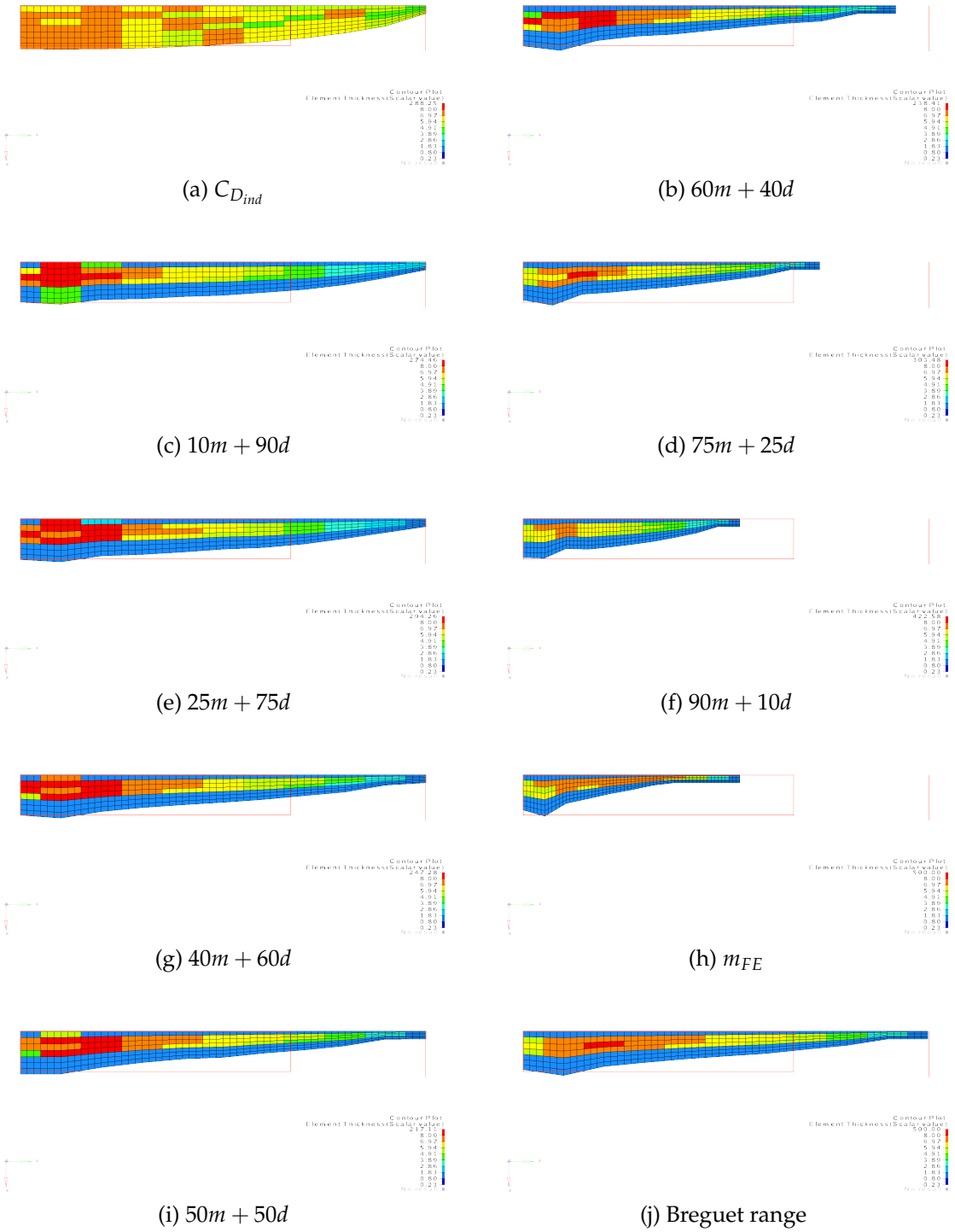

(a) $C_{D_{ind}}$ (b) $60m + 40d$

(c) $10m + 90d$ (d) $75m + 25d$

(e) $25m + 75d$ (f) $90m + 10d$

(g) $40m + 60d$ (h) m_{FE}

(i) $50m + 50d$ (j) Breguet range

Fig. 4.27: Resulting planform shapes and skin thickness distributions of objective function study

One can see in Fig. 4.27 that with high weighting of induced drag all results used the maximum allowed wing span, as it is very effective in reducing induced drag. Starting at weightings of more than 50 % FE mass, the wing span was lowered gradually towards the minimal gage of 8000 mm reached with the FE mass objective. This decreased the FE mass through volume reduction but also allowed lower skin thickness due to a shorter bending moment lever causing less structural load. Apart from the differences in overall wing span, the resulting chord length distributions showed a gradual change from close to elliptic towards a triangular planform with increasing FE mass weighting. This matched the findings of Section 4.1.3.2.

For most results, a lower chord length at the root compared to its adjacent, next outward section could be detected. This was found to be caused by the chosen method of supporting the FE model (see Section 4.1.1.1, Fig. 4.4). Since the mounting reached from the wing root up to the second rib at 500 mm span, the transverse forces were already being reduced outboard of the wing root. Therefore, the root rib had less loads to support making the structure in the area between the mounting points less critical. This allowed lower skin thickness and smaller chord length values at the root, as apparent in Fig. 4.27. Because the nodes involved in the support of the model were also affected by the shape changes, the optimizer exploited this by overly increasing the chord length at the second section to space the mounting of the wing further apart so that any torsional loads on the wing could be better supported. A series of optimizations conducted with an altered mounting approach, which only supported the model at the wing root rib, showed that the maximum chord length was shifted to the root in these cases removing the trailing edge kink.

In Fig. 4.28 the effects on the spanwise aeroelastic lift distributions corresponding to the planform shape changes are presented. With the more and more triangular planform due to higher weighting of the FE mass component, the lift distribution deviated further from the almost elliptic lift distribution of the $10m + 90d$ optimization evolving towards the already mentioned triangular lift distribution. Simultaneously, the wing span was reduced so that the local lift load needed to be increased in order to maintain constant overall lift. This had two effects, first, the induced drag value rose with the increasing deviation from the ellipse and shorter wing span (Fig. 4.29), and second, the lift load was shifted towards the wing root reducing the root bending moment lever. Due to that, the root bending moment was decreased lowering the strain on the structure making further mass savings through the sizing variables feasible.

The result of the Breguet range objective (Fig. 4.27j) showed a similar planform shape as the $50m + 50d$ optimization run. It used the maximum allowed wing span to lower induced drag and adjusted chord length to stay close to the ideal elliptic lift distribution while improving load bearing capabilities for support of the greater span. Since the $60m + 40d$ result already yielded a lower wing span, the planforms were not exactly comparable. However, the relative chord length distribution seemed to match quite closely as well. Because of the very similar planform, the result of the Breguet objective function generated a lift distribution very much alike the $50m + 50d$ design. It showed the lift increase near the root but also followed the ellipse closely. This allowed to find

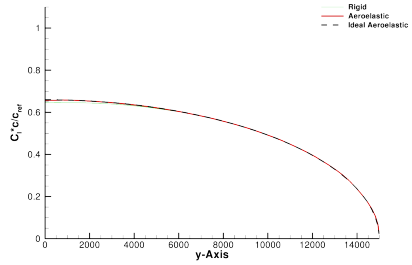

(a) $C_{D_{ind}}$

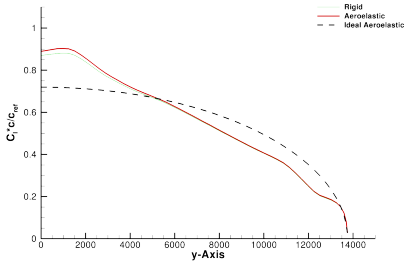

(b) $60m + 40d$

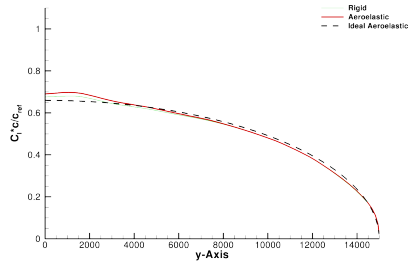

(c) $10m + 90d$

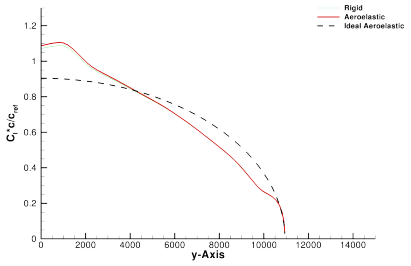

(d) $75m + 25d$

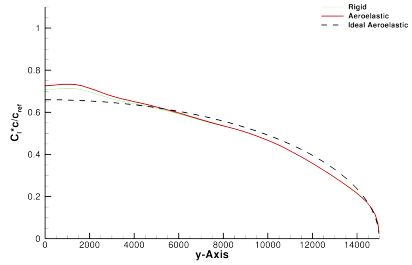

(e) $25m + 75d$

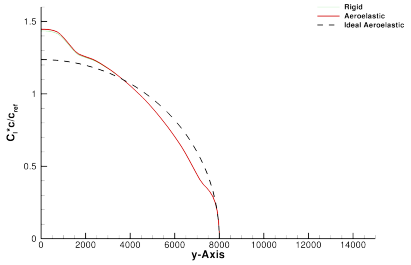

(f) $90m + 10d$

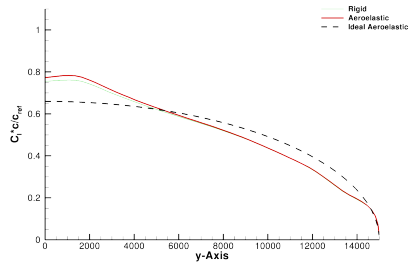

(g) $40m + 60d$

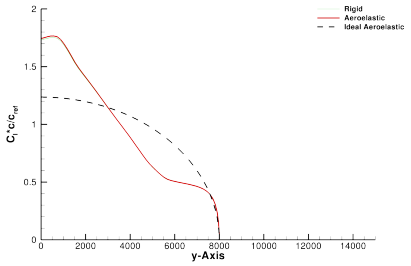

(h) m_{FE}

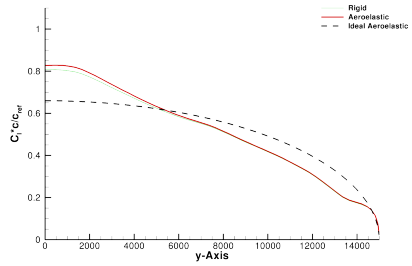

(i) $50m + 50d$

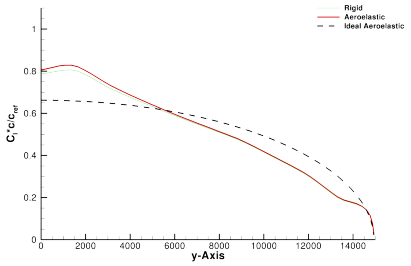

(j) Breguet range

Fig. 4.28: Resulting lift distributions of objective function study

a beneficial compromise between low induced drag generation and mass savings, as the design made good improvements in both responses. This matches well with the findings of Prandtl [Pra33], Jones [Jon50] or Iglesias and Mason [IM01], which showed that the elliptic lift distribution is not the most beneficial solution for a wing, if structural requirements are considered as well. Thus, a deviation from the elliptic lift distribution towards a more triangular one can improve overall performance of the wing.

Thus, the different objective functions produced results with the expected characteristics showing a gradual transition between the two single objective runs. However, from the planform and lift distribution plots alone it was not possible to determine which of these found solutions represented the best wing design for further development. Therefore, the Breguet range performance was calculated for all obtained results.

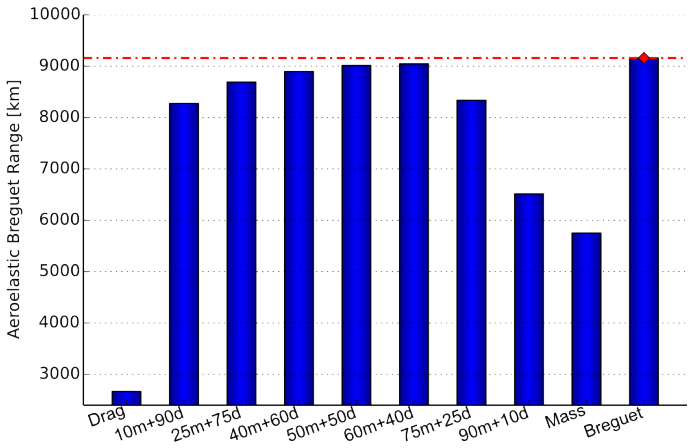

(a) Breguet range

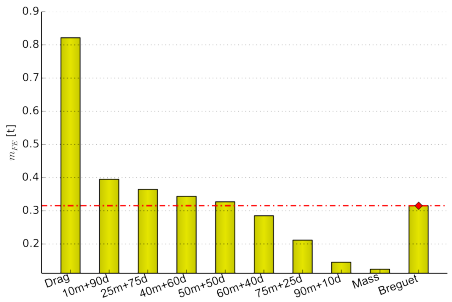

(b) FE mass

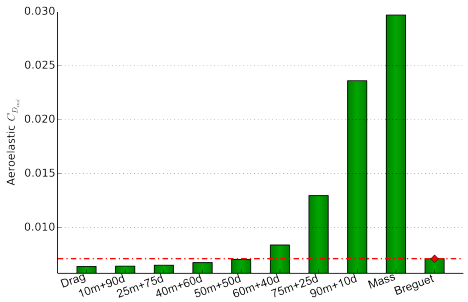

(c) Induced drag

Fig. 4.29: Result quality comparison of objective function study

Fig. 4.29 compares the aeroelastic Breguet ranges and induced drag coefficients as well as the FE masses of the different optimization results. In this case, the shape optimization using the Breguet range objective function achieved the design with the best range performance (highlighted in red). As could be expected from the similar planform geometry and lift distribution, the weighted $50m + 50d$ result closely matched the performance of the Breguet result. However, the $60m + 40d$ result managed to find a design with a range performance

even closer to the Breguet result, although it had an already reduced wing span causing increased induced drag. This was more than balanced by the weight savings due to the lower wing span. Seeing that the best results found by weighted objective functions could be obtained with near equal weighting factors, confirmed the choice of distributing the weighting factors in the way of Table 4.23.

Regarding the single objective solutions, the induced drag optimization obtained the highest FE mass of all examples, while the FE mass optimization resulted in the highest induced drag generation of all optimizations. Considering the aeroelastic Breguet range values of these optimizations revealed that the high FE mass was more harmful to range performance than the high induced drag value, which was also reflected in the better performance of the $60m + 40d$ result compared to equal weighting. In summary, one can say that both optimizations with singular system responses as objectives lead to wing designs with the worst performance regarding Breguet range with slight advantages for the FE mass optimization. This confirmed the previous hypothesis of requiring at least both responses in order to find promising wing designs.

In Fig. 4.30 the aeroelastic induced drag coefficient was plotted over the FE mass for each optimization result. It becomes obvious that a Pareto front (see Section 2.2) is formed by the results through their different weighting factors spanning from the solution of single FE mass to single induced drag. This behaviour is expected for two objectives with opposite gradients requiring a trade-off. The Breguet range optimization result, which also showed the best range performance, is located close to the results with more or less equal weighting between mass and drag. From a numerical point of view all results on the Pareto front are equally good designs only allowing improvement of one property by deteriorating the other. Therefore, the quality measure of the Breguet range performance was used for selecting a design from the Pareto front with the highest potential for engineering application [BSS06, p. 184], which would not have been apparent from the plots alone.

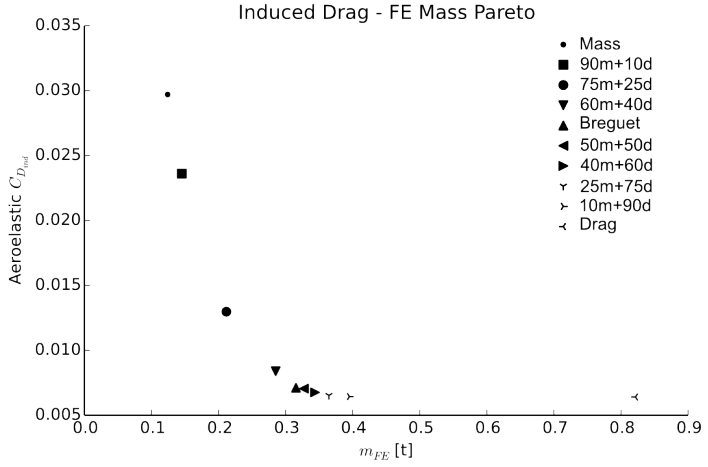

Fig. 4.30: Induced drag/FE mass Pareto plot of objective function study

Conclusion It has been shown through these studies that FE mass, as well as, induced drag need to be considered in the objective function in order to achieve results with good Breguet range performance. Two basic approaches for this were studied; one was to directly use the Breguet range equation in the objective function, the other was to combine the two system responses through a weighted sum. For the examined problems the Breguet range objective function generally managed to find designs with good performance properties. The weighted sum, on the other hand, had the issue of finding the correct weighting factors that correspond to good Breguet range designs. The results closest to the performance of the Breguet design could be obtained for this problem with almost equal weightings slightly leaning towards higher FE mass weighting. Once the beneficial weighting factors were known the weighted sum objective led to promising designs (close to the Breguet results). However, the weighting factor combinations are problem specific so that they have to be determined anew for every optimization problem (e.g. aircraft model).

Therefore, for future shape optimizations it was decided to apply primarily the Breguet range objective function as it led to the designs with the best performance using the same number of iterations. However, since the weighted objective functions could reach designs with similar performance, yet, different planform shape, a number of optimization with changing weightings could be used to verify the result of the Breguet range objective.

4.2.1.3 Influence of Variable Viscous Drag on Results

During the aeroelastic shape optimizations conducted in this chapter only the induced drag component of the aerodynamic drag was considered as variable in the objective function. The remaining drag components of viscous and wave drag were assumed constant. Due to the low Mach number, wave drag was neglected entirely. Yet, the viscous or lift-independent drag coefficient C_{D_0} was initially estimated for the cruise load case using the semi-empirical *FRICTION* program by W. Mason [Mas02] and kept constant for all Breguet range evaluations. However, through the shape optimizations the loft geometry of the wing was altered to a sometimes significant extent also causing the viscous drag coefficient to change which depends on outer shape and wetted area. In order to assess the error that was introduced by the assumption of constant C_{D_0}, all resulting designs of the wing span and chord length optimizations in Section 4.2.1.2 were re-analysed using *FRICTION* to obtain their current C_{D_0} (see Fig. 4.31). The lift independent drag coefficient was estimated for turbulent flow conditions analogue to the initial evaluation, as the Reynolds number for the cruise load case ranged at about $Re = 3.8 \cdot 10^{+6}$, where turbulent flow may be assumed (see e.g. [Ray06]). As a reference the viscous drag coefficient of $C_{D_0} = 0.013$ (Table 4.21) of the initial design was marked in the plot.

With this updated drag information the Breguet range of each design was recalculated. Fig. 4.32 compares the obtained Breguet ranges with constant viscous drag to the ones with updated C_{D_0}. It becomes obvious that the lift independent drag is reduced with increasing FE mass weighting in the weighted objective function falling below the initial value at an FE mass weighting of

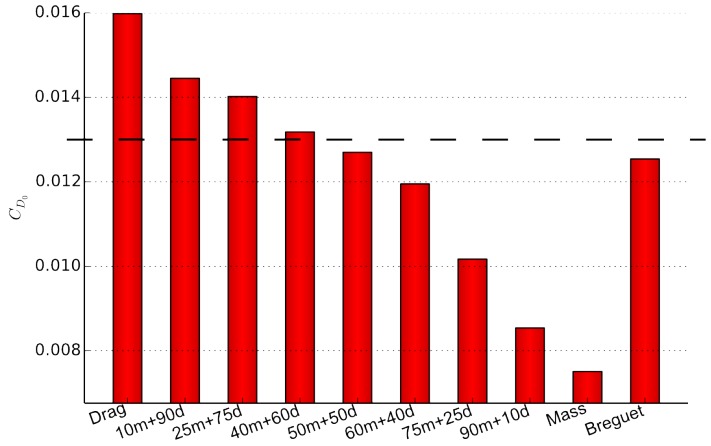

Fig. 4.31: Viscous drag coefficient of wing span & chord length optimization results

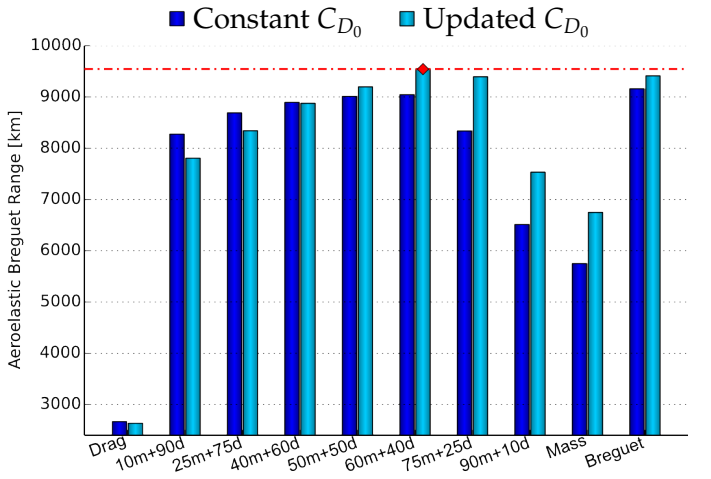

Fig. 4.32: Comparison of Breguet range performance with constant and updated viscous drag

$\geq 50\,\%$, which resulted in increased Breguet range compared to the constant viscous drag performance. This drop in viscous drag is explained by the reduced wetted surface area of the wing due to the tendency of decreasing chord length, as well as, wing span with increasing weighting of structural mass (cf. Fig. 4.27). As the *FRICTION* program uses the wetted area for its estimation of the viscous drag, this surface reduction influences in the resulting viscous drag coefficients.

One can also see that with the updated viscous drag the result obtained through the $60m + 40d$ objective function offered the highest Breguet range performance, while the previously best result of the Breguet objective came in second place. A comparison of the planforms revealed that the reduced wing span of the $60m + 40d$ design reduced the viscous drag component against the Breguet result with maximum wing span.

Summarizing these findings, one can say that the behaviour of the viscous drag coefficient fairly coincides with the selection of objective function for good Breguet range performance. That means with higher weighting of FE mass this drag component was reduced further allowing higher Breguet range performance until the simultaneously increasing drawbacks on the induced drag outweigh these savings. Hence, the previously best results of the Breguet range objective and the $60m + 40d$ weighted objective improved their performance through the updated viscous drag coefficient. Through this, the $60m + 40d$ weighted objective produced the result with the best Breguet range performance. However, this made finding the correct weighting factors for good Breguet range of an arbitrary aircraft model even more complicated as the influence on viscous drag has to be factored into the considerations additionally to effects on FE mass and induced drag. The Breguet objective function result, on the other hand, was reliable to find a good design regarding the combination of FE mass and induced drag and gained additional performance through the lowered viscous drag in most cases. This was identified as a consequence of the Breguet objective function's tendency of producing slender wing planforms making the assumption of a constant viscous drag coefficient conservative. Thus, viscous drag had roughly the same gradient directions as lowering FE mass. In cases where severe increases of wetted surface area could be witnessed the drawbacks on viscous drag could be mitigated by using a geometric constraint limiting the maximum allowed wing area.

Given that *FRICTION* only uses semi-empirical equations that are often employed at early design phases for such estimations, these results need to be verified by higher order aerodynamic analysis methods. However, at the level of fidelity of early design phases the error of assuming constant viscous drag during the shape optimizations could be confirmed to be conservative, as an update in viscous drag resulted in increased Breguet range for the results of the selected objective function. Nevertheless, to assure the performance of a found design a re-analysis of the C_{D_0} coefficient after a shape optimization concluded should be performed to retrieve the current state coefficient.

4.2.2 Application of Shape Design Variables

The shape parameters made available by the model description using the CPACS format and its parametric geometry model were already presented in Section 3.3 (see Table 3.1). In order to have the most effective influence on the aircraft design characteristics with the lowest number of shape design variables, a selection of the most promising shape parameter types was performed (Section 4.2.2.1). After the appropriate shape parameters were chosen to be used as design variables, some issues in applying these in the developed framework were discovered and studied (Section 4.2.2.2).

4.2.2.1 Which Shape Parameters Should be Used?

The two main aspects for the assessment of shape parameter suitability were the fact that this framework's intended application lies in the early aircraft design stages, and additionally the influence, which a certain shape parameter is able to exert on the available objective functions (see Section 4.2.1.2).

In the early aircraft design phases the wing planform is determined among other things, which should be reflected in the shape design variables. The wing planform is specified by the following engineering parameters, which could be used as shape design variables:

- Wing Span
- Chord Length
- Sweep Angle
- Dihedral Angle
- Twist Angle

Additionally, an airfoil geometry must be chosen to define the wing. These airfoil geometries are often object of shape optimizations as well, but were disregarded here, as such optimizations usually are performed in later design phases, where more detailed information is available allowing analyses of higher fidelity. Thus, the airfoil geometry was considered fixed for the shape optimizations conducted here. Many other parameters that are frequently used at early development stages such as e.g. aspect ratio or taper ratio represent a combination of the parameters listed above. In order to give the optimizer as much design freedom as possible these parameters based on the combination of others were not considered as design variables.

Some of the shape parameters listed above had to be excluded by limitations of the developed framework. The sweep angle, for example, is usually determined through the intended Mach number range of the aircraft taking into account the airfoil geometry and the critical local Mach numbers. These effects could not be reproduced by the aerodynamic analysis method applied in this framework (i.e. *AVL*). Therefore, the sweep angle was not used as a design variable, as the physical effects driving this quantity could not be provided by the current version of the framework. A similar issue arose with the dihedral angle

of the wing, which was disregarded as a shape design variable as well. It is generally determined based on factors such as wing installation position or rolling stability, which were also not in scope of the present work. Additionally, the current approach of keeping the coupling transformation matrices unchanged during shape optimizations (see Section 3.2.2) would create unrealistic aerodynamic loads after dihedral changes.

The influence of the remaining shape design variables on the system responses applied in the objective function definitions was evaluated. The main equations for both considered system responses can be seen in the following.

$$C_D = C_{D_0} + \frac{C_L^2}{\pi \Lambda e} \tag{2.8 revisited}$$

$$m_{FE} = \sum_{i=1}^{n_{elem}} m_{elem_i} \tag{4.9}$$

Here, only the drag equation for the uncambered and untwisted wing is shown (see Section 2.1.2.4). However, since Eq. (2.8) is only considered point wise for the design lift coefficient, it can also be applied for twist. Once lift deviates from the design point, Eq. (2.9) for non-planar wings needs to be applied to describe the relation between lift and drag.

Twist has a very effective influence on the aerodynamic loads and their distribution over span (e in Eq. (2.8)). The structural stiffness and mass, on the other hand, is affected only to a negligible extent as long as the twist values do not become too large (e.g. $\pm 10^\circ$). However, twist can be used to achieve beneficial load distributions for the structure. Furthermore, a specific wing twist setting has its best effect only for a very limited angle of attack range [Ray06, pp. 62-63]. During shape optimization, this can be exploited for instance by using twist to have low induced drag in cruise flight while having a lift distribution that is beneficial for the structural needs in the manoeuvre load cases that are flown at different angles of attack. Planform changes alone would not allow this, since a given planform produces qualitatively similar lift distributions for all lift states (disregarding stall). Thus, twist has its main influence on the induced drag component of the objective functions, while FE mass is only indirectly affected through the load distribution and structural constraints.

Chord Length has a significant influence on both the structural FE mass, as well as, the induced drag. The induced drag is affected through the wing planform shape generating a specific lift distribution (e in Eq. (2.8)). On the other hand, its effect on FE mass is caused by volume change of the FE elements (m_{elem} in Eq. (4.9), see also Section 4.1.3.1). Additionally, this shape parameter can be used very effectively for stiffness manipulation, as the wing box height increases with chord length due to constant thickness-to-chord ratio. Mostly, induced drag and FE mass prefer similar chord length distributions (higher values at the root diminishing towards wing tip, see Section 4.2.1.2). Therefore, chord length shape variables could be used to affect both objective function components with gradients possibly pointing in the same direction.

Wing Span is one of the main parameters for influencing induced drag through the aspect ratio (Λ in Eq. (2.8)). Yet from the structural point of view, a higher wing span causes a greater root bending moment. This makes the load on the structure more critical, which ultimately entails higher structural FE mass. Therefore, wing span influences FE mass in two ways; directly through volume increase similar to chord length and indirectly through load effects. Hence, wing span represents a very interesting shape parameter as aerodynamics and structure have directly opposed gradients with respect to it (studied in Section 4.2.2.2). Here, optimization can be used to find a compromise between these competing requirements while improving the wing's performance.

All three shape parameters allow influencing one or both system responses that are used in the objective function formulations. Together with sizing variables these shape parameters can effectively change the wing planform design and simultaneously satisfy the structural constraints. Therefore, the focus for the shape optimizations in this thesis was placed on these three shape parameters.

4.2.2.2 Design Space Studies with Shape Parameters

The first number of shape optimizations using the selected shape parameters and objective function formulations revealed certain issues regarding the combination of shape design variables. One example for this can be seen in [DPD+13a], where twist and chord length shape variables were applied simultaneously minimizing induced drag. This led to undesired planform geometries with discontinuous twist and chord length distributions over the wing span (cf. Fig. 4.33). It was found that this was caused by the ambiguity of chord length and twist variables with respect to the spanwise lift distribution as discussed for example by Phillips [Phi04]. This had the effect of creating a multimodal design space regarding the induced drag objective function, where equal solutions with the same objective function value, yet, with different combinations of local wing twist and chord length could be found.

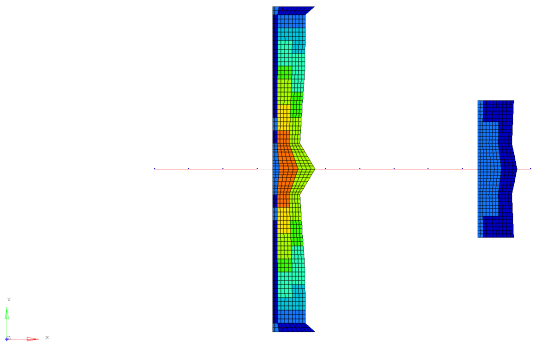

Fig. 4.33: Result of twist/chord length shape optimization on induced drag [DPD+13a]

Induced Drag Design Space To confirm this hypothesis, a design space study considering the relation between twist and chord length shape parameters and the induced drag objective function was conducted. The induced drag optimization result of Section 4.1.3.2 was used as basis for this. Employing that result had the advantage of knowing that at least one point in the scope of this study contained the minimal induced drag value corresponding to an Oswald factor of $e = 1.0$ (i.e. elliptic lift distribution). The base planform of the parametric geometry wing model is presented in Fig. 4.34 along with the numbering of the different sections at which the shape design variables can be defined.

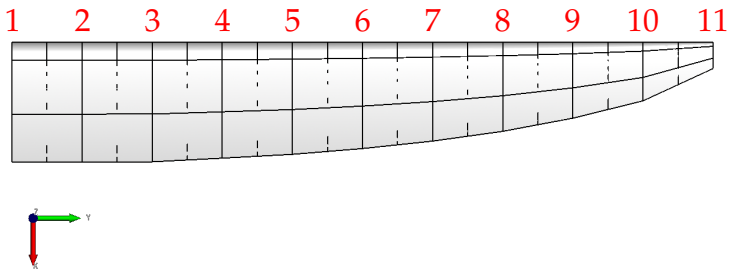

Fig. 4.34: Base configuration of design space study (result of Section 4.1.3.2)

For the first evaluation of this study, a chord length and a twist (YRotation) variable were defined at section 8 (see Fig. 4.34). The section was selected arbitrarily, as the same behaviour could be witnessed in the other positions as well. After that, the values of these variables were varied independently, each time performing an aeroelastic analysis of the cruise load case (defined in Section 4.1.1.2) including induced drag calculation.

The changes to the shape variables caused different lift loads for each evaluation point. Since all performed shape optimizations were formulated in a way that overall lift remained constant, this effect needed to be eliminated from the design space study to ensure comparability. Performing a trimming for each sample point to correct the differing lift load was made infeasible due to the definition of trimming as an optimization problem in the framework and the required number of sample points to resolve the design space appropriately. That means a trimming optimization would have been necessary for each evaluation point of the grid. Therefore, without additional trimming the difference in lift was eliminated from the results by transforming Eq. (2.8) and evaluating the following while neglecting the viscous drag component C_{D_0}:

$$\frac{C_{D_{ind}}}{C_L^2} = \frac{1}{\pi \Lambda e} \tag{4.10}$$

Also the reference surface S_{Ref} used for the aerodynamic coefficients was kept constant. Yet, Eq. (2.8) only applies for planar wings without camber or twist [Ray06]. As twist was varied for this design space study the equation for non-

planar wings (Eq. (2.9)) would have had to be employed.

$$C_{D_{ind}} = C_{D_{ind\ min}} + \frac{\left(C_L - C_{L_{min\ drag}}\right)^2}{\pi \Lambda e} \qquad \text{(2.9 revisited)}$$

However, this would have required determining the terms $C_{D_{ind\ min}}$ and $C_{L_{min\ drag}}$ by analysing the drag polar for each evaluation point, which would have entailed significant manual effort making a design space study with the necessary number of sample points infeasible. Therefore, the magnitude of the error made by assuming Eq. (4.10) for the twist variation was estimated by evaluating the drag polar at a number of points in the range. In the chosen scope of values the equation was found to be precise at zero twist with the error increasing towards the boundaries but staying below 3 %. Furthermore, the mentioned error only occurred with the twist shape parameter; in case of chord length or wing span Eq. (4.10) represents the exact solution, as the wing remains planar. Because of this it was decided to apply Eq. (4.10) for qualitatively representing the induced drag objective for all the following shape parameter combinations.

Thus, the chord length design variable was varied evenly between 300 mm to 1700 mm while the twist (YRotation) design variable ranged from $-10°$ to $10°$ both using 40 sample points. Fig. 4.35 shows a contour plot of the aeroelastic results for the cruise load case of Eq. (4.10). It was generated by evaluating Eq. (4.10) and the structural constraints applying the aeroelastic solution. The absolute values of this equivalent drag function were not of significance, only their qualitative distribution was considered.

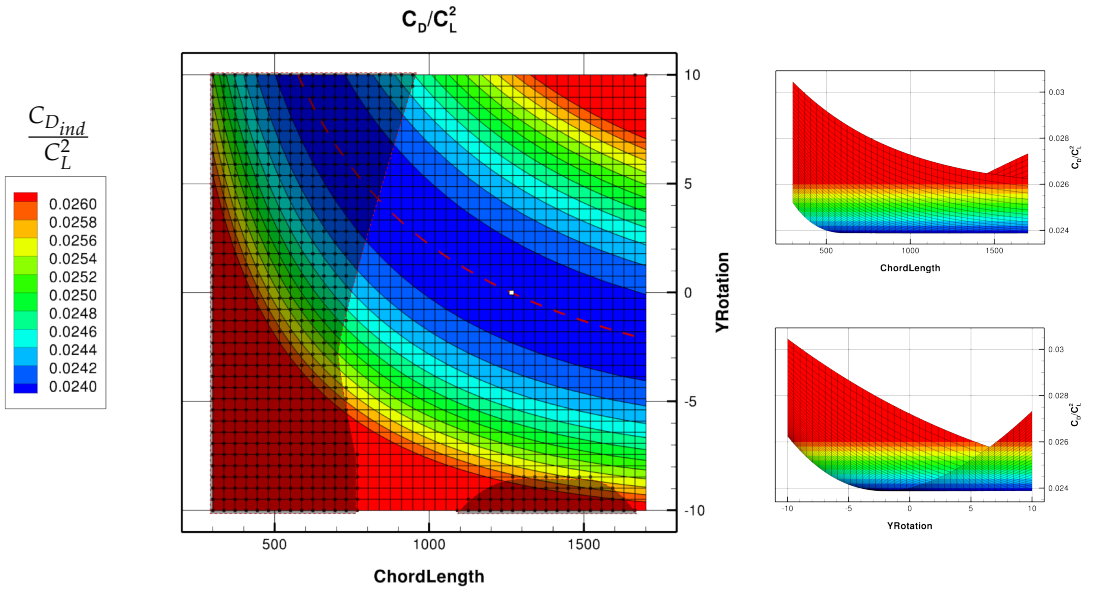

Fig. 4.35: Induced drag design space for twist (YRotation) and chord length shape variables

Fig. 4.35 shows the resulting aeroelastic induced drag design space for these two shape parameters. One can see that an arched valley of minimal values is formed across the value range with the base configuration (white square)

located at its bottom. For this design it was shown in Section 4.1.3.2 that it has an elliptic lift distribution corresponding to the theoretical minimum for the induced drag coefficient. Some further investigations showed that the bottom of the valley is flat exhibiting the same value at all of its lowest points. The results lying in different positions of the valley bottom were found to have an Oswald factor of $e = 1.0$ similar to the base configuration.

An explanation for this can be found in Prandtl's lifting line theory for the slender unswept wings [Pra18], which involves that the spanwise local lift load depends on the product of local chord length and local aerodynamic angle of attack (Eq. (4.11), allowing wing twist α_{Twist} and camber α_{L0}). Phillips [Phi04] states, for example, that in order to achieve a wing with an elliptic lift distribution the result of multiplying the local chord length with the corresponding angle of attack also needs to vary elliptically over span. In other words, for the presented case there are infinitely many combinations of chord length and angle of attack with the same lift distribution as long as the result of their product has the same value. To highlight this, the red dashed line was included in Fig. 4.35 representing all twist/chord length combinations that yield the same result for this product as the initial flat elliptic wing. A similar line can be plotted for each of the 11 sections of the presented wing deriving the needed result value of the product at the respective spanwise positions from the desired elliptic lift distribution. Due to the selected base model of this study the remaining wing sections already satisfy the requirements for an elliptic lift distribution so that any point on the dashed line in Fig. 4.35 corresponds to a wing with an Oswald factor of $e = 1.0$. Hence, from the optimization algorithm's point of view this means that an infinite number of local minima with the same objective function value as the theoretical minimum but different parameter combinations exist, making all of them global minima.

$$C_l(y)c(y) = f\left(c(y) \cdot [\alpha(y) + \alpha_{Twist}(y) - \alpha_{L0}(y)]\right) \tag{4.11}$$

The greyed out areas in Fig. 4.35 mark the solutions with violated structural constraints. For this, the von Mises stress, as well as, the 2D buckling constraints described in Section 4.1.1.4 were included. These areas do not show the exact boundary, where the structural constraints were violated, since the effective overall lift load varied between each evaluation point in the plot. Thus, the boundaries would shift, if each sample point were re-trimmed to the proper flight state. Also, adjusting the sizing variables that were held constant in this study could alter these boundaries. Hence, these highlights in the plots shall clarify the structural requirements in relation to the induced drag behaviour.

Overall this underlined the expected multi-modal problem in case twist and chord length design variables are used simultaneously in an optimization of induced drag. Depending on the starting point the gradient based optimizer would move to the nearest point at the bottom of the valley that satisfies the constraints. Since no objective function gradient is present at the valley floor, the optimization would converge there.

In order to show that for shape parameters in different sections only one minimum exists, his study was repeated twice, once with two chord length and once with two YRotation variables each time located on neighbouring CPACS

sections. This was carried out on sections 8 and 9 (see Fig. 4.34). The parameter values were permuted over the same ranges as in the previous study.

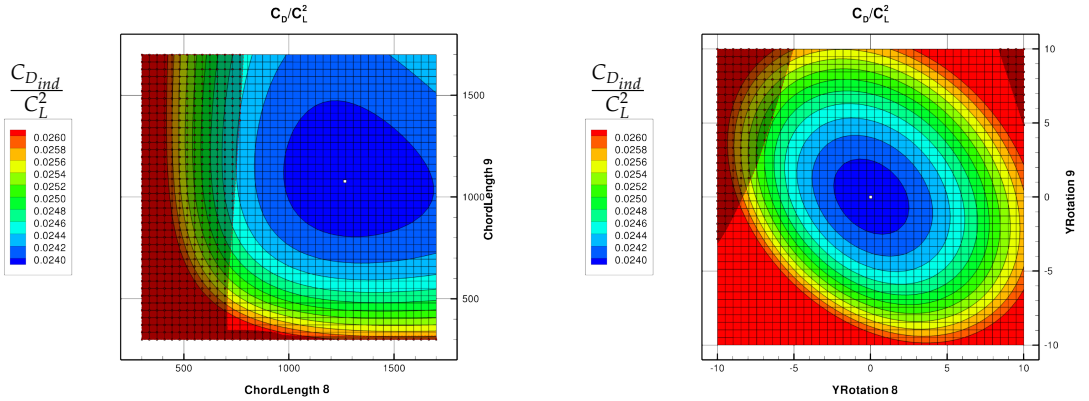

(a) Chord length/chord length

(b) Twist/Twist

Fig. 4.36: Induced drag design space for neighbouring chord length and twist shape variables

Fig. 4.36 shows the induced drag design spaces (Eq. (4.10)) for two neighbouring chord length and two neighbouring twist shape variables respectively. Again, the colour levels in the contour plots qualitatively represent the induced drag value at constant lift. In these plots one can see that for both shape variable types only one combination yielded the minimal induced drag value. This was enabled due to the selection of the base design (white square), which already had an elliptic chord length distribution. In these plots one can see that the product of local chord length and local angle of attack mentioned before still applies here. This means if either chord length or twist are fixed for a section, the value for the respective other parameter is prescribed by the desired lift distribution. But if both are variable at the same spanwise location, as in Fig. 4.35, their combination can be chosen arbitrarily as long as the required value for the result of their product is met. In the context of shape optimization this means that, as soon as a chord length and a twist variable are defined for the same section, infinitely many combinations of these values with the same induced drag value exist for this section (see Fig. 4.35). If only one of the two shape parameters types is variable at a section, while the other one is fixed, only one solution for a specific lift distribution exists.

The third selected shape parameter type (wing span/wing length) was studied regarding the induced drag design space as well. The previously investigated design variable combinations of twist and chord length only affected the Oswald factor e in Eq. (4.10). The wing span, on the other hand, modifies the aspect ratio Λ. As it was explained before, the Oswald factor can only reach a maximum value of 1.0 (for planar wings), whereas the aspect ratio has no such theoretical boundary. Therefore, by increasing the wing span the induced drag value could be reduced until it vanishes at $\Lambda \rightarrow \infty$. Thus, the wing span parameter should not exhibit such defined minima as the other two shape parameters did. This is presented in Fig. 4.37 for a combination of wing and chord length (Note: Due to the high influence of wing span on the induced drag, the range

of the colour legend had to be increased for this plot compared to the previous ones).

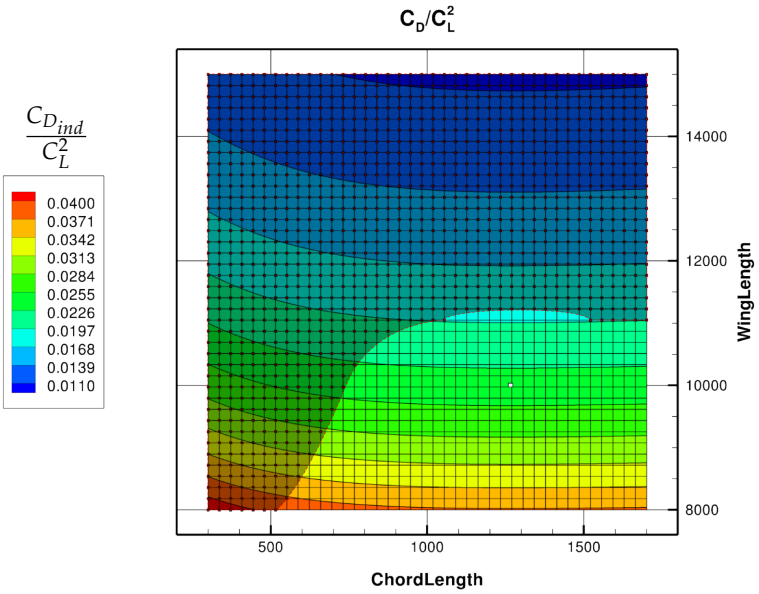

Fig. 4.37: Induced drag design space for chord length and wing span design variables

As expected, the wing span parameter showed a consistent gradient lowering induced drag with higher values, which was only marginally influenced by the chord length variable. No finite minimum could be found in the scope of this study. However, considering Eq. (4.10) no finite minimum could be expected for this combination of shape design variables. The slight curvature of the isolines in Fig. 4.37 shows that for each wing span value one chord length can be found that yields the minimal induced drag (in this case the initial one). This emphasizes the different scales of influence on induced drag between Oswald factor and aspect ratio.

The greyed out area of the plot highlights the area of the design space with violated structural constraints. Again this information cannot be explicitly applied, since no consistent lift state was guaranteed for each evaluation point of the design space. Yet, it underlines the tendency of higher wing span values being more critical for the structure. It also shows that an increase in chord length can help support greater wing spans.

Initial Point Study for Twist/Chord Length Combination As the design space study for a twist/chord length parameter combination clearly revealed a multi-modal design space, its effects on numerical shape optimizations were additionally verified through a number of optimization runs starting at different initial points (analogue to Section 4.1.4.1). Three shape optimizations with twist and chord length design variables were conducted. The objective of these optimizations was to find the minimal induced drag. Table 4.24 shows the included design variables for these optimizations. The three different initial points were created by modifying the chord length and twist values of the

model (see Table 4.25).

Table 4.24: Design variable definition for twist/chord initial point study

Design Variable x	Lower Bound x_{lb}	Upper Bound x_{ub}
Shape		
Chord Lengths x_{c_i}	300 mm	1700 mm
YRotation x_{t_i}	−5°	5°
Sizing x_{Size}		
Skin	0.8 mm	8.0 mm
Stringer	50 mm^2	200 mm^2
Spar Caps	100 mm^2	500 mm^2
Trimming (not for 1 g case)		
α Scale Factor x_α	−50	50

Table 4.25: Initial configurations of twist and chord length study

	Uniform chord length	Uniform YRotation
Run #1	1500 mm	0°
Run #2	1700 mm	−2°
Run #3	1000 mm	2°

For this study the aeroelastic load cases described in Section 4.1.1.2 were considered. All three initial points were trimmed to these flight states in advance of the optimizations to account for the differing configurations. Thus, all optimizations started from a trimmed state. Trimming variables were only defined for the pull-up and push-over load case. The angle of attack for the cruise load case was trimmed initially and, during the shape optimization, trimming was maintained through the YRotation shape variables. This was done to prevent the introduction of another parameter ambiguity between overall angle of attack and wing twist variables (similar to angle of attack/chord length in Section 4.1.4.1). The known structural constraints from Section 4.1.1.4 were included as usual.

All three optimizations managed to find an elliptic lift distribution and converged according to KKT. Yet, the resulting wing designs showed significant differences (Figs. 4.38 and 4.39).

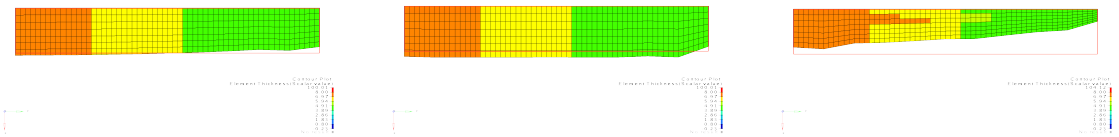

(a) Run #1 (b) Run #2 (c) Run #3

Fig. 4.38: Resulting planform geometries of twist/chord shape optimizations of induced drag

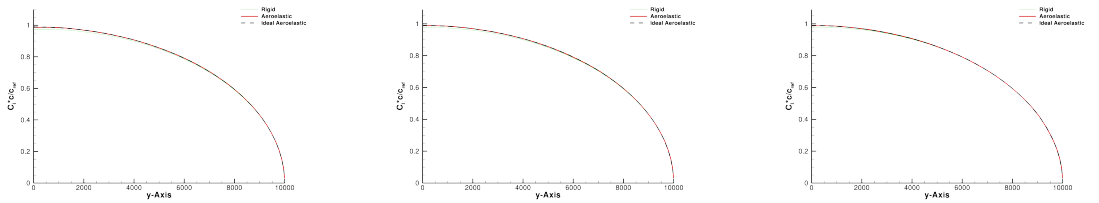

(a) Run #1 (b) Run #2 (c) Run #3

Fig. 4.39: Resulting lift distributions of twist/chord shape optimizations of induced drag

While the results of Run #1 and #2 did not look very promising and did not deviate far from the initial rectangular planform, Run #3 produced a result resembling the designs seen in the chord length optimizations before (Section 4.2.1.2). This difference was caused by the specific initial point of the third run, which started at a significantly lower chord length than the others. Due to this, many more structural constraints (242) than in the first two optimizations (29,17) were active from the beginning taking influence on the path of the optimization. Since chord length has a greater influence on the structural properties than twist, the optimizer used this type of shape design variable in Run #3 to create a planform beneficial for structural purposes aiding in satisfying the constraints. This means the chord length was increased at positions of high structural strain, while less stressed areas kept the initial chord length or were assigned even lower values. As all three results reached an elliptic lift distribution (see Fig. 4.39), they represent equally good results to the optimization algorithm. However, from an engineers point of view none of them seem very suitable for further development.

Cross-referencing these results with the design space plots, the obtained twist and chord length values at CPACS section 8 were extracted and laid over the corresponding design space plot. In Fig. 4.40 one can see that the converged results all aligned near the bottom of the valley.

Thus, the three entirely independent optimizations with differing initial points confirmed the valley shaped design space found through the parameter study. This demonstrated the existence of an initial point problem caused by the combination of twist and chord length parameters. The small deviations of the results from the centre of the valley could by caused by the mentioned error of using the planar induced drag equation for a twisted wing or by slightly differing trim states.

FE Mass Design Space Having found this particular behaviour for the induced drag objective function, all four design space studies shown above were also conducted for the structural FE mass component of the objective function. Since the FE mass is independent of the current trim state, no adjustments as in Eq. (4.10) had to be made to account for the varying lift states between the sample points. Yet, the lift load still influenced the structural constraints so that the boundaries shown in the plots cannot be applied explicitly. For the following studies the scale of the colour legend in Fig. 4.41 had to be adjusted for each

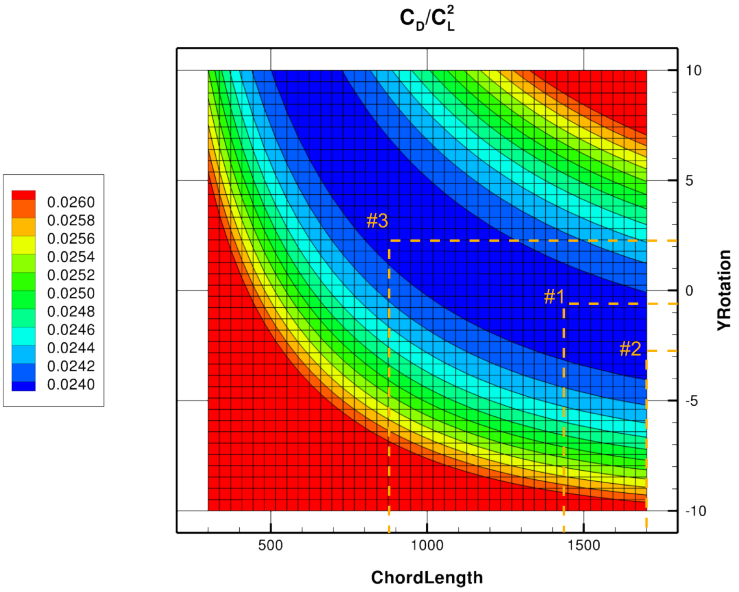

Fig. 4.40: Chord/twist design space for induced drag with results of the three shape optimization

plot individually in order to show the effects of interest.

Fig. 4.41 shows the FE mass design space with respect to the different shape design variable combinations. The colouring of the plot directly represents the mass of the FE model in tonnes. Fig. 4.41a shows that, compared to chord length, twist variables have virtually no influence on the FE mass. This stands in great contrast to their very similar effect on the induced drag coefficient. The combination of wing span and chord length parameters depicted in Fig. 4.41b proves that reducing any of the two variable types directly decreases the FE mass without any apparent minimum. Due to its greater effect on the model the wing span parameter has a steeper gradient than the chord length variable. Comparing it to the corresponding induced drag plot (Fig. 4.37) reveals the previously mentioned opposed gradients of FE mass and induced drag with respect to wing span. This conflicting interest of the two disciplines underlines the potential of using MDO with wing span as shape variable.

The Figures 4.41c and 4.41d are the result of combining two shape variables of the same type located on neighbouring CPACS sections 8 and 9 (cf. Fig. 4.34). In comparison to Fig. 4.36 one can see that the chord length parameter does not have a finite minimum regarding FE mass as opposed to induced drag. Both chord length parameters have an almost equal influence on the FE mass. A slight curve can be observed in the contour lines of this plot. As the chord length is linearly interpolated between two adjacent CPACS sections, the two chosen sections influence the same segment in between, which causes this dependency between the two chord lengths.

The two twist variables, on the other hand, do show a similar influence on FE mass as with respect to induced drag. However, this is simply explained by the fact that starting at an untwisted design an increase of twist in positive or negative direction raises the volume of the affected FE elements. Examining

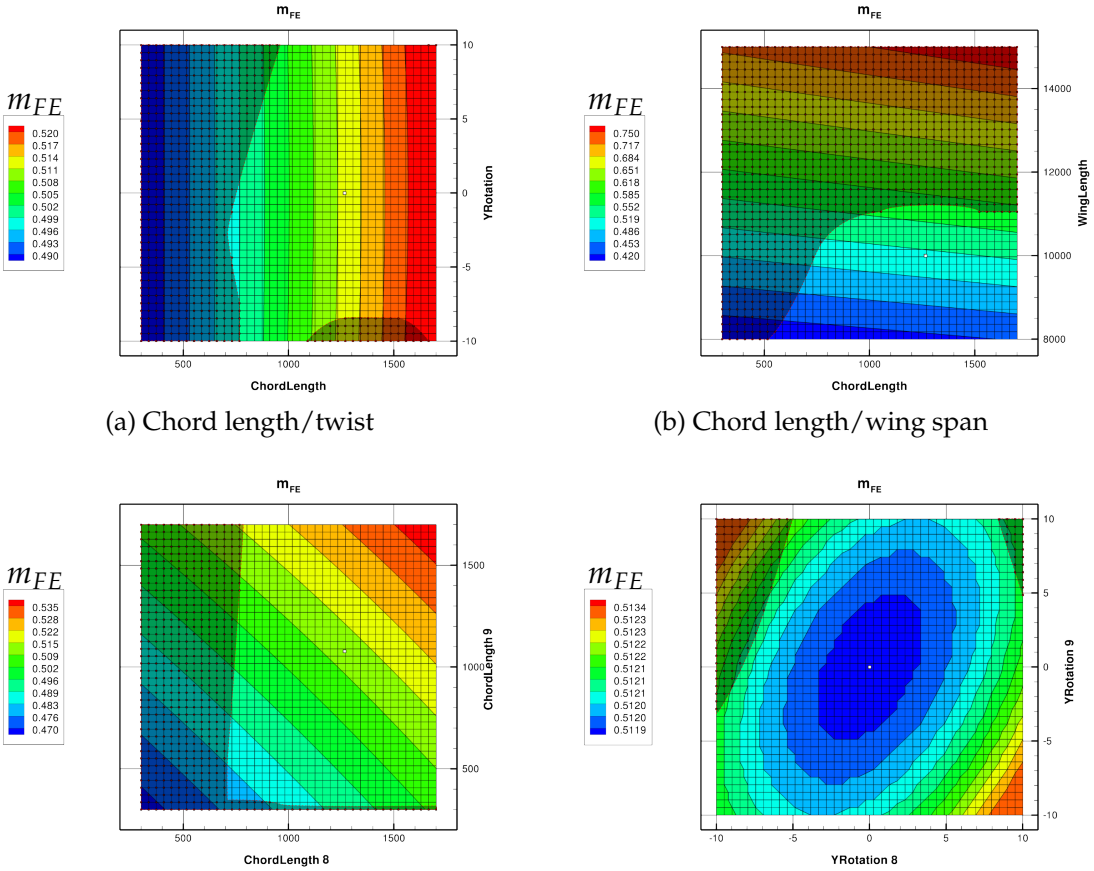

(a) Chord length/twist

(b) Chord length/wing span

(c) Chord length/chord length

(d) Twist/twist

Fig. 4.41: FE mass design space for different shape parameter combinations

the scale of the colour legend reveals that the maximum change depicted in Fig. 4.41d ranges below 2.5 kg (for comparison the differences in the other three plots ranged between 30 kg and 300 kg). Again, this emphasizes how negligible the influence of twist (YRotation) on the FE mass is.

Combined Induced Drag/FE Mass Design Space As the effects found in the induced drag design space could not be detected in the FE mass design space, the possibility of compensating the associated drawbacks through a combination of the two system responses was examined. A weighted sum of both system responses as used before in the combined objective functions (e.g. Section 4.2.1.2) was used for this.

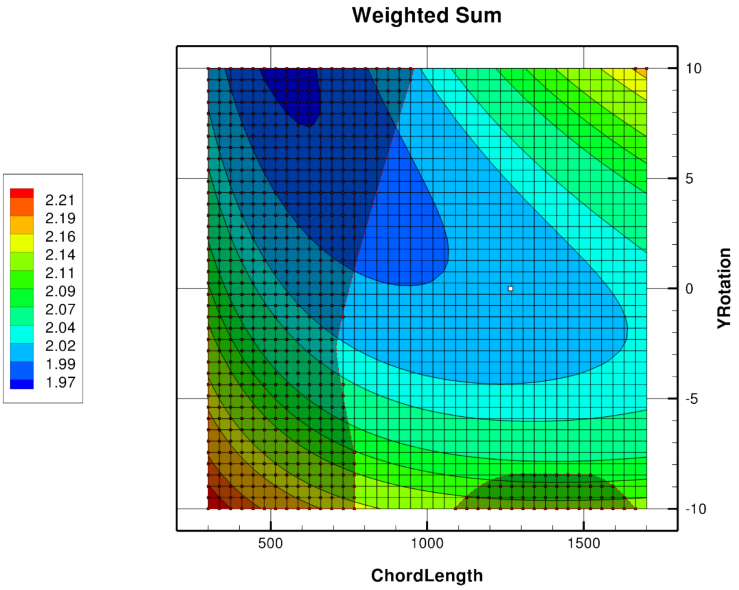

Fig. 4.42: Weighted sum objective design space for twist (YRotation) and chord length variables

Fig. 4.42 shows the design space for a weighted sum objective function with respect to the previously introduced twist and chord length shape variables. Here, the method of summing up the two system responses and their weighting has a strong influence on the magnitude of the caused effect. Therefore, only the qualitative difference compared to the previous plots should be considered. One can see that the general valley shape is still present, however, the addition of the FE mass value has provided a gradient to the bottom of the valley. Therefore, no infinite number of local minima are present any more eliminating the discovered initial point problem.

This change in objective function was plotted with respect to wing span and chord length as well (Fig. 4.43). Comparing it to Fig. 4.37 shows that adding the FE mass system response created a finite minimum in the design space. This was caused by the previously mentioned opposed gradients of induced drag and FE mass. Even though it appears possible to manually deduce the best wing span directly from Fig. 4.43, the violated structural constraints at this point would require adjustment of other design variables such as sizing. Through

these adjustments the FE mass, and hence, the design space plot would be affected as well. Thus, optimization is needed here as well to find a suitable combination of shape and sizing variable settings with improved objective function values.

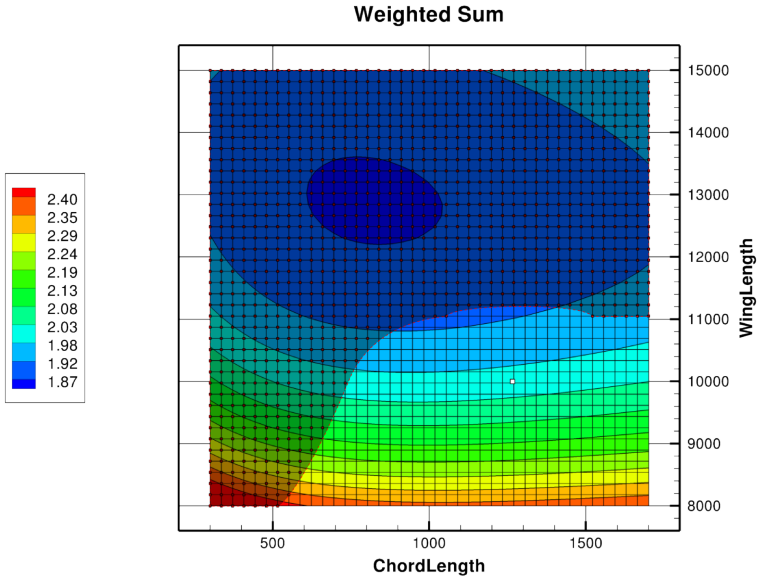

Fig. 4.43: Weighted sum objective design space for wing span and chord length variables

Therefore, the combination of induced drag and FE mass was found to be beneficial for the chosen shape design variables. Additional to the advantages of the combined objective functions discussed in Section 4.2.1.2, the combined design space also proved to be less critical regarding the negative effects of the twist/chord length combination and allowed finding a compromise for wing span. The combined objective may help solving the optimization issues with the non-convex design space, yet, with this alone it is not possible to assess the technical suitability of the design for further development. For this, the approach described in Section 4.2.1.2 needs to be applied.

Summary of found effects As expected twist (YRotation) and chord length shape parameters were found to have very similar effect on induced drag. At each spanwise position the local contribution to the lift distribution could be generated with multiple combinations of twist and chord length. Hence, the induced drag design space for this case formed a valley with an even floor creating this infinite number of local minima for each section. Therefore, when optimizing induced drag with twist and chord length shape design variables, the solutions were mostly dependent on the initial point of the optimizations.

However, it was shown that twist and chord length have a significantly different influence on FE mass, where twist showed almost no effect. Thus, both parameter types could be used effectively for improving structural but also aerodynamic requirements through MDO, each being applied on the discipline it affects most. However, the found ambiguity regarding the aerodynamics

between chord length and twist must be addressed in order to prevent the initial point problem. Several approaches for this are discussed in the subsequent chapter.

Wing span, on the other hand, did not exhibit any such dependency on the other shape parameters regarding induced drag, since it affected a different term in Eq. (4.10). Yet, the mentioned trade-off issue due to opposed gradients of FE mass and induced drag could be visualized by the design space study. This highlighted the possibilities of the wing span shape parameter in MDO.

Overall, the combined objective design space appeared most promising, as it managed to weaken the drawbacks of the induced drag design space through the characteristics of the FE mass component. Therefore, using the selected shape design variables simultaneously in one optimization would be less critical. This supported the decision of the previous Section 4.2.1.2 to use combined objective function formulations for further shape optimizations.

Thus, the three selected shape design variable types (chord length, twist/YRotation and wing span) are used in the following shape optimizations. In order to include twist and chord length distributions in the optimizations the similar effect on induced drag and its implications for the design space have to be accounted for.

4.2.3 Evaluation of Different Approaches to Multidisciplinary Shape Optimizations

In this section different approaches of conducting shape optimizations with the selected shape parameters on the objectives of induced drag and FE mass were studied. Special attention was paid to the issue of combining twist and chord length variables in the same optimization and how to handle the found nonconvex induced drag design space this pair of shape design variable types creates (see Section 4.2.2.2).

As explained in chapter 4.2.1.1, the aeroelastic Breguet range has been selected to function as a measure of quality for the resulting wing designs of the shape optimizations. Thus, with the selected shape parameters chord length, wing span and twist, shape optimizations were conducted attempting to obtain wing designs with the best Breguet range performance. It has already been shown in Section 4.2.1.2 that induced drag, as well as, FE mass have to be considered during the optimization in order to achieve useful results. The Breguet range objective was found to achieve the best designs regarding range performance, but that the weighted objective function could lead to designs of similar performance given the correct weighting factors.

In this section these findings were combined in order to find a shape optimization approach that produces useful results while handling the found issues so that it could be applied in an engineering development process. Three different approaches to aeroelastic shape optimization with chord length, wing span and twist have been derived with this in mind:

1. Combined induced drag/FE mass objective function

2. Induced drag objective with FE mass constraint

3. Sequential optimization: First planform, then twist

These shape optimizations conducted with each approach are presented and finally their results and prospective advantages are compared in the subsequent paragraphs.

4.2.3.1 Combined Objective Function

The first approach of handling the interactions between twist and chord length regarding induced drag was to use a combined objective function considering induced drag, as well as, FE mass. This was based on the findings of Section 4.2.2.2 where the FE mass component were found to counteract the drawbacks of the induced drag design space. A combined objective function also allowed conducting a trade-off with respect to the wing span (Fig. 4.43). Furthermore, it could be shown that this type of objective function would produce wing designs with far better Breguet range performance than singular objectives (Section 4.2.1.2).

In order to find the objective function with the best combination of induced drag and FE mass for this problem a number of shape optimizations with different objectives were conducted (objective functions as in Section 4.2.1.2, Table 4.23). Constraints (Eq. (4.12)) and design variable definitions were realized analogue to that previous study. Only the mentioned twist shape design variables were added to the problem as shown in Table 4.26.

Table 4.26: Design variable definition for twist/chord/span shape optimizations

Design Variable x	Lower Bound x_{lb}	Upper Bound x_{ub}
Shape		
Twist/YRotation x_{t_i}	$-5°$	$5°$
Chord Lengths x_{c_i}	300 mm	1700 mm
Wing half span x_s	8000 mm	15 000 mm
Sizing x_{Size}		
Skin	0.8 mm	8.0 mm
Stringer	50 mm^2	200 mm^2
Spar Caps	100 mm^2	500 mm^2
Trimming		
α Scale Factor x_α	-50	50

$$\mathbf{g}(\mathbf{x}) = \begin{bmatrix} \mathbf{g}_{stress}(\mathbf{x}) \\ \mathbf{g}_{buckling}(\mathbf{x}) \\ \mathbf{g}_{trim}(\mathbf{x}) \end{bmatrix} \leq 0 \tag{4.12}$$

Fig. 4.44 shows the resulting Breguet ranges for all the different objective functions. The ranges presented there are the results after a maximum of 80 iterations, as only the optimization with a single induced drag objective converged

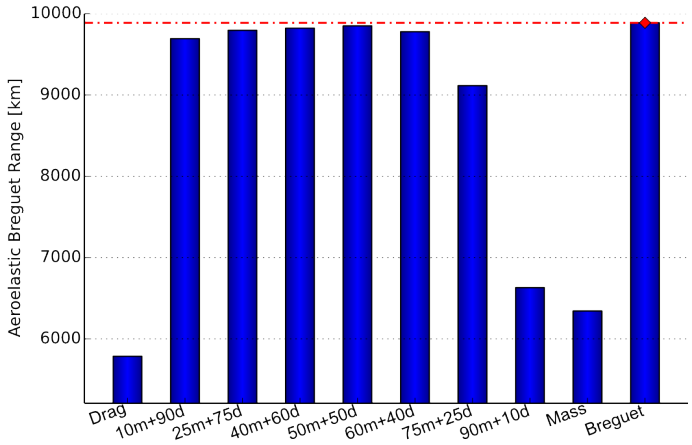

Fig. 4.44: Resulting aeroelastic Breguet ranges from twist/chord/span shape optimizations

according to KKT before that. Convergence of the other optimizations was verified manually as before. In accordance to the previous results the Breguet range objective function achieved the best performing design, while the weighted sum objective with equal weighting ($50m + 50d$) came close to that. Thus, in the following the Breguet objective result was used for comparison between the different approaches.

Table 4.27 provides a summary of this shape optimization result. It shows that induced drag and FE mass could be reduced by about 58 % and 46 % respectively, which resulted in a Breguet range increase by about 5500 km.

Table 4.27: Combined objective shape optimization summary (aeroelastic)

	Initial	Final	Delta %
m_{FE}	0.533 t	0.289 t	-45.79
C_L	0.7787	0.7772	-0.20
$C_{D_{ind}}$	0.0153	0.0064	-57.91
R_{Br}	4345 km	9888 km	+127.59

4.2.3.2 FE Mass Constraint

The second approach to shape optimization with twist, chord length and wing span variables was to use the induced drag objective function and combine it with an FE mass constraint. This should allow providing a gradient to the solutions lying at the flat bottom of the design space valley, analogue to the observations made in run #3 of Section 4.2.2.2. There, the violated structural constraints steered the optimizer towards a different solution, since the induced drag minima closest to the initial point were infeasible. The idea of using an FE mass constraint was based on the fact that FE mass is influenced by both sizing and shape design variables and that it directly affects the Breguet range. Furthermore, it only requires specifying one constraint function for the whole model.

Compared to other structural constraint types such as stress or buckling, this allows better prediction of the effects caused by including this type of constraint.

Thus, the design variable definition, as well as, the optimization constraints were kept exactly the same as in the previous approach (Table 4.26). Additionally to the existing structural criteria, a constraint limiting the maximal FE mass was included. The boundary value for this was taken from the approximate result of the previous approach using the Breguet objective function to have a realistic and achievable value. Hence:

$$m_{FE} \leq 0.289\,\text{t} \tag{4.13}$$

$$\mathbf{g}(\mathbf{x}) = \begin{bmatrix} \mathbf{g}_{stress}(\mathbf{x}) \\ \mathbf{g}_{buckling}(\mathbf{x}) \\ \mathbf{g}_{trim}(\mathbf{x}) \\ g_{mass}(\mathbf{x}) \end{bmatrix} \leq 0 \tag{4.14}$$

Table 4.28: Aeroelastic induced drag with mass constraint optimization summary (aeroelastic)

	Initial	Final	Delta %
m_{FE}	0.533 t	0.289 t	-45.80
C_L	0.7787	0.7772	-0.20
$C_{D_{ind}}$	0.0153	0.0065	-57.44
R_{Br}	4345 km	9853 km	+126.77

The aeroelastic shape optimization ran over the maximum allowed number of iterations and managed to satisfy the given constraints including the mass constraint. Again, the change in objective function value suggested convergence without satisfying the KKT condition. Table 4.28 shows a summary of this shape optimization comparing the initial and final state using the aeroelastic values. It can be seen that the required maximum FE mass of 0.289 t was precisely satisfied, while an aeroelastic induced drag reduction of about 57 % was achieved. This resulted in an increase of aeroelastic Breguet range by around 5500 km.

4.2.3.3 Sequential Optimization

The general idea behind the sequential approach was to separate the two ambiguous shape design variable types (twist and chord length) into two consecutive optimizations, thus, preventing any interference during the optimization between one another. Since twist has only a negligible influence on the structural properties, it was decided to apply chord length and wing span in the first optimization in order to obtain a useful wing planform, then freezing this planform and running a second shape optimization with only twist as shape design variables. In both runs sizing design variables were included as well so that the structural criteria could be satisfied consistently.

The design variable definitions for both consecutive optimizations are presented in Table 4.29. As highlighted, only the applied shape design variables were

altered between the different runs. The remaining sizing and trimming design variables were applied unchanged in both optimizations.

The key problem with this approach was to select the appropriate objective function for each of the two sequential optimization runs. Separating the two system responses of FE mass and induced drag into two singular objectives yielded only suboptimal results. Thus, given the findings of the objective function study in Section 4.2.1.2, the solution with the best Breguet range was selected from the chord length and wing span study. This was found to be the result of the Breguet optimization (see Fig. 4.29), which was taken as the first of the two sequential runs.

Table 4.29: Design variable definition for twist/chord/span shape optimizations

Design Variable x	Lower Bound x_{lb}	Upper Bound x_{ub}
Shape 1st Run		
Chord Lengths x_{c_i}	300 mm	1700 mm
Wing half span x_s	8000 mm	15 000 mm
Shape 2nd Run		
Twist/YRotation x_{t_i}	$-5°$	$5°$
Sizing x_{Size}		
Skin	0.8 mm	8.0 mm
Stringer	50 mm^2	200 mm^2
Spar Caps	100 mm^2	500 mm^2
Trimming		
α Scale Factor x_α	-50	50

In both shape optimizations the same criteria as in the first approach were included (see Eq. (4.12)).

In order to find the objective function with the most promising Breguet range performance for the second shape optimization, a number of different shape optimizations were conducted based on the planform optimization result. Here, the same objective function definitions as in Table 4.23 were applied disregarding the single objectives due to their low performance results. From this, the Breguet range objective function was chosen to be applied for the second shape optimization run as well. It also required the full 80 iterations and was stopped manually after consideration of the optimization history.

Table 4.30 shows a summary of the two consecutive optimizations. Due to the additional twist optimization the Breguet range could be increased by another 250 km compared to the planform optimization result of the first run. This was achieved by reducing the induced drag at constant lift coefficient with only small FE mass increase. This underlines the importance of considering structural mass as well in the twist optimization that mainly focused on aerodynamic improvement.

Table 4.30: Sequential aeroelastic shape optimization summary (aeroelastic)

	Initial	Final 1st run	Final 2nd run	Delta %
m_{FE}	0.533 t	0.315 t	0.318 t	-40.34
C_L	0.7787	0.7772	0.7772	-0.20
$C_{D_{ind}}$	0.0153	0.0071	0.0065	-57.52
R_{Br}	4345 km	9159 km	9409 km	+116.55

4.2.3.4 Comparison of Approaches

All three presented approaches managed to increase the Breguet range performance of the model significantly compared to the baseline as well as the planform results in Section 4.2.1.2 by using chord length, twist and wing span shape variables in combination, as well as, sizing variables. Furthermore, based on the similar results each of the three devised approaches was able to prevent issues originating from the ambiguous influence of twist and chord length parameters on induced drag. Here, the achieved savings were compared while taking into account the effort required to carry out the different optimization approaches.

Figures. 4.45, 4.46 and 4.47 show the planform, twist and lift distribution of the resulting designs of all three approaches. Looking at the planform of the found designs one can say that the negative effects of interaction between twist and chord length shape variables (cf. Section 4.2.2.2) could be avoided by all studied approaches and consistent designs were found by all of them. All in all, the three wing configurations appear to have a balanced design between structural and aerodynamic requirements. The increased chord length near the wing root allows good support of the wing bending moment while the decreasing chord length towards the tip saves weight. This chord length distribution also allowed extending the wing span to its maximal allowed value without violating any structural constraints or adding excessive mass. The first two approaches resulted in very similar planforms while the sequential approach led to a design slightly less slender having greater chord lengths up to about 90 % of span.

Relating the planforms to the respective twist distributions reveals how the twist was adjusted in span direction to account for the changes in planform keeping the lift distribution close to an elliptic one. Even though the shape design variable gages would have permitted, none of the designs exactly reached an elliptic lift distribution. All results came close but showed an increased lift near the wing root and a small dent near 4/5 of the wing span. Although the twist value reached its maximal gage at that position, adjusting the chord length of the wing there would have allowed increasing the local lift towards the ellipse. The mentioned dent in lift distribution was the least notable in the sequential approach being closer to the ellipse due to its greater outboard chord length values. However, a higher FE mass was required there to reach a feasible design, as indicated by the increased skin thickness (Fig. 4.45). Thus, in the first two approaches the optimizer traded the ideal elliptic lift distribution for lower FE mass.

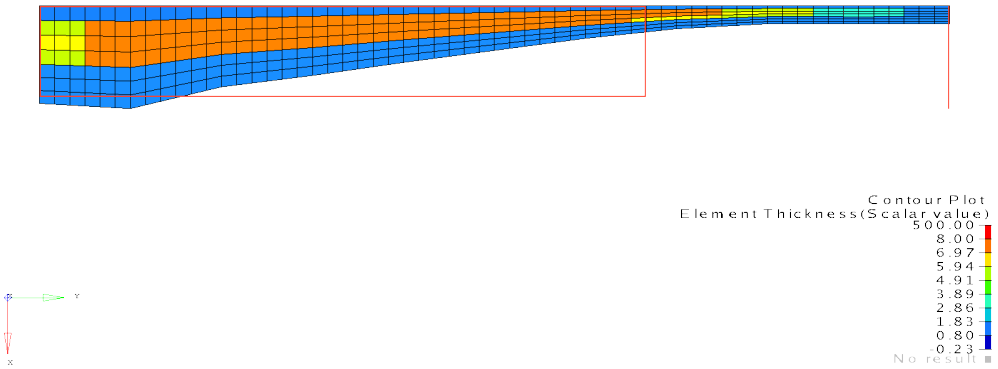

(a) Combined objective

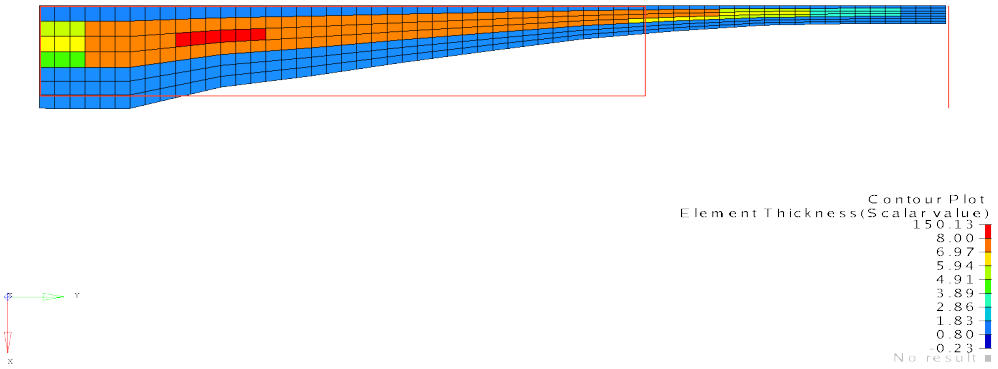

(b) Drag objective with mass constraint

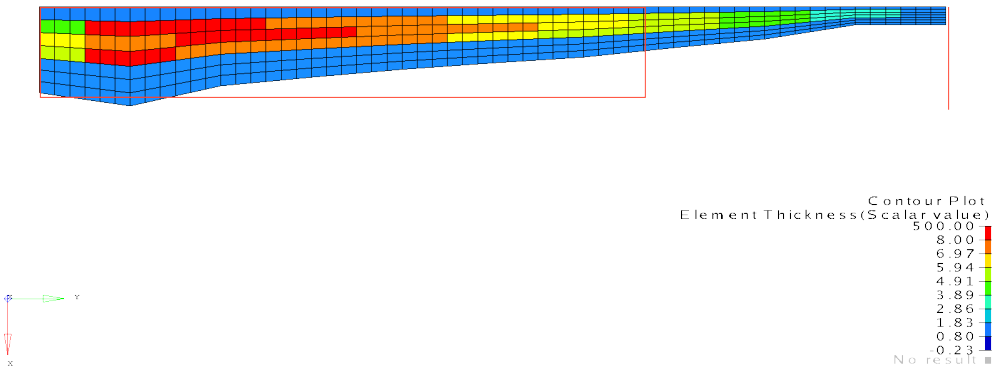

(c) Sequential approach

Fig. 4.45: Comparison of wing planforms and skin thickness distributions obtained by the different optimization approaches

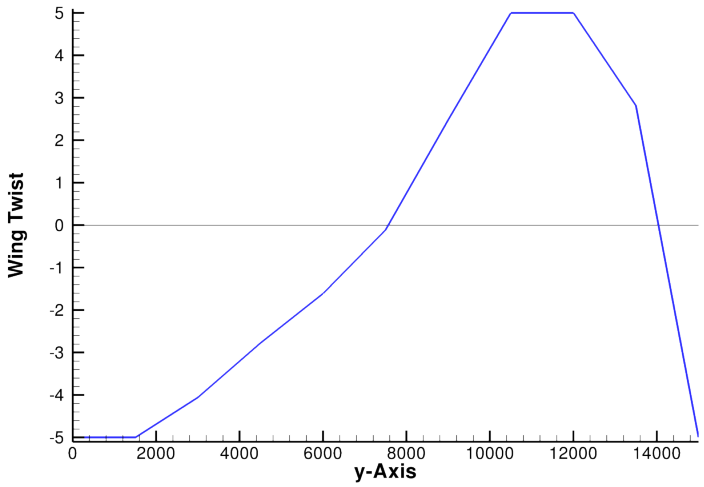

(a) Combined objective

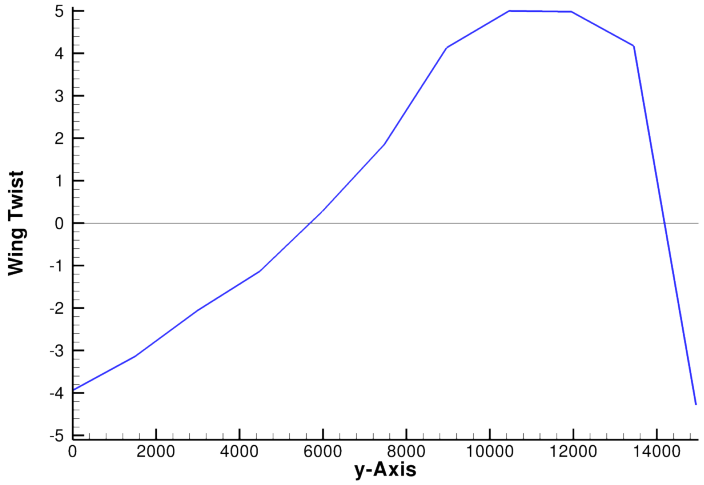

(b) Drag objective with mass constraint

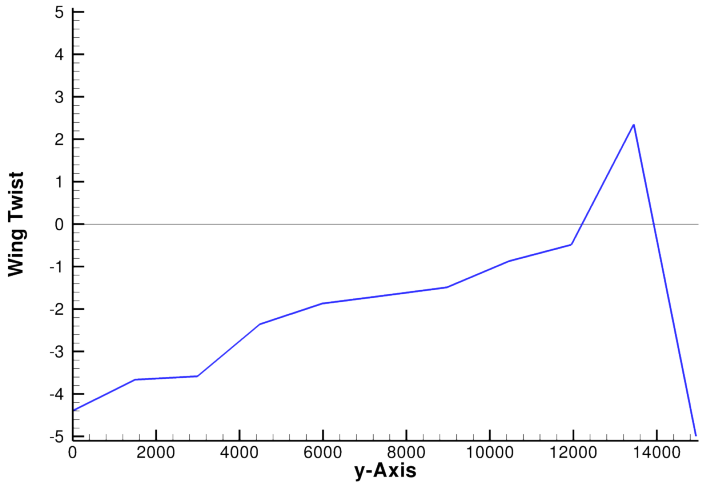

(c) Sequential approach

Fig. 4.46: Comparison of wing twist obtained by different optimization approaches

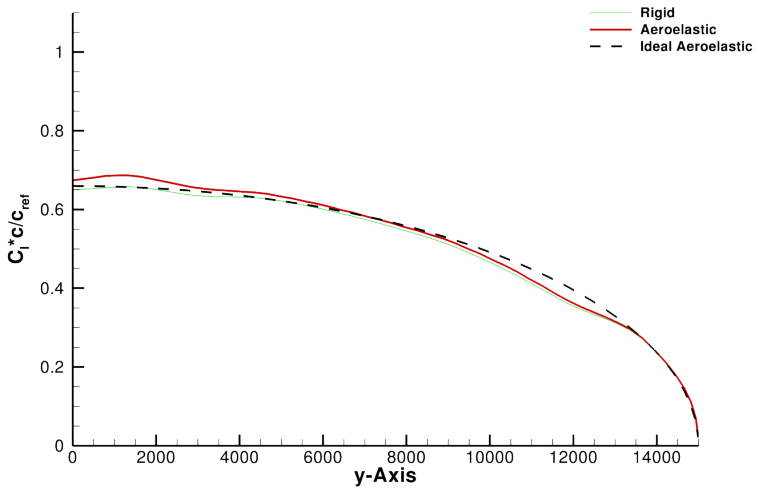

(a) Combined objective

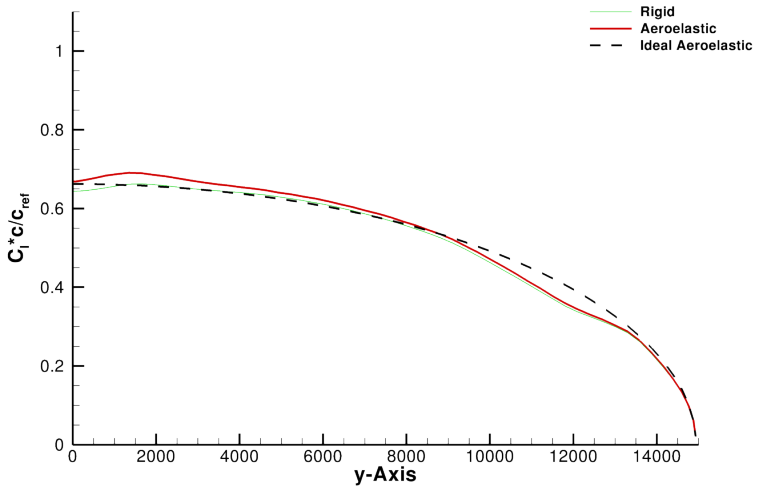

(b) Drag objective with mass constraint

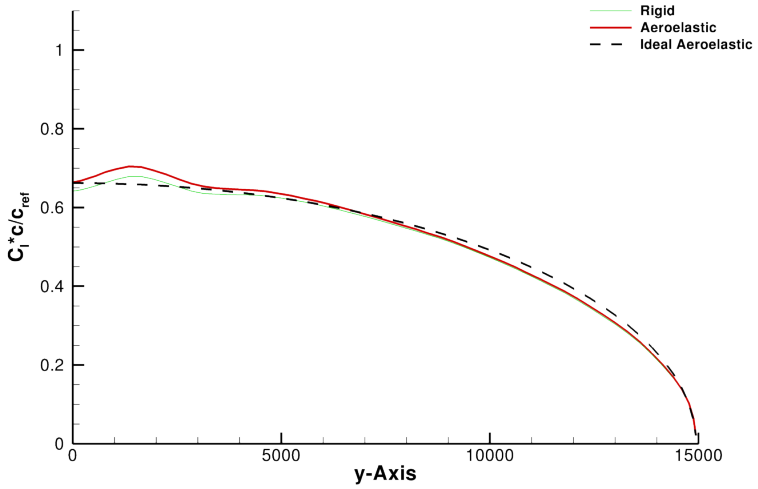

(c) Sequential approach

Fig. 4.47: Comparison of spanwise lift distributions obtained by different optimization approaches

Generally, the combined and the mass constraint approach found very similar design, since the mass constraint allowable was set to the achieved weight of the combined approach. However, even though the combined approach had to consider both system responses at once it managed to find a design with slightly lower induced drag than the singular induced objective run. Table 4.31 provides a comparison between the aeroelastic results of the three different optimization approaches. Again, it becomes obvious that the first two optimization results produced almost the same design with less then 1 % difference in the overall values. Only due to the small advantage in induced drag, the combined approach achieved a slightly higher range performance. The sequential approach, on the other hand, found a design with similar induced drag but higher FE mass. This resulted in about 5 % less range than the other two. The difference in mass originated from the greater chord length values, as well as, the thicker skin of the sequential design.

Table 4.31: Result comparison of the different approaches

Approach	Aeroelastic Breguet Range	Aeroelastic Ind. Drag	FE Mass
Combined	9888 km	0.0064	0.289 t
Mass constraint	9853 km	0.0065	0.289 t
Sequential	9409 km	0.0065	0.318 t

Additional to the achieved improvements of the different shape optimization approaches, the efficiency of each approach in terms of required iterations and preparation effort needed to be taken into consideration as well. Regarding the combined objective approach, the result presented above was found after 80 iterations. Several shape optimizations were conducted with different objective function settings in order to rate the performance of the Breguet objective function. Yet, the Breguet objective function consistently yielded the best designs for the examined cases. Therefore, the other shape optimization runs were only a means of confirmation not necessary to find this solution.

The second approach, using an induced drag objective function together with an FE mass constraint required that a boundary value for the mass constraint is available to set up the optimization. Since this mass constraint is the only part of the optimization problem that forces the optimizer to reduce the mass of the model, finding a good allowable value for this constraint can be crucial to the resulting aircraft performance. If the value is chosen too restrictive the optimization cannot find a feasible design space, which causes severe problems in the optimization progress. If the constraint is defined too weak, material reserves in the model cause performance penalties. Therefore, the boundary value of the mass constraint needs to be selected carefully either from experience or determined by preceding test optimizations. This means, some test runs as conducted for the first approach would have been required for this approach as well. Independent of these required preparations the optimization of this approach took the same number of iterations (80) as the combined objective approach finding almost the same design, but yielded no additional insight as the result of the

first approach was required to set up this optimization.

In comparison to that, the sequential approach did not require any knowledge of the achievable weight savings, yet, a combination of objective functions with beneficial outcome had to be found. Due to the large number of possible combinations it cannot be definitely said that the found combination truly yielded the result with the best performance achievable with this approach. Therefore, a great number of planform optimizations combined with equally many twist optimizations would have to be conducted to obtain a reliable conclusion about this. Additionally, each of these results would require 160 iterations assuming none of them converged according to KKT beforehand. Regardless of the objective function problem, the complete separation of twist and chord length shape variables also prevented all interactions between these two parameter types including beneficial ones. This could be seen in the fact that the resulting design received higher chord length and lower twist values near the wing tip, while the first two approaches used twist more extensively in this region lowering chord length to save FE mass for higher Breguet range.

Summarizing these findings, the first approach using the combined objective with all considered shape design variables was found to be preferable. Overall, the first approach obtained the wing design with the best Breguet range performance requiring the least manual interference and iterations. However, given a realistic guess or even some external mass requirements for allowable FE mass the second approach might be considered as well. Only the sequential approach has been found unsatisfactory as it required the most manual interaction to find the correct settings for the optimization and still could not produce a result with comparable performance.

Therefore, in the following chapter the application of the found aeroelastic shape optimization process on an industrial scale model applies the first approach using the combined objective function with twist, chord length and wing span shape design variables.

4.3 Application to an Industrial Scale Aircraft Model

In order to validate the developed shape optimization framework and the process under more realistic circumstances, the model of a short range passenger aircraft of industrial scale complexity was optimized. For this, the CSR-01 configuration of the CeRAS (Central Reference Aircraft data System) project developed at RWTH Aachen ([RSS+14]) was chosen. This aircraft is comparable to the Airbus A320 class and is built from aluminium. Due to the stronger sweep of the wing and the higher cruise flight velocity, this model promised more critical aeroelastic behaviour than the rectangular wing model discussed in the previous sections. It was also chosen for its extensive dataset, which includes available information about geometry, structure, masses and propulsion. Table 4.32 provides an overview of the aircraft's main characteristics provided on the project's web page [RSS+14].

Table 4.32: Overall characteristics of the CSR-01 configuration

Maximum Take-off Mass m_{MTOM}	77.0	t
Maximum Fuel Mass m_{MFM}	18.7	t
Cruise Mach Number M_{Cr}	0.78	
Wingspan	34.07	m
Reference Area S_{Ref}	122.4	m^2
Reference Chord length c_{Ref}	6.025	m
Mean Aerodynamic Chord MAC	4.18	m

4.3.1 Optimization Problem Definition

In the following the different required models, their parametrization, as well as, the design criteria used in the optimizations of this chapter are described.

4.3.1.1 Modelling

As described in Section 3.3.1.2 a number of different models are required to perform an aeroelastic shape optimization with this framework. These models are described here successively.

First of all a CPACS model for parametric geometry definition was required. This parametrized geometry functioned as a basis for the different analysis models. The CPACS model provided on the CeRAS homepage was extended with a manually regenerated definition of the main wing based on the loft information of the aircraft model. This allowed to place a greater number of sections on the wing than in the original in order to have more locations at which shape variables may be defined. Only the right half model was studied to save computational effort. As a consequence, the vertical tail was not modelled in the analysis models, because no unsymmetrical load cases would be considered. Since the official CPACS definition of the aircraft mainly contained information about the outer geometry of the fuselage and lifting surfaces, internal structure as well as trailing edge devices were added to the CPACS definition of main wing and horizontal tail. These trailing edge devices were not manipulated for flight mechanical purposes, but were used to achieve a realistic stiffness behaviour of the wing (especially torsional stiffness).

Fig. 4.48a shows the parametric geometry model based on the CPACS dataset. The internal structure of spars, ribs and stringers are highlighted in red, whereas the CPACS sections that were used for shape design variable definition are outlined in black. Using symmetry the main wing was constructed out of 8 sections in spanwise direction on the right half, while the horizontal and vertical tail planes consisted of 3 sections each. Since the tail surfaces of the aircraft were not part of the shape optimizations, the lower number of sections was sufficient for describing the geometry. Based on this parametric geometry model the different analysis models were generated and mapped back onto the geometry to allow consistent shape modifications of all models during optimization (see Section 3.6.1).

In Fig. 4.48b one can see the structural FEM model of the aircraft, which was

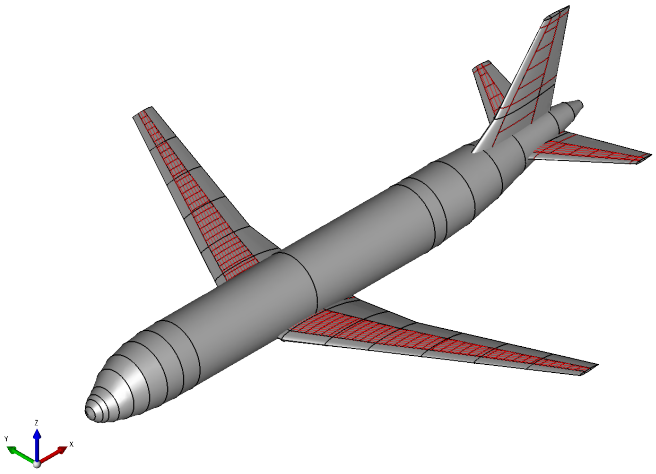

(a) CPACS model

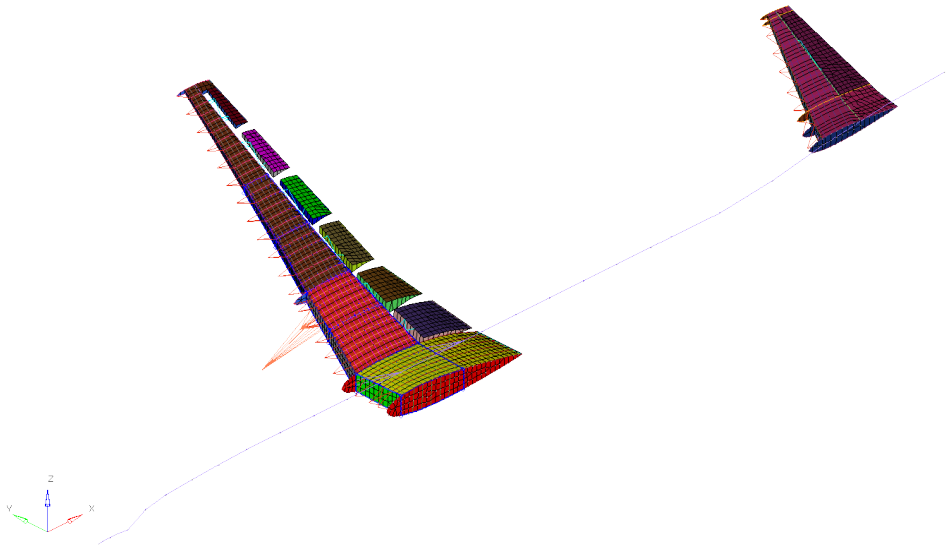

(b) Structural FEM model

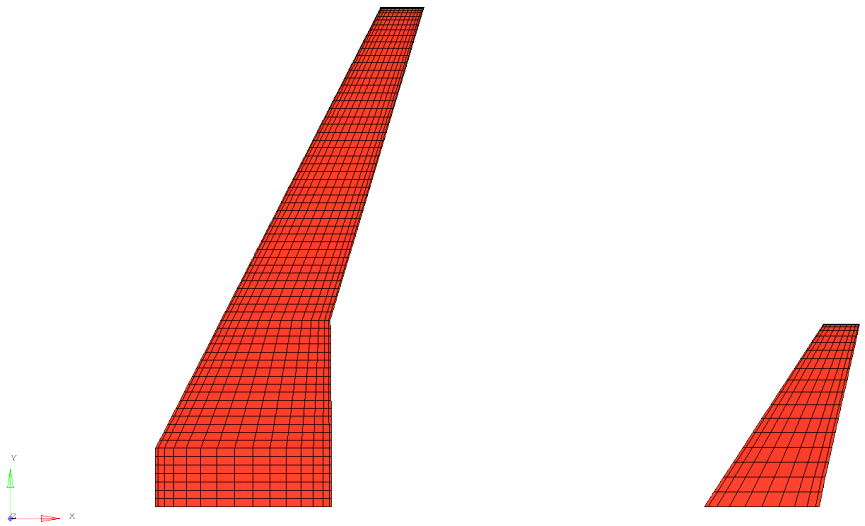

(c) Aerodynamic *AVL* model

Fig. 4.48: Different models of the CSR-01 configuration

constructed out of shell elements combined with 1D stiffeners. The fuselage was modelled only as a stick with point masses, since it was not in scope for the shape optimization and was only required as a flexible connection between wing and tail. Its stiffness properties were deducted from the outer geometry of the fuselage. The right half of the main wing was modelled entirely using the geometrical and structural definition of the CPACS model. The wing box structure was represented realistically using 2 spars and 41 ribs with their caps as 1D elements, as well as, the skin with stringers. Leading and trailing edge areas of the wing were modelled specifically to have no influence on the stiffness of the wing box. However, in order to introduce the aerodynamic forces in these regions correctly, statically determined trailing edge flaps, as well as, three rod trusses at the leading edge were included. This way the aerodynamic loads could be passed into the wingbox without increasing the overall stiffness of the wing. Through these means, it was guaranteed that only the wingbox carried the aeroelastic loads, as in reality the leading and trailing edge parts of the wing are split into many segments housing different kinds of control surfaces or high lift devices not contributing to the stiffness of the wing. The horizontal tail plane (HTP) was modelled similarly with an elevator. The tail was not part of the shape optimization but was employed for pitch moment trimming. This was done by rotating the whole tail plane acting as an all-movable-tail.

The FE model of the CSR-01 represented the maximum take-off mass (MTOM) mass configuration. As only one mass configuration is currently supported by the framework, this one was chosen to provide worst case loads for the structural criteria, even though, the cruise flight would never be conducted in this setting. Initially, all shell elements were defined with a uniform thickness of 3 mm of Aluminium 7075. Concentrated masses were included for engine, pylon and fully filled fuel tanks in the wing (see Fig. 4.49). The masses for fuselage, vertical tail, payload and systems were all applied to the nodes between the fuselage bar elements adjusting the overall FE model mass for MTOM configuration. Secondary wing and HTP structural masses, thus, were also applied on the fuselage due to lack of additional information (through this, the wing was loaded more severely, which made the results conservative). The centre of gravity was placed so that a static margin of 10 % mean aerodynamic chord MAC was met.

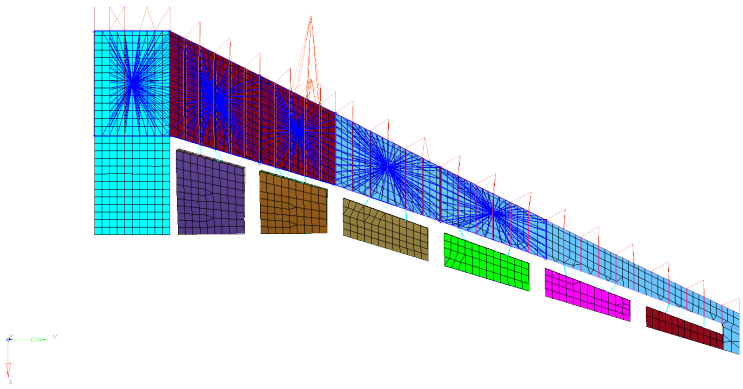

Fig. 4.49: Engine, pylon and fuel tank masses

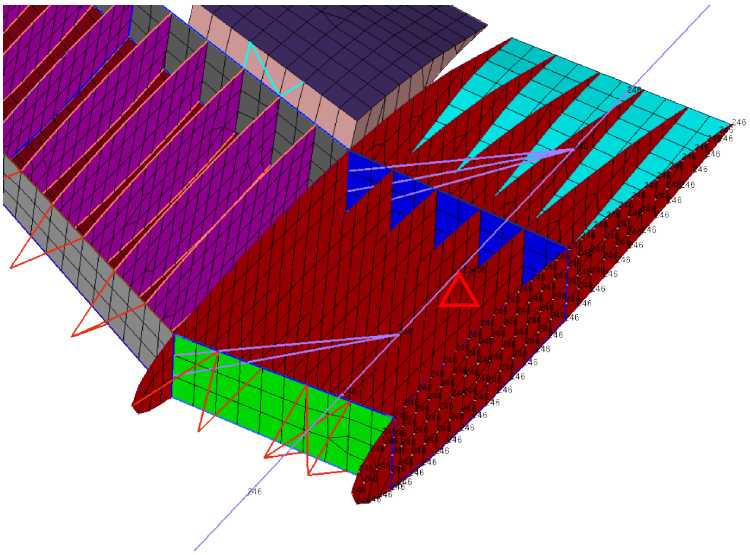

Fig. 4.50: Mounting of the FEM model

The model was mounted in the fuselage at its global centre of gravity (see Fig. 4.50). Wing and tail were connected to the fuselage in the x and z degrees of freedom using rigid elements. The symmetry conditions for the half model were enforced at every point located in the symmetry plane.

The corresponding aerodynamic *AVL* model is depicted in Fig. 4.48c. Accordingly, only the right halves of the main wing and the horizontal tail were modelled for this. In total 1215 horse-shoe vortex elements were used to describe the two lifting surfaces. In chord direction both surfaces were discretised using a cosine distribution. In span direction a segment wise constant discretisation size was chosen except for the tip most segments that were assigned a negative sine distribution.

In order to guarantee physically sound results of the analysis models, mesh convergence studies were conducted for the *AVL*, as well as, the FEM mesh. In case of the FEM mesh, the parametric geometry was meshed with three different element sizes. For each of these three models a force was applied on the wing tip and the displacements were compared. Table 4.33 shows a comparison

Table 4.33: FE mesh convergence study

Element size	Analysis time	Tip displacement	Average Stress
200	3.76 s	1137 mm	142.83 MPa
100	19.65 s	1135 mm	142.79 MPa
50	206.71 s	1136 mm	143.02 MPa

of the results of the FE models with different element coarseness. The displacement was measured at the trailing edge of the wing tip, while the stress was evaluated as an average of all elements in a selected buckling field. Based on the significant difference in analysis time (wall clock time on a single work station) compared to the small deviations in deformation and stress, the FE model with an element size of 200 was chosen.

In case of the aerodynamic vortex lattice model the spanwise, as well as, the chordwise discretisation of the main wing was studied considering the overall lift and induced drag coefficients. From experience a cosine distribution was chosen in chord length while a negative sine distribution was assigned always to the outermost segment in spanwise direction. The remaining segments had an equal spanwise discretisation. As the differences between the results in

Table 4.34: *AVL* mesh convergence study

No. of vortices	C_L	$C_{D_{ind}}$	Time
Spanwise			
29	0.560 09	0.011 88	0.55 s
69	**0.559 14**	**0.011 90**	**1.42 s**
116	0.559 13	0.011 88	3.47 s
Chordwise			
8	0.559 59	0.011 92	0.75 s
15	**0.559 14**	**0.011 90**	**1.42 s**
35	0.559 72	0.011 91	6.27 s

Table 4.34 were very small, the selected discretisation (marked bold) was chosen based on analysis time and result precision.

For aeroelastic analysis, the aerodynamic loads and the structural displacements were coupled using the infinite plate spline method as described in Section 2.1.3.

4.3.1.2 Analysis Load Cases

A similar set of load cases as in the previous optimizations with the rectangular wing was defined for this model. Thus, three aeroelastic and one static load case were considered. In reality many more load cases would be required for MDO of an aircraft. However, with this set it was attempted to represent the most crucial loads without increasing the computational times too severely.

Even though the Mach number of these load cases lies in the transonic region, where the aerodynamic analysis method of the framework is unable to reproduce all prevailing effects (e.g. compression shocks), the realistic Mach number was applied anyway. This was done in order to prevent unrealistically high lift coefficients during the cruise and manoeuvre load cases, which would influence the induced drag coefficients as well. For the future optimization in transonic regions will require higher fidelity aerodynamic methods. However, for the demonstration of the framework's ability to cope with aeroelastic design problems of industrial scale, the compressibility effects were neglected.

As before, the cruise load case was used for induced drag evaluation and the Push-over and Pull-up load cases provided the structurally design critical loads. These three load cases were used for the aeroelastic analysis realistically superposing inertia loads with aerodynamic lift loads while considering structural elasticity. The Parking load case was included as a static state where no

Table 4.35: Load case definition for rectangular wing shape optimizations

Load Case	Mass	Mach Number	Altitude	Load Factor
Cruise	m_{MTOM}	0.78	35 000 ft	1.0 g
Push-over	m_{MTOM}	0.78	35 000 ft	−1.0 g
Pull-up	m_{MTOM}	0.78	35 000 ft	2.5 g
Parking	m_{MTOM}	-	-	1.0 g

aerodynamic forces countered the gravitational load. Through the usage of inertia loads in all cases a realistic representation of the current structural weight was guaranteed at all times during the shape/sizing optimizations.

The cruise load case was used to evaluate the Breguet range performance of the different results. For this, the aeroelastic coefficients were used together with the current mass information. The mission profile for the range evaluation was based on the same definition as in Section 4.2.1.1. Only the required assumptions were adjusted for the current aircraft model, which are presented in Table 4.36. Here, the flight velocity v was taken from the cruise load case defin-

Table 4.36: Data for Breguet range mission of the half model

Parameter	Value	Unit
v	231.3	$\frac{\mathrm{m}}{\mathrm{s}}$
$TSFC$	$1.673 \cdot 10^{-5}$	$\frac{\mathrm{kg}}{\mathrm{N\,s}}$
C_{D_0}	0.015 55	-
g	9.81	$\frac{\mathrm{m}}{\mathrm{s}^2}$

ition, the thrust specific fuel consumption was available in the CeRAS documentation and the viscous drag coefficient C_{D_0} was estimated using FRICTION [Mas02] similar to the rectangular wing model before.

4.3.1.3 Design Variable Definition

Three different types of design variables were defined for the following optimizations, shape variables for the outer geometry, sizing variables for satisfying the structural constraints, as well as, trimming variables for correct flight mechanical loads.

Shape Design Variables The three types of shape variables selected in Section 4.2.2.1 (chord length, twist and wing span) were considered in this optimization. Generally, only the main wing was parametrised, the horizontal tail was merely used for trimming purposes. In Fig. 4.51 the locations of these variables are shown.

One wing span variable, as well as , chord length and YRotation (twist) variables at each CPACS section were defined. This amounted to a total of 17 shape design variables.

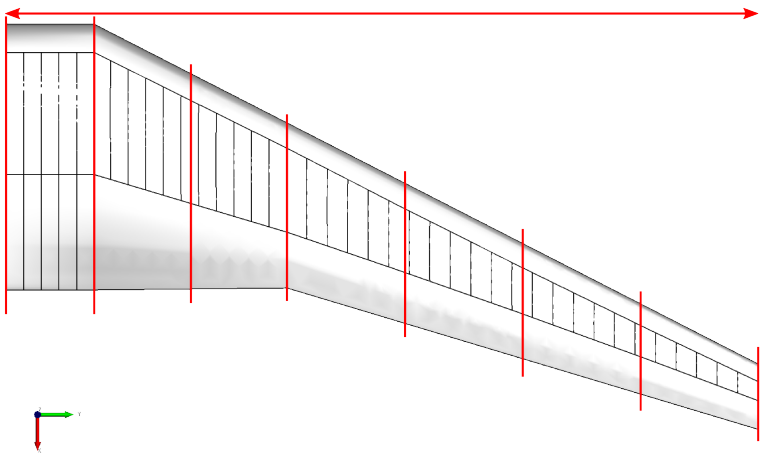

Fig. 4.51: Location of the shape design variables on the CSR-01 aircraft

Sizing Design Variables Only the finite elements of the main wing box were used as sizing design variables, since this carried the main load of the wing. Here, the upper and lower skin, spars, ribs, stringers, as well as, rib and spar caps were parametrised as sizing variables.

The skin thickness and stringer cross section variables were linked region wise using spars, ribs and stringers as boundaries. In total this created 1681 sizing variables.

Trimming Design Variables In order to trim the overall aeroelastic lift load, as well as, the pitching moment around the centre of gravity, two independent trimming design variables were defined for each aeroelastic load case of Table 4.35. Thus, the angle of attack of the main wing and the incidence of the horizontal tail were provided with a scaling factor, as described in Section 3.3.3. This amounted to a total of 6 trimming design variables.

As a summary the 1704 defined design variables are listed together with their gages in Table 4.37.

4.3.1.4 Optimization Constraints

In order to ensure structural integrity of the optimization results, a set of different design criteria was defined. All in all, 26 460 constraints were included considering the four specified load cases. The different types are presented in the following paragraphs.

Von Mises Stress constraints were defined for all finite elements that were part of a sizing design variable. Through this it was guaranteed that the sizing variables were only reduced, if the structural strain could be supported in all affected finite elements. Thus, von Mises stress constraints were defined for wing skin, stringers, spars, ribs and spar/rib caps.

Since the model was entirely constructed from Aluminium 7075, the allowables for the stress constraints were set accordingly to a maximum of 336.67 MPa. This value already included a safety factor of 1.5 to account for any effects that

Table 4.37: Design variable definition for CSR-01 shape optimizations

Design Variable x	Lower Bound x_{lb}	Upper Bound x_{ub}
Shape		
Twist/YRotation x_{t_i}	$-5°$	$5°$
Chord Lengths x_{c_i}	1400 mm	6500 mm
Wing half span x_s	15 000 mm	22 000 mm
Sizing x_{Size}		
Skin, Ribs, Spars	1.0 mm	20.0 mm
Stringer	100 mm^2	500 mm^2
Spar/Rib Caps	50 mm^2	200 mm^2
Trimming		
Wing α_W Scale Factor x_{α_W}	-50	50
HTP α_{HTP} Scale Factor $x_{\alpha_{HTP}}$	-50	50

were not covered by the simulation. Hence, a total of 5926 von Mises stress constraints were evaluated per load case.

Skin Buckling Stability constraints were included to prevent two dimensional buckling of the wingbox skin between leading and trailing edge spar. Thus, the upper and lower skin of the wingbox was segmented into buckling fields by means of spar, rib and stringer crossings (Fig. 4.52). This yielded 686 buckling constraints for each of the four load cases. For each of these buckling fields the geometry and the applied stress were used to calculate a constraint value as described in Section 3.4. Similar to the stress constraints a safety factor of 1.5 was incorporated into the constraint definition to account for inaccuracies of the simulation.

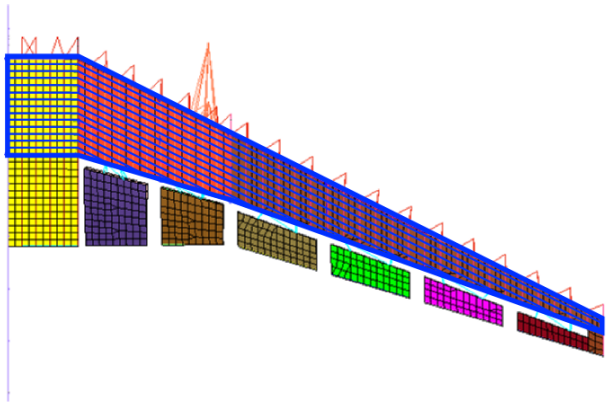

Fig. 4.52: Buckling field definition of the CSR-01 main wing

Trim Constraints Four trim constraints were defined for each of the three aeroelastic load cases in Table 4.35. These were assigned to the aeroelastic loads (including effects of structural flexibility) to guarantee proper overall lift, as

well as, zero pitching moments. As only inequality constraints are supported, minimal and maximal constraints for both responses had to be defined (see Section 3.4.3). Thus, a fixed aeroelastic overall lift based on the MTOM mass and the manoeuvre load factors was required by the constraint considering the effects of mass distribution on the aeroelastic displacements. The pitching moment around the centre of gravity was constrained to a small region around zero.

Therefore, in total 12 trim constraints were defined for the optimization problem assuring constant lift and close to zero pitching moment.

4.3.2 Preliminary Sizing Optimization

Before the shape optimizations were conducted, the initial design was improved through a preliminary sizing optimization. The goal of this optimization was to find a realistic structural design, since the initial design was constructed using uniform thickness and cross section area for the whole model. Furthermore, initially not all structural constraints could be satisfied with the chosen material distribution. Thus, this optimization was also used to find a feasible point in the design space. Hence, a sizing optimization with an FE mass objective function was conducted using all constraints from Section 4.3.1.4 and the design variables listed in Table 4.37 except the shape variables. The optimizer managed to satisfy all constraints (see Fig. 4.55) and increased the structural mass by roughly 300 kg in order to do so.

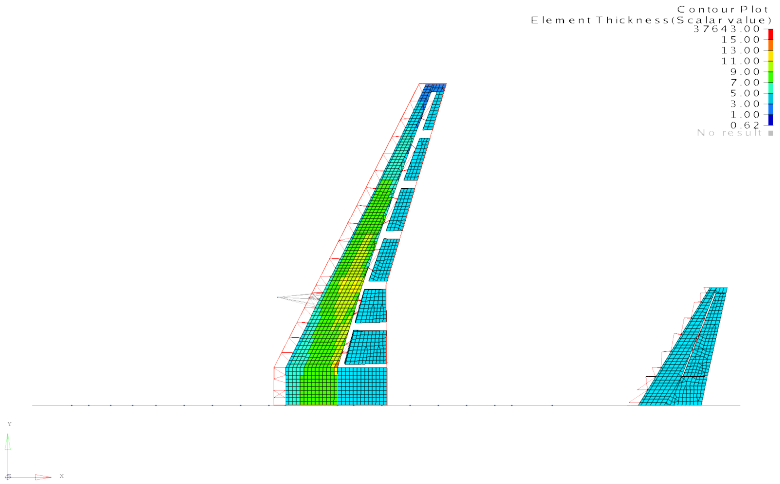

Fig. 4.53: Skin thickness result of preliminary sizing

The resulting skin thickness distribution in Fig. 4.53 shows two regions of material accumulation; one near the trailing edge kink of the wing at roughly $\frac{1}{3}$ of wing span and the other between the innermost flap and the fuselage junction near the rear spar. Comparing this to the aeroelastic displacements in Fig. 4.54 revealed that the highest strain occurred in the wing at $\frac{1}{3}$ of the span due to the low displacements near the root caused by the load relieve through the fuel and engine masses. The second peak in skin thickness can be explained by the connection to the supported fuselage at that point.

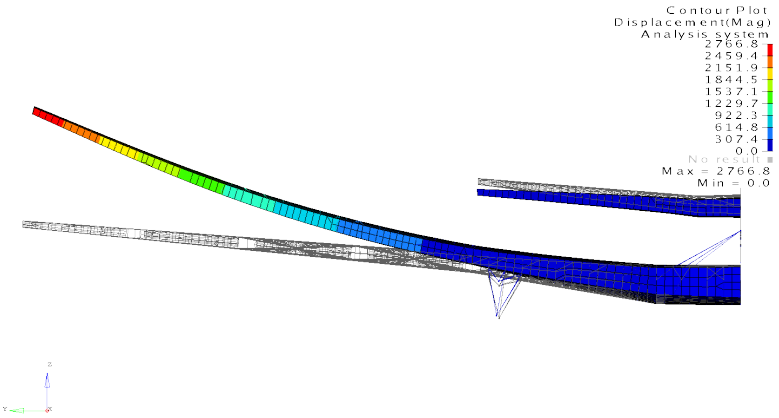

Fig. 4.54: Aeroelastic displacement of pull-up load case (with wire frame of undeformed)

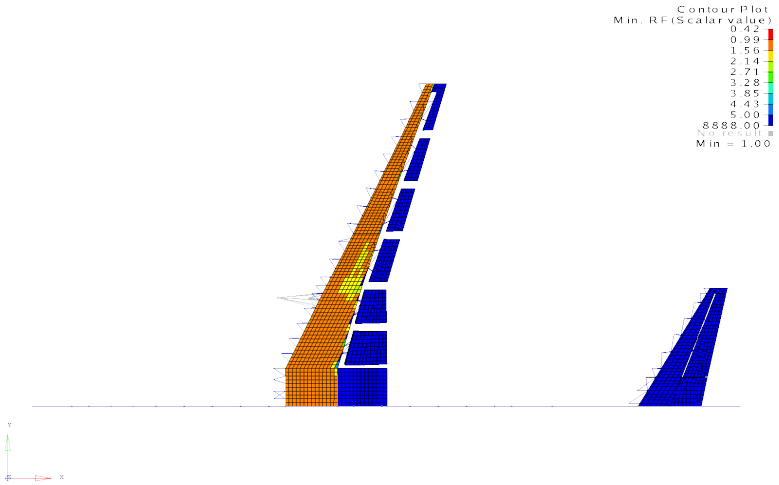

(a) Buckling reserve factor

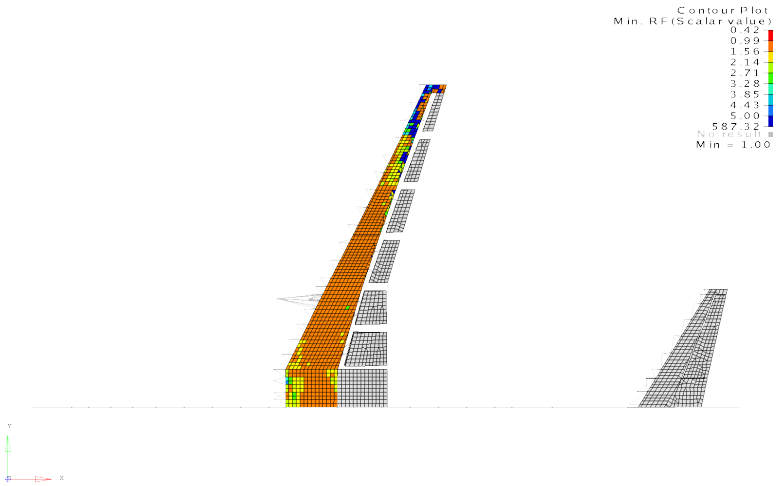

(b) Von Mises reserve factor

Fig. 4.55: Minimal reserve factors after preliminary sizing

The constraint reserve factors in Fig. 4.55 revealed that most of the sizing design variables could be reduced to the point where one or both types of structural constraints become active.

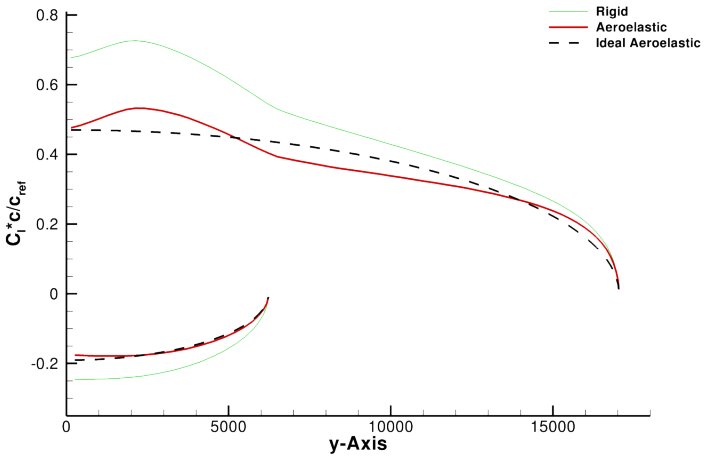

Fig. 4.56: Span wise lift distribution after preliminary sizing

Fig. 4.56 shows the spanwise lift distribution during the cruise load case after the preliminary sizing for both lifting surfaces. Due to the backward sweep a reduction in local lift near the root would be expected [ST01b, p. 74]. However, the twist distribution and planform of the initial geometry increased the local angle of attack up to about $\frac{1}{3}$ of wing span, which can be seen by the bump in the local lift near the wing root. Furthermore, a significant difference between the rigid and the aeroelastic lift distribution could be observed caused by the tendency of backward swept wings to aeroelastic lift reduction [BAH96, pp. 474-475].

This result was taken as an initial point for the subsequent shape optimizations. Hence, it was necessary to adjust the concentrated masses to account for the change in structural mass due to the sizing. Also the centre of gravity was moved to its original position by adjusting the concentrated masses on the fuselage.

Table 4.38: Performance of sizing result during cruise

	Rigid	Aeroelastic
m_{FE}	38.500 t	
C_L	0.7416	0.6049
$C_{D_{ind}}$	0.0222	0.0149
R_{Br}	6164 km	6235 km

As a reference for subsequent optimizations, the performance characteristics of the sized result are presented in Table 4.38 for rigid and aeroelastic analysis. The mission profile of Section 4.2.1.1 together with the assumptions in Section 4.3.1.2 were applied for the Breguet range performance evaluation. The same approach was used for the assessment of any following optimization result.

4.3.3 Aeroelastic Shape Optimization

Based on the result of the preliminary sizing optimization a full aeroelastic shape optimization applying load cases, design variables and constraints, as described in Sections 4.3.1.2 to 4.3.1.4, was conducted. The aeroelastic shape optimization was carried out using the Breguet objective function, since it provided the result with the best performance in Breguet range compared to a number of reference optimizations with weighted objective functions (not presented here) in accordance with the findings of Section 4.2.1.2.

The optimization ran over 40 iterations after which it was stopped manually without satisfying the KKT convergence criterion. The optimization history was examined in terms of constraint violation and change in objective function value. Both suggested a feasible design with very little improvement over the last iterations so that the result was taken as converged without further restarts. At this point, 4708 of the all in all 26 460 constraint functions were active.

The first thing apparent from the resulting wing planform in Fig. 4.57a is the increased wing span compared to the initial planform (red outline), though, not reaching the maximum gage indicated by the red line. The wing half span was increased by roughly 2.5 m finding a trade-off between low induced drag and FE mass as mentioned in Section 4.2.2.2. In terms of chord length, higher values were assigned at the position of the initial trailing edge kink allowing a more homogeneous skin thickness distribution in that area. At about 70 % of half span a trailing edge kink can be seen, where the chord length approached to its minimal gage. Except for a small chord reduction at the root an almost linear chord length distribution was created through this (see Fig. 4.57d). Similar to the preliminary sizing result a peak in skin thickness could be witnessed at the trailing edge spar near the cut-out of the innermost trailing edge flap, where the structural load concentrates due to the geometry and the connection to the fixed fuselage in its vicinity.

Concerning the spanwise aeroelastic lift distribution in Fig. 4.57b one can see that an almost triangular distribution was found with a steeper lift load decrease outboard of 50 % half span compared to the initial state in Fig. 4.56 allocating more lift close to the wing root. The twist distribution Fig. 4.57c shows how this was achieved in collaboration with the chord length distribution. Twist exhibits a small peak corresponding to the position of the newly formed trailing edge kink. This demonstrates that the kink was created due to structural or mass saving requirements and twist was used to moderate the aerodynamic effects of the planform modification. Without the kink both, chord length and twist distribution, could have realized the same lift distribution without peaks in either shape variable type.

With these measures the optimizer managed to decrease induced drag by 22 % limiting the FE mass increase to about 1 % compared to the initial values (cf. Table 4.39). This resulted in an aeroelastic Breguet range based on the given mission profile of 6734 km.

This result was verified by running two additional aeroelastic shape optimizations from different initial points ruling out initial point problems such as described in Section 4.1.4.1. These two shape optimizations had significantly modified initial span, chord length and twist configurations compared to the

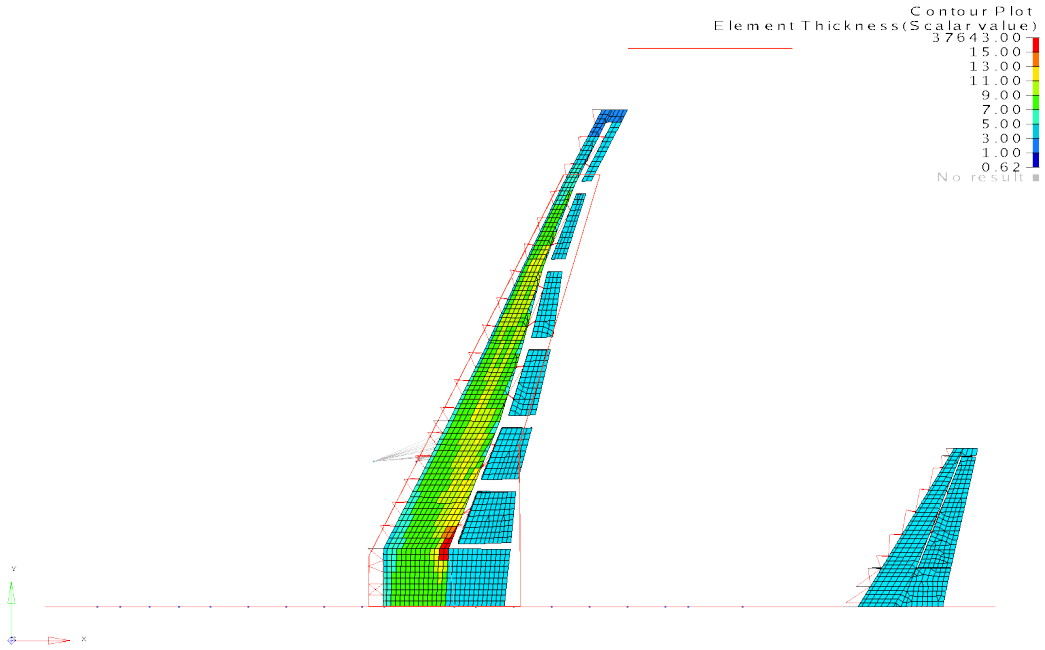

(a) Planform and skin thickness

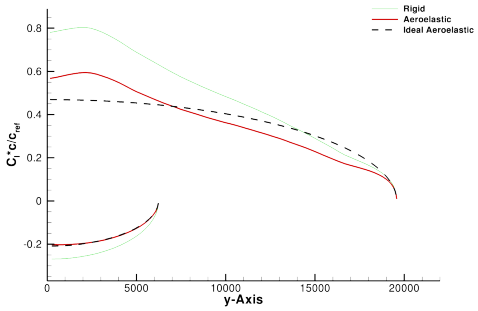

(b) Spanwise lift distribution

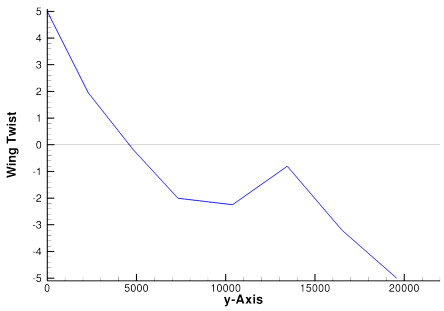

(c) Spanwise twist distribution

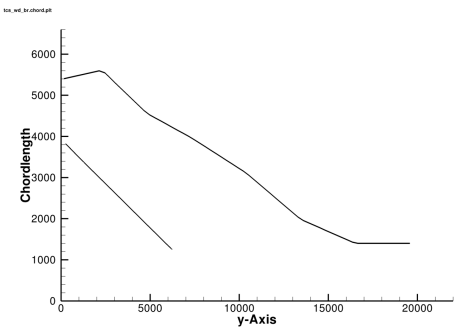

(d) Spanwise chord length distribution

Fig. 4.57: Aeroelastic shape optimization result with Breguet objective

Table 4.39: Result summary of Breguet shape optimization (aeroelastic)

	Initial	Final	Delta
m_{FE}	38.500 t	38.746 t	+0.64 %
C_L	0.6049	0.6049	0.00 %
$C_{D_{ind}}$	0.0149	0.0116	−22.32 %
R_{Br}	6235 km	6734 km	+8.01 %

one presented above. Both of these additional shape optimizations found wing designs with a planform very similar to the one presented here. Thus, the Breguet range performance deviated by less than 0.25 % relative to the first result discussed above. Therefore, one can say that for this specific optimization problem no such issues of a non-convex design space as witnessed in Section 4.2.2.2 could be found. Also, the aircraft design found by the first optimization could be confirmed.

In order to estimate the error done by assuming constant buckling field geometry and coupling matrices during the shape optimization (see Section 3.4, Section 3.2.2), a re-analysis with updated buckling field shapes and coupling matrices was conducted for the shape optimization result. It showed that some of the buckling constraints were violated so that a sizing optimization of this state was performed with the same settings as the shape optimization before to reach a feasible design. This resulted in a small performance reduction of 0.8 % in range. Therefore, the assumption of keeping the buckling field geometry and coupling matrices constant during the shape optimization was considered as non critical in this case.

4.3.4 Comparison to Singular Objective Results

The same aeroelastic shape optimization was repeated once with the single induced drag objective function and once with the single FE mass objective. Both were stopped after 60 iterations and considered converged due to their iteration history without satisfying the KKT. Their results are shown in Fig. 4.58 and Fig. 4.59 respectively. As expected, the induced drag optimization used the maximum allowed wing span for low induced drag, while the FE mass optimization reduced span to the minimal gage for the sake of minimizing weight. The planform of the induced drag optimization showed an almost linear decrease in chord length towards the wing tip with high values near the root to support the increased wing span. In case of the FE mass optimization chord lengths were generally decreased forming a trailing edge kink near two thirds of half span, where the minimal gage chord length was reached. All in all, this allowed significantly lower skin thickness values compared to the induced drag result (see colours in Fig. 4.58 and Fig. 4.59).

For lower FE mass the optimizer also manipulated the lift distribution to reduce the root bending moment by shifting the lift resultant inwards towards the root and severely removing lift load from the tip. In contrast to the optimizations with the single rectangular wing in Section 4.1, the induced drag

optimization did not reach an elliptic lift distribution for the main wing, even though the shape parameters would have allowed. The reason for this could be found in Munk's Stagger Theorem [Mun23] stating that for multiple staggered lifting surfaces with unchanged lift distributions the distance in flow direction has no influence on the overall induced drag. Thus, main wing and horizontal tail plane of this model acted as one wing in the Trefftz Plane, since their separation perpendicular to the flow direction was relatively small. Therefore, the combined lift distribution of wing and tail had to be modified to achieve beneficial induced drag generation characteristics. And since the lift on the tail was prescribed by the pitch moment trimming constraint, the distribution of main wing had to account for that. Among other factors this caused the increase in the main wing lift distribution coinciding with the spanwise location of the horizontal tail. To verify this, the same shape optimization for minimal induced drag was conducted only modelling the main wing of the aircraft, which obtained the expected elliptic lift distribution (not shown here), as no interference of the tail plane was present.

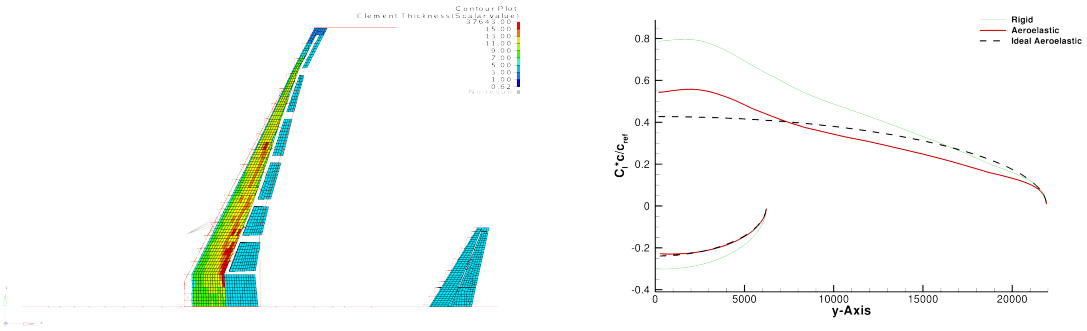

(a) Planform and skin thickness (b) Spanwise lift distribution

Fig. 4.58: Result of singular induced drag optimization

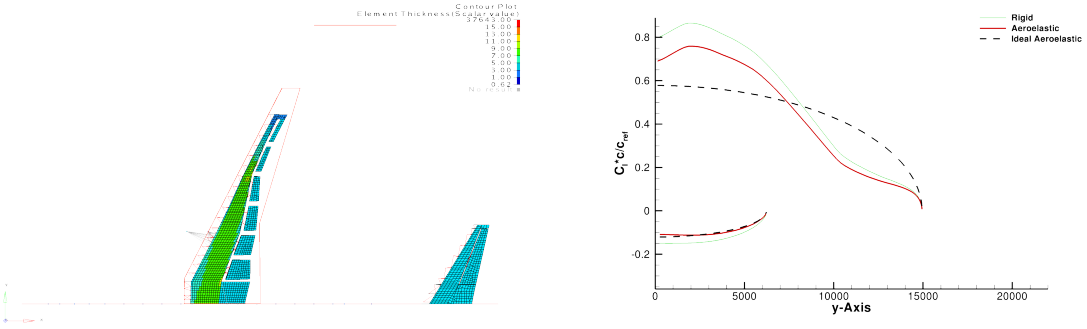

(a) Planform and skin thickness (b) Spanwise lift distribution

Fig. 4.59: Result of singular FE mass optimization

The performance characteristics of the two singular objective results were compared to the Breguet objective function design evaluating the aeroelastic analysis results (see Table 4.40). It becomes obvious that the induced drag result managed to slightly increase the Breguet range with respect to the initial performance of 6235 km, while the FE mass optimization significantly worsened

the Breguet range value. This shows that the weight savings of almost 600 kg could not compensate for the substantial induced drag rise, but the additional 922 kg of the induced drag optimization more than cancelled out the induced drag savings. The Breguet objective result moved toward the induced drag value of the singular optimization but managed to limit the structural mass penalty caused by induced drag reduction measures to less than 250 kg. Through this, the best range performance could be reached by the Breguet objective optimization. Part of this could be realized by finding a good trade-off for the wing span between low induced drag and the mentioned FE mass penalties associated with high wing span.

Table 4.40: Comparison of aeroelastic results with different objective functions

	Initial	Ind. Drag	FE Mass	Breguet
m_{FE}	38.500 t	39.422 t	37.929 t	38.746 t
C_L	0.6049	0.6049	0.6051	0.6049
$C_{D_{ind}}$	0.0149	0.0100	0.0221	0.0116
R_{Br}	6235 km	6390 km	5491 km	6734 km

To estimate the influence of the shape changes on the viscous drag coefficient, FRICTION was applied as in Section 4.2.1.3 to update the viscous drag component based on the resulting geometries of the optimizations. The obtained coefficient values and their corresponding Breguet range performances are listed in Table 4.41.

Table 4.41: Aeroelastic Breguet range comparison with updated viscous drag

	Initial	Ind. Drag	FE Mass	Breguet
C_{D_0}	0.01555	0.01680	0.01394	0.01589
R_{Br}	6235 km	6092 km	5736 km	6650 km

The same tendency as in Section 4.2.1.3 could be found in these results that FE mass as an objective leads to designs with lower viscous drag, while the induced drag objective increased the lift independent drag through greater wetted area. Here, this lead to the induced drag result more than loosing its range benefits achieved through the optimization. Opposed to the previous findings in Section 4.2.1.3, the Breguet objective could not reduce induced and viscous drag simultaneously in this case. Thus, a slight increase in viscous drag can be seen causing the Breguet range to drop by about 1.25 % relative to the corresponding value in Table 4.40, where constant viscous drag was assumed.

Hence, the assumption of constant viscous drag was not conservative in this case. Even though the performance of the design was reduced by only a small amount so that overall the range could still be increased, this underlines the importance of considering all drag components in shape optimizations such as these. Therefore, part of future work will be the implementation of a viscous drag estimation method into the shape optimization framework providing this sensitivity to the optimizer as well.

Another approach could be to include a geometrical constraint on the maximum wing area (see Section 3.4) in the shape optimizations so that an excessive increase in wetted area is prevented (see e.g. [Ken12]). For comparison, the same shape optimization as in Section 4.3.3 was repeated including a geometric constraint limiting the maximum wing area to its initial value. The optimization behaved very similar to the one without the geometric constraint but yielded a Breguet range of about 6714 km with updated viscous drag ($C_{D_0} = 0.015\,59$) and a very similar planform shape. Hence, the negative effects of keeping the viscous drag component constant during the shape optimizations could be countered by constraining the wing area.

4.3.5 Rigid Shape Optimization

To assess the importance of the aeroelastic analysis during the shape optimizations of this model, the Breguet range objective shape optimization was repeated with rigid aerodynamic load calculation disregarding all aeroelastic effects (analogue to Section 4.1.3.3). Thus, the same shape and sizing optimization as in Section 4.3.3 was repeated using the rigid analysis results for the Breguet range objective function and the rigid aerodynamic coefficients. In order to have the same overall load for comparison of the results, the trimming constraints for this optimization were defined for the rigid loads. Through this, the conducted shape optimization solved the same optimization problem, yet, with all aeroelastic interactions disregarded.

Similar to the aeroelastic run, the rigid shape optimization ran over 40 iterations and was stopped manually at that point taking into account its iteration history. Fig. 4.60 shows the corresponding planform and skin thickness distribution result. In comparison to the result of the aeroelastic shape optimization (Fig. 4.57) it appears that both optimizations found very similar solutions only with a slightly higher wing span in the rigid case.

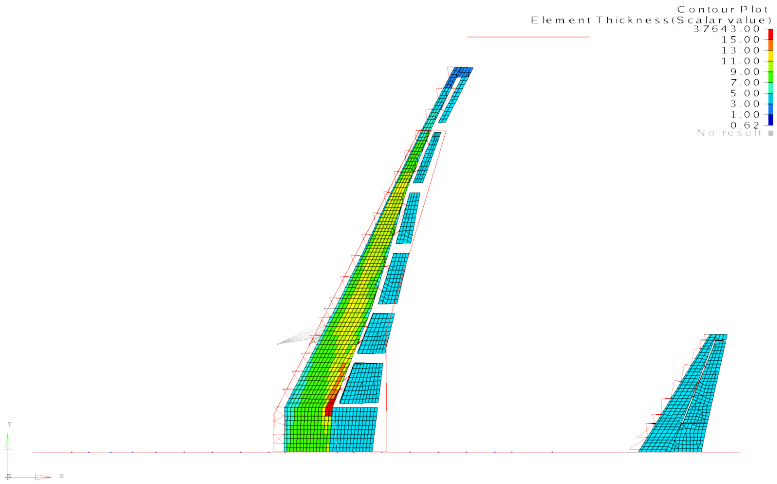

Fig. 4.60: Planform and skin thickness of rigid shape optimization result

Fig. 4.61 shows the resulting chord length and twist distributions of the rigid shape optimization with the values of the aeroelastic run as reference. As

expected from the similar planforms, the chord length and twist distributions show a similar trend. In these plots the slightly increased wing span is more prominent. The differences in the spanwise twist distribution are stronger than the chord length. The rigid optimization shows lower twist angles near the root, while near the wing tip the twist values are similar but shifted outwards due to the higher wing span. The effects of the lower twist angles near the wing root can also be seen in the lift distribution in Fig. 4.62 that includes results of the aeroelastic re-analysis.

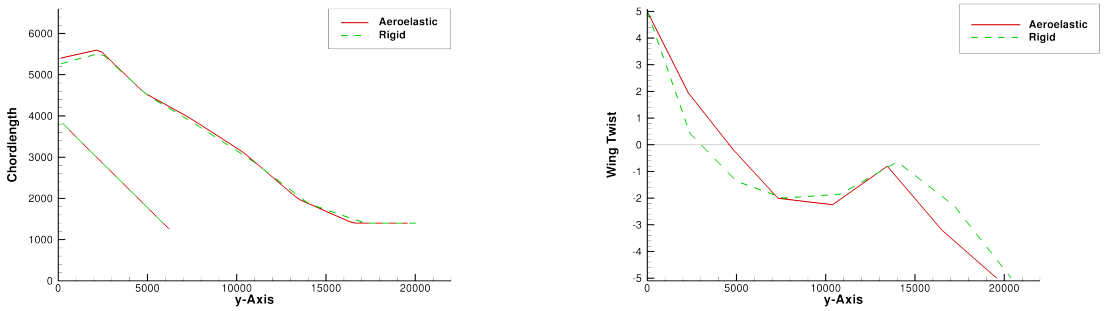

(a) Spanwise chord length distribution (b) Spanwise twist distribution

Fig. 4.61: Result of rigid shape optimization with Breguet objective

The main difference to be seen in Fig. 4.62 is the lower overall lift in case of the rigid optimization result. This was caused by the trimming constraints that restricted the rigid loads in this case. Therefore, the green lift distribution in Fig. 4.62a needs to be compared with the bold red line of Fig. 4.62b, as they were trimmed to the same overall lift. Due to the similar chord length and twist distributions, the corresponding spanwise lift distributions also show a strong analogy.

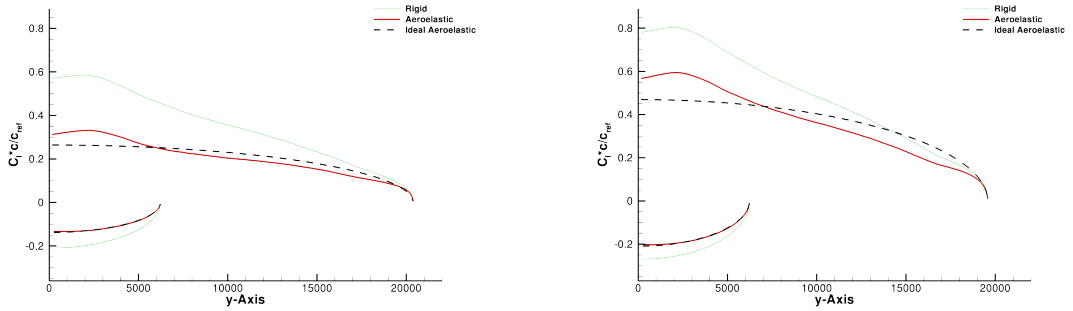

(a) Rigid shape optimization (b) Aeroelastic shape optimization

Fig. 4.62: Spanwise lift distributions

In Table 4.42 the results of the two shape optimizations are compared based on their rigid and aeroelastic performance. The Breguet range values that were considered in the respective objective function are printed in bold letters. Comparing these bold range performance values shows that the rigid shape and sizing optimization found a solution that outperformed the aeroelastic one by

almost 130 km. However, looking at the aeroelastic performance of the rigid result showed a drastic reduction in range by more than 1400 km, whereas the aeroelastic optimization result exhibited far less change between rigid and aeroelastic, even marginally improving with consideration of aeroelasticity. Yet, the presented values of the rigid result were physically infeasible if analysed aeroelastically, as the overall lift was reduced by aeroelastic effects to almost half the value required for a trimmed steady cruise flight (Table 4.42). A reanalysis of this design trimmed to the required aeroelastic lift caused many structural constraints to be violated. Consequently, a sizing optimization of the rigid result using aeroelastic analysis followed in order to gain a design feasible for the aeroelastic load state. Its resulting values are listed in the rightmost column of Table 4.42. Through this, a fair comparison of the different designs was possible, as now structural integrity could be met for the same aeroelastic flight state.

Table 4.42: Result comparison of rigid and aeroelastic Breguet range shape optimizations

	Aeroelastic Shape Run	Rigid Shape Run	Sizing of Rigid Run
m_{FE}	38.746 t	38.800 t	39.111 t
C_L	0.6049	0.3473	0.6049
$C_{D_{ind}}$	0.0116	0.0037	0.0109
R_{Br}	**6734 km**	5399 km	**6502 km**
Rigid C_L	0.8078	0.6049	0.8383
Rigid $C_{D_{ind}}$	0.0207	0.0108	0.0206
Rigid R_{Br}	6724 km	**6860 km**	6586 km

Since the aeroelastic flight state is more relevant for the actual aircraft, the aeroelastic Breguet range was taken for assessment and comparison. After the sizing of the rigid optimization result the aeroelastic Breguet range improved but could not reach the level of the aeroelastic shape optimization. Even though the induced drag value was lower than that of the aeroelastic counterpart, the additional 300 kg due to required increase in skin thickness and cross sections prevented an equally good performance. Another important effect to be seen in Table 4.42 was that the aeroelastic shape optimization design exploited aeroelasticity to gain a slightly more beneficial configuration regarding aeroelastic Breguet range, while the rigid approach generally lost performance, when aeroelastic effects were considered. Through the subsequent aeroelastic sizing optimization of the rigid result, this loss could be reduced but not compensated. On one hand, this was an effect of the low aeroelastic lift after the rigid shape optimization, which caused the induced drag savings to be dominated by the larger lift-independent viscous drag component resulting in a diminished lift to drag ratio. On the other hand, aeroelastic analysis was employed during the sizing optimization allowing to find a feasible design for the aeroelastic state. Hence, this optimization could also exploit aeroelastic effects, however, to a much smaller extent due to the limited influence of the sizing variables on the design compared to the shape variables.

Thus, even though the rigid and the aeroelastic shape optimization roughly found the same design for optimized Breguet range performance, the differences in the details did have a perceivable influence on the final performance of the aircraft. The rigid shape optimization had two major disadvantages. First, the effective overall lift load could not be considered during the optimization making a subsequent sizing optimization necessary to account for the more realistic flight loads influenced by aeroelastic effects. And second, since the system response during the optimization did not contain the aeroelastic behaviour, the optimizer could not actively exploit aeroelasticity for beneficial effects generally called aeroelastic tailoring (also discussed in Section 4.1.3.3).

4.3.6 Summary

The developed shape optimization framework was applied to an aircraft half model of industrial scale complexity in order to demonstrate its capabilities and verify the shape and sizing optimization approach developed in Section 4.2. With this chosen approach, the issues concerning the different shape design variable types and their ambiguity with respect to induced drag (see Section 4.2.2.2) could be managed and a design with improved performance was found for the main wing. Also, this design could be confirmed by a number of similar optimizations from different starting points showing no signs of a non-convex design space. The optimization managed to find a wing span configuration that represented a beneficial trade-off between low induced drag and low structural FE mass for improved Breguet range performance. In agreement with the findings of the previous chapters, the Breguet range objective yielded the best performing design compared to the different available objective function formulations.

Comparing the found design to the results of single objective shape optimizations (induced drag, FE mass) using the aeroelastic coefficients and range performance, confirmed that both disciplines need to be considered during these optimizations to find technically useful designs. Also the penalties of disregarding aeroelastic effects in shape optimizations were studied. This showed that configurations with critical aeroelastic behaviour require aeroelastic loads during shape optimization to obtain feasible and beneficial results that are not weakened by aeroelasticity. Furthermore, by considering aeroelastic effects during shape optimization, solutions could be found that exploited the interaction of structural elasticity and aerodynamic flow conditions for beneficial effects.

Yet, this example showed that the assumption of constant viscous drag over the course of a shape optimization with design variables affecting the planform of an aircraft cannot generally be considered as conservative (as opposed to the results in Section 4.2.1.3). It can be implicitly steered by choosing shape variable gages, objective function weightings or geometrical constraints, but no guarantee can be given that these measures cover all possibilities. In case of the CSR-01 aircraft the viscous drag component was increased through the optimization lowering the benefits achieved by finding a good combination of structural mass and induced drag. Therefore, as part of future work, a method of estimating the lift-independent drag components needs to be included in the

framework.

Apart from this, the successful application of the developed shape and sizing optimization approach to an aircraft model of industrial scale complexity could be demonstrated here.

5 Conclusions

5.1 Summary

In this dissertation a framework was developed allowing combined aeroelastic shape and sizing optimization of aircraft development problems while considering aeroelastic induced drag. This was realized with a levelled shape parametrization approach for consistent geometry changes of the involved analysis models. Furthermore, the framework enabled optimization of large scale problems of industrial complexity considering an extensive criteria model to guarantee the resulting design's feasibility aiding its following certification.

In contrast to the existing research in the field of multidisciplinary shape optimization of aircraft structures described in Section 1.1, the present work focused on a number of aspects crucial to its intended application. First of all, low or medium fidelity analysis methods were used to allow application in early design phases, where great shape design freedom is still present. With these analysis methods, the developed framework was devised with only one overall loop for simultaneous shape and sizing optimization based on the aeroelastic analysis. With this, effective aeroelastic tailoring was enabled using both types of variables influencing the design's properties to reach a beneficial outcome. Furthermore, the different ways and impact of influencing the design of sizing and shape variables also proved advantageous. In order to realize large scale applications of the devised shape optimization capabilities, a gradient based optimization approach was selected. Additionally, the applied direct gradient calculation method with analytical sizing sensitivities made the solution of optimization problems with an extensive multidisciplinary design criteria model possible, which guarantees the feasibility of the acquired optimization results. The applied levelled shape parametrization allowed substantial shape changes with only few shape variables so that finite difference gradients could be used for this design variable type avoiding a significant increase in complexity.

The theory of the different analysis methods required for static aeroelastic analysis was illustrated in Section 2.1. With the targets and requirements of the proposed shape and sizing optimization approach in mind, suitable analysis methods for aerodynamics and structures were identified. Hence, the linear finite element analysis based on thin-walled shell models was chosen for sufficiently precise evaluation of the structural responses and their associated constraints. The aerodynamic solution was selected to be carried out by the vortex lattice method providing lift and induced drag responses so that efficient and robust coupling for aeroelastic analysis could be realized. This method only required low modelling effort but provided reliable results adequate for early design phases. The remaining viscous drag component of the overall drag not provided by vortex lattice was not considered during the optimization and was manually estimated using semi-empirical relations before and after the optimiz-

ations. In order to repeatedly evaluate the aerodynamic loads during the iterative aeroelastic analysis, aerodynamic influence coefficient matrices (AIC) for the pressure distribution but also for the Trefftz Plane induced drag were extracted from the vortex lattice method and provided to the framework. For translation of loads and displacements between the different analysis domains a coupling method based on Infinite Plate Spline [HD72] approach was used.

In Section 2.2 the theoretical aspects of the framework regarding numerical optimization were studied. The gradient based *NLPQL* [Sch86], a variant of the sequential quadratic programming algorithm, was selected as the optimizer. This was found to be an appropriate choice given the size and nature of the proposed application. Additionally, existing approaches for shape parametrization were studied in this section relating their advantages and disadvantages to the given multidisciplinary problem. Hence, a CAD based shape parametrization method using the high level primitives philosophy [LT08] was devised employing the CPACS description format [LH11] to create a central parametric geometry. This allowed consistent shape updates without re-meshing of the different analysis models by mapping the respective mesh nodes to the parametric geometry. Also, a levelled shape design variable paradigm permitting the definition of shape variables with differing complexity and degree of influence was implemented along this course. Different gradient computation methods were studied, as well, regarding applicability and precision for the proposed optimization problems with a great number of design constraints. Finally, theoretical aspects of convergence criteria and multi-objective optimization were treated in this chapter.

Based on the theory and methods selected in the preceding sections, Chapter 3 illustrated the combination and interaction of the different components inside the developed optimization framework. In other words, the required components for defining a multidisciplinary shape and sizing optimization problem such as analysis, parametrization, design criteria and objective function were further detailed. Hence, the aeroelastic analysis process, as well as, the evaluation of aeroelastic induced drag using the Trefftz Plane AIC matrix was shown. Subsequently, the specifics of the devised shape parametrization approach based on the CPACS data format and the defined categories of shape design variables, but also the structural sizing and flight mechanical trim variables were described. Based on the analysis results, the multidisciplinary criteria model was defined and evaluated. Thus, the different available geometric and flight mechanical constraints together with strength, stability and mass constraints for the structural integrity included in the framework were presented. Following this, the different objective function formulations such as induced drag, structural FE mass and combinations of these two (i.e. weighted sum, Breguet range) were discussed. After the specifics of all required components of the developed framework were explained, the work flow and interaction of all components was highlighted paying special attention to the case of sensitivity analysis and the validation of its resulting gradient information.

With the entire multidisciplinary shape optimization framework defined, its application to the design of aircraft wings was studied in Chapter 4. This was split into two main parts. First, an approach of obtaining beneficial wing designs

through aeroelastic shape and sizing optimization was developed. Then, it was applied to the design of a transport aircraft of industrial scale complexity in the second section.

In order to evaluate the capabilities of the framework, aeroelastic shape and sizing optimization was applied to the large aspect-ratio wing of a generic UAV aircraft. A symmetrical airfoil and a rectangular wing planform (20 m wing span) was chosen as a neutral initial design, from which the different effects could be separately studied. The configuration of the parametric CPACS model of this wing was determined in a way so that shape variables could be defined at 11 evenly distributed span wise stations. A number of test optimizations were conducted in order to validate the physically sound behaviour of the developed approach. Hence, solutions for minimal induced drag and for minimal FE mass were compared with and without structural constraints assuring that the optimization would find the theoretically known minima. Additionally, the correct consideration of aeroelastic effects was validated by comparing the results of optimizations with and without aeroelastic analysis.

As gradient based optimizations can be strongly dependent on the initial point of the optimization for non-convex design spaces, initial point studies with a number of optimizations starting at different configurations were conducted for the induced drag and the FE mass objective. A non-convex design space could be detected for the induced drag objective function caused by an ambiguity of chord length and trimming design variables. For practical applications the found issue would be limited by a number of aspects, but nevertheless special attention would have to be paid to results achieved exclusively based on the induced drag objective function. Since the first number of optimizations already showed significant differences in their convergence behaviour, specifics in the optimization problem definition were identified that impeded convergence according to the Karush-Kuhn-Tucker criterion. This could be attributed to the number of active constraints at the end of the optimization process. Optimizations with an FE mass objective exhibited a greater number of active constraints at the end due to the usually opposed gradients of structural constraints and the mass objective. Induced drag optimizations, on the other hand, mainly showed an influence of the starting point on the number of active constraints at the end of the process overall allowing a more good-natured convergence behaviour.

In order to establish a procedure of applying the shape and sizing optimization framework to practical aircraft development a number of issues needed to be addressed (Section 4.2.1). First of all, a definition was sought as to how a *good* wing design was characterised and how to achieve a result with such attributes using the given framework. Hence, based on general considerations and the experience of the preceding shape optimizations already carried out, it was deduced that only a quality measure comprised of both, structural mass and induced drag, responses could sufficiently characterise the performance and quality of a wing design. For this, the Breguet range equation was chosen, as it combines both mentioned attributes in a physically meaningful way. Thus, different resulting wing designs could be evaluated and rated according to their achievable Breguet range. Next, the available objective functions in the frame-

work were studied and their optimization results compared using the Breguet range quality measure. As expected, the single discipline objectives of single FE mass and single induced drag led to the worst range performances, as the response of the respective other discipline was traded in for better objective function values. In case of the weighted objective functions combining normalized values for FE mass and induced drag, the issue of finding the most suitable weighting factor combination to reach a wing design with high Breguet range was discussed. In the presented case, an objective function with almost equal weighting slightly favouring the FE mass could produce the most promising results. However, no guarantee could be given that this represents a general rule. Yet, the objective function with the reduced Breguet range formulation described in Section 3.5 provided a result outperforming all other approaches. Thus, for further applications the Breguet range objective function was identified as the most suitable choice, since it did not require finding a beneficial weighting.

Based on the results of the different objective functions the assumption of keeping the viscous drag component constant during the shape optimization was verified. Re-analysing all obtained results regarding their viscous drag using flat plate skin friction with form factors [Ray06, p. 328] showed that considering the FE mass in the objective function would reduce the wetted surface area of the wing to which the viscous drag component is proportional according to the applied methods. Hence, the Breguet performance was improved by updating the viscous drag component to the current values for the Breguet range objective result but also for the best weighted objective results. Therefore, it was concluded that keeping the viscous drag coefficient constant during the optimizations was conservative and would not impede the performance of the results.

With the objective function selected, the most appropriate shape variable types to be used for optimizing aircraft wings with the developed framework were selected. Based on their individual characteristics and influence on the considered system responses, a combination of chord length and twist angle distributions, as well as, the overall wing span was chosen. For these shape parameters the design spaces regarding induced drag and FE mass were examined (Section 4.2.2.2), as general theory and previous tests suggested that this combination could cause non-convex design spaces. It was found that an infinite number of combinations between twist and chord length parameters exists for each spanwise station on the wing that yielded the theoretical minimum of induced drag. This interaction created a particular valley shaped design space with an even floor, which could be verified by a number of optimizations with different initial points. The wing span parameter, on the other hand, did not show any such interference with the other shape parameter types. Similar studies of the FE mass design space revealed that this behaviour would not have to be expected with any of the chosen shape parameters for this response type. Finally, the design space of a combined weighted objective was studied revealing that the issues with induced drag could be compensated by the tendencies of the FE mass response. This also showed that induced drag and FE mass have opposing gradients with respect to the wing span parameter underlining the

fact that finding the best wing span can only be achieved through a trade-off between the aerodynamic and structural disciplines.

Given the issues regarding the chosen shape parameter types and their respective design spaces, Section 4.2.3 presented and compared three different ways of approaching aeroelastic shape and sizing optimization with this combination of variables. The first one was to use a combined objective function (Breguet range) considering induced drag, as well as, FE mass responses so that the mentioned compensating effect of the FE mass component could be exploited. Secondly, an induced drag objective function was combined with a constraint on maximum FE mass making only parts of the mentioned design space valley floor feasible. The third approach was to separate the shape parameters into two consecutive shape optimizations so that no interference could arise between the chord length and twist design variables. All of these approaches included sizing variables and the full structural criteria model to assure physically feasible results. A comparison of results showed that the combined objective function approach yielded the result with the best performances followed closely by the second procedure with the mass constraint, which was explained by the fact that the boundary value for the mass constraint was taken from the first approaches' result. The sequential approach exhibited the worst range performance requiring two optimization runs. Comparing the resulting performance values and the manual interaction required to reach them, the first approach using the Breguet range objective function was confirmed as the most suitable procedure for technical application.

Based on the findings of the first part of Chapter 4, the wing tail configuration of a transport aircraft comparable to the Airbus A320 class (CSR-01 configuration of the CeRAS project [RSS+14]) was optimized applying the procedure derived in the preceding sections. This model was chosen to demonstrate the applicability of the framework to problems of industrial size and complexity. Using the parametric geometry definition, analysis meshes for aerodynamics and structures were derived setting up the optimization model with shape (chord length, twist, wing span), trimming and structural sizing design variables (over 1700 in total). The criteria model consisted of von Mises stress constraints, skin buckling and flight mechanical trim (lift force and pitch moment) constraints (roughly 26 000). These were evaluated on the results of one static parking load case and three aeroelastic flight states (cruise, push-over, pull-up), where cruise was used for induced drag evaluation and the remaining two provided the structural limit loads. After a preliminary sizing optimization to reach a feasible and realistic starting point, the shape and sizing optimization was carried out with the Breguet range objective function. The wing span was increased by this while adjusting the planform yielding a Breguet range increase of 8 % at almost constant aircraft mass. Problems originating from the non-convex induced drag design space found before could be ruled out by performing two additional shape optimizations with differing initial points that obtained almost the same designs.

The found wing design was compared to results achieved by the single discipline objective functions showing that only a compromise between both disciplines would yield designs with desirable performance. Also, the viscous

drag change after the optimizations was evaluated highlighting that for this model the assumption of constant viscous drag during the shape optimization was not conservative, but that the slight decrease in range by 1.3 % still left a significant performance improvement with respect to the initial design. Additionally, it could be shown that a constraint on the maximum wing area could account for this issue in the current state of the approach. Furthermore, the obtained result was compared to the solution of a corresponding rigid shape and sizing optimization not considering the aeroelastic effects in the process, which achieved a higher rigid Breguet range. An aeroelastic analysis of this rigid result showed significant losses in overall lift due to elastic deformation and, after aeroelastic re-trimming, substantial constraint violations were present. In order to reach a feasible design comparable to the original result, an aeroelastic sizing optimization was conducted based on the planform shape resulting of the rigid run. Along this course, a substantial mass increase was required to satisfy the structural constraints leading to a lower range performance than that of the original aeroelastic shape result. Additionally, it became obvious that considering aeroelasticity throughout the entire shape and sizing optimization allowed the optimizer to exploit aeroelastic effects for a beneficial outcome so that aeroelastic deformation would result in an increased range performance as opposed to the decrease in range shown by the rigid shape optimization.

In conclusion, this work treated the problem of developing a framework for aeroelastic shape and sizing optimization focusing on aeroelastic induced drag and FE mass suitable for application to aircraft design problems of industrial scale complexity. By using lower fidelity analysis methods and coupling them for aeroelastic analysis, a time efficient aeroelastic shape optimization with elastic induced drag evaluation was enabled applicable to earlier aircraft design phases, where a greater design freedom is still present. Furthermore, the framework's architecture of one central optimization loop for the shape, as well as, the sizing optimization using a combination of direct analytical sizing gradient computation and numerical shape gradients allowed the application to industrially relevant problems with a large criteria model guaranteeing technical feasibility of the results. Along the course of this work, the different components of the framework were studied and their physically sound behaviour verified. Furthermore, an optimization procedure was devised regarding a suitable objective function, an effective shape parameter combination and the general approach to such an optimization problem. Finally, the developed aeroelastic shape and sizing optimization framework was successfully applied to the wing design of an industrial scale aircraft model improving the aircraft's mission performance through this.

5.2 Outlook

In order to further increase the developed approach's fidelity and applicability to aircraft design, some extensions to its abilities should be included in the future.

As found by the different applications in Chapter 4, the viscous drag compon-

ent of the overall drag does have a significant influence on the Breguet range performance and cannot generally be presumed constant during the shape optimizations. Therefore, a viscous drag analysis suitable for early design such as the flat plate skin friction method combined with form factors (see e.g. [Mas02; Ray06]) should be included in the framework. This way, the sensitivities of the viscous drag component would be available to the optimizer allowing it to take into account the viscous drag response to any shape change as well.

Furthermore, the spanwise section lift coefficient was not limited in the optimizations conducted in this work. By modifying the planform shape of a wing through optimization, the maximum section lift coefficient can be reached for portions of the wing. If this value is exceeded, local stalling will occur inhibiting the aircraft controllability. The section lift coefficient can be reduced by lowering the local angle of attack (including twist) while increasing the local chord length. Thus, including constraints on the maximum local section lift coefficient during the shape optimizations would improve the quality of the achieved results.

In Section 3.3, the shape parameters were classified in different levels regarding their complexity and area of influence. In this work, only the first and second level shape parameters have been applied for global and component area shape changes. The remaining third level shape parameters for point wise geometry manipulation have not been used so far. This type of shape variables offers great potential for design problems in later aircraft development phases. However, to properly represent the effects caused by such minute changes, higher fidelity analysis methods would also be required. Therefore, an extension of the framework to higher fidelity methods (e.g. Euler, Navier-Stokes) and activating the third level shape parameters would expand its applicability also to problems in the detailed design phase.

The current implementation of the buckling constraints did not allow updating the buckling field geometry definition during the shape optimizations (see Section 3.4.2.2). Thus, the outer shape of the buckling fields was kept constant during the optimizations. Through this, only their sensitivity with respect to the element stress but not with respect to the buckling field geometry could be considered. The effect of this was found to be limited so that small adjustments to the sizing variables of a resulting design could correct any issues with violated buckling constraints. However, for future applications the buckling constraint implementation should be improved to also account for shape changes of the buckling field.

For usage in the Breguet objective function a fixed mission definition was applied in this thesis allowing to optimize the range of only one leg in the mission profile. To allow optimizing a wing design for more complex design missions considering the performance in more than one mission segment, the Breguet range analysis functionality should be extended. With this, missions simulating e.g. ingress, egress, loiter and detour segments could be optimized combining the performance of several of these legs into one objective function. Hence, the abilities of the developed framework could be applied to more realistic mission scenarios.

Bibliography

[AR68] E. Albano and W. Rodden. 'A Doublet Lattice Method for Calculating Lift Distributions on Oscillating Surfaces in Subsonic Flows'. In: *AIAA 6th Aerospace Sciences Meeting*. 1968 (cit. on pp. 23, 50).

[BAH96] R. L. Bisplinghoff, H. Ashley and R. Halfman. *Aeroelasticity*. Dover Publications, 1996 (cit. on pp. 15, 20, 113, 116, 174).

[BB90] G. W. Brune and P. W. Bogataj. 'Induced Drag of a Simple Wing from Wake Measurements'. In: *Aerospace Technology Conference and Exposition*. 1990 (cit. on p. 31).

[BD13] D. Boehnke and F. Dorbath. *CPACS 2.1 Documentation*. DLR. Oct. 2013. URL: `http://code.google.com/p/cpacs/downloads/detail?name=CPACS_21_Documentation.zip&can=2&q=` (cit. on p. 58).

[BG03] J. Brezillon and N. R. Gauger. '2D And 3D Aerodynamic Shape Optimisation Using The Adjoint Approach'. In: *Deutscher Luft- und Raumfahrtkongress*. 2003 (cit. on p. 41).

[BH88] B. Barthelemy and R. T. Haftka. 'Accuracy Analysis Of The Semi-Analytical Method For Shape Sensitivity Calculation'. In: *29th Structures, Structural Dynamics and Materials Conference*. 1988 (cit. on pp. 45, 46).

[BM05] M. A. Buonanno and D. N. Mavris. 'A New method for Aircraft Concept Selection Using Multicriteria Interactive Genetic Algorithms'. In: *43rd AIAA Aerospace Sciences Meeting and Exhibit*. 2005 (cit. on pp. 2, 3).

[BM08] M. Barcelos and K. Maute. 'Aeroelastic Design Optimization for Laminar and Turbulent Flows'. In: *Computer Methods in Applied Mechanics and Engineering* 197 (2008), pp. 1813–1832 (cit. on pp. 10, 12).

[BRM+10] D. Brujic, M. Ristic, M. Mattone, P. Maggiore and G. P. D. Poli. 'CAD Based Shape Optimization For Gas Turbine Component Design'. In: *Structural and Multidisciplinary Optimization* 41 (2010), pp. 647–659. DOI: `10.1007/s00158-009-0442-9` (cit. on pp. 40, 41).

[BSM+01] I. N. Bronstein, K. A. Semendjajew, G. Musiol and H. Mühlig. *Taschenbuch der Mathematik*. 5th ed. ISBN 3-8171-2005-2. Harri Deutsch Verlag, 2001 (cit. on p. 52).

[BSS06] H. Baier, C. Seeßelberg and B. Specht. *Optimierung in der Strukturmechanik*. LSS Verlag, 2006 (cit. on pp. 34, 36, 38, 46–48, 117, 118, 135).

[Bar87] A. H. Barr. 'Global and Local Deformations of Solid Primitives'. In: *Readings in Computer Vision* (1987), pp. 661–670. DOI: 10.1016/B978-0-08-051581-6.50064-7. URL: http://www.sciencedirect.com/science/article/pii/B9780080515816500647 (cit. on pp. 40, 58).

[Bru73] E. F. Bruhn. *Analysis and Design of Flight Vehicle Structures*. Jacobs Publishing Inc., 1973 (cit. on p. 68).

[CE04] N. Camprubi-Estebo. 'Design and Analysis in Shape Optimization of Shells'. PhD thesis. Technische Universität München, 2004 (cit. on pp. 40, 83).

[CIK+10] V. V. Chedrik, F. Z. Ishmuratov, S. I. Kuzmina and M. C. Zichenkov. 'Strength/Aeroelasticity Research at Multidisciplinary Structural Design of High Aspect Ratio Wing'. In: *27th International Congress of the Aeronautical Sciences, ICAS2010*. 2010 (cit. on p. 7).

[CIK06] V. V. Chedrik, F. Z. Ishmuratov and S. I. Kuzmina. 'Multidisciplinary Structural Analysis And Optimization Of Different Configuration Wings'. In: *11th AIAA/ISSMO Multidisciplinary Analysis and Optimization Conference*. 2006 (cit. on p. 7).

[CIK12] V. V. Chedrik, F. Z. Ishmuratov and S. I. Kuzmina. 'Aero-structural optimization of high-aspect-ratio wings'. In: *12th AIAA Aviation Technology, Integration, and Operations (ATIO) Conference and 14th AIAA/ISSM*. 2012 (cit. on pp. 7, 27).

[CIK14] V. Chedrik, F. Z. Ishmuratov and S. I. Kuzmina. 'Two-Level Multidisciplinary Design Investigation Of High-Aspect-Ratio Wing With Swept-Wing-Tip'. In: *4th Aircraft Structural Design Conference*. 2014 (cit. on pp. 7, 12).

[CN07] P. Castonguay and S. K. Nadarajah. 'Effect Of Shape Parameterization On Aerodynamic Shape Optimization'. In: *45th AIAA Aerospace Sciences Meeting and Exhibit*. 2007 (cit. on p. 41).

[CRR+08a] L. Cavagna, L. Riccobene, S. Ricci, A. Bérard and A. Rizzi. 'A Fast MDO Tool for Aeroelastic Optimization in Aircraft Conceptual Design'. In: *12th AIAA/ISSMO Multidisciplinary Analysis and Optimization Conference*. AIAA 2008-5911. 2008 (cit. on pp. 2, 6).

[CRR+08b] L. Cavagna, L. Riccobene, S. Ricci, A. Berard and A. Rizzi. 'A Fast Tool For Structural Sizing, Aeroelastic Analysis And Optimization In Aircraft Conceptual Design'. In: *12th AIAA/ISSMO Multidisciplinary Analysis and Optimization Conference*. 2008 (cit. on pp. 6, 12).

[CRR09] L. Cavagna, S. Ricci and L. Riccobene. 'A Fast Tool For Structural Sizing, Aeroelastic Analysis And Optimization In Aircraft Conceptual Design'. In: *50th AIAA/ASME/ASCE/AHS/ASC Structures, Structural Dynamics, and Materials Conference*. 2009 (cit. on pp. 6, 17, 21).

[CRT10a] L. Cavagna, S. Ricci and L. Travaglini. 'NeoCASS: An Integrated Tool For Structural Sizing, Aeroelastic Analysis And MDO At Conceptual Design Level'. In: *AIAA Atmospheric Flight Mechanics Conference*. 2010 (cit. on pp. 6, 12).

[CRT10b] L. Cavagna, S. Ricci and L. Travaglini. 'Structural Sizing And Aeroelastic Optimization In Aircraft Conceptual Design Using NeoCASS Suite'. In: *13th AIAA/ISSMO Multidisciplinary Analysis Optimization Conference*. 2010 (cit. on p. 6).

[Che13] V. Chedrik. 'Two-Level Design Optimization Of Aircraft Structures Under Stress, Buckling And Aeroelasticity Constraints'. In: *10th World Congress on Structural and Multidisciplinary Optimization*. 2013 (cit. on p. 18).

[DAK+13] J. Dillinger, M. Abdalla, T. Klimmek and Z. Gürdal. 'Static Aeroelastic Stiffness Optimization and Investigation of Forward Swept Composite Wings'. In: *10th World Congress on Structural and Multidisciplinary Optimization*. 2013 (cit. on pp. 18, 21).

[DDK+06] L. Daumas, Q. Dinh, S. Kleinveld and G. Roge. 'Fuselage Shape Automatic Optimization With Geometric Constraints Using A CAD Based Process'. In: *11th AIAA/ISSMO Multidisciplinary Analysis and Optimization Conference*. 2006 (cit. on p. 40).

[DDM+15] F. Daoud, S. Deinert, R. Maierl and Ö. Petersson. 'Integrated Multidisciplinary Aircraft Design Process Supported by a Decentral MDO Framework'. In: *16th AIAA/ISSMO Multidisciplinary Analysis and Optimization Conference, AIAA Aviation*. AIAA 2015-3090. 2015.

[DMS04] P. W. De Baets, D. N. Mavris and J. Sobieszczanski-Sobieski. 'Aeroelastic Design by Combining Conventional Practice with Bi-Level Integrated System Synthesis (BLISS)'. In: *10th AIAA/ISSMO Multidisciplinary Analysis and Optimization Conference*. 2004 (cit. on pp. 7, 12).

[DPD+12] F. Daoud, Ö. Petersson, S. Deinert and P. Bronny. 'Multidisciplinary Airframe Design Process: Incorporation Of Steady And Unsteady Aeroelastic Loads'. In: *12th AIAA Aviation Technology, Integration, and Operations (ATIO) Conference and 14th AIAA/ISSMO Multidisciplinary Analysis and Optimization Conference*. 2012 (cit. on p. 50).

[DPD+13a] S. Deinert, Ö. Petersson, F. Daoud and H. Baier. 'Aeroelastic Tailoring Through Combined Sizing and Shape Optimization Considering Induced Drag'. In: *4th CEAS Air & Space Conference*. 2013 (cit. on pp. 69, 72, 75, 141).

[DPD+13b] S. Deinert, Ö. Petersson, F. Daoud and H. Baier. 'Aircraft Loft Optimization With Respect To Aeroelastic Lift And Induced Drag Loads'. In: *10th World Congress on Structural and Multidisciplinary Optimization*. 2013 (cit. on pp. 42, 59, 94).

[DY10] M. Drela and H. Youngren. *AVL 3.30 User Primer*. 2010. URL: http://web.mit.edu/drela/Public/web/avl/ (cit. on pp. 22, 50).

[Dao05] F. Daoud. 'Formoptimierung von Freiformschalen Mathematische Algorithmen und Filtertechniken'. PhD thesis. Technische Universität München, 2005 (cit. on pp. 36–38, 40, 43, 45).

[ET14] A. Elham and M. J. L. van Tooren. 'Effect of Wing-Box Structure on the Optimum Wing Outer Shape'. In: *The Aeronautical Journal* 118 (2014), pp. 1–30 (cit. on p. 127).

[FLL98] C. Farhat, M. Lesoinne and P. LeTallec. 'Load And Motion Transfer Algorithms For Fluid/Structure Interaction Problems With Non-Matching Discrete Interfaces: Momentum And Energy Conservation, Optimal Discretization And Application To Aeroelasticity'. In: *Computer Methods In Applied Mechanics And Engineering* 157 (1998), pp. 95–114 (cit. on p. 21).

[FP04] C. A. Felippa and K. C. Park. *Synthesis Tools for Structural Dynamics and Partitioned Analysis of Coupled Systems*. University of Colorado at Boulder. 2004. URL: http://www.colorado.edu/engineering/CAS/courses.d/FSI.d/NATO-ARW.Felippa.paper.rev.pdf (cit. on p. 15).

[Fel14] C. Felippa. *Introduction to Finite Element Methods*. Website. Feb. 2014. URL: http://www.colorado.edu/engineering/CAS/courses.d/IFEM.d/Home.html (cit. on pp. 17, 67, 83).

[Fir10] M. Firl. 'Optimal Shape Design of Shell Structures'. PhD thesis. Technischen Universität München, 2010 (cit. on pp. 40, 45).

[Fle70] R. Fletcher. 'A New Approach to Variable Metric Algorithms'. In: *The Computer Journal* 13.3 (1970), pp. 317–322. DOI: 10.1093/comjnl/13.3.317 (cit. on p. 43).

[GBM+10] O. Gur, M. Bhatia, W. H. Mason, J. A. Schetz and R. K. Kapania. 'Development of Framework for Truss-Braced Wing Conceptual MDO'. In: *51st AIAA/ASME/ASCE/AHS/ASC Structures, Structural Dynamics, and Materials Conference*. 2010 (cit. on pp. 5, 12, 27, 76, 126).

[GBS+10] O. Gur, M. Bhatia, J. A. Schetz, W. H. Mason and R. K. Kapania. 'Design Optimization of a Truss-Braced-Wing Transonic Transport Aircraft'. In: *Journal of Aircraft* 47.6 (2010), pp. 1907–1917 (cit. on pp. 5, 12).

[GKC+12] S. S. Ghoman, R. K. Kapania, P. C. Chen, D. Sarhaddi and D. H. Lee. 'Multifidelity, Multistrategy, and Multidisciplinary Design Optimization Environment'. In: *Journal of Aircraft* 49 (2012), pp. 1255–1270 (cit. on pp. 8, 12, 76, 126).

[GWR02] R. Gilmore, S. Wakayama and D. Roman. 'Optimization of High-Subsonic Blended-Wing-Body Configurations'. In: *9th AIAA/ISSMO Symposium on Multidisciplinary Analysis and Optimization*. 2002 (cit. on pp. 6, 12).

[Giu99] A. A. Giunta. 'Sensitivity Analysis Method For Aeroelastic Aircraft Models'. In: *Aircraft Design* 2 (1999), pp. 207–230 (cit. on pp. 18, 21).

[Gol70] D. Goldfarb. 'A Family of Variable-Metric Methods Derived by Variational Means'. In: *Mathematics Computation* 24 (1970), pp. 23–26 (cit. on p. 43).

[Gun04] J. F. Gundlach. 'Multi-Disciplinary Design Optimization Of Subsonic Fixed-Wing Unmanned Aerial Vehicles Projected Through 2025'. PhD thesis. Virginia Polytechnic Institute and State University, 2004 (cit. on pp. 5, 12, 27).

[HD72] R. L. Harder and R. N. Desmarais. 'Interpolation Using Surface Splines'. In: *Journal of Aircraft* 9 (1972), pp. 189–191 (cit. on pp. 33, 186).

[HG85] R. T. Haftka and R. V. Grandhi. 'Structural Shape Optimization - A Survey'. In: *Computer Methods In Applied Mechanics And Engineering* 57 (1985), pp. 91–106 (cit. on p. 38).

[HG92] R. T. Haftka and Z. Gürdal. *Elements of Structural Optimization*. Springer Science & Business Media, 1992 (cit. on p. 43).

[HGR06] J.-L. Hantrais-Gervois and M. Rapin. 'Aerodynamic And Structural Behaviour Of A Wing Equipped With A Winglet At Cruise'. In: *44th AIAA Aerospace Sciences Meeting and Exhibit*. 2006 (cit. on p. 21).

[HM12] J. T. Hwang and J. R.R. A. Martins. 'GeoMACH: Geometry-Centric MDAO of Aircraft Configurations with High Fidelity'. In: *14th AIAA/ISSMO Multidisciplinary Analysis Optimization Conference*. 2012 (cit. on pp. 9, 12, 42, 60).

[HML12] S. Haghighat, J. R.R. A. Martins and H. H. T. Liu. 'Aeroservoelastic Design Optimization of a Flexible Wing'. In: *Journal of Aircraft* 49 (2012), pp. 432–443 (cit. on pp. 6, 12, 17, 21, 76, 126).

[HNS+08] S. M. Hitzel, L. Nardin, K. Sørensen and H. Rieger. 'Aerodynamic Optimization Of Aircraft Configurations With Multidisziplinary Aspects'. In: *26th International Congress Of The Aeronautical Sciences*. 2008 (cit. on p. 41).

[Hah10] A. S. Hahn. 'Vehicle Sketch Pad: A Parametric Geometry Modeler for Conceptual Aircraft Design'. In: *48th AIAA Aerospace Sciences Meeting*. 2010 (cit. on p. 41).

[Har08] L. Harzheim. *Strukturoptimierung - Grundlagen und Anwendung*. 1st. Harri Deutsch Verlag, 2008 (cit. on pp. 35–37, 43, 46–48).

[Hed66] S. Hedman. *Vortex Lattice Method For Calculation Of Quasi Steady State Loadings On Thin Elastic Wings In Subsonic Flow*. Tech. rep. Flygtekniska Försöksanstalten, 1966 (cit. on pp. 22, 23, 30).

[Hö93] H. R.E. M. Hörnlein. 'Lokale Stabilität als Nebenbedingung in der Strukturoptimierung'. In: *COMETT-Seminar: Computerunterstützte Strukturoptimierung*. Wissenschaftszentrum Schloß Thurnau, Bayreuth, 1993 (cit. on pp. 68, 69).

[Hü10] F. Hürlimann. 'Mass Estimation of Transport Aircraft Wingbox Structures with a CAD/CAE Based Multidisciplinary Process'. PhD thesis. ETH Zurich, 2010 (cit. on pp. 8, 12).

[IC03] F. Z. Ishmuratov and V. V. Chedrik. 'Argon Code: Structural Aeroelastic Analysis And Optimization'. In: *International Forum on Aeroelasticity and Aerodynamics*. 2003 (cit. on p. 21).

[IM01] S. Iglesias and W. Mason. 'Optimum Spanloads Incorporating Wing Structural Weight'. In: *First AIAA Aircraft Technology, Integration, and Operations Forum*. AIAA-2001-5234. 2001 (cit. on pp. 5, 76, 126, 134).

[JKM14] K. A. James, G. J. Kennedy and J. R. Martins. 'Concurrent aerostructural topology optimization of a wing box'. In: *Computers and Structures* 134 (2014), pp. 1–17 (cit. on pp. 2, 8, 12, 21).

[JPM10] P. W. Jansen, R. E. Perez and J. R.R. A. Martins. 'Aerostructural Optimization of Nonplanar Lifting Surfaces'. In: *Journal of Aircraft* 47.5 (2010), pp. 1490–1503 (cit. on pp. 7, 12, 76, 126).

[Jon50] R. T. Jones. *The Spanwise Distribution of Lift for Minimum Induced Drag of Wings Having a Given Lift and a Given Bending Moment*. Tech. rep. 2249. National Advisory Committee for Aeronautics, 1950 (cit. on pp. 5, 134).

[KE06] R. M. Kolonay and F. E. Eastep. 'Induced Drag Minimization Of A Free Flying Flexible Vehicle Using Trailing Edge Control Surfaces'. In: *11th AIAA/ISSMO Multidisciplinary Analysis and Optimization Conference*. 2006 (cit. on p. 21).

[KIK+03] S. Kuzmina, F. Ishmuratov, V. Kuzmin and Y. Sviridenko. 'Estimation Of Flying Vehicle Induced Drag Changing Due To Deformation Of Lifting Surfaces'. In: *International Forum on Aeroelasticity and Structural Dynamics*. 2003 (cit. on pp. 7, 12).

[KIK04] S. Kuzmina, F. Ishmuratov and V. Kuzmin. 'Minimization Of Induced Drag Of Elastic Airplane'. In: *10th AIAA/ISSMO Multidisciplinary Analysis and Optimization Conference*. 2004 (cit. on pp. 7, 30).

[KKM10] G. K. Kenway, G. J. Kennedy and J. R.R. A. Martins. 'A CAD-free Approach To High-fidelity Aerostructural Optimization'. In: *13th AIAA/ISSMO Multidisciplinary Analysis Optimization Conference*. 2010 (cit. on pp. 9, 12, 21, 76).

[KKM12] G. K. Kenway, G. J. Kennedy and J. R.R. A. Martins. 'A Scalable Parallel Approach for High-Fidelity Aerostructural Analysis and Optimization'. In: *53rd AIAA/ASME/ASCE/AHS/ASC Structures, Structural Dynamics, and Materials Conference*. 2012 (cit. on pp. 9, 27, 76, 126).

[KL09] T. M. Kier and G. H. N. Looye. 'Unifying Manoeuvre And Gust Loads Analysis Models'. In: *International Forum of Aeroelasticity and Structural Dynamics IFASD*. 2009 (cit. on pp. 23, 24, 30, 50).

[KP01] J. Katz and A. Plotkin. *Low-Speed Aerodynamics*. Ed. by M. J. Rycroft and W. Shyy. 2nd. Cambridge University Press, 2001 (cit. on pp. 19, 20, 22–28, 30, 104, 114).

[Ken12] G. J. Kennedy. 'Aerostructural Analysis And Design Optimization Of Composite Aircraft'. PhD thesis. University of Toronto, 2012 (cit. on pp. 8, 12, 21, 180).

[Kim90] S. Kimmich. 'Strukturoptimierung und Sensibilitätsanalyse mit Finiten Elementen'. PhD thesis. Universität Stuttgart, 1990 (cit. on p. 43).

[Kle07] B. Klein. *FEM - Grundlagen und Anwendungen der Finite-Element-Methode im Maschinen- und Fahrzeugbau*. Ed. by H. K. von Burgsdorff. 7th. Friedr. Vieweg & Sohn Verlag, 2007 (cit. on p. 17).

[Kro01] I. Kroo. 'Drag due to Lift : Concepts for Prediction and Reduction'. In: *Annual Review of Fluid Mechanics* 33 (2001), pp. 587–617 (cit. on pp. 4, 25).

[LH11] C. M. Liersch and M. Hepperle. 'A Distributed Toolbox For Multidisciplinary Preliminary Aircraft Design'. In: *CEAS Aeronautical Journal* 2 (2011), pp. 57–68 (cit. on pp. 49, 56, 59, 186).

[LT08] G. La Rocca and M. J. van Tooren. 'Knowledge Based Engineering to Support Aircraft Multidisciplinary Design and Optimisation'. In: *26th International Congress of the Aeronautical Sciences*. 2008 (cit. on pp. 9, 41, 186).

[MA04] K. Maute and M. Allen. 'Conceptual Design Of Aeroelastic Structures By Topology Optimization'. In: *Structural and Multidisciplinary Optimization* 27 (2004), pp. 27–42. DOI: 10.1007/s00158-003-0362-z (cit. on p. 21).

[MAL+14] M. J. Martin, E. Andres, C. Lozano and E. Valero. 'Volumetric B-Splines Shape Parametrization For Aerodynamic Shape Design'. In: *Aerospace Science and Technology* 37 (2014), pp. 26–36 (cit. on p. 40).

[MAR08] A. Morris, C. Allen and T. Rendall. 'Wing Design By Aerodynamic And Aeroelastic Shape Optimisation'. In: *26th AIAA Applied Aerodynamics Conference*. 2008 (cit. on pp. 18, 21, 55).

[MAW+10] M. Martín, E. Andrés, M. Widhalm, P. Bitrián and C. Lozano. 'CAD-based Aerodynamic Shape Design Optimization With The DLR Tau Code'. In: *27th International Congress Of The Aeronautical Sciences*. 2010 (cit. on p. 42).

[MNF01] K. Maute, M. Nikbay and C. Farhat. 'Coupled Analytical Sensitivity Analysis and Optimization of Three-Dimensional Nonlinear Aeroelastic Systems'. In: *AIAA Journal* 39.11 (2001), pp. 2051–2061 (cit. on pp. 9, 12).

[MPD13] R. Maierl, Ö. Petersson and F. Daoud. 'Automated Creation Of Aeroelastic Optimization Models From A Parameterized Geometry'. In: *International Forum on Aeroelasticity & Structural Dynamics*. 2013 (cit. on pp. 42, 49, 59).

[MTC11] F. Mastroddi, M. Tozzi and V. Capannolo. 'On The Use Of Geometry Design Variables In The MDO Analysis Of Wing Structures With Aeroelastic Constraints On Stability And Response'. In: *Aerospace Science and Technology* 15 (2011), pp. 196–206. DOI: 10.1016/j.ast.2010.11.003 (cit. on p. 18).

[MV01] K. Meyberg and P. Vachenauer. *Höhere Mathematik 1*. 6th. Springer-Verlag, 2001 (cit. on p. 43).

[Mar02] J. R.R. A. Martins. 'A Coupled-adjoint Method For High-fidelity Aero-structural Optimization'. PhD thesis. Stanford University, 2002 (cit. on pp. 9, 11, 12, 36, 37).

[Mas02] W. Mason. *FRICTION v3*. Webpage. 2002. URL: http://www.dept.aoe.vt.edu/~mason/Mason_f/MRsoft.html#SkinFriction (cit. on pp. 22, 27, 127, 136, 169, 191).

[Mel00] T. Melin. 'A Vortex Lattice MATLAB Implementation for Linear Aerodynamic Wing Applications'. MA thesis. Royal Institute of Technology (KTH), Department of Aeronautics, 2000 (cit. on p. 30).

[Mun23] M. M. Munk. *The Minimum Induced Drag Of Aerofoils*. Tech. rep. NACA-TR-121. NACA, 1923 (cit. on p. 178).

[NBK+12] A. Nurdin, N. W. Bressloff, A. J. Keane and C. M. E. Holden. 'Shape Optimisation Using CAD Linked Free-Form Deformation'. In: *The Aeronautical Journal* 116 (2012), pp. 915–939 (cit. on p. 40).

[NCB08] D. Neufeld, J. Chung and K. Behdinan. 'Development of a Flexible MDO Architecture for Aircraft Conceptual Design'. In: *EngOpt 2008 - International Conference on Engineering Optimization*. 2008 (cit. on pp. 5, 12).

[NKS08] B. Nagel, M. Kintscher and T. Streit. 'Active and Passive Structural Measures for Aeroelastic Winglet Design'. In: *ICAS Congress 2008*. 2008 (cit. on p. 10).

[NRM+06] B. Nagel, M. Rose, H. P. Monner and R. Heinrich. 'An Alternative Procedure for FE-Wing Modelling'. In: *Deutscher Luft- und Raumfahrtkongress*. 2006 (cit. on p. 10).

[Nas] *MSC Nastran 2013.1.1 Quick Reference Guide*. MSC.Software Corporation. 2014 (cit. on p. 96).

[PAK04] P. Piperni, M. Abdo and F. Kafyeke. 'The Application of Multi-Disciplinary Optimization Technologies to the Design of a Business Jet'. In: *10th AIAA/ISSMO Multidisciplinary Analysis and Optimization Conference*. 2004 (cit. on pp. 7, 12).

[PCK07] S. Pierret, R. F. Coelho and H. Kato. 'Multidisciplinary And Multiple Operating Points Shape Optimization Of Three-dimensional Compressor Blades'. In: *Structural and Multidisciplinary Optimization* 33 (2007), pp. 61–70. DOI: 10.1007/s00158-006-0033-y (cit. on p. 41).

[Phi04] W. F. Phillips. 'Lifting-Line Analysis for Twisted Wings and Washout-Optimized Wings'. In: *Journal of Aircraft* 41.1 (2004), pp. 128–136 (cit. on pp. 141, 144).

[Pra18] L. Prandtl. 'Tragflügeltheorie'. In: *Nachrichten von der Gesellschaft der Wissenschaften zu Göttingen* Mathematisch-Physikalische Klasse (1918), pp. 451–477 (cit. on p. 144).

[Pra33] L. Prandtl. 'Über Tragflügel kleinsten induzierten Widerstandes'. In: *Zeitschrift für Flugtechnik und Motorluftschiffahrt* 24 (1933), pp. 305–306 (cit. on pp. 4, 134).

[RMS95] P. J. Röhl, D. N. Mavris and D. P. Schrage. 'Combined Aerodynamic and Structural Optimization of a High-Speed Civil Transport Wing'. In: *36th Structures, Structural Dynamics and Materials Conference*. 1995 (cit. on pp. 3, 5, 6, 12, 72).

[RSS+14] K. Risse, K. Schäfer, F. Schültke and E. Stumpf. *CeRAS - Central Reference Aircraft data System*. Webpage. 2014. URL: http://ceras.ilr.rwth-aachen.de/trac (cit. on pp. xx, 163, 189).

[Ray06] D. P. Raymer. *Aircraft Design: A Conceptual Approach*. Ed. by J. A. Schetz. 4th. American Institute of Aeronautics and Astronautics, 2006 (cit. on pp. 1, 19–22, 24, 26, 27, 76, 116, 126, 136, 140, 142, 188, 191).

[SB00] J. A. Samareh and K. G. Bhatia. 'A Unified Approach to Modeling Multidisciplinary Interactions'. In: *8th AIAA/USAF/NASA/ISSMO Symposium on Multidisciplinary Analysis and Optimization*. 2000 (cit. on pp. 42, 59).

[SCH+07] J. A. Samareh, P. Chwalowski, L. G. Horta, D. J. Piatak and A.-M. R. McGowan. 'Integrated Aerodynamic/Structural/Dynamic Analyses Of Aircraft With Large Shape Changes'. In: *48th AIAA/-ASME/ASCE/AHS/ASC Structures, Structural Dynamics, and Materials Conference*. 2007 (cit. on p. 21).

[SDP+12] G. Schuhmacher, F. Daoud, Ögmundur Petersson and M. Wagner. 'Multidisciplinary Airframe Design Optimisation'. In: *28th International Congress of the Aeronautical Sciences*. 2012 (cit. on pp. 50, 64, 65, 67, 70, 75, 79, 81, 83, 85, 87).

[SK93] S. C. Smith and I. M. Kroo. 'Computation of Induced Drag for Elliptical and Crescent-Shaped Wings'. In: *Journal of Aircraft* 30 (1993), pp. 446–452 (cit. on p. 25).

[SM01] J. E. Shigley and C. R. Mischke. *Mechanical Engineering Design*. McGraw-Hill, 2001 (cit. on p. 67).

[SP86] T. W. Sederberg and S. R. Parry. 'Free-form Deformation of Solid Geometric Models'. In: *ACM SIGGRAPH Computer Graphics* 20.4 (1986), pp. 151–160. DOI: 10.1145/15886.15903. URL: http://dl.acm.org/citation.cfm?id=15903 (cit. on pp. 40, 58).

[SSK+14] C. M. Shirley, J. A. Schetz, R. K. Kapania and R. T. Haftka. 'Tradeoffs of Wing Weight and Lift/Drag in Design of Medium-Range Transport Aircraft'. In: *Journal of Aircraft* 51.3 (2014), pp. 904–912 (cit. on pp. 3, 5, 27).

[ST01a] H. Schlichting and E. Truckenbrodt. *Aerodynamik des Flugzeuges Erster Band*. 3rd. Springer, 2001 (cit. on pp. 18–20, 22, 24, 26, 28, 101).

[ST01b] H. Schlichting and E. Truckenbrodt. *Aerodynamik des Flugzeuges Zweiter Band*. Springer, 2001 (cit. on pp. 105, 174).

[Sam99] J. A. Samareh. 'A Survey Of Shape Parameterization Techniques'. In: *CEAS/AIAA/ICASE/NASA Langley International Forum on Aeroelasticity and Structural Dynamics*. 1999 (cit. on pp. 8, 9, 39–41, 58).

[San72] R. S. Sandhu. *A Survey Of Failure Theories Of Isotropic And Anisotropic Materials*. Tech. rep. AFFDL-TR-72-71. Wright-Patterson Air Force Base, Ohio, 1972 (cit. on p. 67).

[Sch86] K. Schittkowski. 'NLPQL: A Fortran Subroutine For Solving Constrained Nonlinear Programming Problems'. In: *Annals of Operations Research* 5 (1986), pp. 485–500 (cit. on pp. 38, 43, 186).

[Sha70] D. F. Shanno. 'Conditioning of Quasi-Newton Methods for Function Minimization'. In: *Mathematics Computation* 24.111 (1970), pp. 647–656 (cit. on p. 43).

[Str12] M. H. Straathof. 'Shape Parameterization In Aircraft Design: A Novel Method, Based On B-splines'. PhD thesis. TU Delft, 2012 (cit. on pp. 39, 40).

[Tre21] E. Trefftz. 'Prandtlsche Tragflächen- und Propeller-Theorie'. In: *Zeitschrift für angewandte Mathematik und Mechanik* 1 (1921), pp. 206–218 (cit. on pp. 5, 7, 25, 50).

[VIW+11] C. Vidy, D. M. Iatrou, D. C. Weishäupl, D. Fleischer, M. Förster and D. C. Breitsamter. 'Development Of Aerodynamic Influence Coefficients Based On CFD Codes For Aeroelastic Applications'. In: *International Forum on Aeroelasticity and Structural Dynamics*. 2011 (cit. on p. 50).

[VS86] J. Vinson and R. Sierakowski. *The Behaviour of Structures Composed of Composite Materials*. Ed. by J. Przemieniecki and G. A. Oravas. Martinus Nijhoff Publishers, 1986 (cit. on p. 67).

[Van07] G. N. Vanderplaats. *Multidiscipline Design Optimization*. Vanderplaats Research & Development, Inc., 2007 (cit. on pp. 2, 11, 34, 36–38, 42, 45–47).

[Van80] G. N. Vanderplaats. 'Comment on "Methods of Design Sensitivity Analysis in Structural Optimization"'. In: *AIAA Journal* 18, No. 11 (1980), pp. 1406–1407 (cit. on p. 45).

[WDD00] T. A. Weisshaar, D. K. Duke and A. Dobbins. 'Active Aeroelastic Tailoring With Adaptive Continuous Control Surfaces'. In: *41st AIAA/ASME/ASCE/AHS/ASC Structures, Structural Dynamics and Materials Conference and Exhibit*. 2000 (cit. on pp. 3, 72, 113).

[WK95] S. Wakayama and I. Kroo. 'Subsonic Wing Planform Design Using Multidisciplinary Optimization'. In: *Journal of Aircraft* 32 (1995), pp. 746–753 (cit. on pp. 6, 12, 27).

[Wak00] S. Wakayama. 'Blended-Sing-Body Optimization Problem Setup'. In: *8th AIAA/USAF/NASA/ISSMO Symposium on Multidisciplinary Analysis and Optimization*. 2000 (cit. on p. 6).

[Wei47] J. Weissinger. *The Lift Distribution of Swept-Back Wings*. Tech. rep. 1120. National Advisory Committee for Aeronautics, 1947 (cit. on p. 5).

[Wun13] T. F. Wunderlich. 'Multidisziplinäre Optimierung von Flügeln für Verkehrsflugzeuge mit Berücksichtigung der statischen Aeroelastizität'. PhD thesis. Technische Universität Carolo-Wilhelmina zu Braunschweig, 2013 (cit. on pp. 2, 10, 12, 18, 21, 36, 39–41, 76, 126).

[ZT05] O. C. Zienkiewicz and R. L. Taylor. *The Finite Element Method*. 6th. Butterworth-Heinemann, 2005 (cit. on pp. 17, 67, 68, 83).

[De 11] R. De Breuker. 'Energy-based Aeroelastic Analysis And Optimisation Of Morphing Wings'. PhD thesis. Technische Universiteit Delft, 2011 (cit. on pp. 5, 12, 17, 21).

[Ope13] Open CASCADE S.A.S. *Open CASCADE Technology - 3D modeling & numerical simulation*. Apr. 2013. URL: `www.opencascade.org` (cit. on pp. 41, 49, 59).